The members of the Committee approve the dissertation of Gianluigi Boca defended on December 15th 1989.

D. Levinthal
Professor Directing Dissertation

G. Ricciardi
Outside Committee Member

L. Dennis
Committee Member

D. Duke
Committee Member

V. Hagopian
Committee Member

FERMILAB
LIBRARY

EXPERIMENTAL DETERMINATION OF THE AVERAGE FRACTION OF JET MOMENTUM CARRIED BY LEADING HADRONS PRODUCED AT LARGE TRANSVERSE MOMENTA

(Publication No.)

Gianluigi Boca, Ph.D.
The Florida State University, 1990

Major Professor: David A. Levinthal, Ph.D.

The average fraction ($\equiv < \mathcal{Z} >$) of jet momentum carried by the associated charged leading hadron has been determined in the reaction $p + N \rightarrow h_1 + h_2 + X$ where h_1 and h_2 were two high $P_\perp$ hadrons, leading particles of two jets produced at high $P_\perp$. A 800 GeV/c proton beam and four nuclear targets: beryllium, aluminium, iron and tungsten were used. The data were taken at the Fermi National Accelerator Laboratory from November 1987 - February 1988.

The detector was a double arm magnetic spectrometer, with two sampling calorimeters for real-time event selection and was capable of operating at a high interaction rate ($\approx 2.5 \times 10^6$ interactions per second).

$< \mathcal{Z} >$ has been determined as a function of the transverse momentum of the leading hadron and the cosine of the scattering angle of the leading hadron pair in the di-hadron C.o.M. system, for positive, negative and both sign charges of the leading hadron and for each target.

The fragmentation process was found to be independent of nuclear effects

and the amount of nuclear matter the fragmenting parton went through. The $< \mathcal{Z} >$ distributions agree with the QCD-parton model predictions for single independent parton-parton scattering and independent fragmentation process.

Agreement has also been found between these data and previously published results obtained in a *pp* collider experiment confirming the independence of the fragmentation process from nuclear effects in high $P_{\perp}$ interactions.

to my daughter,

Marina

This research was supported in part by funds from the U. S. Department of Energy, grant number DE-FG05-87ER-40319. Permission is granted to copy this dissertation.

ACKNOWLEDGEMENTS

I would like to thank first of all my major professor D. Levinthal for leading the experiment and understanding my particular urgency of having the Ph.D. done as soon as possible. I would also like to thank Professors L. Dennis, D. Duke, G. Riccardi and V. Hagopian for serving on my committee. I would like to thank all those persons who helped build and run the E711 experiment, first of all M. Cummings, Dr. K. Turner-Streets, Dr. J. Streets and then M. Bertoldi, M. Crisler, C. Georgiopoulos, J. Goldman, R. Gustafson, S. Hagopian, V. Hagopian, K. Johnson, A. Lathrop, D. Levinthal, F. Lopez, S. Pordes, H.L. Sawyer, H. White, J. Volk and C. Young

Finally a very special thank to Professor S. Ratti of Pavia University, Italy for his patience and understanding and the generous financial support he gave me to perform the data analysis and finish my thesis.

TABLE OF CONTENTS

CHAPTER 1: INTRODUCTION 1

1.1 Motivation of the experiment 2

1.1.1 QCD theoretical framework 3

1.1.2 Jets at low energies 3

1.2 Analysis contained in the dissertation 5

1.2.1 Parton model, distribution functions 6

1.2.2 Fragmentation functions 7

1.2.3 Fragmentation and existing data 7

1.2.4 Subject of the present dissertation 7

1.2.5 The detector 11

1.2.6 Calculation of $< \mathcal{Z} >$ using the jet neutral energy 11

CHAPTER 2: EXPERIMENTAL APPARATUS 15

2.1 Introduction 15

2.2 Design considerations 16

2.3 Beam line 17

2.3.1 Beam line used by E711 18

2.3.2 The beam spill structure 18

2.4 The target 21

2.5 The magnetic spectrometer 22

2.5.1 Characteristics of the analyzing magnets 22

2.5.2 $P_{\perp}$ kick of the two magnet system 23

2.6 The Drift chambers 25

2.6.1 Description of the MWPC and their location 26

2.6.2 Description of the wires 27

2.6.3 Active and desensitized regions of the MWPC 28

2.6.4 Voltages 29

2.6.5 Gas mixtures 30

2.6.6 System to amplify and take the signal out to the TDCs 31

2.6.7 Efficiency of the chambers 31

2.7 The hodoscopes and calorimeters 32

2.7.1 Hodoscope description 33

2.7.2 Shower development in a calorimeter 35

2.7.3 Sampling calorimeters 36

2.7.4 Calorimeter purpose 37

2.7.5 Calorimeter description and dimensions 37

2.7.6 Hodoscope calibration 43

2.7.7 Calorimeter calibration 43

2.8 The luminosity and beam monitor system 47

2.8.1 Ion chamber calibration 48

2.8.2 90° luminosity monitors 49

2.8.3 Total luminosity and its systematic uncertainties 51

CHAPTER 3: TRIGGER, DATA ACQUISITION and ONLINE MONITORING 54

3.1 The Trigger 55

3.1.1 Q signal 57

3.1.2 $P_{\perp}$ signal 59

3.1.3 $\bar{m}$ signal, HM signal 60

3.1.4 $Q \cdot P$, $Q \cdot P \cdot \bar{m}$, $Q \cdot P \cdot HM$ trigger signals 61

3.2 The Data Readout System 62

3.2.1 A-interrupt 62

3.2.2 B-interrupt 63

3.2.3 'Computer busy', dead time, live time 64

3.3 The online monitoring system 65

3.3.1 Beam line monitoring 65

3.3.2 Data online monitoring 66

3.4 The data-taking runs 69

CHAPTER 4: THE DATA PROCESSING 70

4.1 DST production 71

4.1.1 The trackfinder 72

4.1.2 The trackfitter 73

4.1.3 Momentum calculation 73

4.1.4 Cross checks on the reconstruction programs 75

4.2 DSF production 77

4.3 MDF production 77

CHAPTER 5: DATA ANALYSIS 79

5.1 Introduction 79

5.2 Selection of the trigger tracks 82

5.2.1 Vertex cut 82

5.2.2 Duplicate tracks elimination 83

5.2.3 Calorimeter fiducial volume cut 86

5.2.4 Q · P latch cut and $\bar{m}$ latch cuts 86

5.2.5 P_y distribution and cut 89

5.2.6 Electron rejection 89

5.2.7 Consistency between chamber and calorimeter measurements 90

5.3 Selection of the 'good events' 93

5.3.1 Presence of a top and a bottom trigger particle and definition of leading particle 93

5.3.2 $P_{\perp total}$ cut 96

5.3.3 Di-hadron mass cut 96

5.4 Calculation of $E_{non\ leading\ neutral}$ 97

5.4.1 Evidence of jets 99

5.4.2 Definition of the jet spray cone 100

5.4.3 Determination of the ratio f 107

5.4.4 Calculation of the jet neutral energy 109

5.4.5 Correction to the error introduced by the definition of the jet cone 110

5.5 Corrections and systematic errors of the calculation of the energy of the jet 113

5.5.1 Correction for absorption of γs in the target 113

5.5.2 Correction for the energy released by the leading particle in the EM section of the calorimeter 116

5.5.3 Calculation of the systematic error on $< \mathcal{Z} >$ induced

correcting $E_{non\ leading\ neutral}$ 120
CHAPTER 6: THEORETICAL INTERPRETATION 122
6.1 QCD-parton model description of high $P_\perp$ jet production 123
6.1.1 Di-jet cross section 125
6.1.2 Di-hadron cross section 128
6.1.3 Meaning of the Q^2 parameter 130
6.1.4 QCD calculation of $\frac{d\sigma}{d\hat{t}}$ 133
6.2 Calculation of $< \mathcal{Z} >$ 134
CHAPTER 7: PHYSICS RESULTS 138
7.1 Introduction 138
7.2 Comparison between different types of targets 139
7.2.1 Comparison 140
7.2.2 Conclusions 140
7.3 Comparison between previous data 140
7.4 Comparison between the E711 data and theory 147
7.4.1 Theoretical predictions 147
7.4.2 Data plots and theoretical comparison 152
7.4.3 Conclusions 152
CHAPTER 8: CONCLUSIONS 190
REFERENCES 191
APPENDIX A 195
A.1 Introduction 195
A.2 Calibration of the electromagnetic shower 200
A.3 Calibration of the hadronic shower 203

APPENDIX B 209

LIST OF TABLES

2.1	Target dimensions and atomic weights	21
2.2	Drift chamber wire spacings	27
2.3	Drift Chamber Wire Diameters	28
2.4	Active area of drift chamber dimensions	29
2.5	Drift chamber typical operating voltages	30
2.6	Drift chamber plane efficiencies	32
2.7	Hodoscope front and back module dimensions	34
2.8	Calorimeter module dimensions	42
2.9	Calorimeter module layer thickness and muon energy deposition in the calorimeter modules	46
2.10	Total integrated luminosity	53
3.1	Correspondence between calorimeter segments and modules	59
3.2	Readout during A interrupt	63
3.3	Readout during B interrupt	64
4.1	DST production percentages	72
4.2	Momentum resolution	75
4.3	Event summary	78
5.1	$< \cos\Theta_{soft} >$ as a function of $P_\perp$ of the hadron	107
5.2	f for different $P_\perp$ $\cos\theta^\star$ and $x_\perp$ ranges	108

5.3 Ratio $R \equiv \frac{E_{neutral\ all}}{E_{in\ cone}}$ calculated for various $P_\perp$ and $\cos\theta^\star$ of the leading hadron ranges 114

5.4 Average fraction of neutral energy detected by the calorimeters for different targets and energy of the primary γ 117

5.5 Average energy released in the active part of the calorimeter EM section by hadrons of various energy 121

6.1 Parton-parton scattering subprocess and corresponding matrix elements divided by $16\pi^2\alpha_s^2$ 137

7.1 List of $< \mathcal{Z} >$ as a function of $\cos\theta^\star$ of the leading hadron for the Be target 143

7.2 List of $< \mathcal{Z} >$ as a function of $\cos\theta^\star$ of the leading hadron for the Al target 144

7.3 List of $< \mathcal{Z} >$ as a function of $\cos\theta^\star$ of the leading hadron for the Fe target 145

7.4 List of $< \mathcal{Z} >$ as a function of $\cos\theta^\star$ of the leading hadron for the W target 146

A.1 Results of the simulation of electromagnetic showers in the EM section of the calorimeters 205

A.2 Mean radius of electromagnetic showers in the EM section of the calorimeter 205

A.3 Results of the analysis performed on the hadron calibration data of the calorimeters[36] 207

LIST OF FIGURES

1.1 Representation of a high $P_\perp$ reaction factorized into parton distribution functions (G), parton fragmentation functions (D) and hard scattering subprocess 4

1.2 CCOR collaboration data[24] : distribution of $< \mathcal{Z} >$ as a function of $P_\perp$ of the leading hadron 8

1.3 EMC collaboration data[61] : fragmentation functions of partons into π^+, π^-, K^+, K^-, p, $\overline{p}$ 9

1.4 EMC collaboration data[61] : fragmentation functions of partons into π^+, π^- 10

1.5 Side view and coordinate system of the E711 detector 12

2.1 Tevatron beamlines and fixed target experiments (1897) at Fermilab 19

2.2 E711 beamline final part 20

2.3 Intensity of the magnetic field along $\hat{\mathbf{z}}$ in the analyzing magnets 24

2.4 Side view of calorimeters 38

2.5 Front view of calorimeters 40

2.6 Calorimeter module (top view) in section H3 41

2.7 Diagram of R2154 photomultiplier tube base 44

2.8 Diagram of the 90° monitors mounted on the front face of the first magnet 50

3.1 Diagram of one of 24 identical trigger segments and the formation of the final triggers 58

3.2 Example of online latch histogram 67

3.3 Typical event display showing the detector, the triggering tracks and the energy deposition in the calorimeters 68

4.1 Illustration of the bending plane and track momentum calculation 76

5.1 Distributions of the y coordinate of the tracks at vertex 84

5.2 Distributions of the y coordinate of the tracks at vertex 85

5.3 Distribution of D in two different scales 87

5.4 Distribution of track position on face of calorimeters after the fiducial volume cut 88

5.5 Distribution of $\frac{E_{em}}{E_{calo}}$ before the electron rejection cut 91

5.6 Plot of $\mathcal{D}$ before the cut 94

5.7 Lego plot of $\mathcal{D}$ before the cut 95

5.8 Di-hadron system mass after cut at 7 GeV/c^2 98

5.9 Distribution of $\eta_{leading} - \eta_{soft}$ for the experimental data 101

5.10 Distribution of $\eta_{leading} - \eta_{soft}$ for the experimental data when the leading hadron has been substituted with the one of the previous event 102

5.11 Distribution of $\eta_{leading} - \eta_{soft}$ for the experimental data when the leading hadron has been replaced with a simulated one 103

5.12 Distribution of $\cos\Theta_{soft}$ for experimental data 104

5.13 Distribution of $\cos\Theta_{soft}$ for the experimental data when the leading hadron has been substituted with the one of the previous event 105

5.14 Distribution of $\cos\Theta_{soft}$ for the experimental data when the leading hadron has been replaced with a simulated one 106

5.15 Auxiliary frame used in the calculation of $E_{non\ leading\ neutral}$ 111

5.16 Diagram indicating the solid angle covered by the neutral jet particle flux expressed as a function of $\cos\phi'$ and $\tan\theta'$ 112

5.17 $< \mathcal{Z} >$ of all the selected events as a function of $\cos\Theta$, cosine of the cone aperture angle of the jet 115

5.18 Energy of the leading particles measured by the calorimeter 119

6.1 First order Feynman graphs of the parton-parton scattering subprocesses according to QCD 132

6.2 Radiative correction Feynman graphs of the parton-parton scattering subprocesses according to QCD 132

7.1 $< \mathcal{Z} >$ as a function of $\cos\theta^\star$ for different targets and single jet events 141

7.2 $< \mathcal{Z} >$ as a function of $\cos\theta^\star$ for different targets and two jet events 142

7.3 Comparison between the inclusive CCOR[24] data with single π° detected and the E711 data. Plot of $< \mathcal{Z} >$ versus $P_\perp$ of the leading hadron 148

7.4 Comparison between the CCOR[24] data with two π° detected and $M_{\pi^\circ\pi^\circ} > 8$ GeV/c^2 and the E711 data. Plot of

$< \mathcal{Z} >$ versus $P_\perp$ of the leading hadron 149

7.5 Comparison between the inclusive CCOR[24] data with single π° detected and the E711 data. Plot of $< \mathcal{Z} >$ versus $x_\perp$ of the leading hadron 150

7.6 Comparison between the CCOR[24] data with two π° detected and $M_{\pi^\circ\pi^\circ} > 8$ GeV/c^2 and the E711 data. Plot of $< \mathcal{Z} >$ versus $x_\perp$ of the leading hadron 151

7.7 $< \mathcal{Z} >$, function of $P_\perp$ of the leading hadron for single jet events 154

7.8 $< \mathcal{Z} >$, function of $P_\perp$ of the leading hadron for two jet events 155

7.9 $< \mathcal{Z} >$, function of $P_\perp$ of the leading hadron for single jet events and positive leading hadron charge 156

7.10 $< \mathcal{Z} >$, function of $P_\perp$ of the leading hadron for two jet events and positive leading hadron charge 157

7.11 $< \mathcal{Z} >$, function of $P_\perp$ of the leading hadron for single jet events and negative leading hadron charge 158

7.12 $< \mathcal{Z} >$, function of $P_\perp$ of the leading hadron for two jet events and negative leading hadron charge 159

7.13 $< \mathcal{Z} >$, function of $\cos\theta^\star$ of the leading hadron for single jet events 160

7.14 $< \mathcal{Z} >$, function of $\cos\theta^\star$ of the leading hadron for two jet events 161

7.15 $< \mathcal{Z} >$, function of $\cos\theta^\star$ of the leading hadron for single

jet events and positive leading hadron charge 162

7.16 $< \mathcal{Z} >$, function of $\cos\theta^\star$ of the leading hadron for two jet events and positive leading hadron charge 163

7.17 $< \mathcal{Z} >$, function of $\cos\theta^\star$ of the leading hadron for single jet events and negative leading hadron charge 164

7.18 $< \mathcal{Z} >$, function of $\cos\theta^\star$ of the leading hadron for two jet events and negative leading hadron charge 165

7.19 $< \mathcal{Z} >$, function of $\cos\theta^\star$ of the leading hadron for single jet events and $7 < M_{di-hadron} < 8$ GeV/c^2 166

7.20 $< \mathcal{Z} >$, function of $\cos\theta^\star$ of the leading hadron for two jet events and $7 < M_{di-hadron} < 8$ GeV/c^2 167

7.21 $< \mathcal{Z} >$, function of $\cos\theta^\star$ of the leading hadron for single jet events and $7 < M_{di-hadron} < 8$ GeV/c^2 and positive leading hadron charge 168

7.22 $< \mathcal{Z} >$, function of $\cos\theta^\star$ of the leading hadron for two jet events and $7 < M_{di-hadron} < 8$ GeV/c^2 and positive leading hadron charge 169

7.23 $< \mathcal{Z} >$, function of $\cos\theta^\star$ of the leading hadron for single jet events and $7 < M_{di-hadron} < 8$ GeV/c^2 and negative leading hadron charge 170

7.24 $< \mathcal{Z} >$, function of $\cos\theta^\star$ of the leading hadron for two jet events and $7 < M_{di-hadron} < 8$ GeV/c^2 and negative leading hadron charge 171

7.25 $< \mathcal{Z} >$, function of $\cos\theta^\star$ of the leading hadron for single

jet events and $8 < M_{di-hadron} < 9$ GeV/c^2 172

7.26 $< \mathcal{Z} >$, function of $\cos\theta^\star$ of the leading hadron for two jet events and $8 < M_{di-hadron} < 9$ GeV/c^2 173

7.27 $< \mathcal{Z} >$, function of $\cos\theta^\star$ of the leading hadron for single jet events and $8 < M_{di-hadron} < 9$ GeV/c^2 and positive leading hadron charge 174

7.28 $< \mathcal{Z} >$, function of $\cos\theta^\star$ of the leading hadron for two jet events and $8 < M_{di-hadron} < 9$ GeV/c^2 and positive leading hadron charge 175

7.29 $< \mathcal{Z} >$, function of $\cos\theta^\star$ of the leading hadron for single jet events and $8 < M_{di-hadron} < 9$ GeV/c^2 and negative leading hadron charge 176

7.30 $< \mathcal{Z} >$, function of $\cos\theta^\star$ of the leading hadron for two jet events and $8 < M_{di-hadron} < 9$ GeV/c^2 and negative leading hadron charge 177

7.31 $< \mathcal{Z} >$, function of $\cos\theta^\star$ of the leading hadron for single jet events and $9 < M_{di-hadron} < 10$ GeV/c^2 178

7.32 $< \mathcal{Z} >$, function of $\cos\theta^\star$ of the leading hadron for two jet events and $9 < M_{di-hadron} < 10$ GeV/c^2 179

7.33 $< \mathcal{Z} >$, function of $\cos\theta^\star$ of the leading hadron for single jet events and $9 < M_{di-hadron} < 10$ GeV/c^2 and positive leading hadron charge 180

7.34 $< \mathcal{Z} >$, function of $\cos\theta^\star$ of the leading hadron for two jet events and $9 < M_{di-hadron} < 10$ GeV/c^2 and positive

leading hadron charge 181

7.35 $< \mathcal{Z} >$, function of $\cos\theta^\star$ of the leading hadron for single jet events and $9 < M_{di-hadron} < 10$ GeV/c^2 and negative leading hadron charge 182

7.36 $< \mathcal{Z} >$, function of $\cos\theta^\star$ of the leading hadron for two jet events and $9 < M_{di-hadron} < 10$ GeV/c^2 and negative leading hadron charge 183

7.37 $< \mathcal{Z} >$, function of $\cos\theta^\star$ of the leading hadron for single jet events and $M_{di-hadron} > 10$ GeV/c^2 184

7.38 $< \mathcal{Z} >$, function of $\cos\theta^\star$ of the leading hadron for two jet events and $M_{di-hadron} > 10$ GeV/c^2 185

7.39 $< \mathcal{Z} >$, function of $\cos\theta^\star$ of the leading hadron for single jet events and $M_{di-hadron} > 10$ GeV/c^2 and positive leading hadron charge 186

7.40 $< \mathcal{Z} >$, function of $\cos\theta^\star$ of the leading hadron for two jet events and $M_{di-hadron} > 10$ GeV/c^2 and positive leading hadron charge 187

7.41 $< \mathcal{Z} >$, function of $\cos\theta^\star$ of the leading hadron for single jet events and $M_{di-hadron} > 10$ GeV/c^2 and negative leading hadron charge 188

7.42 $< \mathcal{Z} >$, function of $\cos\theta^\star$ of the leading hadron for two jet events and $M_{di-hadron} > 10$ GeV/c^2 and negative leading hadron charge 189

A.1 Simulation of the ionization energy loss of muons in the EM

CHAPTER 1

INTRODUCTION

The physics of elementary particles studies the nature of interactions between subatomic particles. Scattering experiments are a way to achieve that goal. Successively larger machines have been (and are being) built to accelerate particles and induce their collisions. In this way, the comparison between scattering measurements and theoretical predictions can be made and a deeper understanding of the fundamental forces achieved.

The larger the momentum transfer between a beam particle and a target particle, the smaller the distance at which the interaction can be studied. With today's accelerators high momentum transfers can be obtained that imply distance

scales of the order of 10^{-18} cm. Consequently the inner structure of nucleons can be investigated.

Fermi National Accelerator Laboratory (FNAL) experiment 711, a fixed target experiment and the topic of this thesis, was designed to measure the inclusive production of two high and opposite $P_\perp$ hadrons at $\sqrt{s} = 38.$ GeV in the process

$$pN \rightarrow h_1 + h_2 + X$$

where p implies the beam 800 GeV/c proton, N the target nucleon, h_1 and h_2 the outgoing hadrons, X is whatever else is produced. The charge of h_1 and h_2 were also determined enabling the study of like- and unlike-charged states. The experimental data was accumulated from November 1987 until February 1988.

1.1 Motivation of the experiment

The objective of experiment 711 was the study of the inclusive production of two high and opposite transverse momentum ($P_\perp$) hadrons, which can be interpreted as the dynamics of the hard scattering of the hadronic constituents. The QCD[1] predictions for such processes can be tested by comparison with this data. QCD is a theory which describes the interactions between quarks and gluons (collectively called partons), believed to be the constituents of the observed hadrons[2].

1.1.1 QCD theoretical framework

In the QCD theoretical framework, the high $P_\perp$ di-hadron production is due to the scattering at high momentum transfer of quasi-free point-like partons, one in the beam with the other in the target[3]. Such a scattering is calculable perturbatively. The scattered partons then fragment into collimated sprays (jets) of hadrons with large transverse momenta. The resulting event contains four jets : two at high $P_\perp$ (which are the product of the scattered partons) and two at very low $P_\perp$, products of the fragmentation of the spectator (non interacting) partons of the beam and target (see figure 1.1).

The QCD predictions were dramatically confirmed by experiments at the CERN SPS collider.[4] Experimentally it was found that at high energies ($\sqrt{s} =$ 540 to 630 GeV) collimated jets at high momentum transfer ($P_\perp$) where copiously produced and their production cross sections could be predicted. At lower energies ($\sqrt{s} \simeq$ 30 to 60 GeV) jets are much less collimated, consequently in this experimental situation (such as the one E711 was performed in) it is more difficult to recognize and define with no ambiguity the spray of particles resulting from a high momentum transfer parton interaction.

1.1.2 Jets at low energies

Two experimental observations help select and study high momentum transfer interactions at low energies. Triggering on events in which a high $P_\perp$ hadron is produced one observes :

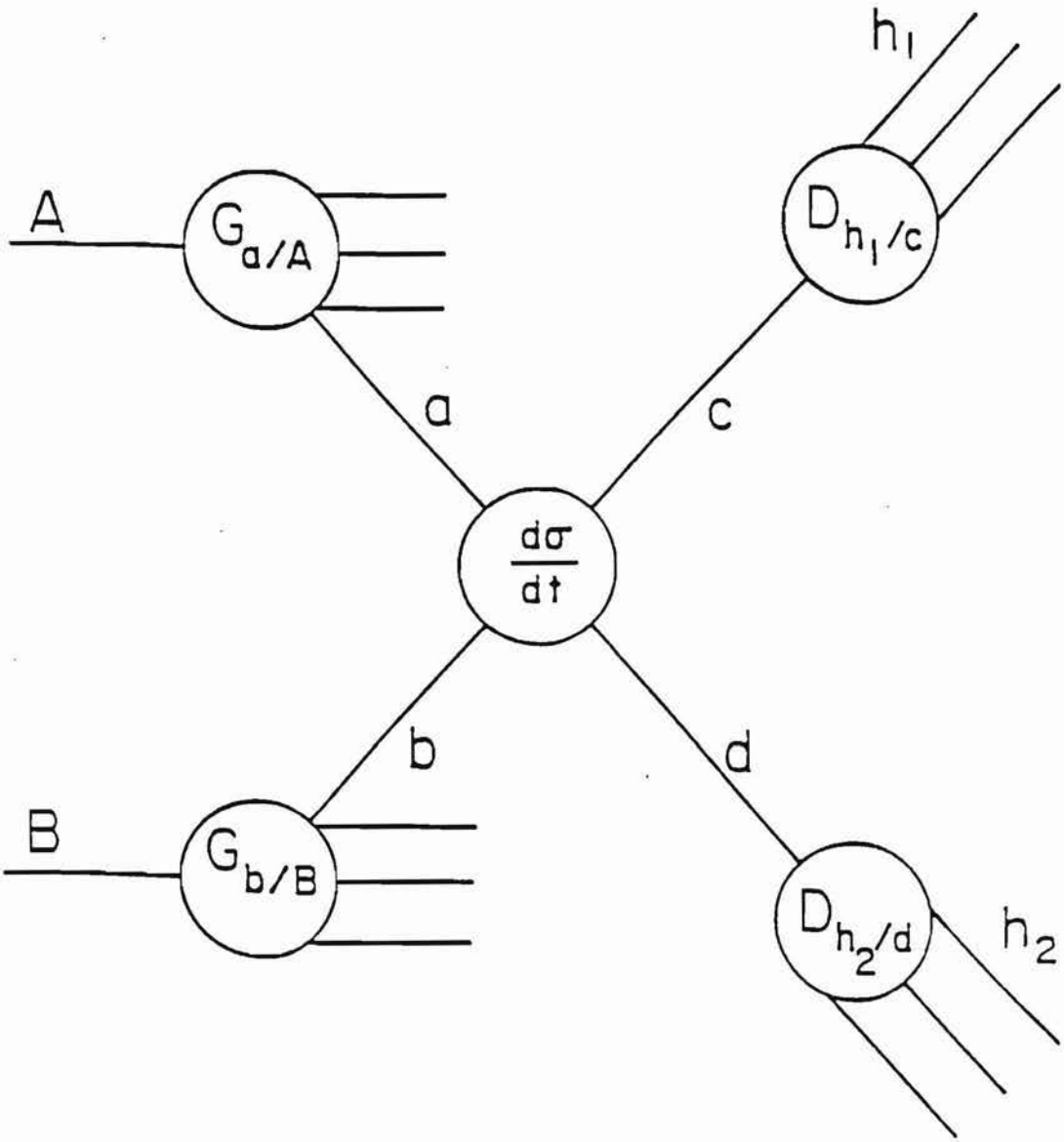

Representation of a high $P_\perp$ reaction factorized into parton distribution functions (G), parton fragmentation functions (D) and hard scattering subprocess

Figure 1.1

1) the high $P_\perp$ hadron is part of a jet[5][6]; a jet recoils against the trigger particle if $P_\perp$ is sufficiently high[6] ($P_\perp > 7$ GeV/c). Therefore triggering on high $P_\perp$ hadrons is equivalent to selecting jet events.

2) The fraction of the trigger side momentum taken by the trigger particle ranges from 75 % to 90 %[5] (increasing with $x_\perp = 2P_\perp/\sqrt{s}$, the so called "trigger bias"[7]) and, more important, the direction of the trigger particle momentum is parallel (within $\pm 5°$ on average) to that of the jet.[5]

Thus, triggering on a pair of high $P_\perp$ hadrons selects events where the two scattered partons can be experimentally measured. Experiment E711 triggered on two high $P_\perp$ hadrons with approximately equal and opposite transverse momenta. That brought the further advantage of discarding events in which the colliding partons have a large intrinsic momentum (due to Fermi motion of the partons inside nucleons[8][9][10]) and facilitated the theoretical interpretation of the cross section.

1.2 Analysis contained in this dissertation

The subject of the present dissertation is the study of $< \mathcal{Z} >$, the average fraction of energy of the high $P_\perp$ jet, carried by the 'leading hadron'.

$$< \mathcal{Z} > \equiv \left\langle \frac{E_{leading}}{E_{jet}} \right\rangle$$

where $E_{leading}$ is the energy of the 'leading hadron', namely of the hadron which, as described in the previous paragraph, takes the most of the jet momentum. E_{jet} is the energy of the jet.

1.2.1 Parton model, distribution functions

According to the parton model, the colliding hadrons are bound states of quarks and gluons. The interaction among them is described in quantum field theory by the QCD hamiltonian. Presently, mathematics cannot exactly solve the equations of motion, and the hadron state must be described phenomenologically by means of distribution functions, $G_{a/A}(x, Q^2)$, giving the probability $G_{a/A}(x, Q^2)dx$ to a parton a (quark, antiquark or gluon) in a hadron A of having a momentum fraction between x and $x + dx$. Q^2 is a parameter, typical scale of the process (scale violation), which can be defined as

$$Q^2 \equiv k\mathrm{P}_\perp^2$$

where $\mathrm{P}_\perp$ is the two jet high transverse momentum and k is a constant, equal to 1 in the analysis of the E711 data.

In a high $\mathrm{P}_\perp$ scattering process, partons can be treated as quasi-free point-like and massless particles. The scattering is described by the collision between partons (see figure 1.1) with the initial state described by these distribution functions. After the collision, two partons emerge at high $\mathrm{P}_\perp$. The scattering between partons is described by the differential scattering cross section $\frac{d\sigma}{d\hat{t}}$, where $\hat{t}$ is the momentum transfer between colliding and scattered partons. After the collision, partons 'fragment' into jets, namely they vaporize into a spray of hadrons whose total energy and momentum are the energy and momentum of the parent parton.

1.2.2 *Fragmentation functions*

As we are not able to exactly calculate the fragmentation process of a parton, we can only describe it phenomenologically by the fragmentation functions $D_{c/H}(z, Q^2)$ that give the probability $D_{c/H}(z, Q^2)dz$ to find a hadron H of a jet with momentum fraction of the parent parton c, between z and $z + dz$. The fragmentation functions assume a dependence not only on z but also on the parameter Q^2 defined above for the structure functions.

1.2.3 *Fragmentation and existing data*

Recent data on the fragmentation mechanism were obtained by the CCOR collaboration[5] at C.o.M. of the reaction energies ($\sqrt{s}$) similar to E711. Their data, shown in figure 1.2, were taken at $\sqrt{s} = 31$, 44.8 and 62.4 GeV and prove that at low $\sqrt{s}$ the fragmentation mechanism produces a leading hadron which takes from 75 % to 90 % of the jet momentum.

More recent data was taken by the European Muon Collaboration (EMC)[11] which measured the fragmentation function of the u quark into π^+, π^-, K^+, K^-, p, $\overline{p}$ shown in figure 1.3 and 1.4 in a muon-proton and muon-deuteron scattering experiment at $\sqrt{s} = 22.93$ GeV .

1.2.4 *Subject of the present dissertation*

The subject of this dissertation, the mean value of the fragmentation variable

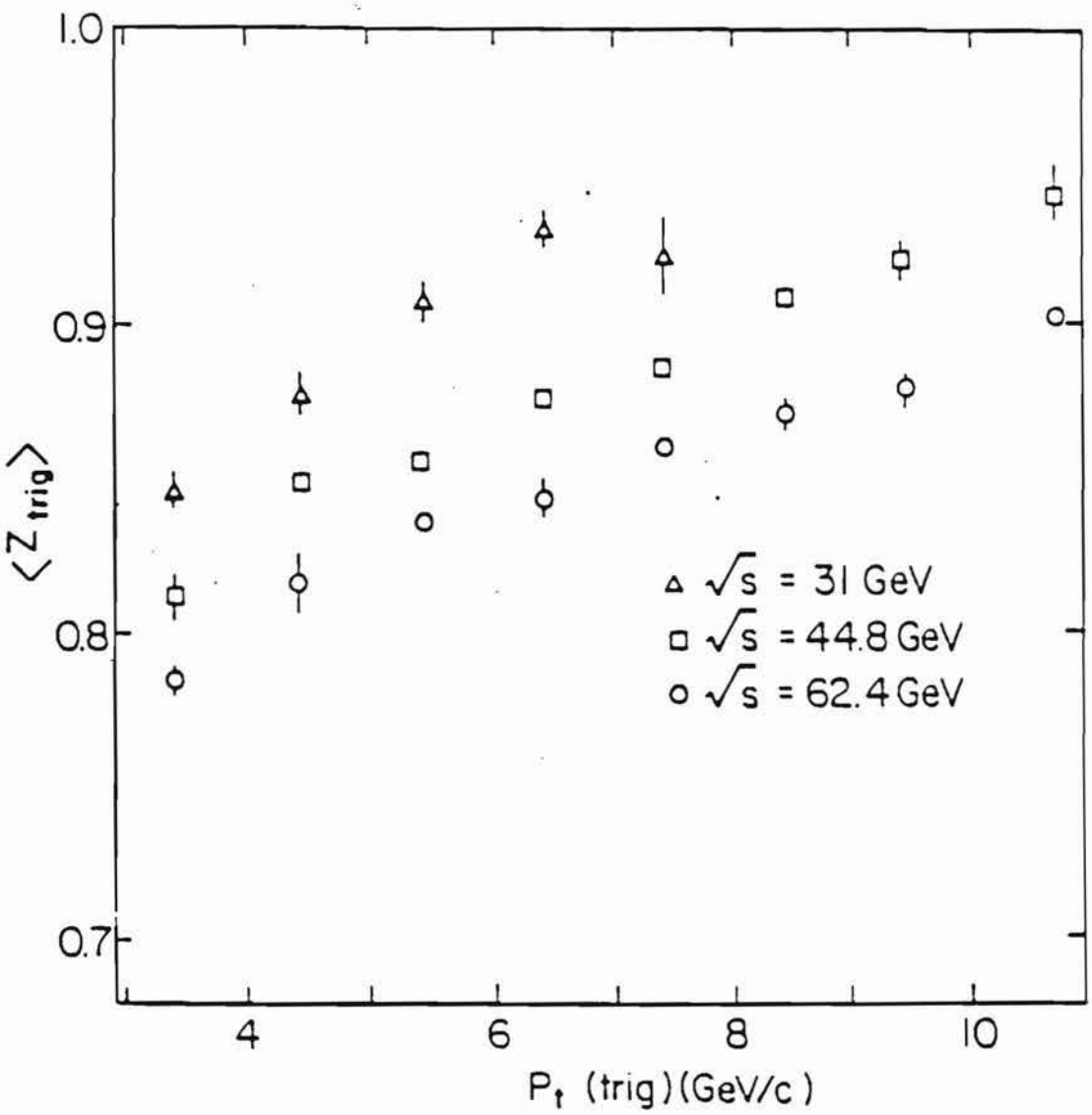

CCOR collaboration data[24] : distribution of $< \mathcal{Z} >$ as a function of $P_\perp$ of the leading hadron

Figure 1.2

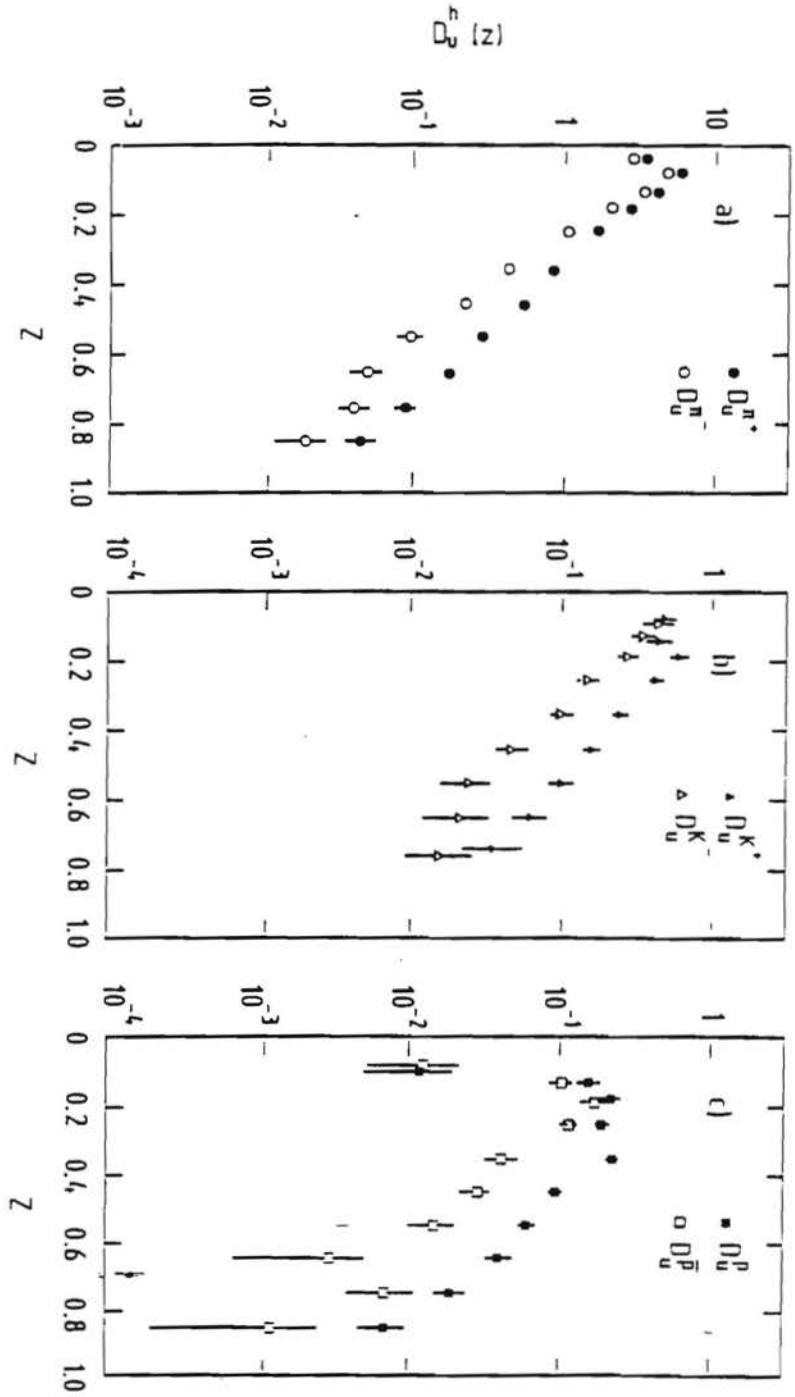

EMC collaboration data[61] : fragmentation functions of partons into π^+, π^-, K^+, K^-, p, $\overline{p}$

Figure 1.3

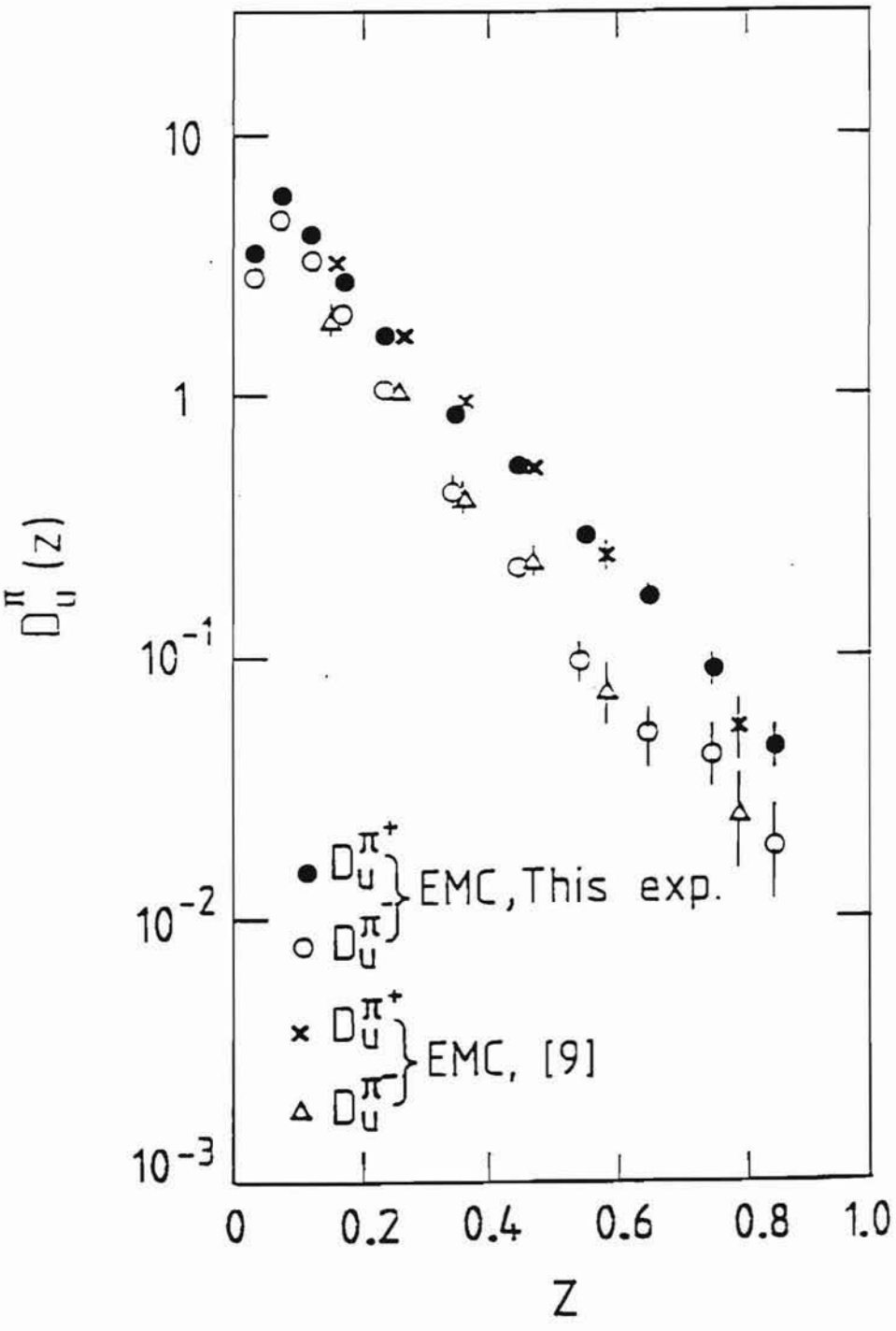

EMC collaboration data[61] : fragmentation functions of partons into π^+, π^-

Figure 1.4

z, is related, for high $P_\perp$ particles, to the distribution functions, scattering cross section and fragmentation functions and provide a test on the QCD-parton description of high $P_\perp$ scattering. The fragmentation mechanism can be described well for different energies and processes in e^+e^-, pp, $p\bar{p}$ reactions in a collider machine[12]. In principle, the fragmentation process could be affected by the presence of the nuclear forces or the amount of nuclear matter which partons have to cross while fragmenting into observables hadrons when using fixed nuclear targets. The question rises : can fragmentation still be described by functions independent of the rest of the surrounding environment, or are they influenced by these nuclear forces? This dissertation will give an answer by comparing plots of $< \mathcal{Z} >$ for different nuclear targets (Be, Al, Fe and W) and by comparing them with the QCD predictions valid for independent single particle scattering.

1.2.5 The detector

The detector used in this experiment is shown in figure 1.5 (side view). It can be described as a double arm spectrometer, where each arm can detect the presence of the products of a high $P_\perp$ collision, the jet fragments.

The thin nuclear target was followed by two analyzing magnets, five multiwire proportional chambers and two calorimeters. The next chapter will provide a detailed description of the experimental components.

1.2.6 Calculation of $< \mathcal{Z} >$ using the jet neutral energy

To determine $< \mathcal{Z} >$ from the E711 data, $E_{leading}$ was calculated by means

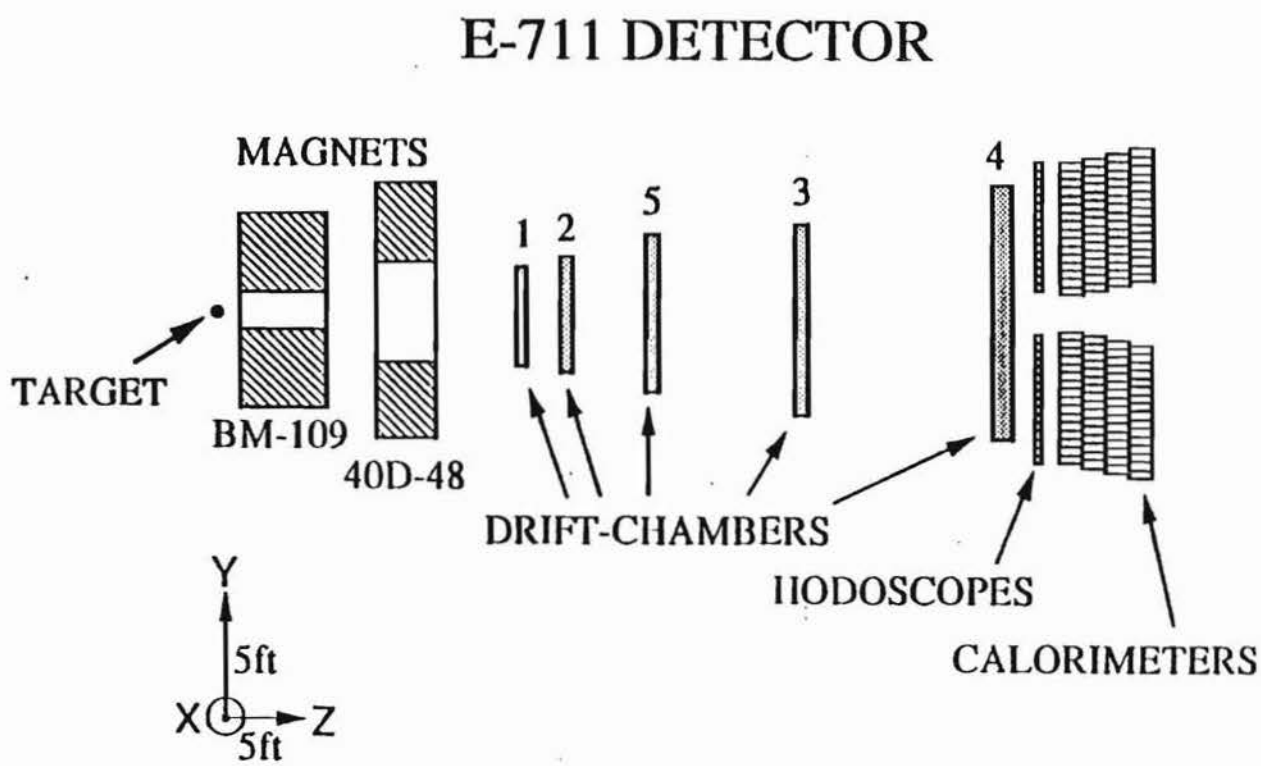

Side view and coordinate system of the E711 detector

Figure 1.5

of the chambers and the analyzing magnets. At these energies the mass of the leading hadron is negligible compared to its momentum and consequently $E_{leading} \simeq \mathrm{P}_{leading}$, where $\mathrm{P}_{leading}$ is the momentum measured by the chambers. E_{jet} was measured by also including the calorimetric measurement and

$$E_{jet} = E_{leading} + E_{non\ leading}$$

where $E_{non\ leading}$ is the jet energy remaining excluding the contribution of the leading charged hadron. An average value can be more accurately determined as average corrections can be applied. Therefore

$$< z >= \left\langle \frac{\mathrm{P}_{leading}}{\mathrm{P}_{leading} + E_{non\ leading}} \right\rangle = \frac{1}{1 + \langle \frac{E_{non\ leading}}{\mathrm{P}_{leading}} \rangle} \tag{1.1}$$

$< E_{non\ leading} >$ can be calculated by measuring the jet neutral particle energy released in the calorimeter. The choice of measuring the neutrals is due to a geometrical acceptance reason since they were undeflected by the analyzing magnets and could reach the calorimeter. On the other hand, the relatively soft charged particles forming the rest of the jet were swept away from the detector by the analyzing magnets. The energy carried by the non leading particles was :

$$\begin{aligned} < E_{non\ leading} > &= < E_{non\ leading\ neutral} + E_{non\ leading\ charged} > \\ &= f < E_{non\ leading\ neutral} > \end{aligned}$$

where $E_{non\ leading\ neutral}$ is the jet neutral energy and

$$f \equiv \left\langle \frac{E_{jet} - \mathrm{P}_{leading}}{E_{non\ leading\ neutral}} \right\rangle$$

Consequently from (1.1)

$$
\begin{aligned}
< \mathcal{Z} > &= \left\langle \frac{\mathrm{P}_{leading}}{\mathrm{P}_{leading} + E_{non\ leading}} \right\rangle \simeq \frac{< \mathrm{P}_{leading} >}{< \mathrm{P}_{leading} > + f < E_{non\ leading\ neutral} >} \\
&\simeq \left\langle \frac{\mathrm{P}_{leading}}{\mathrm{P}_{leading} + f E_{non\ leading\ neutral}} \right\rangle \\
&\simeq \frac{1}{1 + f \langle \frac{E_{non\ leading\ neutral}}{\mathrm{P}_{leading}} \rangle}
\end{aligned}
\tag{1.2}
$$

CHAPTER 2

THE EXPERIMENTAL SET-UP

2.1 Introduction

The experiment was designed to study the production cross section of ++, +− and −− hadron pairs with high and opposite $P_{\perp}$, and hence high mass, produced over a wide angular range in proton-nucleon collisions. A double arm spectrometer was used, designed for high momentum resolution measurement and capable of functioning at high interaction rates. Figure 1.5 shows the experimental apparatus. The incident proton beam hit a point-like target. 10% inelastic interaction length metal targets of Be, Al, Fe and W were used. The magnetic spectrometer consisted of two analyzing dipole magnets and five multiwire proportional chambers (MWPCs) and was positioned for tracking the particle trajectories downstream the magnets. The pointlike target allowed to avoid

upstream tracking. This system was followed by 4 scintillator hodoscopes and 2 sampling calorimeters which generated fast signals used for high speed real time electronic event selection (trigger).

The digitized data from each interaction which satisfied the trigger requirements was read by a dedicated computer (PDP-11) and written onto tape. The readout was done according to two formats, the 'A-interrupt' used for the experimental events during the spill and the pedestal events, and the 'B-interrupt', used for the readout of scalers after each spill.

Throughout this thesis the following convention is adopted for the laboratory reference frame : the z direction is horizontal along the beam line pointing downstream; the y direction is vertical, pointing upwards; the x direction is according to a right-handed reference frame.

2.2 Design considerations

As the production cross section for massive di-hadron states decreases rapidly with their mass[13], a high luminosity, and consequently a high beam intensity, was necessary ($\simeq 2.5 \times 10^7$ protons/sec beam intensity). The high beam intensity required a fast selection system (trigger) as only a small fraction of the total interaction rate ($\simeq 2.5 \times 10^6$ interactions/sec) was of interest. The apparatus was designed to produce signals from which a fast (typically less than 50 nsec) electronic event selection could be formulated with standard commercial electronic logic modules. To bear the high intensity flux, the spectrometer was desensitized

in the middle region around the beam line and the hodoscopes and calorimeters were placed above and below the beam line. Due to the high intensity beam wire chambers could not be used between target and magnets to track the particles. Consequently a short and narrow target was used in order to constrain the x position of the beam interaction, making tracking devices between target and analyzing magnets unnecessary.

The design consideration were also aimed at ensuring the capability of the detector to trigger on two high and opposite $P_\perp$ hadrons. The calorimeters produced an output pulse, used by the trigger, proportional to the P_y of the particles. They covered a region of $\pm 25.3°$ in azimuthal angle. Due to the narrow azimuthal coverage they accepted mainly particles for which $P_\perp \simeq P_y$. Since the magnetic field of the two analyzing magnets was pointing in the vertical direction, the P_y of the particles was unaffected. Consequently the transverse momenta as deduced from the calorimeter signals were unaffected by the magnetic deflection. The size of the aperture of the first magnet was small and the iron yoke surrounding it was a good shield from the beam halo for chambers, hodoscopes and calorimeters. This facilitated the correct functioning of the detector.

2.3 Beam line

A beam line is the ensemble of construction and devices (tunnels, magnets, tracking devices, splitting devices) which steers the extracted beam from the accelerator main ring to the experimental hall. Proper setting of the magnet

currents and other beamline parameters is critical in order to have a high intensity beam with low halo background and a proper focus on the target. The Tevatron accelerator at Fermilab produced a proton beam of 800 GeV/c . This beam was extracted and split among many different beam lines, as shown in figure 2.1.

2.3.1 Beam line used by E711

The beam line used by the experiment is shown in figure 2.2. The devices directly controlled by E711 were NEBE (horizontal deflection dipoles), NEBV (dipole), NEBQ2 (horizontally defocusing quadrupole), NECQ (horizontally focusing quadrupole), NECH (dipole), NEEAN1 (dipole) and NEEAN2 (dipole). In particular, NECH and NEBV, were the devices used to control the horizontal and the vertical deflection of the beam and adjust it on the target. NEEAN1 and NEEAN2 were the experimental analyzing magnets (magnets used to measure the momentum of charged tracks).

2.3.2 The beam spill structure

A primary 800 GeV/c proton beam was used in the experiment. The beam spill was of $\sim$ 20 seconds and its intensity had a time structure (because of the Tevatron acceleration process) such that each spill was formed ultimately by protons grouped into so called 'buckets' approximately 2 nsec long, separated from each other by 18.2 nsec. The beam profile was focused so that a thin vertical target could be used. This alleviated the need for particle tracking upstream

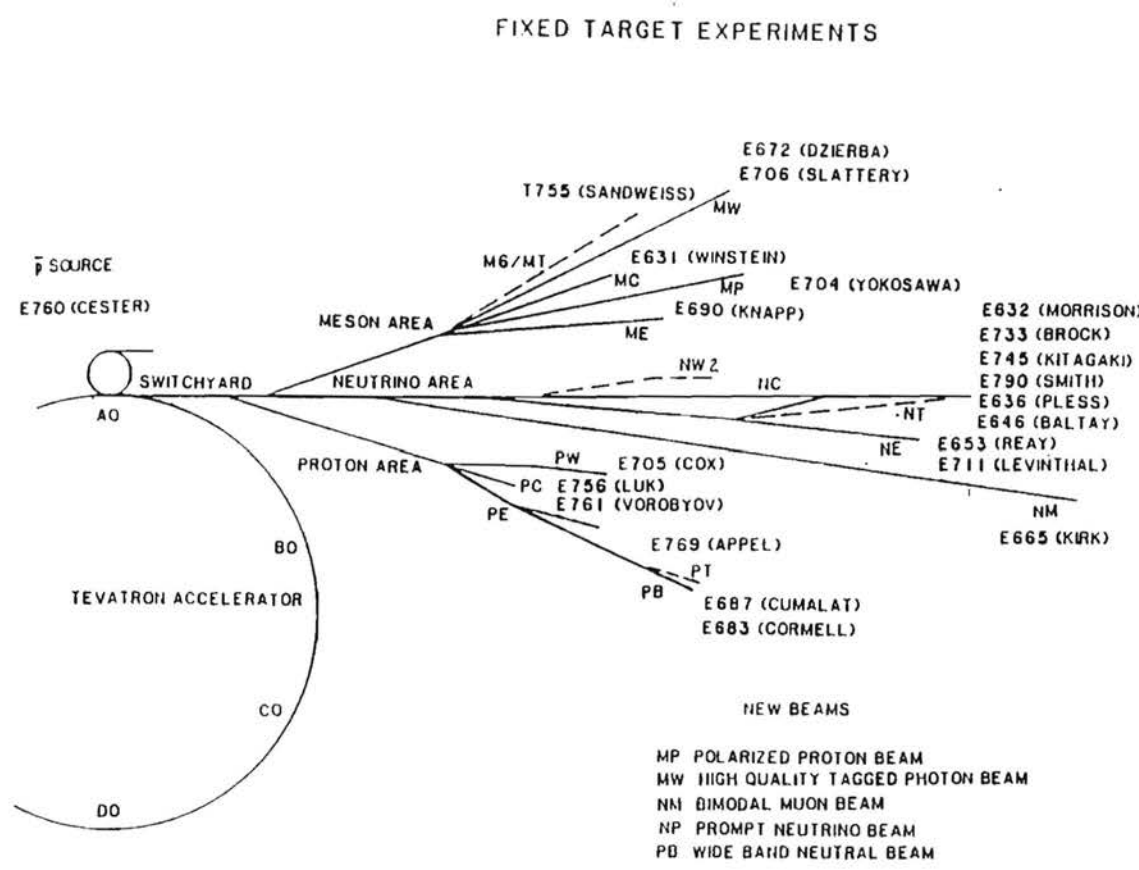

Tevatron beamlines and fixed target experiments (1897) at Fermilab

Figure 2.1

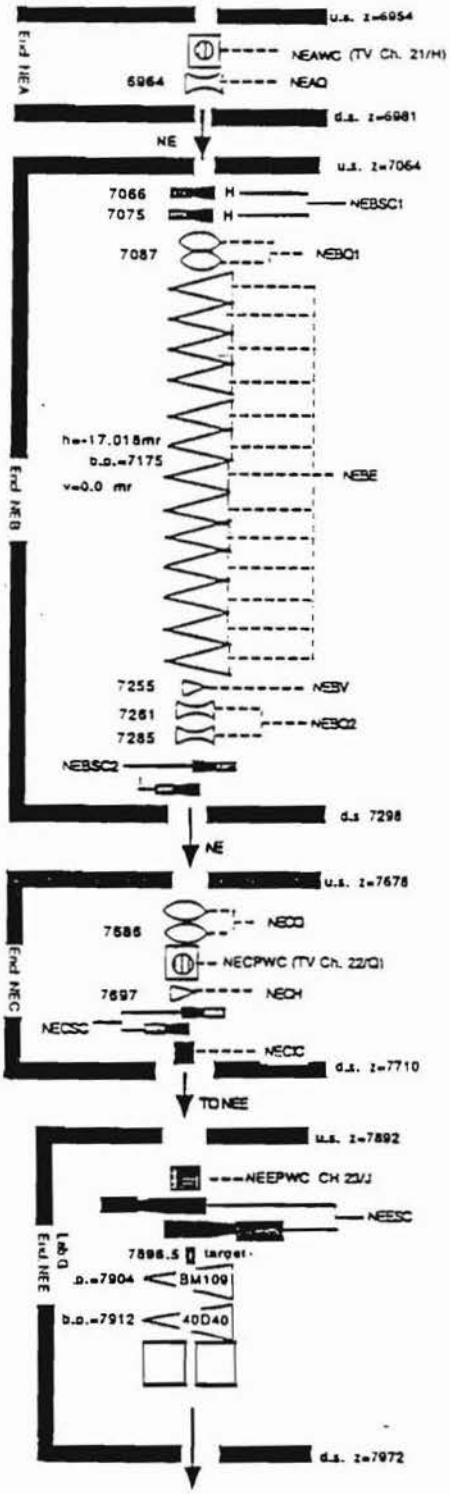

E711 beamline final part

Figure 2.2

TABLE 2.1

Target characteristics

Target type	A	$x(cm) \times y(cm) \times z(cm)$	Interaction lengths (%)
Be	9.01	$0.10225 \times 2.5 \times 4.066$	9.99
Al	26.98	$0.08357 \times 2.5 \times 3.951$	10.03
Fe	55.85	$0.04892 \times 2.5 \times 1.670$	9.97
W	183.85	$0.10211 \times 2.5 \times 0.956$	9.97

of the magnets where the particle fluxes are high. The beam intensity distribution on the target could be represented by a gaussian whose sigma was typically $\sim$ .38 mm horizontally. The typical beam flux used during the experiment was 2.5×10^7 protons/sec (5×10^8 protons per spill).

2.4 The target

The data were taken using four nuclear targets : Be, Al, Fe and W each of 10% inelastic interaction lengths (their dimensions and atomic weights are shown in TABLE 2.1). At the typical beam intensity used in the experiment, the rate of inelastic interactions was 2.5×10^6 interactions/sec.

2.5 The magnetic spectrometer

In order to determine accurately the momentum components of the secondary particles produced in the inelastic collisions it is necessary to know the interaction position, the magnetic deflection and the downstream trajectory. Two analyzing magnets were used in the experiment in order to provide sufficient magnetic deflection. Charged particles originated in the target were deflected horizontally by the analyzing magnets then their trajectories downstream the magnets were measured by the drift chambers.

2.5.1 Characteristics of the analyzing magnets

The analyzing magnets, NEEAN1 and NEEAN2, were about $2 \times 2.5 \times 3.3$m and $2.7 \times 2.5 \times 3.8$ m respectively in their overall dimensions, with apertures of $50.8 \times 43.3 \times 182.9$ cm and $101.6 \times 93.7 \times 122.6$ cm. The z position of the center of the magnets were 1.14 m and 3.63 m downstream of the target.

The field inside the magnets was vertical to a high degree of accuracy and its intensity independent of the x and y position around the axis of the aperture of the magnets[14] (10 KGauss and 8 KGauss for NEEAN1 and NEEAN2 respectively). Figure 2.3 shows the intensity of the magnetic field along the z axis at operational currents. The measurement was done with the ZIPTRACK measurement system.[15] This magnetic field strength measurement system consisted of three mutually perpendicular coils on a cart that could move on aluminium

tracks positioned parallel to the magnet aperture axis. The current induced in the three coils as the cart was moved along the tracks through the magnetic field was integrated and digitized by mean of an analog-to-digital (ADC) converter. That enabled the calculation of the three components of the magnetic field over the volume of the magnet aperture to a 1% accuracy.

2.5.2 $P_\perp$ *kick of the two magnet system*

Since the magnetic field in the magnets was vertical, the particle deflection occurred in the X-Z plane. The initial momentum of a charged particle ($\mathbf{p}_{in}$) was modified after the particle passed through the magnetic field region. The resulting outgoing momentum ($\mathbf{p}_{out}$) was for high momentum particles :

$$\overline{\mathbf{p}}_{out} = \overline{\mathbf{p}}_{in} + \overline{\mathbf{p}}_t$$

where $\overline{\mathbf{p}}_t$ is the so called '$P_\perp$ kick' of the magnets. The $\overline{\mathbf{p}}_t$ kick is given by :

$$\overline{\mathbf{p}}_t = \frac{-e}{c} \int \overline{\mathbf{B}} \times d\overline{\mathbf{l}}$$

where the integration path can be approximated by a straight line from the target along the z direction for particles in the spectrometer acceptance. The value found for the combined analyzing magnet system was : $|\mathbf{p}_t| = 1.16$ GeV/c. Montecarlo simulations using the measured field map indicated that a single bend plane approximation was accurate to better than 1.5% for the high $P_\perp$ particles ($P_\perp > 2.5$ GeV) under study.

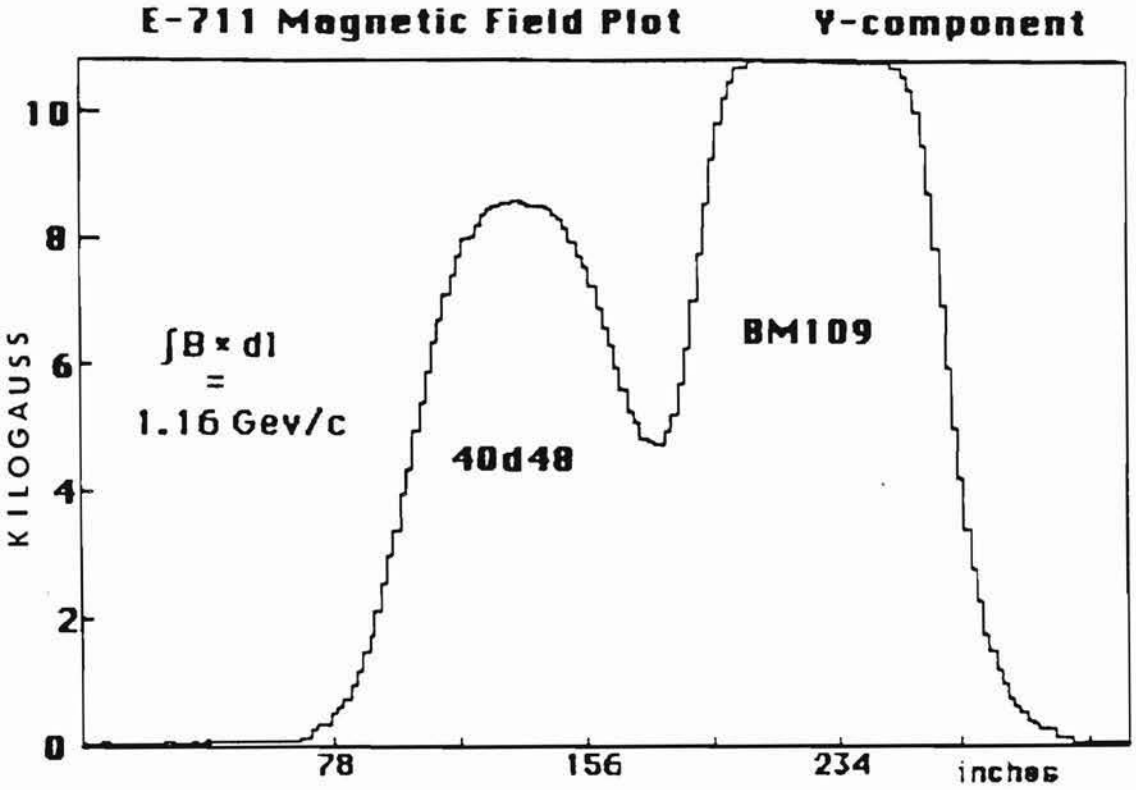

Intensity of the magnetic field along $\hat{\mathbf{z}}$ in the analyzing magnets

Figure 2.3

2.6 The drift chambers

The multiwire drift proportional chambers[16] (MWPC) are tracking devices which measure the positions along the trajectories of the charged particles passing through them. In E711 they were placed downstream the magnets, before the hodoscopes and calorimeters (see figure 1.4). The parameters of the calculated trajectory together with the knowledge of the $P_{\perp}$ kick of the magnets and the target position enabled the offline calculation of the momentum components of the charged particles.

An incident charged particle passing through a chamber ionizes the gas contained in it. The electrons produced, under high electric field drift to the closest anode. Near the anode wire the $\frac{1}{r}$ field is intense enough to accelerate the electrons to the atomic ionizing energy within one mean free path between atomic collisions. Such collisions then ionize the atoms, producing an exponential amplification in the number of electrons. In that way an electron avalanche is produced near the anode sense wire and a detectable signal can be collected. The identification of the wire which 'fires' gives the coordinate component of the particle perpendicular to the wire. Drift timing allows interpolation of the spatial position to a fraction of a sense wire spacing.

There were five MWPCs in the detector, with different wire spacings. The wire spacings were chosen to make a projective geometry. From now on the five MWPCs will be called DC1, DC2, DC5, DC3 and DC4 in increasing distance from the target.

2.6.1 Description of the MWPC and their location

Each chamber had four sense wire planes : X, Y, U, V. The X plane gave information on the x position of a track, having the wires strung vertically, the Y plane gave information on the y position (wires strung horizontally). The U and V planes were strung at $\pm 10°$ from the vertical and gave the corresponding projected coordinates. Four planes per chamber were necessary to resolve possible ambiguities in the association of the projected trajectories found by the pattern recognition programs.

The wire plane stack was completed with the ground and cathode planes. Cathode planes are necessary to produce the field directed perpendicularly to the planes which accelerates electrons toward anodes. The ground planes, which sandwiched each chamber, were necessary to shield the anode wires from external electromagnetic noise. Calling G, C, X, Y, U, V the ground, cathode, X sense, Y sense, U sense and V sense planes the disposition of the planes in the chambers was (starting from the most upstream plane going downstream) :

DC1 and DC2 : G C U C X C G gap G C V C Y G

DC3, DC4 and DC5 : G C U C V C X C Y C G

Because of the larger spacing between wires in DC3 and DC4 (see TABLE 2.2), field shaping wires were placed between the sense wires in the anode plane in order to make the field strength and the drift velocity more uniform, improve the

TABLE 2.2

Drift chamber wire spacings

	Anode wires (mm)	Cathode wires (mm)	Field wires (mm)	Ground wires (mm)
DC1 (X, Y, U, V)	2.03	1.0	-	2.0
DC2 (X, Y, U, V)	2.53	1.0	-	2.0
DC3 (X, Y)	4.17	2.0	4.17	2.0
DC3 (U, V)	4.11	2.0	4.11	2.0
DC4 (X, Y)	5.56	2.0	5.56	2.0
DC4 (U, V)	5.47	2.0	5.47	2.0
DC5 (X, Y, U, V)	3.05	2.0	-	2.0

linearity of the drift time-distance relation and shorten total drift time to prevent pile up of signals. DC1, DC2, DC5, DC3 and DC4 were positioned downstream the magnets at 5.39, 6.75, 8.23, 11.18 and 14.86 m from the target in order to form a projective geometry with the different chamber wire spacings with respect to the target to simplify the pattern recognition programs.

2.6.2 Description of the wires

Cathode and ground wires were an alloy of Cu 97% and Be 3% with nickel

TABLE 2.3

Drift chamber wire diameters

	Anode wires (μm)	Cathode wires (μm)	Field wires (μm)	Ground wires (μm)
DC1	25.4	63.5	-	127.0
DC2	25.4	76.2	-	127.0
DC3	25.4	76.2	76.2	127.0
DC4	25.4	76.2	76.2	127.0
DC5	25.4	76.2	-	127.0

coating, while the anode wires were very pure W (99.9%) in order to bear high tensile force, with a layer of Au to make the soldering to the readout pads possible. In TABLE 2.3 the diameter of the wires is listed.

2.6.3 Active and desensitized regions of the MWPC

All the MWPCs were desensitized in the central region in order not to detect the high flux of non interacting beam particles and the low $P_{\perp}$ particles in the beam fragmentation region. The desensitized regions were obtained by lowering

TABLE 2.4

Active area of drift chamber dimensions

	x (cm)	y (cm)
DC1	103.9	110.4
DC2	129.5	137.6
DC3	224.7	226.8
DC4	299.1	302.5
DC5	169.3	175.7

the cathode voltages on a central group of the horizontal strung cathode wires by approximately 400 Volt forming a deactivated horizontal band. The active regions of the chambers, whose size is listed in TABLE 2.4, were such that high $P_\perp$ particles coming from the target and impinging upon the calorimeter elements would intersect them. Between the desensitized region and the sensitive one, approximately 16 cathode wires had voltage midway between the other two in order to avoid high field gradients and consequent sparking.

2.6.4 Voltages

A negative high voltage (ranging from -2000. to -3700) was applied between

TABLE 2.5

Chamber typical operating voltages

	Cathodes (kVolt)	Field (kVolt)
DC1	-3.05	-
DC2	-3.30	-
DC3	-2.40	-1.40
DC4	-2.30	-1.45
DC5	-3.65	-

the cathode and sense planes. The wires of the cathode planes were connected to the power supply with 4.7 MΩ resistors for protection against breakdowns. The sense wires were connected to ground through electronic preamplifier circuits. In TABLE 2.5 the typical cathode and field voltages are listed.

2.6.5 Gas mixtures

The gas mixtures used were 50% argon 50% C_2H_6 (bubbled through ethyl alcohol at 0°C) for DC3 and DC4. This mixture gives the better chamber efficiency and good time distance relations[16]. For DC1, 2 and 5 the gas mixtures used were 17% CO_2, 0.4% freon and balance argon (the electron producer) since

it was impossible to operate those chambers with the argon-ethane mixture due to their wire spacings.

2.6.6 System used to amplify and take the signal out to the TDCs

The signals were picked up at the end of each sense wire and sent to the inputs of the preamplifiers. The preamplifiers were assembled on a PC board in groups of 16 channels and the boards were inserted into sockets on the chamber frames. The gain of the preamplifiers was $\simeq 20$ and allowed the chambers to be operated at a lower voltage and consequently at a higher rate ($\equiv$ higher beam intensity) without the gas becoming sufficiently ionized to cause voltage breakdown. The outputs of the preamplifiers were connected with ribbon cables to commercial (Nanometrics 272) amplifier/discriminator circuits that transformed the analogic signal into an ECL pulse (emitter coupled logic, -.8 to -1.6 Volt). Delay cables connected the logic signal outputs to Lecroy time-to-digital converters (TDC's). The TDC start was given by the sense wire signal, while the STOP was produced by a trigger pulse. The timing measurement allowed a more accurate estimate of the particle coordinates through the deduced time distance relation. The maximum drift times varied from 150 to 400 nsec depending on the different spacings between sense wires of the different chambers (the larger the spacing, the longer the maximum drift time).

2.6.7 Efficiency of the chambers

The efficiency of a given sense plane was calculated offline using tracks in

TABLE 2.6

Chamber plane efficiencies

Chamber	Y	X	U	V
DC1	0.698	0.778	0.742	0.837
DC2	0.740	0.895	0.883	0.814
DC3	0.899	0.887	0.885	0.934
DC4	0.912	0.946	0.952	0.948
DC5	0.644	0.776	0.776	0.753

which the other 4 planes of that projection were on, ensuring an independent recognition of the particle trajectory by pattern recognition programs. The results are listed in TABLE 2.6.

2.7 The hodoscopes and calorimeters

Two sampling calorimeters and two hodoscope pairs were used to trigger the detector in order to select high mass charged hadron pairs in real time. The fast response of the calorimeters and hodoscopes was ensured by the use of polyvinyl toluene as scintillator and fast photomultipliers combining for a typical signal

rise time of 5 nsec. The calorimeters yielded a signal proportional to the particle $P_\perp$ which could be used to trigger the data acquisition using the approximation $M_{1,2} \simeq P_{\perp 1} + P_{\perp 2}$. The hodoscopes, placed just upstream the calorimeters, were used to identify the charged particles impinging the calorimeters. The calorimeter and hodoscopes formed an approximately projective geometry pointing at the target, facilitating the electronic trigger logic.

The calorimeters and hodoscopes were placed symmetrically with respect to the horizontal plane containing the beam (see figure 1.4). Hence the non interacting beam particles and forward scattered particles (produced for instance in diffractive processes) could pass through without hitting them, allowing a high beam intensity.

The calorimeter was also used as an offline check of the reconstructed track momenta and, particularly in this analysis, to calculate the energy of the jet associated to the leading hadron. That was possible since all the output signals from the calorimeter photomultipliers were integrated and digitized by ADCs (analog to digital converters) whose information was readout and written onto magnetic tape.

2.7.1 Hodoscope description

Each calorimeter had two vertically segmented scintillation hodoscopes placed upstream to identify the wide angle particles incident upon them as charged. From now on the two hodoscopes are called HF (Hodoscope Front,

TABLE 2.7

x and y hodoscope (front and back) module dimensions

Module	x (cm)	y (cm)
1	29.5	6.35
2	33.8	6.35
3	38.1	6.35
4	42.2	6.35
5	46.5	6.35
6	52.8	8.89
7	59.2	8.89
8	65.8	8.89
9	72.1	8.89
10	82.6	14.00
11	93.2	14.00
12	103.9	14.00
13	114.3	14.00
14	125.0	14.00
15	134.6	14.00
16	146.3	14.00

the more upstream) and HB respectively. Each of them consisted of 16 pieces of scintillator, each viewed at both ends, by a PMT through a lucite light guide. The thickness of the scintillator pieces was 1.27 cm. In TABLE 2.7 the x and y dimensions of the 16 pieces (called from now on 'modules') are listed.

2.7.2 *Shower development in a calorimeter*

Hadrons, electrons and γs release their energy in the calorimeter through the particle production cascade called showering. A shower develops because the incoming particle interacts with nuclei inelastically producing more particles. The produced particles, in their turn, interact inelastically producing more particles and so the 'shower' develops. In electromagnetic showers (produced by γs, e^- and e^+) hadrons are not produced, the only mechanisms essentially being bremsstrahlung γs and e^+, e^- pair production. In the hadronic showers, produced by protons, neutrons, kaons and pions, $\simeq \frac{1}{3}$ of the particles produced in each interaction are π^os which decay into $\gamma\gamma$ and subsequently develop as an electromagnetic shower. This quickly leads to all of the particles in a hadronic shower being electromagnetic though their spatial distribution is much more elongated by the initial hadronic processes. In the showering process energy is released in the calorimeter by ionization loss of the charged particles produced in the shower. Until interacting inelastically a charged particle deposits an uniform amount of energy per unit length by ionization loss (see Bethe-Bloch formula (A.1) in APPENDIX A) :

$$\frac{dE}{dx} = k \times \rho \tag{2.1}$$

where ρ is the density of medium crossed and

$$k \simeq 2 \frac{\text{MeV}}{\text{gm} \times \text{cm}^2}$$

This holds when $\frac{1}{\sqrt{1-\beta^2}}$ of the particle $\geq$ 3.57 which is always the case for electrons produced in the GeV energy range showers. In this case a particle

releases the least amount of energy (the particle is a minimum ionizing particle, m.i.p.).

For a hadronic and an electromagnetic shower part of the energy is undetectable and the rest is detected through ionization loss of the calorimeter material. On average, the latter is proportional to the energy of the impinging particle (linearity of the calorimeter) with a different proportionality factor for electromagnetic and for hadronic showers due to the different amount of undetected energy. From (2.1) the energy deposited in the calorimeter by a charged particle is :

$$E = k \times \rho \times L$$

where L is the length of material crossed and ρ its density. Consequently the total energy deposited in a showering process is

$$E = k \sum_{i}^{N} \rho \times L_i$$

where the sum runs over the number of charged particles produced in the shower.

2.7.3 Sampling calorimeters

A sampling calorimeter has layers of active and passive material assembled one after the other. The energy deposited is measured only in the active layers. The number of charged particles that have gone through one active + passive plate thickness on average can be approximated by $\frac{PH}{PH_{(m.i.p.)}}$, where PH is the pulse height of the signal produced in an active layer and $PH_{(m.i.p.)}$ is the pulse

height produced on average by a m.i.p. in the same layer. As a result we have

$$E = k \sum_j \frac{PH_j}{PH_{j,(m.i.p.)}} \times (\rho_{active} L_{active} + \rho_{passive} L_{passive})_j$$

where the sum runs over the number of active + passive sections of the calorimeter.

2.7.4 *Calorimeter purpose*

Each calorimeter in E711 was divided into four sections in depth, from now on called EM (electromagnetic), H1 (first hadronic), H2 and H3. Each section was also divided vertically in 16 modules (as one can see in figure 2.4, side view of the calorimeters). The vertical segmentation allowed the PMT gains to be set proportionally to $\sin\theta_y$, where θ_y was the polar angle along the vertical direction between the beam line and the line connecting the target and the module. In that way the output signal produced by an impinging particle showering in a module was proportional to $E \times \sin\theta_y \simeq \mathrm{P}_y$.

2.7.5 *Calorimeter description and dimensions*

The 16 modules of a longitudinal calorimeter section were constructed as a sandwich of active (scintillator) and passive (lead or steel) layers. Their construction is illustrated in figures 2.5 and 2.6. The vertical segmentation had the further advantage of enabling localization of the energy released so that shower energy measurement could be associated to single tracks detected by the chambers. There were 14 pieces of $\frac{1}{4}$" scintillator in the EM and H1 modules, 7 pieces

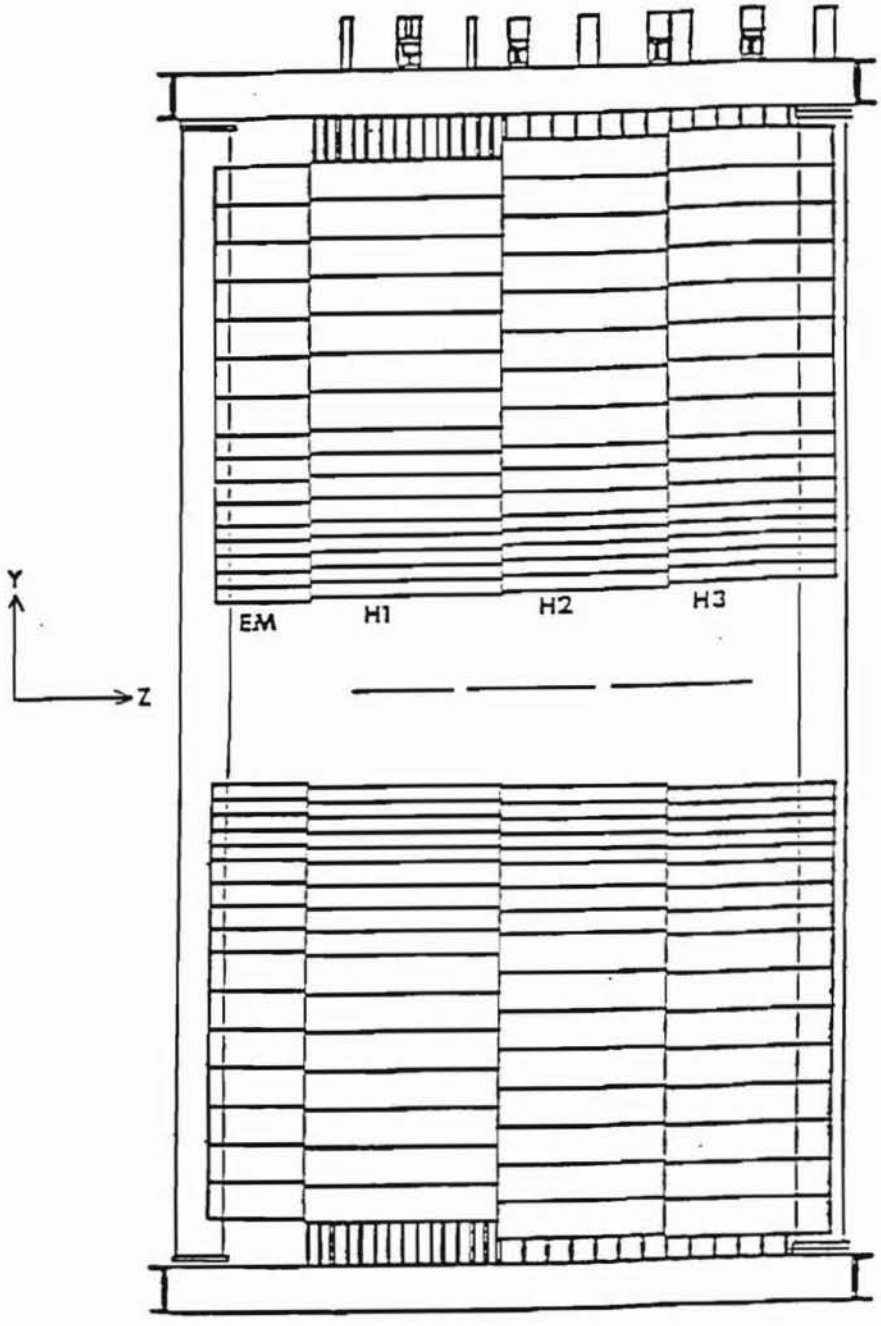

Side view of calorimeters

Figure 2.4

of $\frac{1}{4}$" scintillator in the H2 and H3 modules. The passive material was Pb in the EM section (13 plates of $\frac{1}{2}$") and steel in the H1 (14 plates of 1.25"), H2 and H3 sections (7 plates of 2.5" in each section). Figure 2.6 shows the design and dimensions of the scintillator of an H3 module. Each end of the 7 scintillator pieces was connected by light guides to a phototube, which converted the light pulse into an electronic signal.

The EM section consisted of 29.7 radiation lengths in depth. The complete calorimeter (EM + H1 + H2 + H3) made a total of 9.24 interaction lengths. Consequently the hadronic showers were completely contained in the calorimeter and the electromagnetic ones were completely contained in the EM section of it. The dimensions of all the calorimeter modules are listed in TABLE 2.8 Like the wire chambers, the hodoscopes and calorimeters formed an approximately projective geometry in the sense that the target, the center of a hodoscope element and calorimeter module formed a straight line.

The fast response time of the calorimeter was needed to avoid signal pile up from the high interaction rate. The scintillator used for the hodoscopes and calorimeters was PVT made by Bicron (BC 408) with a 1.5 m attenuation length and a 1 nsec deexcitation time [17]. The photomultiplier tubes were linear focussed Hamamatsu 10 stage type R 2154 for the calorimeters (2" of diameter) and linear focussed Hamamatsu 12 stage type R 329 for the hodoscopes. The rise time of the signal produced was typically $\simeq$ 3.4 nsec and $\simeq$ 2.6 nsec for the calorimeters and hodoscopes respectively.

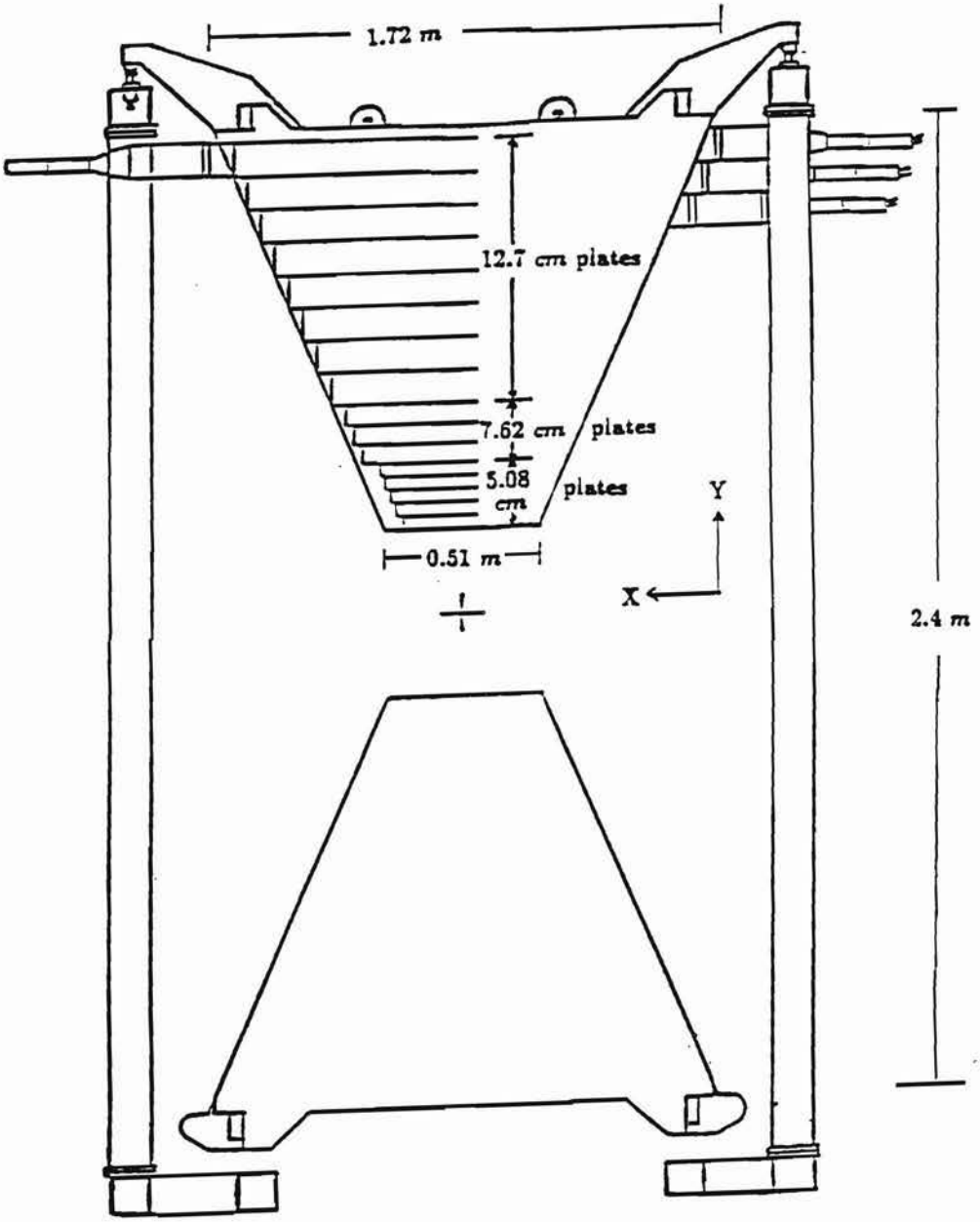

Front view of calorimeters

Figure 2.5

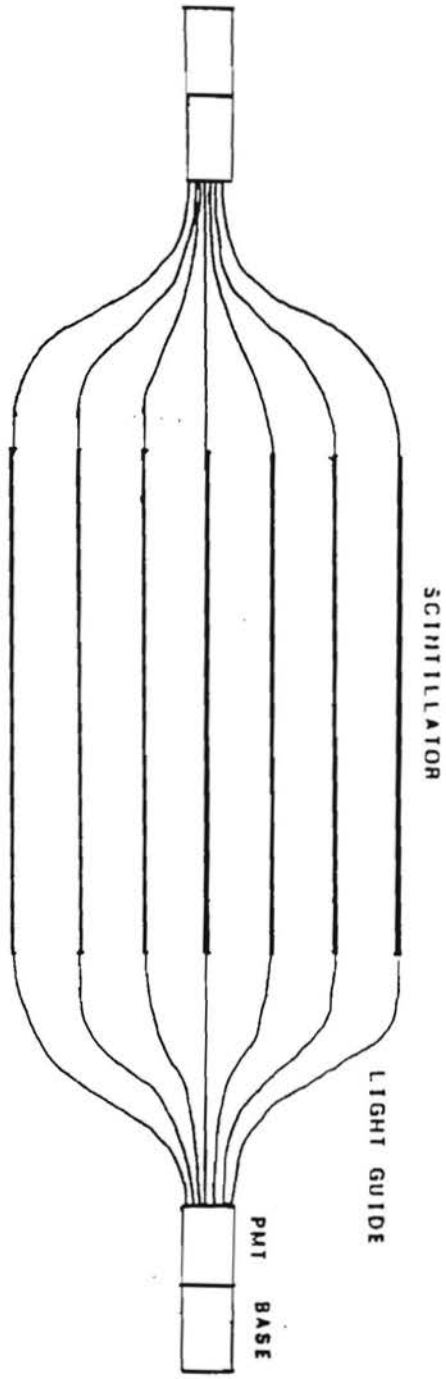

Calorimeter module (top view) in section H3

Figure 2.6

TABLE 2.8

Calorimeter module x and y dimensions

Module #	EM and H1 x (cm) by y (cm)	H2 and H3 x (cm) by y (cm)
1	44.7 × 5.1	49.0 × 5.1
2	49.0 × 5.1	53.3 × 5.1
3	53.3 × 5.1	57.4 × 5.1
4	57.4 × 5.1	61.7 × 5.1
5	61.7 × 5.1	66.0 × 5.1
6	68.1 × 7.6	74.4 × 7.6
7	74.4 × 7.6	81.0 × 7.6
8	81.0 × 7.6	87.4 × 7.6
9	87.4 × 7.6	97.8 × 12.7
10	97.8 × 12.7	108.5 × 12.7
11	108.5 × 12.7	119.1 × 12.7
12	119.1 × 12.7	129.5 × 12.7
13	129.5 × 12.7	140.2 × 12.7
14	140.2 × 12.7	150.9 × 12.7
15	150.9 × 12.7	161.5 × 12.7
16	161.5 × 12.7	172.0 × 12.7

The photomultipliers were mounted on bases which provided the high voltage partition and collected the output signal. The base schematic used for the R 2154 is shown in figure 2.7. A relay connected to the 6th dynode enabled the gain of

the tube to be set to two different values from now on called *High Gain* and *Low Gain*. A 50 KΩ potentiometer in series with a fixed resistor connected to the 5th and 7th dynodes with the relay determining whether the variable or fixed point of the potentiometer established the voltage at the 6th dynode. Since the total voltage across the entire dynodes was the same for *High Gain* and *Low gain*, the time characteristics of the signal produced by the phototube did not change for the two settings. Finally a Lecroy 1440 high voltage system, operated by a VAX-780 computer, controlled the PMT high voltages.

2.7.6 Hodoscope calibration

All the charged particles impinging the hodoscope elements behaved as minimum ionizing particles (m.i.p.). For this reason the phototubes attached to the hodoscope ends were set at a voltage such that a m.i.p. gave a pulse height of -100. mVolt in order to easily set standard Lecroy discriminator circuits.

2.7.7 Calorimeter calibration

The purpose of the calorimeter calibration was to have from each section of the calorimeters output electronic pulses proportional to the transverse energy ($E \times \sin\theta_y = \mathrm{P}_y \simeq \mathrm{P}_\perp$) released in the sections. The calibration was done in two steps. First the responses of all the calorimeter modules within a section were equalized at high gain and the relative gains of each section were adjusted such that the pulse heights of the output signals were proportional to the energy released by a m.i.p. in the active + passive layers of each section. Then the

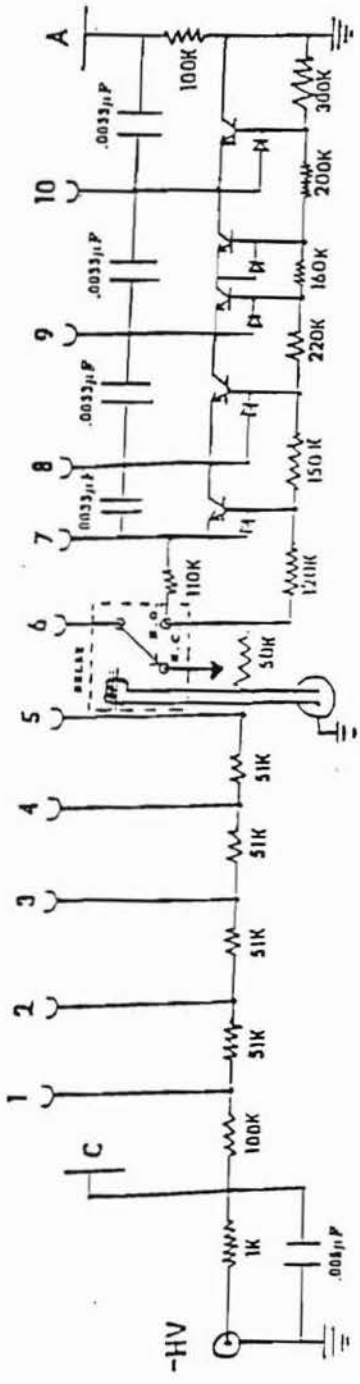

Diagram of R2154 photomultiplier tube base

Figure 2.7

low gain settings of each module were set so that the pulse height of the output signals were proportional to $\sin\theta_y$ for a fixed light source. In this way the output signals would be approximately proportional to $P_\perp$.

The first step of the calibration of the calorimeters was performed using muons, which deposited a constant amount of energy in each module of a section. However, the pulse heights generated by the calorimeter by muons were much lower than those produced by hadrons (as in the case of the experimental data) and they could not be digitized accurately by the same 15-bit Lecroy 2285 ADC scale. For this reason the calibration of muons was done using the higher gain setting. The PMT's of the modules in the same calorimeter section had gains set such that the response to muons was uniform namely that the peak of the energy distribution of the muons in ADC counts was positioned to the same number. This was done taking special dedicated muon runs before and during the data taking thereby monitoring the gain stability. Then the gains of the four sections were at the relative ratio

$$0.44 : 1 : 1 : 1$$

which are the ratios of the energy deposition of a m.i.p. in the material crossed in EM (lead + scintillator), H1 (iron + scintillator), H2, H3. This voltage setting was the *High Gain*. In TABLE 2.9 the thickness of scintillator and of the passive material of each section and the corresponding m.i.p. energy deposition in MeV are listed. For the EM section one obtains, assuming the typical deposition of 2 MeV/g $\cdot$ cm^2, that the energy deposition is

$$2. \times 16.51 \times \rho_{lead} + 2 \times 8.89 \times \rho_{scintillator} = 208.5 \text{ MeV}$$

TABLE 2.9

	thickness of scintillator	thickness of lead	thickness of steel	peak of μ energy deposition spectrum
EM	8.89 cm	16.51 cm	–	208.5 MeV
H1	8.89 cm	–	44.45 cm	490.9 MeV
H2	4.45 cm	–	44.45 cm	483.2 MeV
H3	4.45 cm	–	44.45 cm	483.2 MeV

The analogous calculation was performed for the other sections. The ratios 0.44 : 1 : 1 : 1 are obtained from the values

$$\frac{208.5}{490.5} : \frac{490.5}{490.5} : \frac{483.2}{490.5} : \frac{483.2}{490.5}$$

the difference between $\frac{483.2}{490.5}$ from one being neglected. Finally, the *Low Gain* setting of each module was adjusted by the factor $\sin\theta_y$ where θ_y was the polar angle along the vertical direction subtended by the center of the module.

$$\sin\theta_y = \frac{y}{\sqrt{y^2 + z^2}}$$

y being the height from the beam axis to the center of the module and z the distance of the calorimeter section from the target. The $\sin\theta_y$ factor was introduced in order to obtain a calorimeter pulse size proportional to the transverse energy of the impinging hadron.

During the data taking, the *Low Gain* settings were used. *High Gain* and *Low Gain* of a given module of a certain section of the calorimeter were related according to the following relation :

$$Low\ Gain = C \times High\ Gain \times \sin\theta_y$$

where C was a constant (the same for all the modules and sections) necessary to keep the PMT pulse heights and the corresponding ADC counts in a reasonable range. The *Low Gain* settings were made by measuring the base current caused by flashing LEDs and making the ratio of the currents in *Low Gain* and *High Gain*

$$\frac{Low\ Current}{High\ Current} = C \times \sin\theta_y$$

by adjusting the potentiometer between the 5th and 7th dynodes. During the data taking special dedicated muon runs were used to monitor the gain and adjust the *High Gain* voltages. The *Low Gain* to *High Gain* ratios were measured periodically, but required virtually no adjustment.

2.8 The luminosity and beam monitor system

The knowledge of the luminosity of the experiment is essential to calculate any cross section from the number of experimental events produced in a reaction. In general the luminosity $\mathcal{L}$ is defined as :

$$\mathcal{L} \equiv \frac{N_{event}}{\sigma}$$

where N_{event} is the number of events produced in a reaction with cross section σ. In detail :

$$\mathcal{L} = NF \int_0^l \frac{N_{scatt}}{V} e^{-z/\lambda_i} dz$$

therefore

$$\mathcal{L} = NF\lambda_i \frac{N_{scatt}}{V} [1 - e^{-l/\lambda_i}] \tag{2.2}$$

where

$N \equiv$ incident beam particles

$F \equiv$ fraction of beam hitting the target

$\frac{N_{scatt}}{V} \equiv$ number of scattering centers/volume

$l \equiv$ target length

$\lambda_i \equiv$ proton inelastic interaction length in the target material.

In (2.2) the parameters l, λ_i, $\frac{N_{scatt}}{V}$ are calculable just knowing the dimensions and material of the target used. N and F depend on the beam and must be measured directly. In the E711 experiment they were measured on a spill by spill basis : the incident beam flux (N) by an ion chamber just upstream the experimental hall and F by four arrays of 3 scintillator counters in coincidence (the 90° luminosity monitors).

2.8.1 Ion chamber and its calibration

The ion chamber just upstream the experimental hall (NEEPWC in figure 2.2) measured the beam flux on a spill by spill basis. The use of an ion chamber was necessary because direct counting of the incident particles by scintillation counters was not possible at the high beam rates used in E711. The beam, passing

through the chamber, liberated an amount of electron ion pairs proportional to the number of beam particles. The value of the total charge collected on the ion chamber plates was digitized by a scaler. The ion chamber was calibrated to a 2% level using a low intensity beam ($\simeq 10^5$ protons/sec) where two small scintillation counters in coincidence could be used to directly count the incident particle flux.

2.8.2 90° *luminosity monitors*

The 90° monitors count the rate at which particles are into their acceptance. This rate produced at wide angle is proportional to the total interaction rate through an unknown but constant factor. The number of particles detected is proportional to the beam flux hitting the target, while their rate is low enough (being produced at 90°) so that they could be counted by scintillators. Figure 2.8 shows a front view of the four arrays of scintillators. They were mounted on the front face of the first magnet, approximately in the plane containing the target and perpendicular to the beam line at a distance of at least 1.5 m from the target.

Each luminosity monitor was calibrated by means of horizontal target scans. The scans were performed by moving the beam horizontally pulse by pulse by a small amount. The quantity $N_{lum,i}$ was parametrized as

$$N_{lum,i} = B_i \times N_{beam} + K_i \times F \times N_{beam}$$

where N_{beam} was the number of beam particles, F the fraction of beam actually hitting the target, K_i was the proportionality constant relating the number of

90° MONITORS

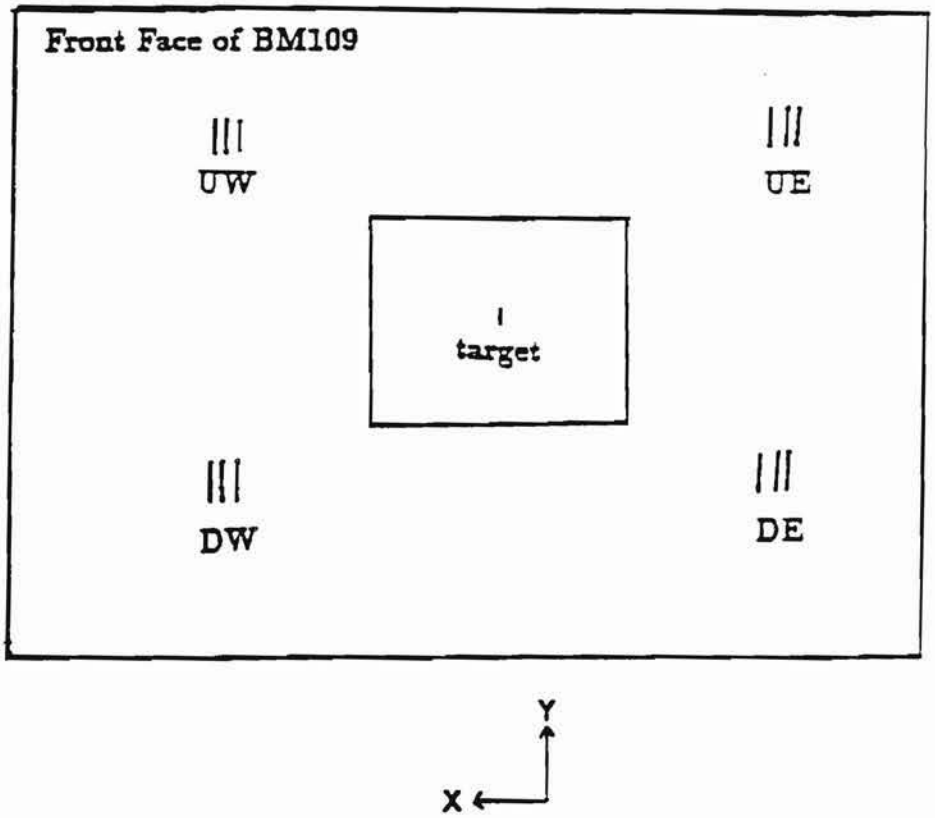

Diagram of the 90° monitors mounted on the front face of the first magnet

Figure 2.8

particles hitting the target ($= N_{beam} \times F$) to the number of counts $N_{lum,i}$ of the ith luminosity monitor. The quantity $B_i \times N_{beam}$ was the background contribution, due to interactions of the beam halo in air or in the target stand. F was given by

$$F = \int_{x_0-\frac{w}{2}}^{x_0+\frac{w}{2}} f(x, x_b) dx.$$

where x_b was the horizontal position of the beam intensity peak, x_0 the position of the target, w its width, $f(x, x_b)$ the horizontal distribution of beam intensity. x_0 and w were known from survey measurements, x_b was calculated by means of the beam line control devices. The function $f(x, x_b)$ was found to be properly parametrized with a gaussian centered in x_b. Using the target scan data, the $N_{lum,i}$ distributions for all the four luminosity monitors were fit to determine K_i and B_i.

Each luminosity monitor enabled an independent calculation of the fraction of beam hitting the target during the data taking runs and hence an estimate of the beam shape dependent systematic errors. The four independent measurements agreed at worse to within 4% and in average within 1%. The target scans were taken periodically during the data taking runs in order to calibrate the monitors. The observed differences were mainly due to the type of target and small corrections were due to changes in the beam profile and consequent background hitting the monitors.

2.8.3 Total luminosity and its systematic uncertainties

When a trigger was accepted, a certain amount of time ($\simeq$ 5 msec) was

necessary for the PDP-11 computer to read the event out and write it onto tape. During that time ('dead time') the detector was disabled from accepting further triggers. The luminosity has to be measured only for the time when the detector could accept triggers ('live time'). For each spill, the counts of the four monitors were recorded by electronic scalers, enabled to count during the detector live time, and the and read out during the subsequent B interrupt. This allowed the calculation of the actual experimental sensitive luminosity.

Once calibrated, the monitor scaler counts enabled the calculation of the integrated luminosity, listed in TABLE 2.10 for the four different targets. The overall error had negligible statistical component. The systematic uncertainties arose from the ion chamber (2%) calibration error and the background variations between the horizontal target scans. They were estimated to be $< 4\%$ for the Be target and $< 2\%$ for Al, Fe, W.

TABLE 2.10

Total integrated luminosity

Target	$\mathcal{L}$ per nucleus (barn^{-1})	$\mathcal{L}$ per nucleon (barn^{-1})
Be	1.774×10^{12}	1.598×10^{13}
Al	2.258×10^{11}	6.090×10^{12}
Fe	2.756×10^{11}	1.539×10^{13}
W	3.534×10^{10}	6.497×10^{12}

CHAPTER 3

TRIGGER, DATA ACQUISITION and ONLINE MONITORING

The trigger is an online, real time event selection causing the event which produced it to be recorded by the data acquisition system and stored onto magnetic tape. The intensity of the beam used in E711 was $\simeq 2.5 \times 10^7$ proton/sec, giving an interaction rate of $\simeq 2.5 \times 10^6$. It would have been impractical and even impossible to record all the interactions onto magnetic tape. The interesting events (two high $P_\perp$ hadron events) were a very small fraction of the total number of interaction produced ($\simeq 10^{-6}$). The trigger was designed to select and write only them onto tape, discarding all the other events.

The data acquisition system read out and transferred the digitized data of the events that triggered it, into the memory of a dedicated computer (a PDP-11 in

the case of E711). When the trigger logic accepted an event, a logical NIM level enabled the digitizing electronics (ADCs and TDCs) to store all the information of the event as the delayed copies of the signals arrived at the ADC and TDC inputs. Then the PDP-11 computer began to read out all the digitized information through CAMAC into its memory. The information was subsequently written onto magnetic tape and a subset transferred to the 'backend' online analysis VAX 11/780. Typically $\simeq$ 45000 events could be stored per tape.

The time interval required for an events' information to be digitized and read out was typically 5 to 10 msec. During this 'dead time' the trigger logic was disabled. This dead time decreased the effective luminosity of the experiment.

The online monitoring system consisted in a set of software programs that monitored the quality of the data online and checked the stability of the detector. It is an essential tool in every high energy experiment, since it enables the discovery and subsequent repair of the malfunctions of the apparatus.

3.1 The trigger

The trigger selected events with two high $P_\perp$ hadrons, hitting the top and the bottom calorimeters. In first approximation

$$P_{\perp 1} + P_{\perp 2} = M_{di-hadron}$$

where $M_{di-hadron}$is the effective mass of the di-hadron system and the labels 1 and 2 refer to the two hadrons. Therefore, selecting high $P_\perp$ di-hadron events was equivalent to selecting a high di-hadron mass system.

The trigger was formulated from a set of logical signals in successive coincidences forming increasingly selective event requirements. The successive coincidences corresponded to the following requirements on the physical interaction :

1) two charged particles with $P_{\perp} > 2$ GeV/c each, hitting the upper and lower calorimeters

.AND.

2a) $M_{di-hadron} \simeq P_{\perp 1} + P_{\perp 2} > 6$ GeV/c^2 ($Q \cdot P \cdot \tilde{m}$ logic signal)

.OR.

2b) $M_{di-hadron} \simeq P_{\perp 1} + P_{\perp 2} > 8.5$ GeV/c^2 ($Q \cdot P \cdot HM$ logic signal). The $P_{\perp}$, $\tilde{m}$ and HM logic signals were produced by discriminating analog signal sums of the calorimeter PMT outputs. The information that the impinging particle was charged was given by the hodoscopes (Q logic signals). With the above logical signals the final trigger signals (defined in 2a and 2b) were obtained.

For reasons of clarity from now on the modules of the calorimeters and hodoscopes will be numbered from 1 to 16 going from the closest to the beam line to the outermost, for the top and bottom calorimeters. Also, the word *segment* will be used to indicate the set of four adjacent modules of the four longitudinal sections of the calorimeters. For instance, segment # 1 is the set of modules # 2,3,4,5 of EM, H1, H2 and H3. In TABLE 3.1 the components of each segment (either in the top or in the bottom sections of the calorimeter) in terms of calorimeter modules is shown. Adjacent segments overlapped to make a smooth coverage, over the calorimeter, of the showers produced by particles coming from

the target. The first calorimeter modules of the top and bottom (# 1) were not included in the trigger system. In figure 3.1 a representative schematic is shown of one of the logic circuits of the 24 identical segments of the trigger, 12 for the top calorimeter and hodoscopes, 12 for the bottom ones.

3.1.1 Q signal

The signal coming from the hodoscope elements were fed to Lecroy 621 BL discriminators in order to create the logic signals indicating the passage of a charged particle into the calorimeters. The Q logic signals were defined as follows :

$$\mathrm{Q}_i \equiv [(HF_{east,i+2} \cdot HF_{west,i+2}) \cdot (HB_{east,i+2} \oplus HB_{west,i+2})].\mathbf{OR}.$$
$$[(HF_{east,i+3} \cdot HF_{west,i+3}) \cdot (HB_{east,i+3} \oplus HB_{west,i+3})]$$

where Q_i means the Q logical signal relative to the ith segment (top or bottom), $HF_{east,i+2}$ is the discriminated signal coming from element # $i+2$ of the front hodoscope, east side. $HB_{east,i+2}$ means the analog signal coming from the back hodoscope element # $i+2$ east side. $HB_{west,i+2}$ means the analog signal from the back hodoscope, west side. The symbol $\oplus$ means that the two input analogic signals were summed by means of fan in/fan out modules and then discriminated. In this way the Q_i signal indicated the passage of a charged particle through the $i^{th}+2$ or $i^{th}+3$ adjacent hodoscope elements corresponding, due to the projective geometry of hodoscopes and calorimeters, to the center of the ith calorimeter segment sum.

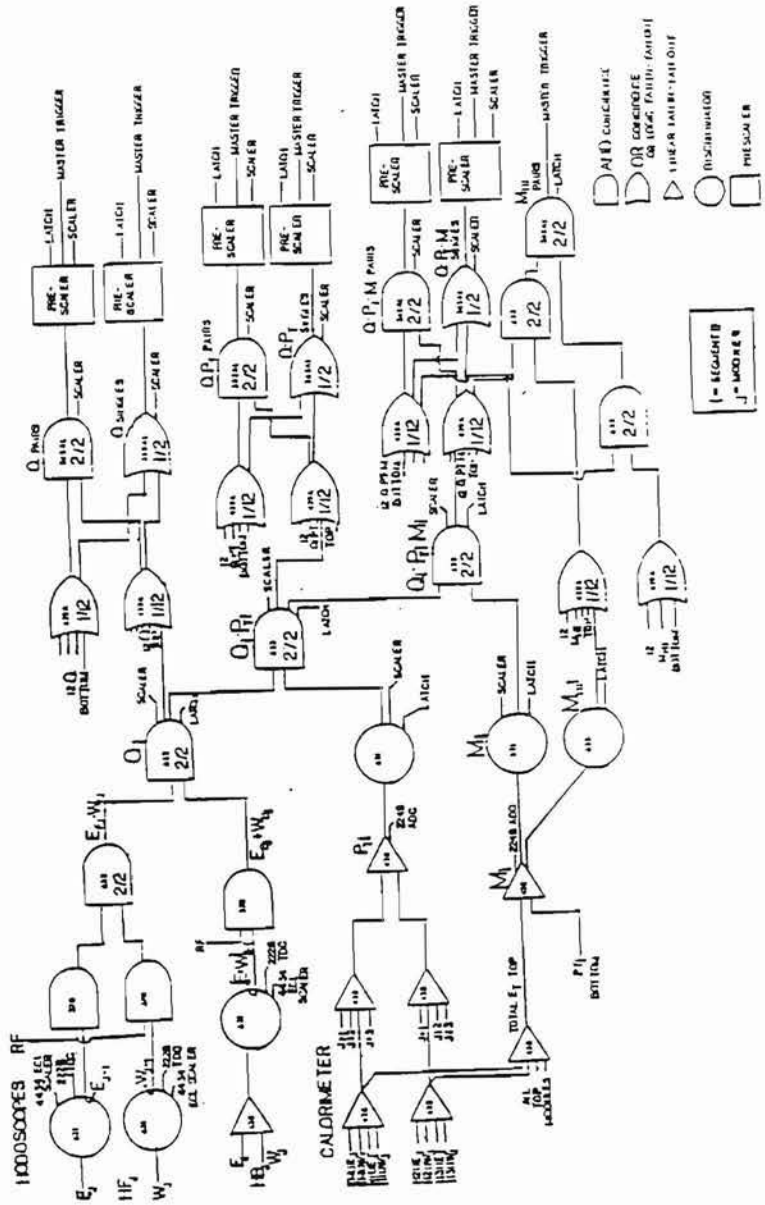

Diagram of one of 24 identical trigger segments and the formation of the final triggers

Figure 3.1

TABLE 3.1

Segment	Calorimeter Modules	and	Hodoscope Elements
1	2-3-4-5		3-4
2	3-4-5-6		4-5
3	4-5-6-7		5-6
4	5-6-7-8		6-7
5	6-7-8-9		7-8
6	7-8-9-10		8-9
7	8-9-10-11		9-10
8	9-10-11-12		10-11
9	10-11-12-13		11-12
10	11-12-13-14		12-13
11	12-13-14-15		13-14
12	13-14-15-16		14-15

3.1.2 $P_\perp$ *signal*

To achieve an accurate estimate of the $P_\perp$ of the incident particle which produced a shower, the PMT analog signals of an entire segment were summed together by means of Lecroy linear fan in-fan out modules. The reason for doing it was that a hadronic showers' transverse spread was certainly smaller than the height of any segment, which ranged from 20.32 cm to 50.8 cm in the vertical direction. Consequently, the shower of a particle coming from the target and impinging the sensitive area of the calorimeter was fully contained in at least one

of the overlapping calorimeter segments. When a particle hit the calorimeter, the segment containing the shower produced an analog sum signal proportional to $P_\perp$ of the particle (see chapter 2). The segment sums were discriminated by Lecroy 621 BL modules in order to select the minimum desired $P_\perp$ of the showering particle. The threshold of the discriminators was set such that $P_\perp$ had to be greater than 2 GeV/c to produce the logical output pulse ($P_\perp$ logic signal).

3.1.3 $\tilde{m}$ signal, HM signal

These logical signals enabled the selection of a high mass hadron pair. Using the approximation $M_{di-hadron} \simeq P_{\perp 1}+P_{\perp 2}$, calculating and selecting the mass of a di-hadron pair in principle it would have required 144 analog sums of all pairwise combinations of the 12 upper and lower calorimeter segments signals and then discriminate all of them. In order to reduce the amount of electronics needed, the $\tilde{m}$ signals were formed. For each segment, the $P_\perp$ analog sum signal was summed with the total opposite calorimeter transverse energy (namely the analog sum of all the PMT pulses of the opposite calorimeter). The resulting analog signal was discriminated by Lecroy 821 modules at a lower threshold producing the $\tilde{m}_i$ logic signals, or at a higher threshold by Lecroy 623 B discriminators producing the HM_i logic signals (the subscript i refers to the ith segment, either top or bottom). The $\tilde{m}$ and HM logical signals indicated that a high mass 'jet'-single particle state (one hadron in one calorimeter, jet energy in the opposite calorimeter) had been detected with $M_{jet-hadron} \geq 6.$ GeV/c^2 ($\tilde{m}$ signal) or with $M_{jet-hadron} \geq 8.5$ GeV/c^2 (HM signal). By requiring one such signal from a top segment in

coincidence with one from a bottom segment a reasonable approximation of a two particle high mass trigger could be achieved.

3.1.4 $Q \cdot P$, $Q \cdot P \cdot \tilde{m}$, $Q \cdot P \cdot HM$ *trigger signals*

The $Q \cdot P$, $Q \cdot P \cdot \tilde{m}$ and $Q \cdot P \cdot HM$ pair logical signals used as triggers were defined by the following coincidences of Q, $P_\perp$, $\tilde{m}$ and HM logic signals :

$$Q \cdot P_{top} \equiv (Q_{1top} \cdot P_{\perp 1top} \oplus Q_{2top} \cdot P_{\perp 2top} \oplus \ldots \oplus Q_{12top} \cdot P_{\perp 12top})$$

$$Q \cdot P_{bot} \equiv (Q_{1bot} \cdot P_{\perp 1bot} \oplus Q_{2bot} \cdot P_{\perp 2bot} \oplus \ldots \oplus Q_{12bot} \cdot P_{\perp 12bot})$$

$$Q \cdot P \equiv Q \cdot P_{top} \cdot Q \cdot P_{bot}$$

$$Q \cdot P \cdot \tilde{m}_{top} \equiv (Q_{1top} \cdot P\perp 1top \cdot \tilde{m}_{1top} \oplus \ldots \oplus Q_{12top} \cdot P\perp 12top \cdot \tilde{m}_{12top})$$

$$Q \cdot P \cdot \tilde{m}_{bot} \equiv (Q_{1bot} \cdot P\perp 1bot \cdot \tilde{m}_{1bot} \oplus \ldots \oplus Q_{12bot} \cdot P\perp 12bot \cdot \tilde{m}_{12bot})$$

$$Q \cdot P \cdot \tilde{m} \equiv (Q \cdot P \cdot \tilde{m}_{top}) \cdot (Q \cdot P \cdot \tilde{m}_{bot})$$

$$Q \cdot P \cdot HM \equiv Q \cdot Ptop \cdot (HM_{1top} \oplus \ldots \oplus HM_{12top}) \cdot$$
$$\cdot Q \cdot Pbot \cdot (HM_{1bot} \oplus \ldots \oplus HM_{12bot})$$

All the triggers indicated that a charged particle intersected the top and the bottom calorimeters (Q signal). The $Q \cdot P$ trigger selected events with a hadron in each calorimeter with $P_\perp \geq 2$ GeV/c and consequently a di-hadron pair with $M_{di-hadron} \geq 4.$ GeV/c^2 ($M_{di-hadron} \simeq P_{\perp 1} + P_{\perp 2}$). The $Q \cdot P \cdot \tilde{m}$ and $Q \cdot P \cdot HM$ triggers selected di-hadron pairs with $M_{di-hadron} \geq 6.$ GeV/c^2 and ≥ 8.5 GeV/c^2 respectively.

All of the three logic signals were used as triggers at the same time. In order to have a nearly equal amounts of each type of trigger in the data the $Q \cdot P$

and $Q \cdot P \cdot \tilde{m}$ were prescaled during the run since these lower mass triggers ran at too high a rate. The prescaling factors were usually $\frac{1}{128}$ and $\frac{1}{2}$ respectively. This enabled measurements of the trigger turnon efficiencies by using the events selected by lower mass triggers to determine the efficiencies, as a function of mass, of the higher mass triggers.

3.2 The data readout system

When a trigger was generated, a NIM logical signal was sent to the PDP-11 computer dedicated solely to the data taking. A computer program[18] then issued a command to the CAMAC[19] system (through the JORWAY branch driver) to read out the digitized information stored in the CAMAC modules and write it onto magnetic tapes. There were two types of readouts sequences, the A-interrupt and B-interrupt, during which different parts of the digitizing electronics were read out.

3.2.1 A-interrupt

The A-interrupt readout sequence was enabled by the triggers just described. The ADC values of each calorimeter phototube channel, the TDC information of the wire chambers, all the latched information of the trigger logic signals and some luminosity scalers were read out and recorded. The A-interrupt sequence was also issued 16 times before each spill to record the pedestal levels of each ADC when no signal came from the PMTs due to the high $P_\perp$ particles. That was essential information since in the offline analysis the average pedestal had

TABLE 3.2

Readout during the A-interrupt

Readout electronics	readout information
Lecroy 2285 ADC	hodoscope and calorimeter PMT charge
Lecroy 4290 TDC	chambers wire drift time
EG&G C124 latches	Q segment logic signals
EG&G C124 latches	$P_\perp$ segment logic signals
EG&G C124 latches	$\bar{m}$ segment logic signals
EG&G C124 latches	$Q \cdot P_\perp$ segment logic signals
EG&G C124 latches	$Q \cdot P_\perp \cdot \bar{m}$ logic signals
EG&G C124 latches	$Q \cdot P_\perp \cdot HM$ logic signals
EG&G C124 latches	trigger type signals
JORWAY scalers	luminosity monitors

to be subtracted from each ADC in order to obtain the real amount of charge produced by the PMTs. In TABLE 3.2 it is listed a summary of the quantities read out during an A-interrupt

3.2.2 B-interrupt

A B-interrupt readout sequence was initiated after each 20 second beam spill, to record the information about the spill luminosity, the analyzing and beam line magnet currents (and consequently their magnetic fields), and the number and types of triggers collected during the spill. The information was recorded onto magnetic tape for offline analysis. In TABLE 3.3 a list of the quantities read out

TABLE 3.3

Readout during the B-interrupt

Readout electronics	readout information
JORWAY scalers	spectrometer and beam line magnet currents
JORWAY scalers	ion chamber counts
JORWAY scalers	90° monitors
JORWAY scalers	trigger types counts, prescaled
JORWAY scalers	trigger types counts not prescaled
JORWAY scalers	Q logic signal counts
JORWAY scalers	$P_\perp$ logic signal counts
JORWAY scalers	$\bar{m}$ logic signal counts
JORWAY scalers	$Q \cdot P_\perp$ logic signal counts
JORWAY scalers	$Q \cdot P_\perp \bar{m}$ logic counts

during a B-interrupt sequence is presented.

3.2.3 'Computer busy', dead time, live time

When a trigger was generated, the PDP-11 sent a NIM level ('computer busy' signal) to the electronic logic in order to prevent any other trigger from being issued as the digitizing electronics was unable to process new data until the current event was completely read out. That caused a 'dead time' of the apparatus that lasted typically $\simeq$ 5-10 msec per event. The 'live time' was the period of time during which the data acquisition system was ready to accept new triggers. The knowledge of the 'dead time' and 'live time' of the apparatus is

essential to correctly determine the experiments' sensitive luminosity. The beam particles that arrived when the detector was 'dead' count as if essentially they had never arrived at all. The dead time fraction for typical running conditions in E711 was 10 to 15%.

3.3 The online monitoring system

The online monitoring system consisted of the set of computer programs for checking beam line devices, trigger efficiencies, detector stability and to display the recorded events during the data taking. Such a control was essential in order to detect and fix malfunctions of the apparatus, to correct magnet current settings whenever the beam characteristics changed or to adjust MWPC voltages according to the beam conditions.

3.3.1 Beam line monitoring

The most relevant beam line magnet currents were checked and set during the data taking period with a program running on a dedicated beam line PDP-11[20]. Real time plots of the SWIC (Segmented Wire Ion Chambers) charge distributions gave essential information on the beam position, profile, and direction. The ion chamber measured the beam intensity. The magnet currents were set in order to maximize the amount of beam intercepting the target at all times, tracking the beam characteristics changes. The amount of beam actually hitting the target was on average about 94% of the intensity transported by the beam line. The current of the last horizontal beam line control magnet (NECH) was

varied to perform target scans necessary to calibrate the 90° luminosity monitors and maintain the high targeting fraction.

3.3.2 Data online monitoring

The online monitoring of the quality of the experimental data was implemented using the backend VAX 11-780 computer. The VAX 11-780 received about 10% of the events through a link to the PDP-11 dedicated to the data taking. A program[21] read events written into the VAX 11-780 memory and performed a detailed data analysis. It checked the performance of all the detector. The chambers were checked looking at the TDC time and wire hit distributions. The hodoscopes were checked looking at the hit module distributions. Many plots were periodically made to check the calorimeter performance. The single PMT ADC count plots and $P_\perp$ segment sum distributions, by longitudinal sections and for the total, the $\bar{m}$ sum ADC counts and the hit module distributions were scrutinized to find anomalies and irregularities. The trigger performance was checked looking at the latch distributions, see figure 3.2, and the $P_\perp$ discriminator, $\bar{m}$ discriminator and HM discriminator turn on curves. A pattern recognition program was used to find tracks and their momenta online and check the requested $P_\perp$ characteristics by means of an event display program. The information was displayed on a set of computer monitors (see figure 3.3) together with the hodoscope and calorimeter energy deposition in the segment hit by the track. This allowed an online comparison of the calorimeter data with reconstructed tracks indicating the operation of the trigger.

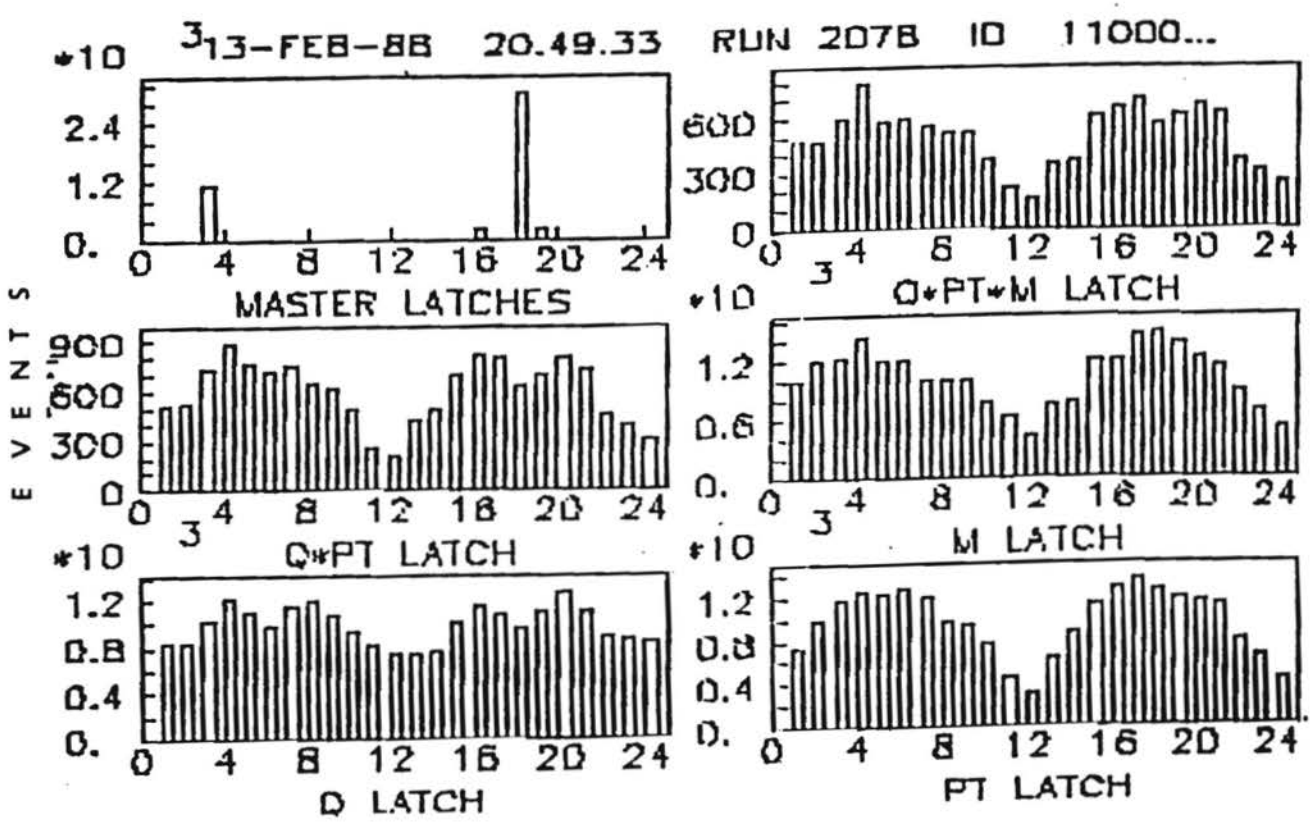

Example of online latch histogram

Figure 3.2

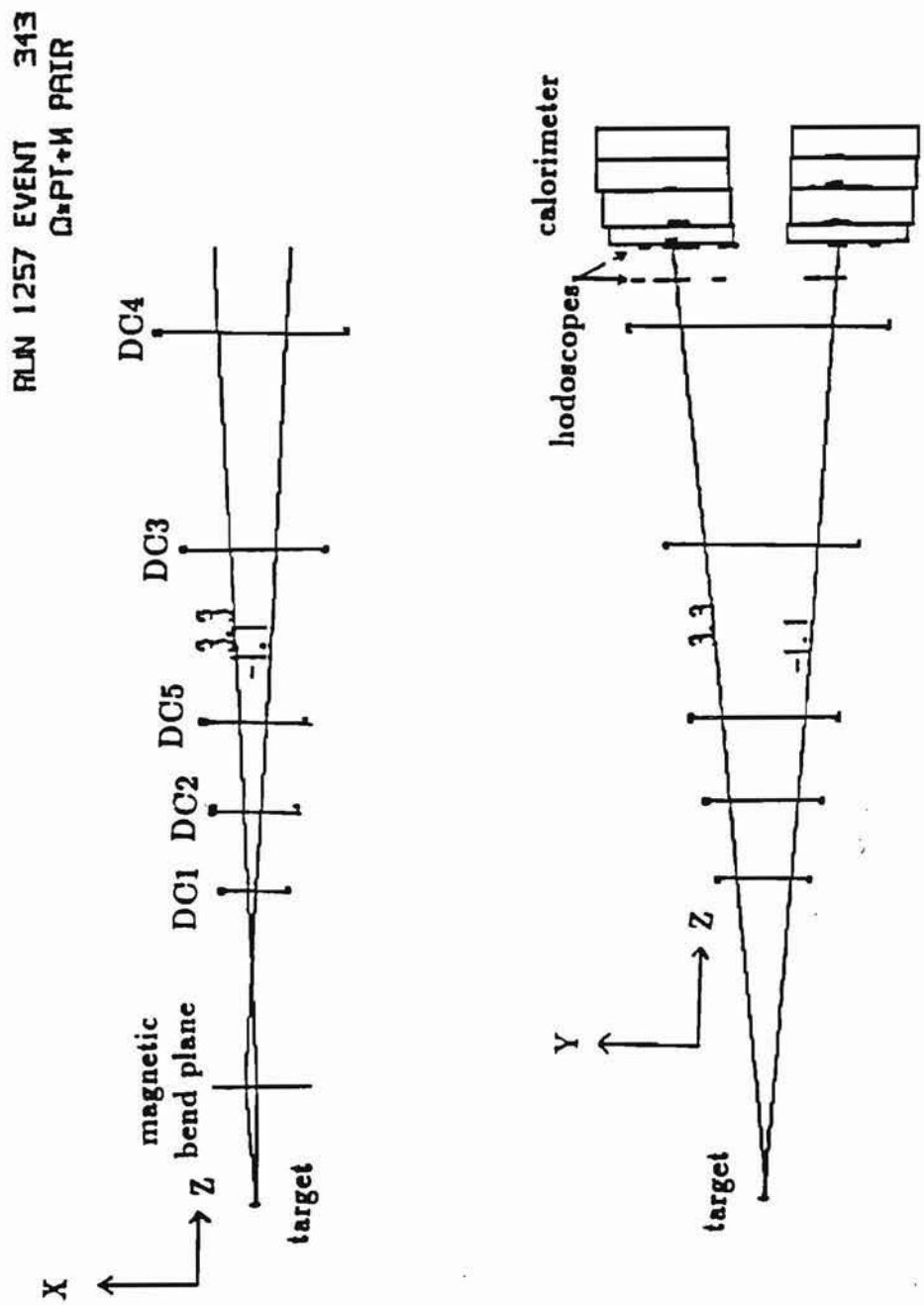

Typical event display showing the detector, the triggering tracks and the energy deposition in the calorimeters

Figure 3.3

3.4 The data taking runs

The data taking period extended from November 1987 until February 1988. On average, about 40,000 events could be written onto a 6250 BPI magnetic tape. 455 tapes were written in total. Some study and dedicated calibration runs were also taken :

1) the target scan and target out runs enabling the study and calibration of the 90° luminosity monitors

2) data taking runs in which the analyzing magnets were turned off in order to determine the target position in the MWPC coordinate system in the magnet bend view (X). The y, z position of the target could be determined by vertex reconstruction in the non bend Y view;

3) low intensity beam runs, necessary to calibrate the ion chambers

4) runs in which a dedicated muon trigger was used to calibrate the hodoscopes and calorimeters and also to locate the hodoscopes and calorimeter modules in the MWPC coordinate system.

CHAPTER 4

THE DATA PROCESSING

The event information written to magnetic tape by the dedicated PDP-11 is called the 'raw data'. It is not practical to perform a physics analysis using the raw data tapes as the pattern recognition code requires a huge amount of computer time. Therefore in virtually all high energy experiments data summary tapes are written containing the results of the pattern recognition and other essential data. In E711 such data processing was done in several steps :

1) the MWPC pattern recognition code was run and the subsequent output tapes, called DSTs, while having the track parameter output had the MWPC raw data (TDC data) suppressed.

2) On VAX calorimeter, analysis consisting of pedestal subtraction and energy cluster finding, was done, and uncorrected ADC data were suppressed (production of the DSF tapes).

3) Most relevant physics quantities for each event were calculated and selection performed. The skimmed events were written onto Mini Data summary Files (MDF) with limited information. The data/event was reduced from 4.5 Kbytes/event to $\simeq$ 200 bytes for the selected events.

4.1 DST production

The DST's were produced at Florida State University, on a CDC Cyber 205 and ETA 10, with a vectorized pattern recognition and fitting algorithm[21] ('trackfinder' and 'trackfitter'). The trackfinder found MPWC wire hits associated with a straight track downstream of the magnet. The track parameters (slopes and intercepts) were calculated by means of the trackfitting algorithm which used the TDC information of the hit wires and measured time-to-distance relations to determine the distance from the wire at which the particle passed. The whole reconstruction algorithm had an average processing time of about 22 msec/event on the ETA 10, compared to about 5 sec/event for a similar code on a scaler VAX-780. Several criteria had to be satisfied in order to accept a track as reconstructed. The number of hits had to be at least 15 (out of the 20 possible) with at least 3 hits per view (X, Y, U, V) out of the possible 5. The χ^2 of the fitted track had to be less than 15 and its momentum had to be ≥ 1.0 GeV/c . The reconstruction efficiency of the program was found to be 0.904 ± 0.005 (the error is statistical).

The DST tapes had the trackfitter and trackfinder results added. For each raw input magnetic tape an output magnetic tape was produced. Events were

eliminated if no tracks were found. The percentage of the surviving events is listed in TABLE 4.1

TABLE 4.1

DST production percentages

Target	percentage : $\frac{\text{DST events}}{\text{Raw tape events}}$
Be	0.52
Al	0.61
Fe	0.60
W	0.41

4.1.1 The trackfinder

The information from the chamber planes (namely the hit positions of the 20 sense wire planes) was used to find candidate straight line trajectories in two iterations. First the projected straight trajectory candidates were found in each of the 4 views (X, Y, U, V). The 2-dimensional straight lines were found comparing the hit patterns to precomputed tables of all possible patterns. The second step

was the 3-dimensional matching of the projected 2-dimensional tracks. This was done by looking at all combinations in a vectorized mode.

4.1.2 The trackfitter

The track fitting was accomplished using the TDC information of the hit wires. The drift time-distance relations were used to estimate how far the ionizing particle passed from the hit wire. The ambiguity on which side of the hit wire the track passed was solved with an algorithm first for the hits with larger drift time and then for the remaining ones. Finally a χ^2 minimization fit of the track parameters gave slopes and intercepts of the straight trajectory. Tracks with too bad χ^2 tracks were discarded. The output of the track fitting program was the X-Z and Y-Z projected slopes and intercepts of each track found.

4.1.3 Momentum calculation

The track momentum was calculated using slopes and intercepts of the track trajectories found with the trackfitter, the magnetic $P_\perp$ kick and the target position in the MWPC coordinate system. The y-component of the momenta were unaffected by the vertical magnetic field. The bending of the trajectories in the X-Z plane was approximated by the impulse approximation applied at an imaginary 'bending plane', perpendicular to the beam line, placed at

$$z_{bend} = L_1 + L_2 + \delta - (L_2 + \delta)\frac{\int_1 B_1 dl_1}{\int_1 B_1 dl_1 + \int_2 B_2 dl_2}$$

where z_{bend} is the distance of the target from the bending plane, L_1, L_2 are the length in the z direction of the first and second analyzing magnet, δ is the

distance between the downstream face of the first magnet and the upstream face of the second one (see figure 4.1). Also the interaction was assumed to occur at the target center. Upon those assumptions the following independent equations must all be valid :

$$\begin{cases} \mathrm{P}_x^d = \mathrm{P}_x^u + \mathrm{P}_{\perp kick} \\ (\mathrm{P}_x^u)^2 + (\mathrm{P}_z^u)^2 = (\mathrm{P}_x^d)^2 + (\mathrm{P}_z^d)^2 \\ \mathrm{P}_x^d = \mathrm{P}_z^d k_x^d \\ \mathrm{P}_y = \mathrm{P}_z^d k_y^d \\ \mathrm{P}_x^u = \mathrm{P}_z^u k_x^u \\ \mathrm{P}_y = \mathrm{P}_z^u k_y^u \\ k_x^u z_{bend} = k_x^d z_{bend} + x_{intercept} \quad \text{(see figure 4.1)} \end{cases}$$

where the superscripts 'u' and 'd' mean 'upstream the two magnet system' and 'downstream the two magnet system'. $\mathrm{P}_{\perp kick} = 1.16$ GeV/c and k_x^u, k_x^d,k_y^u,k_y^d are the X-Z and Y-Z slopes of the trajectory before and after the bending plane respectively. The system has 7 equations in 7 unknown variables : k_x^u, k_y^u, P_x^u, P_x^d, P_y, P_z^u, P_z^d. The solution for the momentum of a track before being bent is :

$$\begin{cases} \mathrm{P}_z^u = \frac{\mathrm{P}_{\perp kick}[k_x^u(1+(k_x^d)^2)+k_x^d\sqrt{(k_x^d)^2(k_x^u)^2+(k_x^u)^2+(k_x^d)^2+1}]}{(k_x^d)^2+(k_x^u)^2} \\ \mathrm{P}_x^u = \mathrm{P}_z^u k_x^u \\ \mathrm{P}_y^u = \mathrm{P}_z^u k_y^u \end{cases}$$

The errors on the momenta, listed in TABLE 4.2, are mainly due to width and length of the target (and consequent imprecision in the determination of the interaction vertex) and to the chamber resolution of slopes and intercepts. Other

types of errors were found to be negligible. The constant term comes from the target length while the term $\propto$ P is due to chamber resolution and target width.

TABLE 4.2

Momentum resolution

Target	$\frac{\Delta P}{P}$ P measured in GeV/c
Be	$2.80 \times 10^{-4}P + 5.26 \times 10^{-3}$
Al	$2.70 \times 10^{-4}P + 5.12 \times 10^{-3}$
Fe	$2.54 \times 10^{-4}P + 2.16 \times 10^{-3}$
W	$2.79 \times 10^{-4}P + 1.23 \times 10^{-3}$

4.1.4 Cross checks on the reconstruction programs

The track reconstruction and momentum calculation programs were checked with a scaler pattern recognition code run on a VAX 11-780. The results were found to be consistent within the resolutions listed above. Another check was made adding two montecarlo generated tracks to the data and computing the differences between the reconstructed momenta and the montecarlo generated

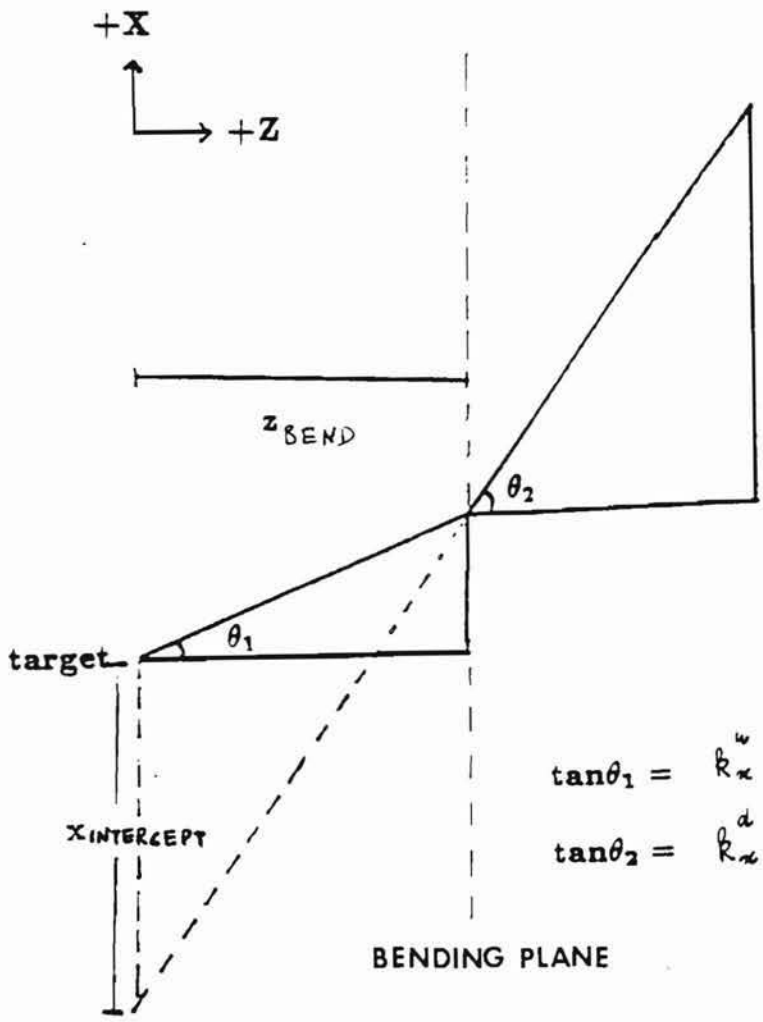

Illustration of the bending plane and track momentum calculation

Figure 4.1

momenta. Again consistency was found within the errors and the reconstruction efficiency was calculated to be 0.904 ± 0.005 .

4.2 DSF production

The next step of the data compaction was the production of the Data Summary Files from the DSTs. It was done on a VAX cluster at Florida State University. Most of the electronic information was eliminated so that the size of the events was considerably reduced. For each event the pedestals were subtracted from the ADC values. The energy deposited (according to the hadron calibration discussed in Appendix A) was calculated for each module and section of the calorimeter and written onto the output magnetic tape. The fitted track momenta and the latch information were written in a compact form. It was chosen to make an output magnetic tape for each DST input magnetic tape (338 DST's analyzed).

4.3 MDF production

The last stage of compaction was stripping the events from the DSFs, which triggered the $Q \cdot P_{\perp} \cdot \bar{m}$ or $Q \cdot P_{\perp} \cdot HM$ triggers, with additional selections ensuring that the event had at least two reconstructed opposite high $P_{\perp}$ hadrons belonging to a phase space region in which the triggers were efficient. After the selections the events were written onto Mini Data summary Files (MDF). Each record contained the essential information about track momenta and parameters, the calorimeter modules and segment energies, and the latch informations. In

TABLE 4.3 the number of events on DSFs and MDFs are listed for each of the targets.

TABLE 4.3

Event summary

Target	# DSF tapes	# DSF events	# DSF events $Q \cdot P_\perp \cdot \bar{m}$ or $Q \cdot P_\perp \cdot HM$ triggers	# events written onto MDF
Be	67	1.58×10^6	1.45×10^6	59137
Al	29	0.941×10^6	0.762×10^6	40106
Fe	66	1.80×10^6	1.68×10^6	85102
W	71	1.09×10^6	0.861×10^6	60202
Total	233	5.11×10^6	4.753×10^6	244547

CHAPTER 5

DATA ANALYSIS

5.1 Introduction

The objective of this analysis is the study of the quantity $< \mathcal{Z} >$:

$$< \mathcal{Z} > \equiv \left\langle \frac{E_{leading}}{E_{jet}} \right\rangle \simeq \left\langle \frac{\mathrm{P}_{leading}}{\mathrm{P}_{leading} + f E_{non\ leading\ neutral}} \right\rangle \tag{5.1}$$

where $\mathrm{P}_{leading}$ is the momentum of the leading hadron and $E_{non\ leading\ neutral}$ is the energy of the neutral particles of the jet associated to the leading hadron. $< \mathcal{Z} >$ is calculated for events with two high and opposite $\mathrm{P}_{\perp}$ charged hadrons which carried the highest momentum ('leading particles') of the charged jet particles. Such events were selected in hardware by the trigger. During the data acquisition $\simeq$ 20 million triggers were collected. After the data were processed

244547 events were selected, written onto the MDFs and subsequently used in this analysis.

The logic followed in the data analysis can be summarized as follows :

1) identification of the high $P_\perp$ hadrons which triggered the detector ('trigger tracks'), and selection of the events having at least one trigger track hitting the top, one the bottom calorimeter;

2) choice of the leading hadron on the top side and the leading hadron on the bottom side of the detector;

3) selection of the events where the two leading hadrons alone would efficiently satisfy the trigger requirements $M_{di-hadron} > 7$ GeV/c^2 and $P_{\perp di-hadron} < 2$ GeV/c ;

4) definition of the cone in which the jet particles were contained and selection of the leading particles for which the neutral jet particle energy cone was fully contained in the calorimeter active area;

5) calculation of $E_{non\ leading\ neutral}$ and corrections to it;

6) calculation of $< \mathcal{Z} >$ and its systematic errors.

To be more specific, the logic was implemented as follows. For each event, ghost tracks found by the trackfinder and trackfitter algorithms were removed, first the tracks which did not come from the target, then the 'duplicate tracks', namely fake tracks that were creation of the reconstruction algorithms differing by a small amount of MWPC hits. Then the events were required to have at least a pair among the selected tracks with one hitting the upper and one the lower calorimeter. The one up and one down tracks had to be capable of satisfying

the trigger thresholds by themselves to have an unbiased measurement and the momenta of each track had to be consistent with the calorimeter energy. This last requirement eliminated the very high momentum tail created by the pattern recognition program (selection of the 'trigger tracks'). After this the two opposite $P_\perp$ leading hadrons were selected by simply choosing the largest momentum tracks in the top and bottom spectrometer arms. Events with too large a $P_\perp$ imbalance of the two leading hadrons, and with $M_{di-hadron} < 7$ GeV/c^2 were discarded. The events selected by these criteria are called 'good events'.

For each leading hadron, the cone in which the neutral particles of the associated jet were contained was calculated. If the cone intersection with the calorimeter surface was not contained in the calorimeter sensitive region, the neutral jet particle energy could not be measured completely and the leading hadron was excluded from the calculation of $\mathcal{Z}$. After the jet cone was defined, the energy deposited in the EM calorimeter modules hit by the neutral jet particles was calculated. Only the EM section was used since the neutral energy of the jet was formed essentially by π°s which decay into $\gamma\gamma$. The leading hadrons were required to have deposited most of their energy in the hadronic section of the calorimeter. This cut eliminated the events where early shower development by the leading hadrons left energy in the EM section which would otherwise have been mistakenly identified with the neutral jet. After this $< \mathcal{Z} >$ was figured using (5.1) correcting $E_{non\ leading\ neutral}$ for the small release of energy of the leading hadron in the EM calorimeter section and for the absorption of photons coming from the π° decay in the target. $P_{leading}$, the other quantity entering in formula (5.1), was calculated with the chamber information. Finally

the systematic errors on $< \mathcal{Z} >$ were estimated.

The calculation of the energy released by electromagnetic and hadronic showers in the calorimeters plays an essential role in the analysis outlined above. As mentioned in chapter 2, the response of the calorimeter in the two cases is quite different, the energy release in the scintillator layers being totally diverse. The calibrations of the calorimeters for hadron and electromagnetic showers are extensively described in appendix A.

5.2 Selection of the trigger tracks

The set of cuts described in this section were aimed at identifying the tracks coming from the target that were not duplicate tracks, were in a phase space region for which the detector acceptance and trigger efficiency were good. The track momentum measured with the chambers was required to be consistent with the calorimeter measurement and the tracks were required to be associated with the recorded trigger logic signals.

5.2.1 Vertex cut

The y coordinate of each track extrapolated to the z position of the center of target had to be in the fiducial volume occupied by the target. During the run the four different targets (Be, Al, Fe, W) were switched 7 times. The z position of their center was maintained by construction of the target stand. It was 0.25

cm for all the targets. The x position extension of the targets were calculated in software using events taken when the analyzing magnets were off. The y position could be found by reconstructing multi particle vertices in the non bend view, even when the magnet was on. Figure 5.1 and 5.2 show y of the track at the vertex for the seven different times the target was changed or moved. It is clear from these figures that in all cases a reasonable cut was

$$-2.\ \text{cm} < y_{vertex} < 1.6\ \text{cm}$$

5.2.2 Duplicate track elimination

The duplicate tracks were 'invented' by the track finder program during the geometrical reconstruction of the event. Most of the times a duplicate track differed from another track by just for one hit in the chamber planes. In that case the geometry reconstruction program found two different tracks with essentially the same trajectory parameters and momenta. To recognize and eliminate these types of tracks the quantity :

$$\mathrm{D} \equiv \sqrt{\sum_{i=1}^{5}\Big((x_{i1} - x_{i2})^2 + (y_{i1} - y_{i2})^2\Big)}$$

was calculated for all the possible pairs of tracks in each event. x_{i1} and y_{i2} were the coordinates of the position of the first track of the pair at the ith drift chamber position. Figure 5.3a and 5.3b show the distributions of D in two different scales. One can notice the large peak at zero due to duplicate tracks, and the much broader one peaked around 220 cm corresponding to the random combination of two physically distinct tracks. If D $\geq$ 1. cm the two tracks were defined as

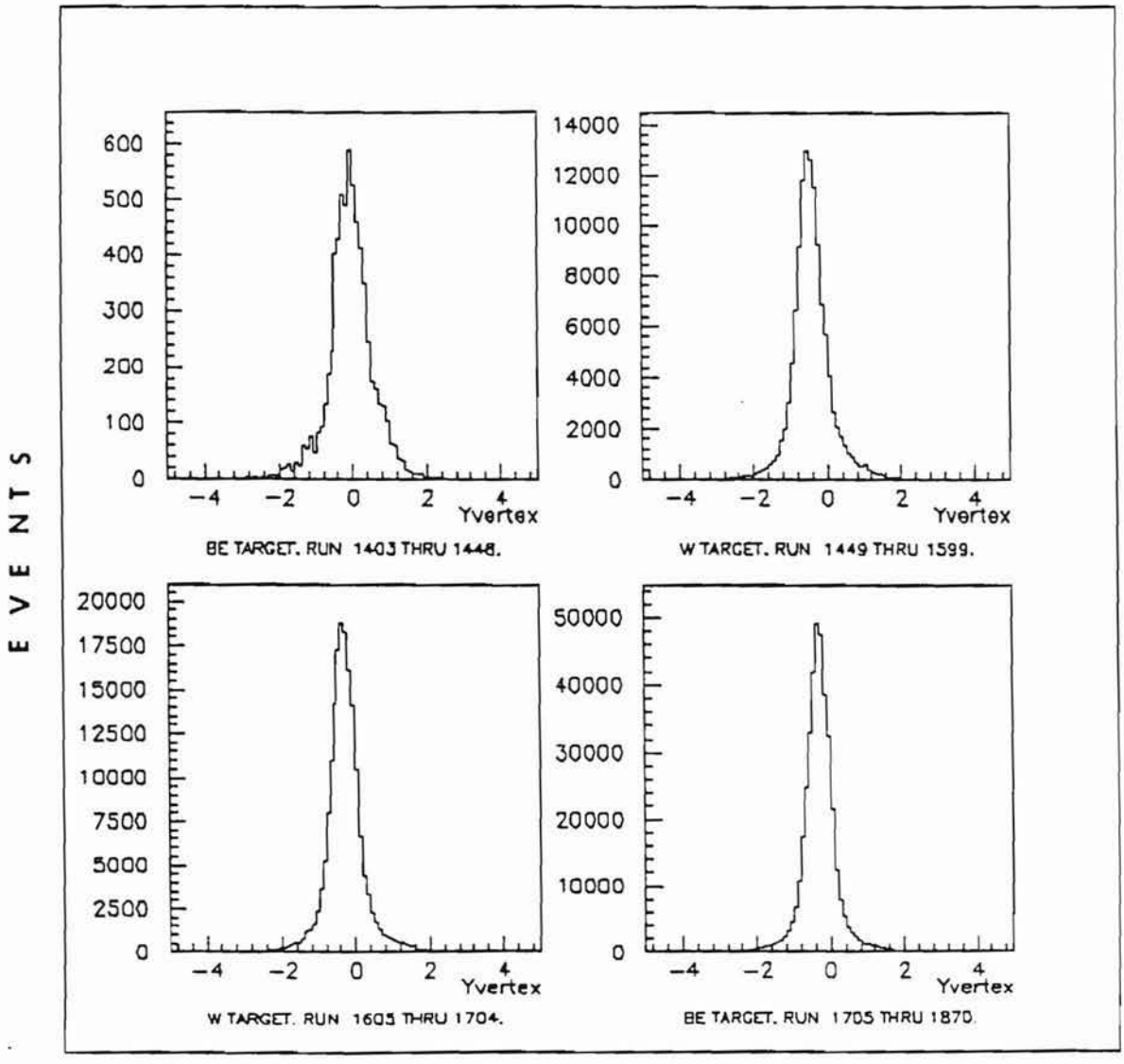

Distributions of the y coordinate of the tracks at vertex

Figure 5.1

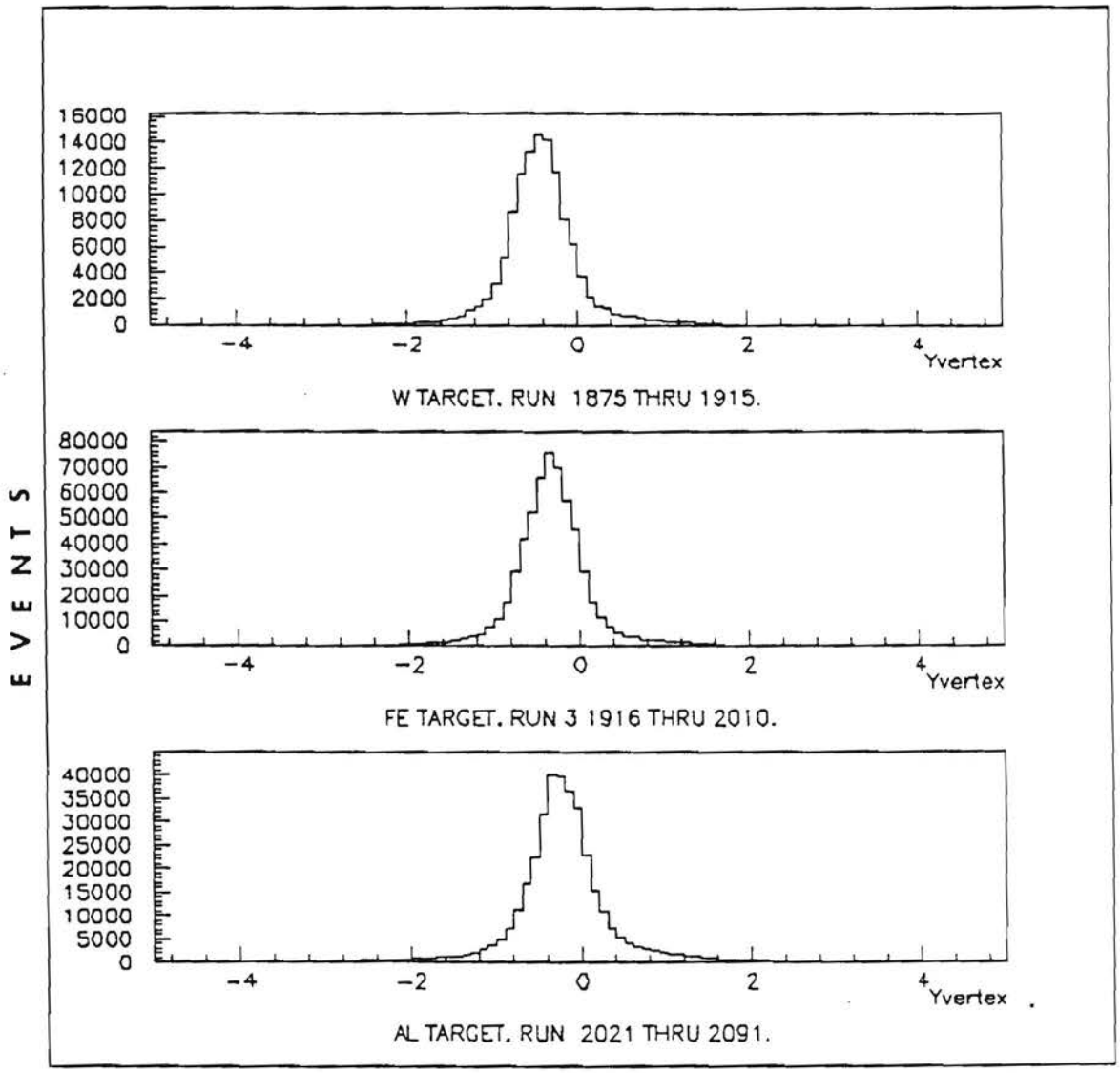

Distributions of the y coordinate of the tracks at vertex

Figure 5.2

different. If D < 1. cm one of the tracks was discarded according to the following criteria :

1) if both tracks hit the calorimeter fiducial volume the track with the best agreement between momentum measured by the chambers and energy measured by the calorimeter was selected;

2) otherwise the track with the best χ^2 from the momentum fit was chosen.

5.2.3 Calorimeter fiducial volume cut

The tracks were required to hit the calorimeters in the fiducial volume to ensure complete transverse containment of the hadronic shower of the trigger particles. The conservative cut

$$42.\ \text{cm} \leq |Y_{calo}| \leq 145.\ \text{cm}$$

and

$$|\Phi_{calo}| \leq 22°30'$$

was imposed. The actual physical size of the calorimeter scintillator was from 32.6 to 177.3 cm in $|Y_{calo}|$ and $24°30'$ in $|\Phi_{calo}|$. Y_{calo} was the vertical position of the track at the calorimeter surface and Φ_{calo} the azimuthal angle measured from the Y axis of the track at this surface. Figure 5.4 shows the plot of Y_{calo} versus X_{calo} of the tracks when the calorimeter fiducial volume cut has been applied.

5.2.4 $Q \cdot P$ *latch cut and* $\tilde{m}$ *latch cuts*

These selections were aimed at finding the particles that triggered the detector. Since the trigger particles were charged high $P_\perp$ hadrons, they had to

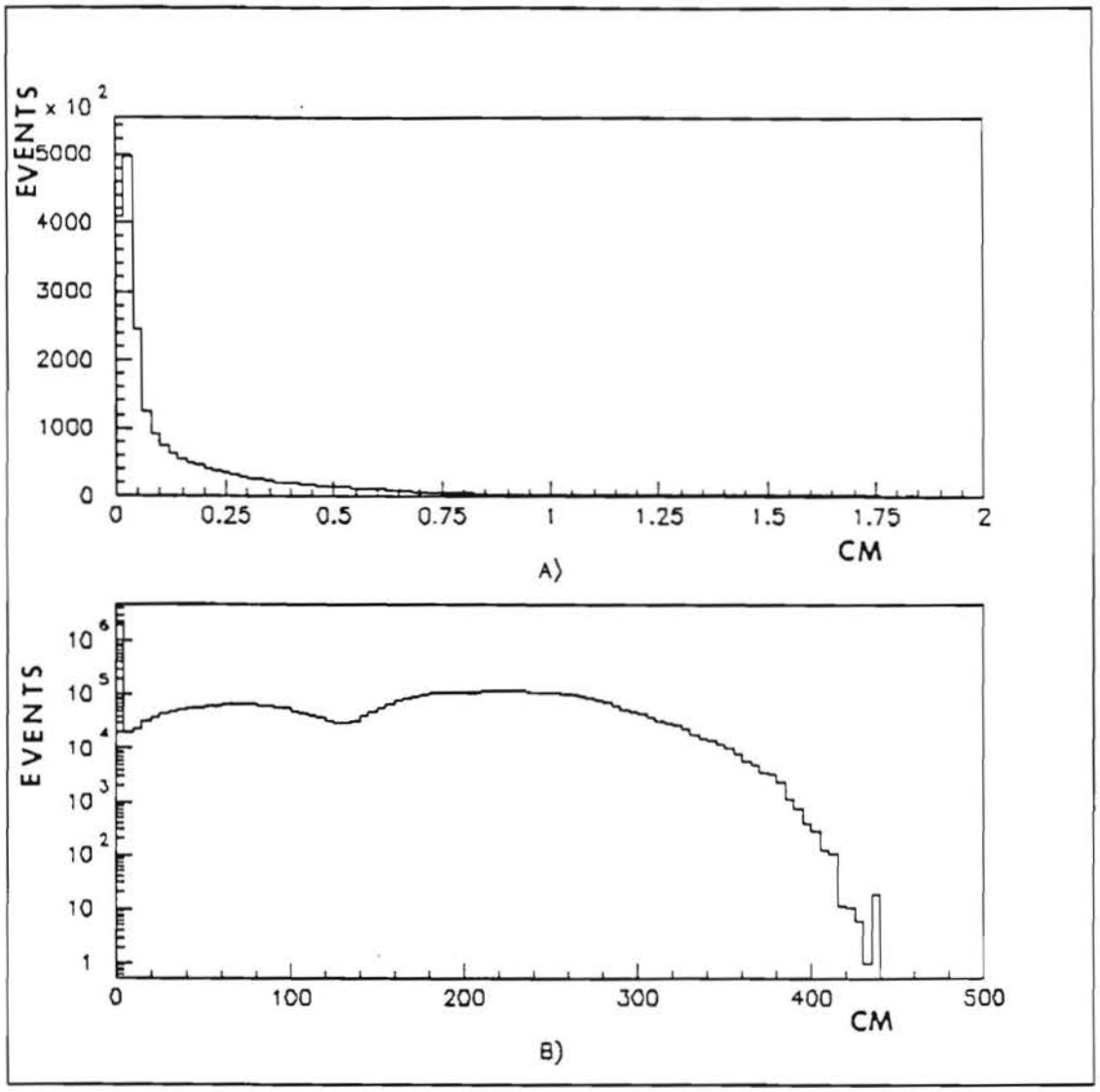

Distribution of D in two different scales

Figures 5.3a and 5.3b

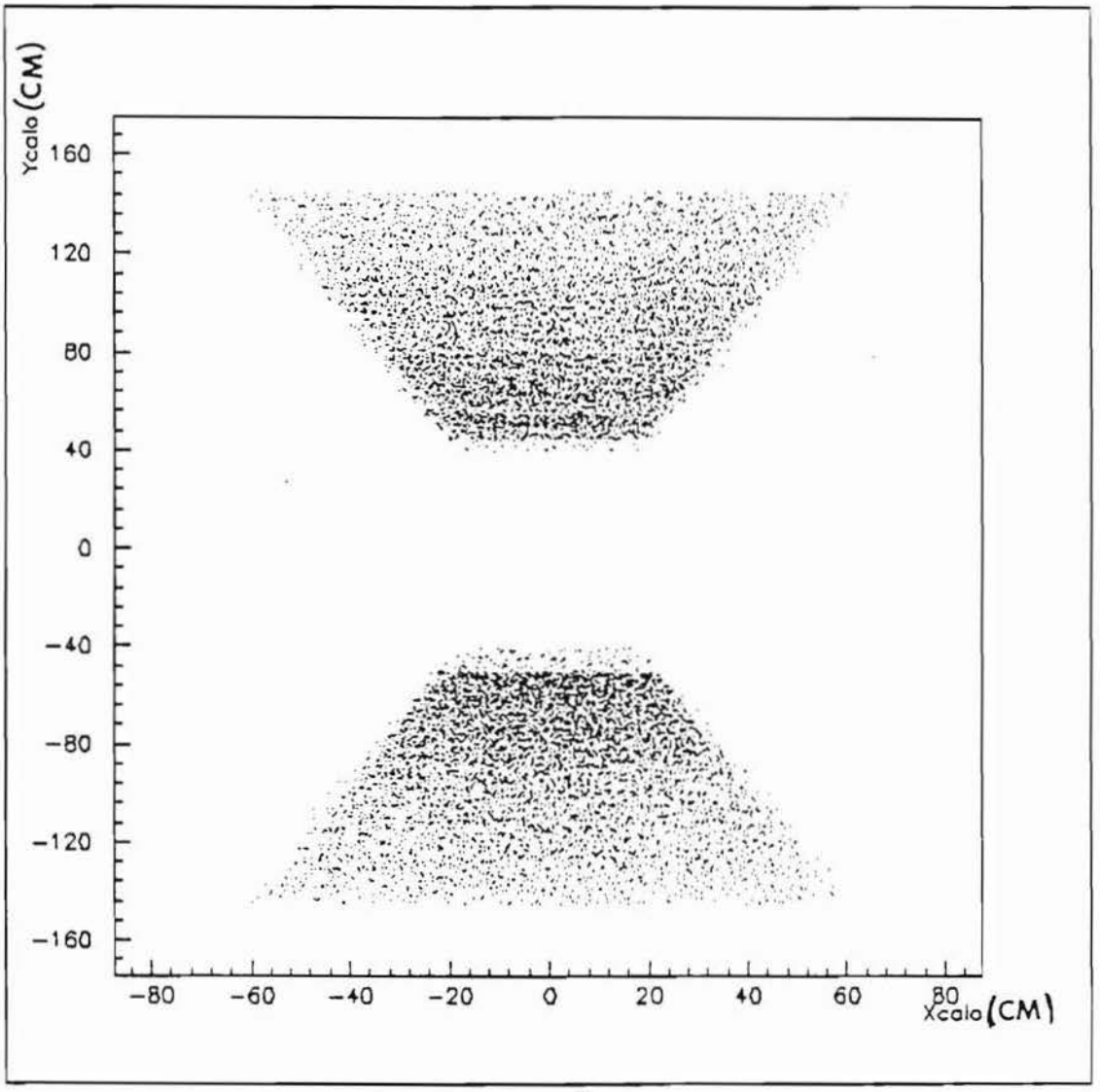

Distribution of track position on face of calorimeters after the fiducial volume cut

Figure 5.4

produce a signal in a hodoscope module and, in coincidence, deposit enough transverse energy in the corresponding calorimeter segment to fire the segment discriminators. Consequently, the $Q \cdot P$ logic signal was expected from the hodoscope module and calorimeter segment hit by the particle, otherwise the particle was discarded. Since the particles that triggered the detector satisfied the $Q \cdot P \cdot HM$ and/or the $Q \cdot P \cdot \bar{m}$ triggers, a $\bar{m}$ logic signal should also have been set by the segment hit by them.The presence of $Q \cdot P$ and $\bar{m}$ logic signals was indicated by a set of latches read out for each event. Only the particles which had the proper $Q \cdot P$ and $\bar{m}$ latches set on were selected as candidate trigger particles.

5.2.5 P_y distribution and cut

The cut

$$|P_y| \geq 1. \text{ GeV/c}$$

was imposed on the tracks. P_y was the y component of the momentum of the track, measured by the chambers. This was essentially a cut on the transverse momentum of the particle due to the fact that $P_\perp \simeq P_y$ because of the particular geometry of the calorimeters. The cut corresponds to the hardware trigger selection performed by the P discriminator used in the $Q \cdot P \cdot \bar{m}$ and $Q \cdot P \cdot HM$ triggers.

5.2.6 Electron rejection

The possibility that an electron simulated a high $P_\perp$ hadron in the calorime-

ters was checked by plotting the quantity E_{em}/E_{calo} shown in figure 5.5 E_{em} and E_{calo} were the energy deposited by the particle in the electromagnetic segment hit by the track and in all of the calorimeter segments hit by the track, respectively. Electrons would produce a peak around $E_{em}/E_{calo} = 1.$, since their shower would be completely absorbed in the first section of the calorimeter. No such enhancement is observed in figure 5.5. On the contrary, a strong peak at 0 indicates that the trigger particles were mostly hadrons showering in the hadronic sections of the calorimeters. Even though no electron peak was present, a conservative cut

$$E_{em}/E_{calo} < .98$$

was imposed on the tracks.

5.2.7 *Consistency between chamber and calorimeter measurements*

A loose matching of the particle momentum measured by the drift chambers and the energy measured by the calorimeters provided a selection to reject grossly misfit tracks by the chambers. For each particle, the quantity

$$\mathcal{D} = \frac{E_{calo} - P_{tot}}{\sqrt{\sigma^2_{E_{calo}} + \sigma^2_{P_{tot}}}}$$

was calculated. E_{calo} was the energy of the segment containing the particle shower measured by the calorimeter, P_{tot} the track momentum measured by the chambers. $\sigma_{E_{calo}}$ was the error on the measure of the calorimeter energy, $\sigma_{P_{tot}}$ the error on the momentum measured by the chambers. The calorimeter energy resolution for hadrons turned out to be

$$\sigma_{E_{calo}} = 0.7\sqrt{E}$$

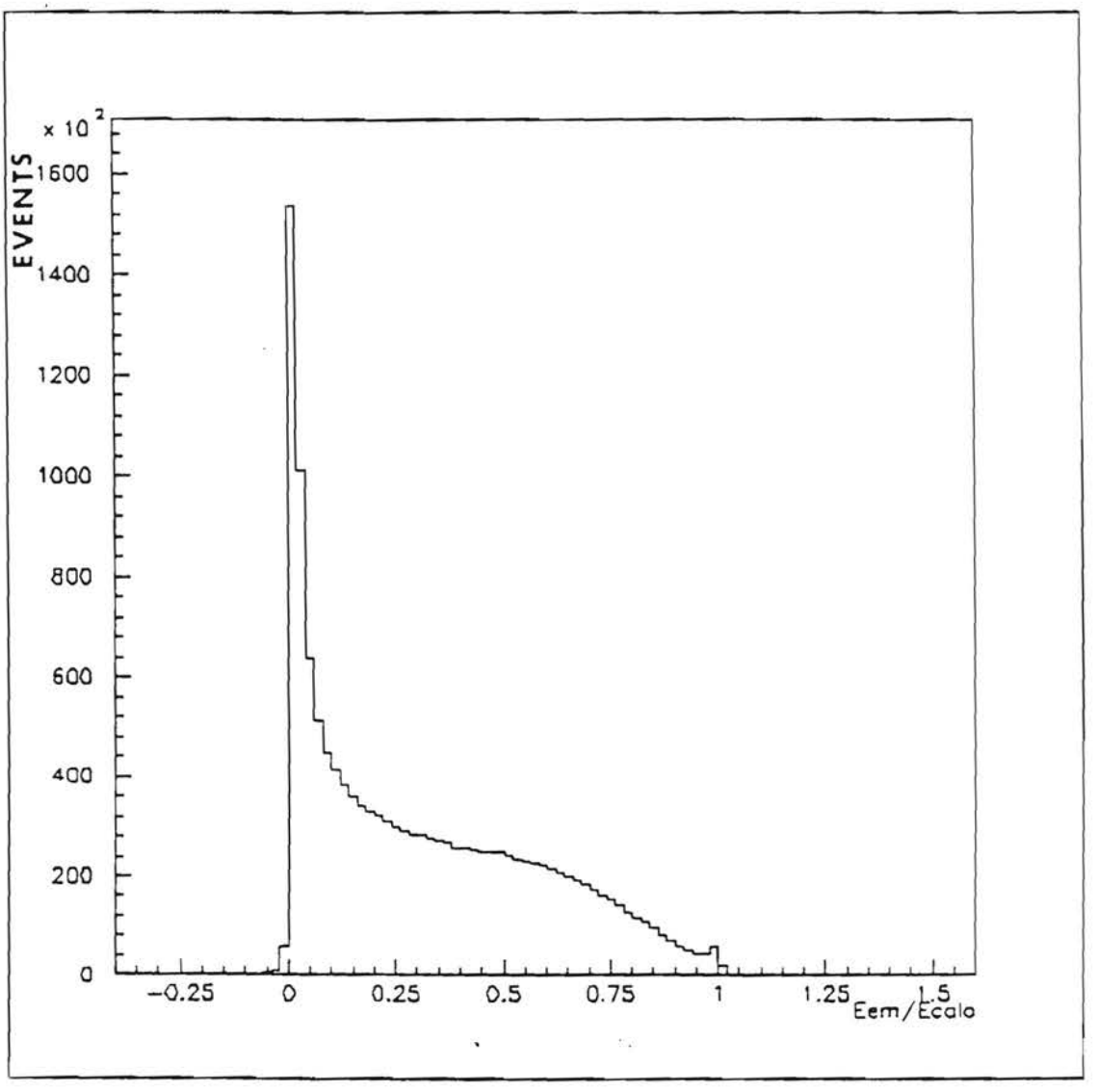

Distribution of $\frac{E_{em}}{E_{calo}}$ before the electron rejection cut

Figure 5.5

(see appendix A), where E is the energy of the incident particle. This is a behaviour typical of lead-scintillator-iron-scintillator sampling calorimeters. Hence,

$$\sigma_{E_{calo}} \simeq 0.7\sqrt{\mathrm{E}_{calo}}$$

where the approximation $\sqrt{\mathrm{E}} \simeq \sqrt{\mathrm{E}_{calo}}$ has been used. $\sigma_{P_{tot}}/\mathrm{P}^2_{tot}$ ranged from 2.5×10^{-4} to 2.8×10^{-4} $(\mathrm{GeV/c})^{-1}$ for the four targets. The value 2.5×10^{-4} was assumed throughout this analysis. However a problem arose with some tracks which had anomalously large values of P_{tot}, due to the failure in the pattern recognition. Consequently for these tracks $\mathcal{D}$ assumed values close to zero because $\sigma_{P_{tot}}$ was enormous and the tracks were accepted even though the track should clearly have been rejected. A way to cure this problem was to replace P_{tot} with E_{calo} in the expression of $\sigma_{P_{tot}}$ as the calorimeter was free of this pattern recognition difficulty. Hence,

$$\mathcal{D} = \frac{\mathrm{E}_{calo} - \mathrm{P}_{tot}}{\sqrt{.49 \times \mathrm{E}_{calo} + (2.5 \times 10^{-4})^2 \times \mathrm{E}^4_{calo}}}$$

The distribution of $\mathcal{D}$ is plotted in figure 5.6 It peaks at zero, the long tail of large positive values is due to events in which more than one particle hit the same segment and does not indicate a disagreement between chamber and calorimeter measurement. The elimination of grossly misfit tracks was achieved cutting only on the large negative values of $\mathcal{D}$. Figure 5.7 shows the lego plot of $\mathcal{D}$ versus P_{tot} of the track. The shape of the distribution of $\mathcal{D}$ for different slices of P_{tot} is essentially the same, as expected from the independence of the chamber and calorimeter measurements. By these arguments the selection :

$$\mathcal{D} > -10.$$

was imposed on the particle tracks. Those particles which passed all the cuts described so far were the 'trigger tracks'. They formed the set of tracks from which the two leading hadrons were chosen.

5.3 Selection of the 'good events'

The cuts described in this section selected the type of events (called from now on 'good events') relevant to this analysis, namely two high and opposite $P_\perp$ leading particle events, with $M_{di-hadron} > 7$ GeV/c^2 and small $P_{\perp total}$ imbalance.

5.3.1 Presence of a top and a bottom trigger particle and definition of leading particle

Among all the selected trigger particles at least one had to hit the upper and at least one the lower calorimeter. This cut down the statistics to 214370 events for all the targets. The selection of the leading hadrons was done choosing from the set of remaining trigger tracks after all the previously described selections. From the physical point of view, the leading particle is the one which took the largest fraction of momentum of the jet produced by the fragmentation of a parton. If one trigger track in the bottom (top) side of the apparatus remained after the previous selections, it was automatically chosen as the leading particle of the bottom (top) side. Otherwise the bottom (top) leading particle was defined simply as the one having the largest momentum among all the bottom (top) trigger particles.

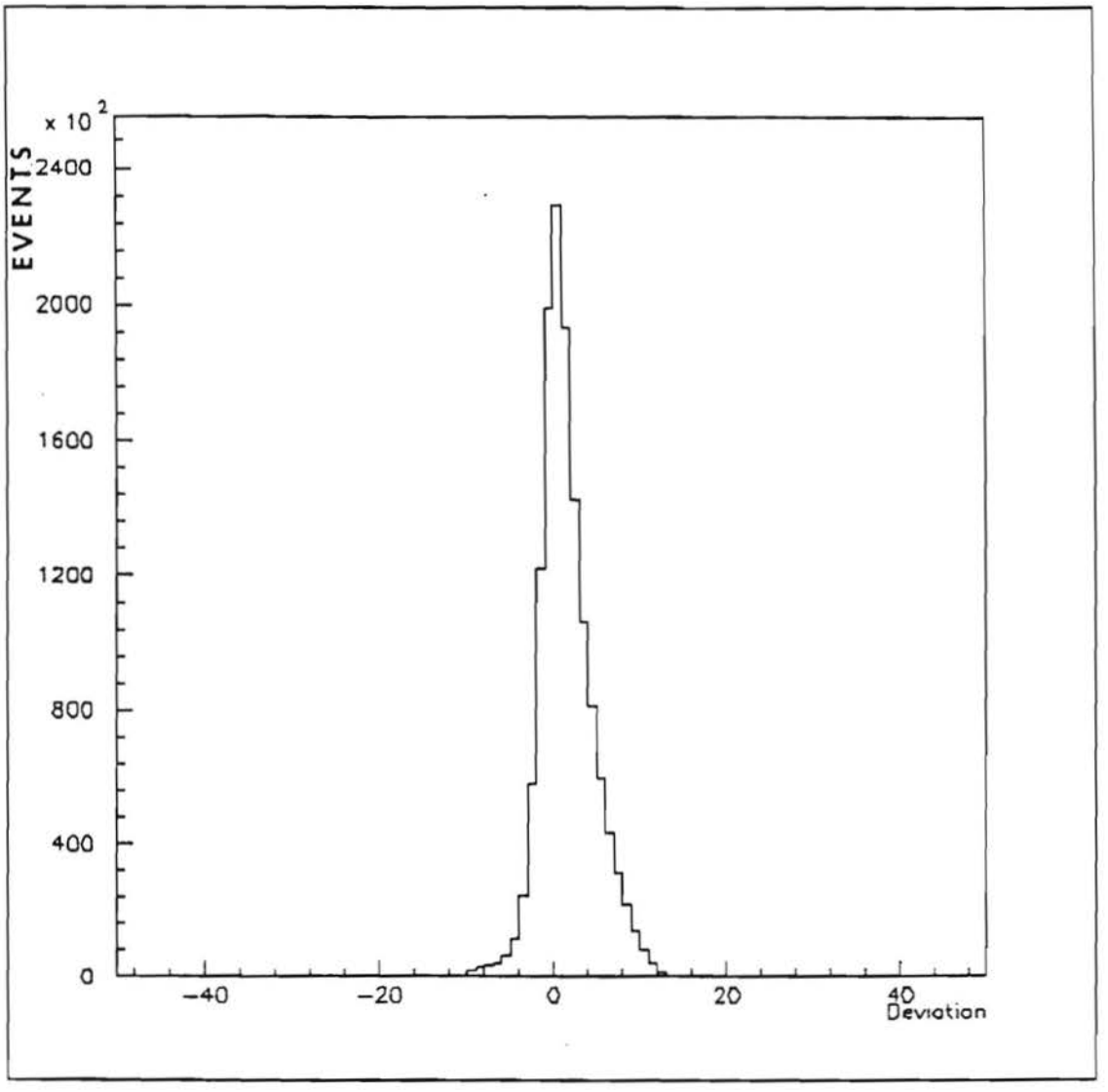

Plot of $\mathcal{D}$ before the cut

Figure 5.6

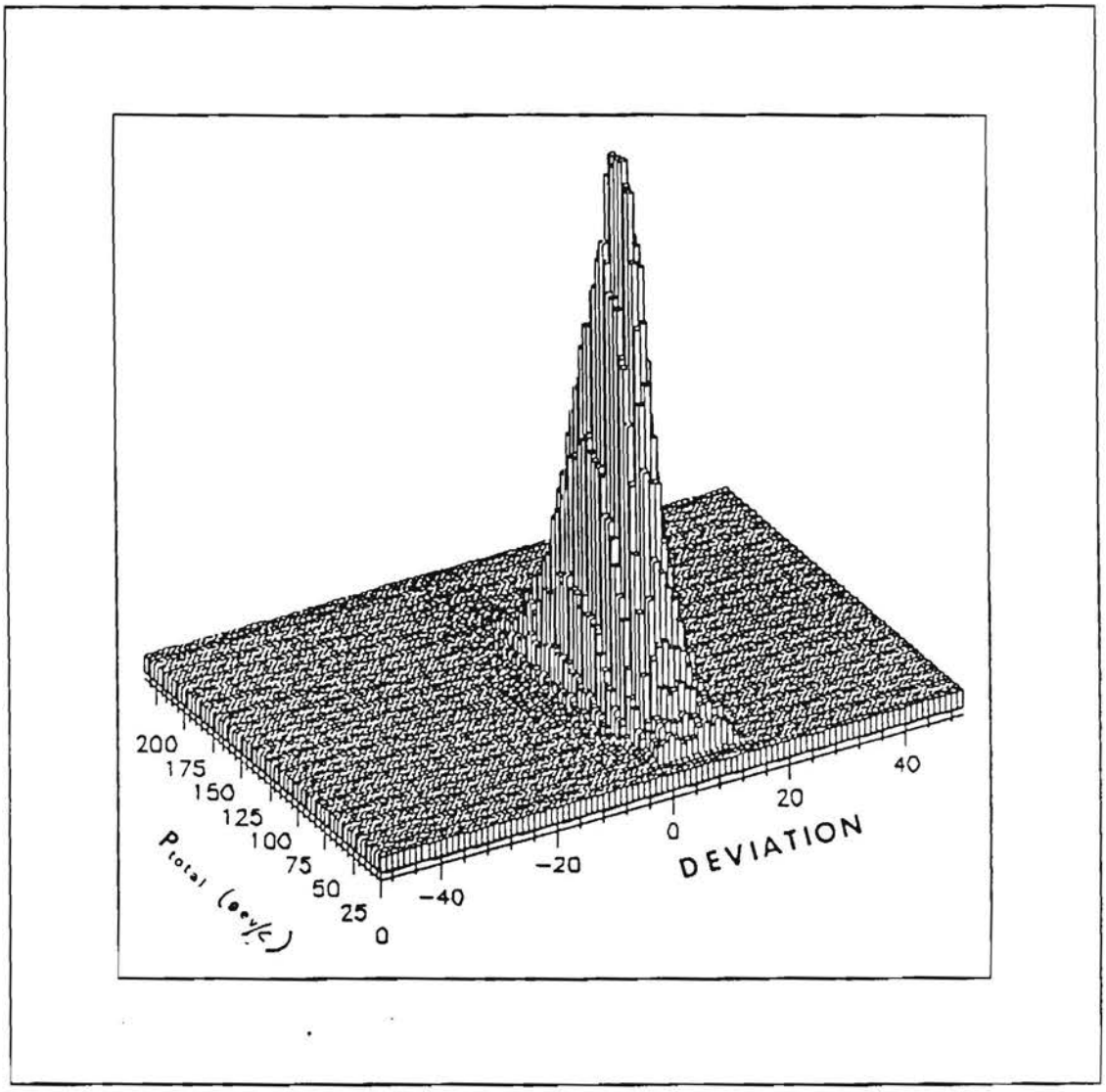

Lego plot of $\mathcal{D}$ before the cut

Figure 5.7

5.3.2 $P_{\perp total}$ cut

$P_{\perp total} \equiv \sqrt{(P_{xtop} + P_{xbottom})^2 + (P_{ytop} + P_{ybottom})^2}$, the total momentum imbalance of the high $P_\perp$ di-hadron system was expected to be small. In the collinear approximation

$$P_{\perp total} = P_\perp |z_1 - z_2| \quad .$$

where $P_\perp$ is the transverse momentum of each scattered parton and z_1, z_2 are the fraction of parton momentum taken by each leading hadron. Consequently

$$< P_{\perp total} > \simeq < P_\perp > < |z_1 - z_2| >$$

Due to the high $< z >$ of the leading hadrons ($\simeq 0.8$) $< |z_1 - z_2| >$ is small but still remains the major cause of the $P_\perp$ imbalance of the hadrons. The cut

$$P_{\perp total} < 2. \text{ GeV/c}$$

was imposed on the events to reduce the uncertainty in the determination of the scattering angle in the colliding parton C.o.M. system.
The selected events for all the targets were 141955 out of 214370.

5.3.3 *Di-hadron mass cut*

The di-hadron pairs were required to have a mass of 7 GeV/c^2 or greater which was the hardware trigger threshold obtained from the analysis of the turn-on curves of the P and $\bar{m}$ discriminators. Figure 5.8 shows the di-hadron effective mass after the selection. The number of events passing this cut were $\simeq$ 14% of

the 141955 events selected previously. The events passing all the cuts described above were 20487, $\simeq 10\%$ of the initial sample. They are called 'good events'.

5.4 Calculation of $E_{non\ leading\ neutral}$

The next steps of this analysis were finding evidence of jet structure, determining the cone in which the spray of jet particles associated to each leading hadron were contained and the calculation of $E_{non\ leading\ neutral}$, the energy of the neutral jet particles. Evidence of jets was searched for and found by looking at the distributions of $\eta_{leading} - \eta_{soft}$, and $\cos\Theta_{soft}$. $\eta_{leading}$ was the pseudorapidity ($\equiv -\ln\tan\frac{\theta}{2}$) of the leading particle in the reference frame, fixed with respect to the laboratory, in which the momentum of the di-hadron system was along the $\hat{\mathbf{z}}$ direction. η_{soft} was the pseudorapidity of any charged 'soft' particle detected by the chambers in the same reference frame. By 'soft' particle we mean any charged particle, different from the leading hadrons, which came from the target and was not a duplicate track. Θ_{soft} was the angle between leading hadron and soft track in the di-hadron C.o.M. system. The comparison with the $\eta_{leading} - \eta_{soft}$ and $\cos\Theta_{soft}$ plots of simulated events proved the presence of a cluster of soft particles around the direction of each leading hadron and justified the cut $\cos\Theta_{soft} \geq 0.93$, which defined the aperture of the cone around each leading hadron direction in which the jet particles were enclosed. Such a cone was initially defined in the di-hadron C.o.M. By the calculation explained in detail in appendix B, the intersection between the cone and the calorimeter surface was subsequently calculated in the laboratory frame. Almost all the neutral jet parti-

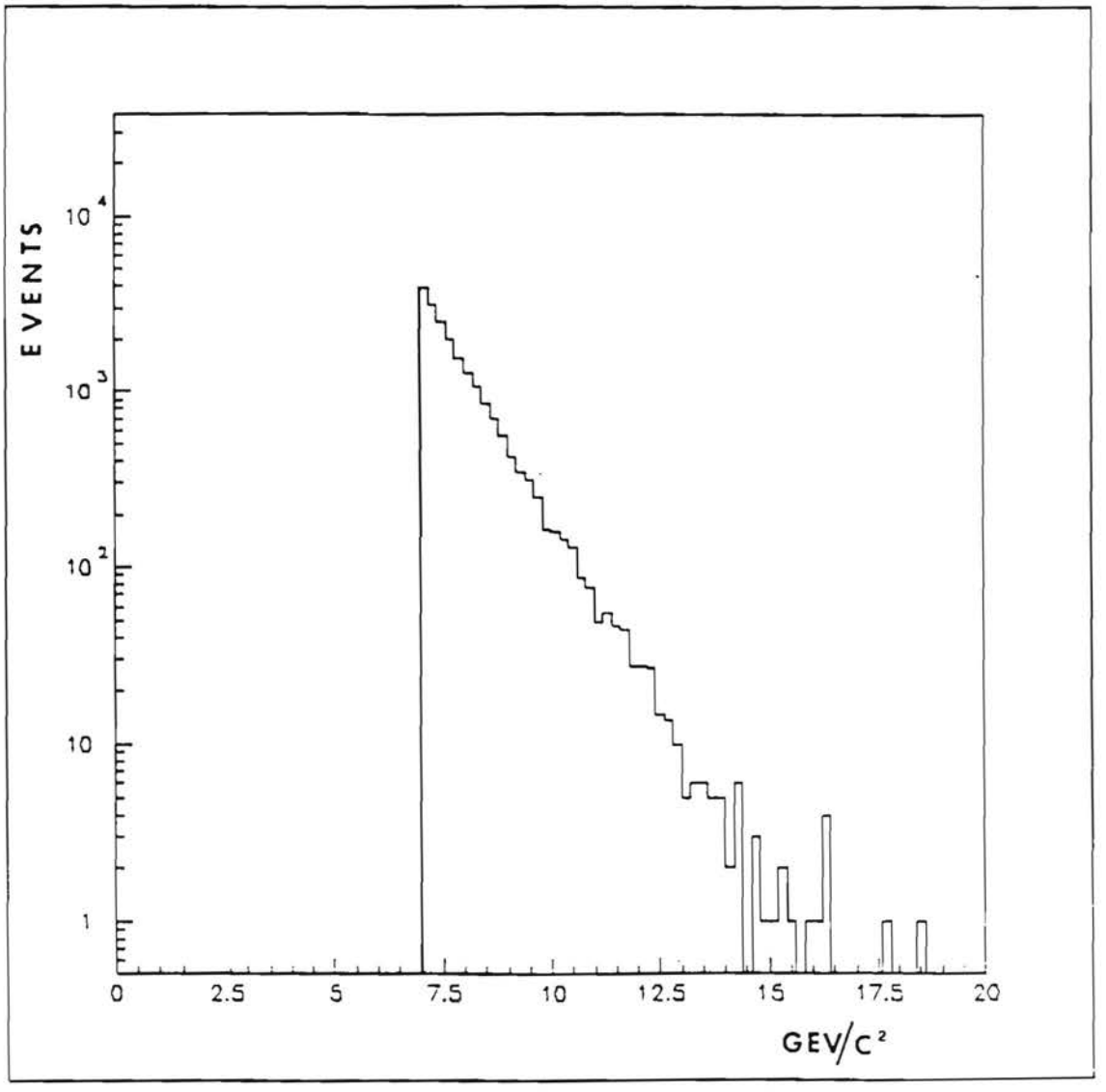

Di-hadron system mass after cut at 7 GeV/c^2

Figure 5.8

cles hit the calorimeter in this area and if this cone was not completely contained in the calorimeter sensitive zone, the leading hadron was discarded. Otherwise the energy deposited in the EM section of the calorimeter modules covered by the jet particle flux was calculated and defined as $E_{non\ leading\ neutral}$.

5.4.1 Evidence of jets

In E711 the jet direction was known from the beginning since it coincided with the trajectory of the leading hadron. Evidence of jets was searched for by analyzing the soft tracks. All the soft particles having $P_y > 0$ were associated with the top leading hadron and the others with the bottom leading hadron. Figure 5.9 shows the plot of $\eta_{leading} - \eta_{soft}$. In the presence of jets there should be an accumulation of events around zero indicating clusters of soft particles around the direction of the leading hadron. This is shown in figure 5.9. To rule out the possibility that this effect was due only to the acceptance of the apparatus, the events were analyzed substituting the two leading hadron tracks with the ones of the previous analyzed event. In this way random leading particles were used instead of the real ones. The result of this calculation is shown in figure 5.10. The peak at zero disappeared, broadened considerably in a bump indicating that the peak shown in figure 5.10 was not merely an acceptance effect. Another simulation procedure was used as a cross check and gave an analogous result. There, true leading particles were substituted by two fake ones generated by a montecarlo. The two fake leading hadrons were constrained to have the same effective mass and $P_{\perp total}$ of the real ones and were in the chamber and calorimeter fiducial volumes. Again the $\eta_{leading} - \eta_{soft}$ distribution, shown in

figure 5.11 was much broader than the corresponding ones shown in figure 5.9. The same type of analysis was performed using $\cos\Theta_{soft}$ ($\equiv$ angle between the soft particle and the leading one in the di-hadron system C.o.M). Figure 5.12 shows the distribution obtained using experimental data. There is a sharp peak for values near 1 as expected when jets are present. When the same histogram was calculated using the leading tracks of the previous selected event, the plot of figure 5.13 was obtained. The peak at 1 disappeared into a much broader bump. An analogous result was obtained using the second type of simulation technique (figure 5.14).

5.4.2 Definition of the jet spray cone

The definition of the jet cone was achieved studying the $\cos\Theta_{soft}$ distribution. As expected if the fragmentation process is independent on the way the parton was produced the $\cos\Theta_{soft}$ distribution shape did not change when the transverse momentum of the leading particle varied over the range from $\sim$ 1. GeV/c up to $\sim$ 8. GeV/c . This is shown in TABLE 5.1 where the mean values of $\cos\Theta_{soft}$ and statistical errors are listed. By inspection of figure 5.12 the angle for which

$$\cos\Theta = 0.93$$

was defined as the half-angle of the jet cone in the di-hadron C.o.M.

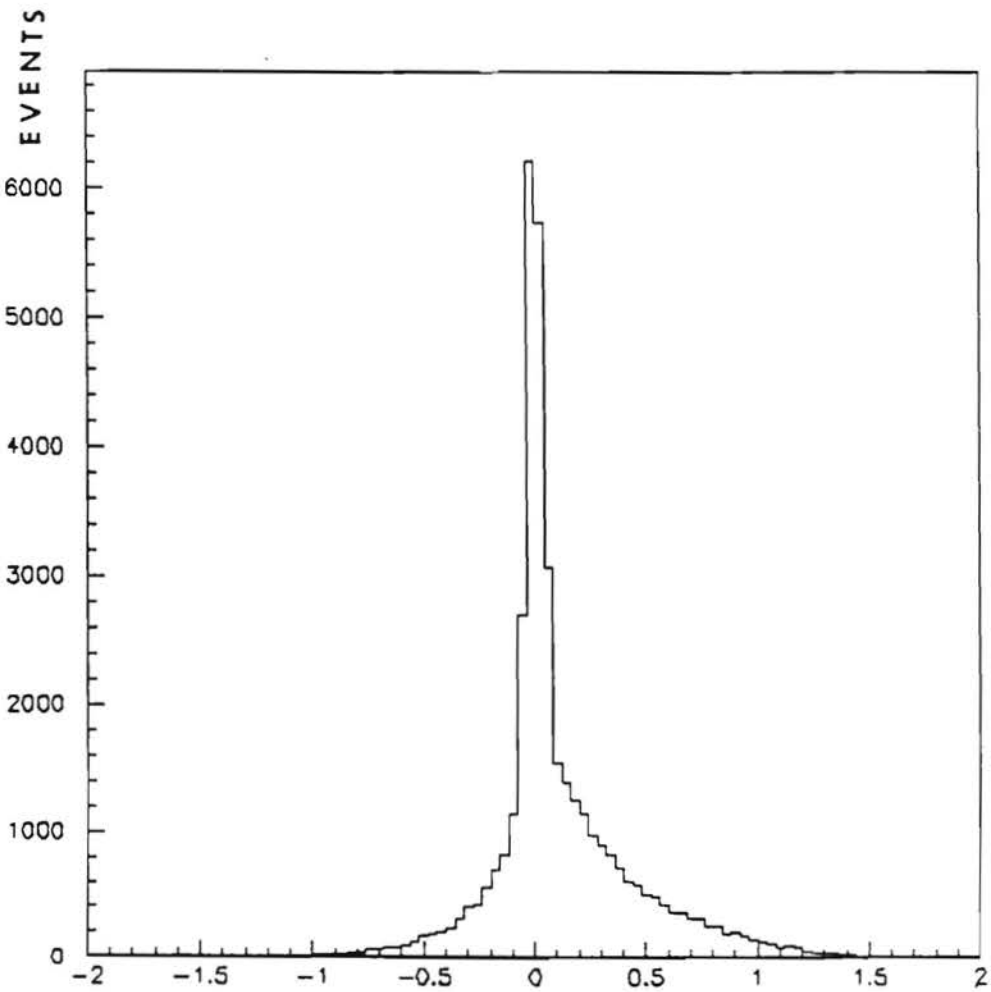

Distribution of $\eta_{leading} - \eta_{soft}$ for the experimental data

Figure 5.9

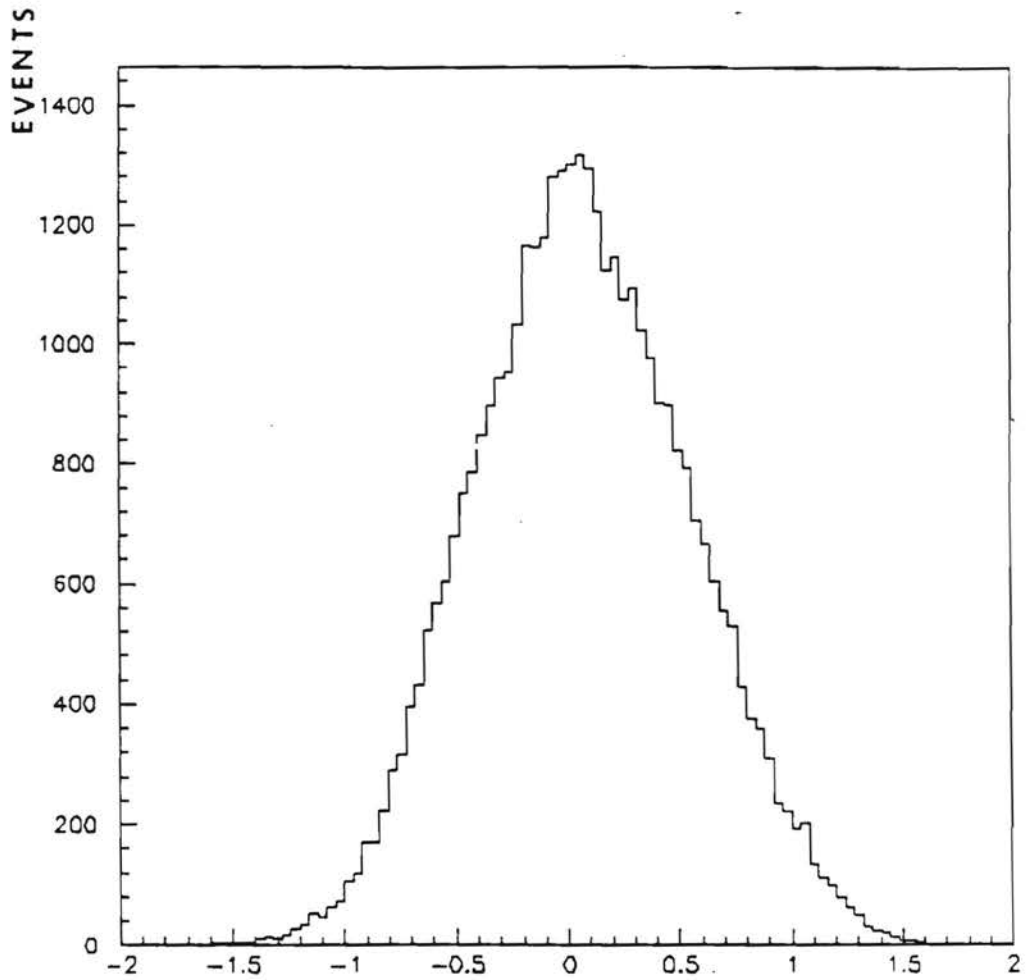

Distribution of $\eta_{leading} - \eta_{soft}$ for the experimental data when the leading hadron has been substituted with the one of the previous event

Figure 5.10

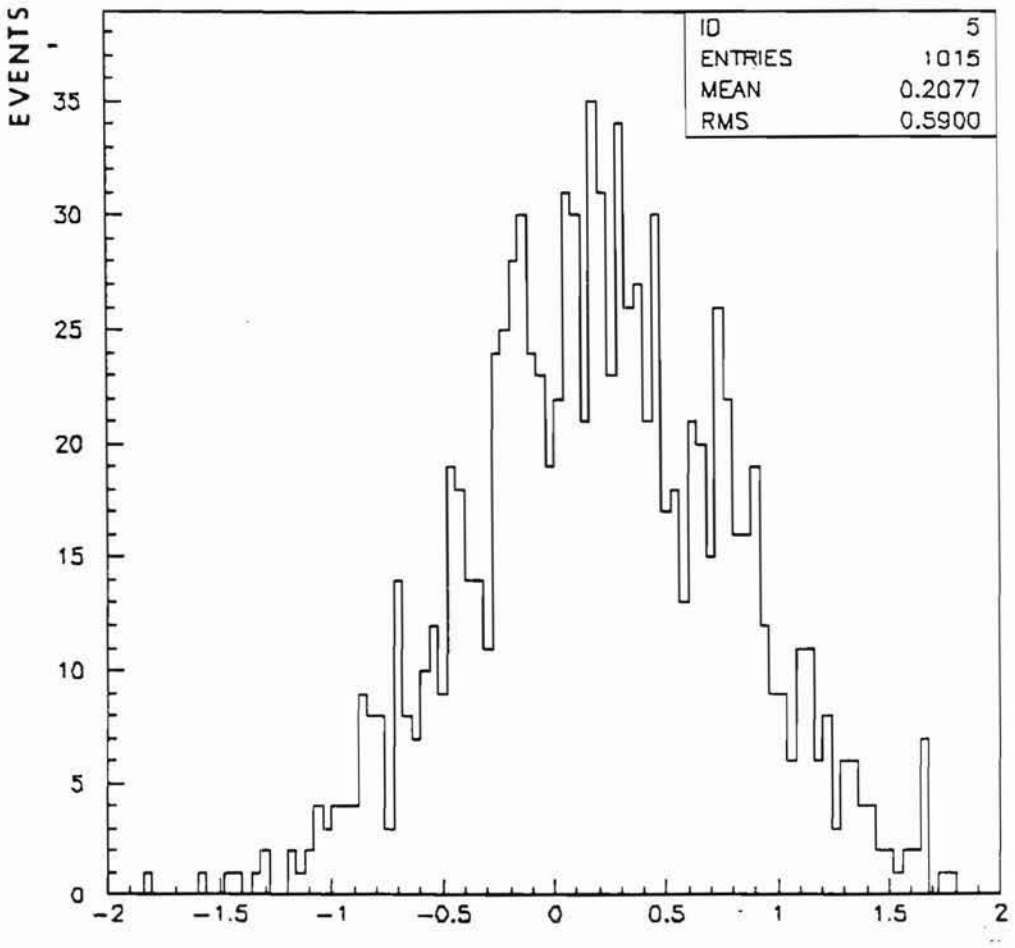

Distribution of $\eta_{leading} - \eta_{soft}$ for the experimental data when the leading hadron has been replaced with a simulated one

Figure 5.11

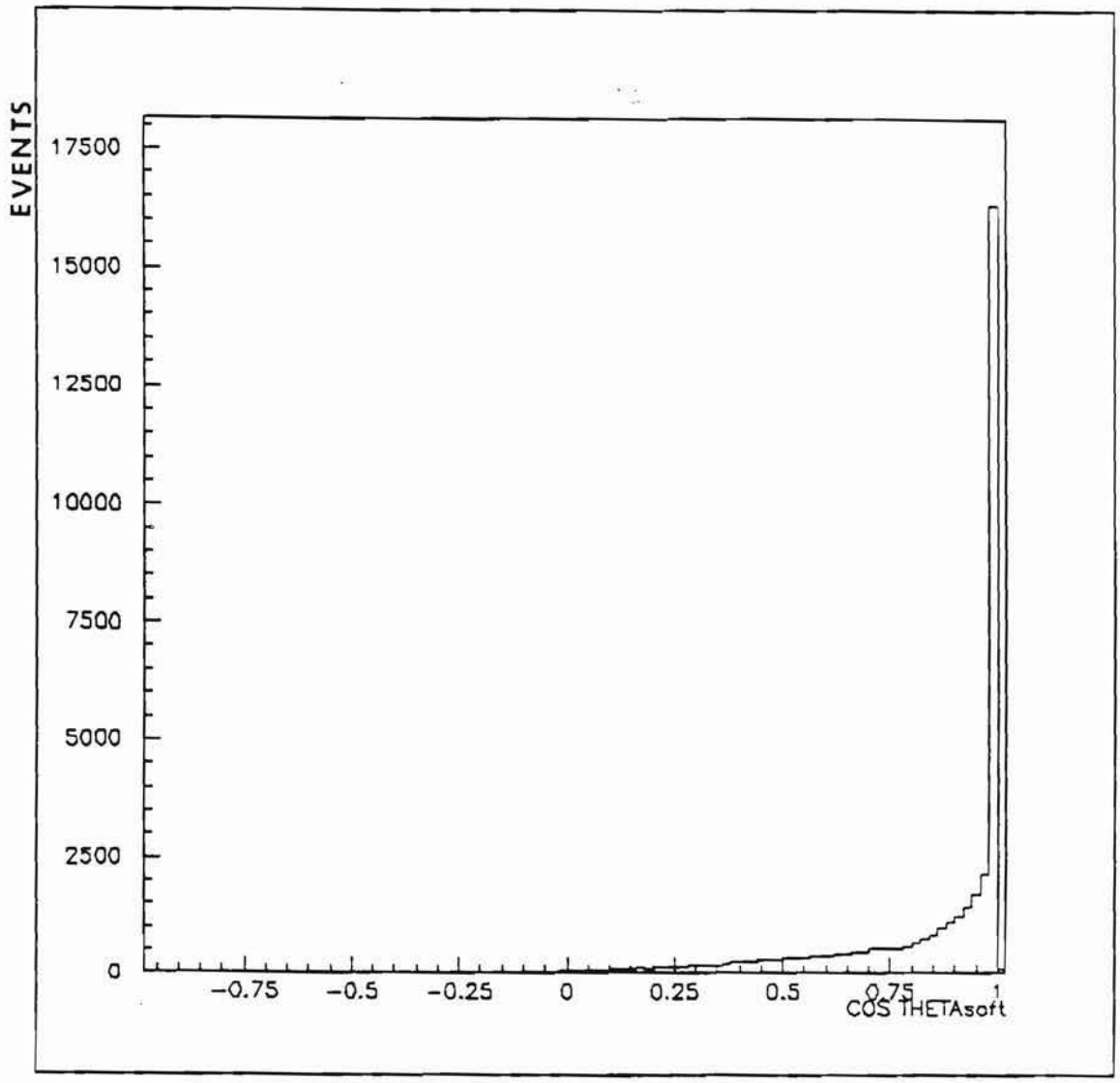

Distribution of $\cos\Theta_{soft}$ for experimental data

Figure 5.12

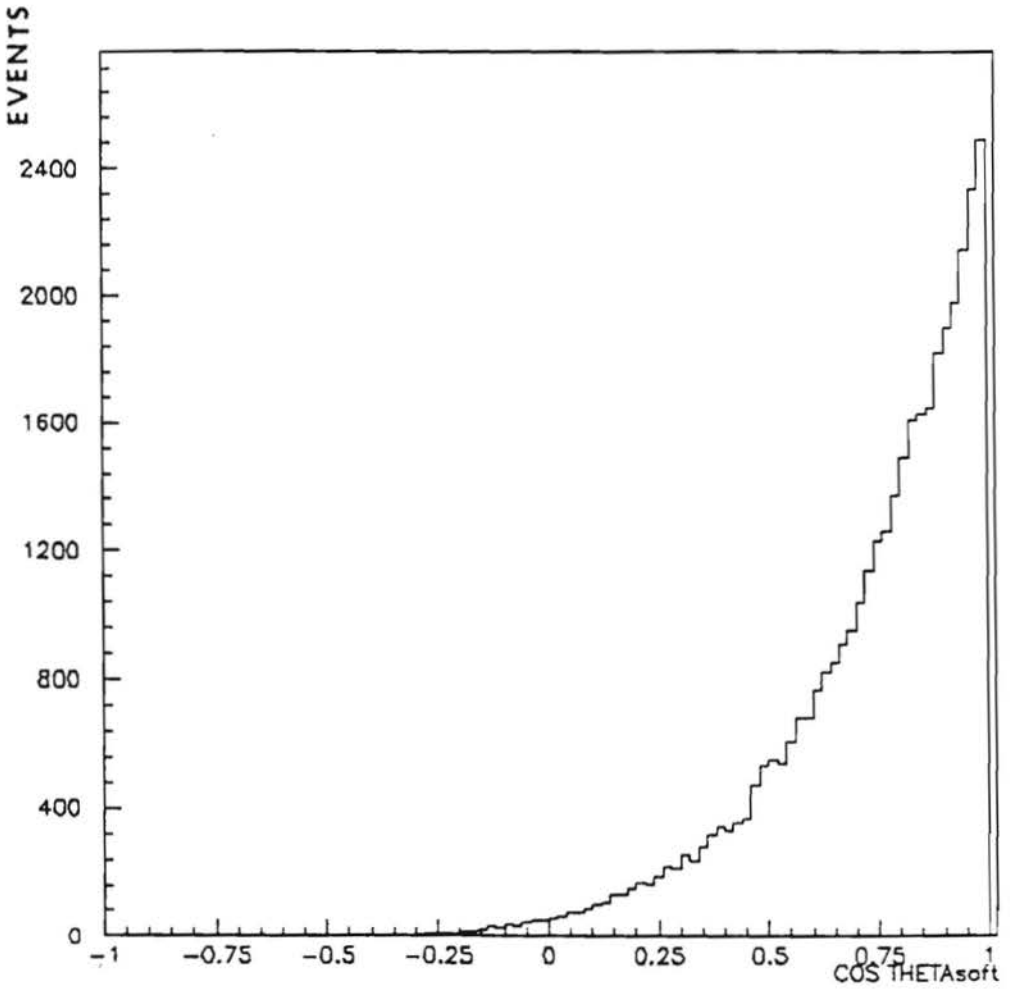

Distribution of $\cos\Theta_{soft}$ for the experimental data when the leading hadron has been substituted with the one of the previous event

Figure 5.13

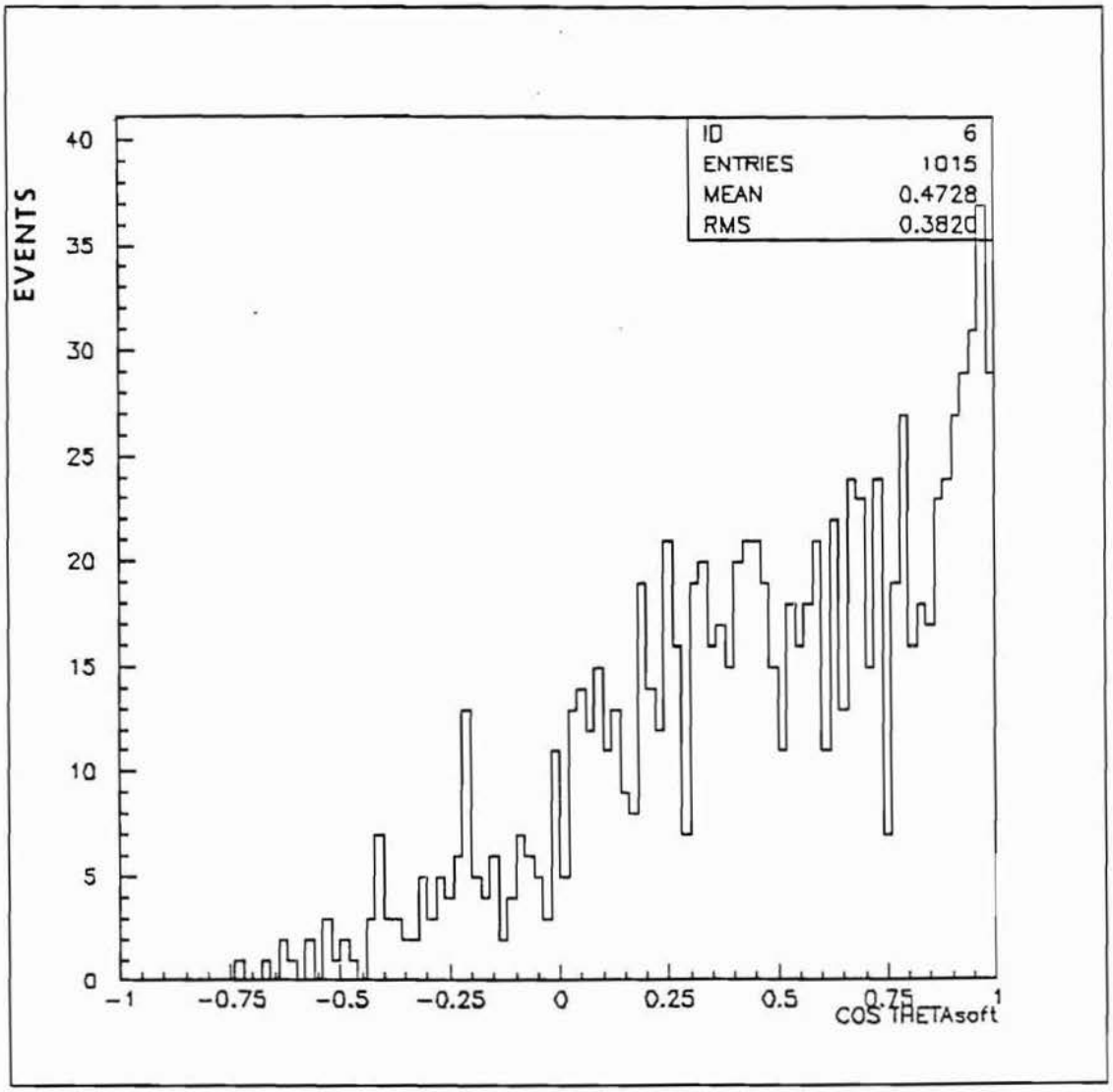

Distribution of $\cos\Theta_{soft}$ for the experimental data when the leading hadron has been replaced with a simulated one

Figure 5.14

TABLE 5.1

$P_\perp$ range	$< \cos\Theta_{soft} >$
$P_\perp < 2.5$ GeV/c	$0.858 \pm (0.2\%)$
$2.5 < P_\perp < 4.$ GeV/c	$0.815 \pm (0.2\%)$
$4. < P_\perp < 5.5$ GeV/c	$0.840 \pm (0.6\%)$
$P_\perp > 5.5$ GeV/c	$0.88 \pm (2\%)$

5.4.3 Determination of the ratio f

The determination of the ratio

$$f \equiv \left\langle \frac{E_{jet} - P_{leading}}{E_{non\ leading\ neutral}} \right\rangle$$

in formula (5.1) was calculated running the PYTHIA[22] montecarlo which simulated the particles forming two high $P_\perp$ jets produced in the E711 experimental conditions. Parallel montecarlo jobs were runned on the Florida State University High Energy Physics VAX cluster using different initial seeds for the random number generator of each job. About 20 day CPU total time was used. Nevertheless the generated events passing the analysis cuts were only 276. To increase the statistics I followed a suggestion by Prof. Levinthal. Each of the 276 events

TABLE 5.2

$P_\perp$ leading	f	σ_f
2.5 - 3.5	3.056	0.030
3.5 - 4.5	3.006	0.018
4.5 - 5.5	3.121	0.024
5.5 - 6.5	3.003	0.069
6.5 - 7.5	3.003	0.07

$\cos\theta^\star$ leading	f	σ_f
-0.8 - -0.6	3.232	0.080
-0.6 - -0.4	3.002	0.078
-0.4 - -0.2	3.054	0.030
-0.2 - 0.0	3.131	0.025
0.0 - 0.2	3.153	0.022
0.2 - 0.4	3.166	0.028
0.4 - 0.6	3.003	0.060
0.6 - 0.8	3.000	0.060

consisted of two opposite $P_\perp$ jets for a total of 552 jets. New events were generated making all the pairwise combinations of the 552 jets. One jet particle momenta were kept the same, the second jet particle momenta were rotated by the same angle in the X-Y plane so that the two jets had approximately opposite $P_\perp$ directions. In that way $\frac{552\times551}{2} \simeq 150,000$ events were generated of which $\simeq 60,000$ passed the analysis cuts. f was calculated for different $P_\perp$ and $\cos\theta^\star$ ranges of the leading hadron. The values are listed in TABLE 5.2.

5.4.4 *Calculation of the jet neutral energy*

In order to find the solid angle covered by the jet cone in the laboratory frame the method described in appendix B was used. To simplify the calculations an auxiliary frame, fixed in the laboratory, was used. It had the $\hat{\mathbf{z}}$ direction along the direction of the leading particle; the $\hat{\mathbf{x}}$ direction in the plane formed by the leading particle direction and $\mathbf{P}_{total}$ of the di-hadron system (see figure 5.15), in the direction opposite to $\mathbf{P}_{total}$ with respect to $\hat{\mathbf{z}}$. The $\hat{\mathbf{y}}$ direction was according to the right hand rule.

In the previous paragraph the condition $a \leq \cos\Theta_{soft} \leq 1$, with $a = 0.93$ defined a soft particle belonging to the jet. In the auxiliary frame such a condition corresponds to the inequality

$$0 < \tan\frac{\theta'}{2} < \frac{-B\cos\phi' + \sqrt{B^2\cos^2\phi' - 4AC}}{2A} \tag{5.2}$$

where

$\theta' \equiv$ polar angle of the soft particle in the auxiliary frame

$\phi' \equiv$ azimuthal angle of the soft particle in the auxiliary frame

$A \equiv a + 1 - \beta^2(a\cos^2\alpha - \cos^2\alpha + 2)$

$B \equiv 2(1-a)\beta(\beta\cos\alpha)\sin\alpha$

$C \equiv (a-1)(1-\beta\cos\alpha)^2$

where α is the angle ($\leq 90°$) between $\hat{\mathbf{z}}$ and $\mathbf{P}_{total}$ of the di-hadron system, in the auxiliary frame $\beta \equiv$ v/c of the di-hadron system in the laboratory reference frame. In appendix B the proof of (5.2) can be found. Since $A > 0$, $B \leq 0$, $C \leq 0$ the allowed values of $\tan\theta'$ depend on $\cos\phi'$ as shown on the graph of

figure 5.16 by the shadowed area. The equation of the boundary of solid angle enclosed by (5.2) is

$$\tan\frac{\theta'}{2} = \frac{-B\cos\phi' + \sqrt{B^2\cos^2\phi' - 4AC}}{2A}. \tag{5.3}$$

With a montecarlo technique, using (5.3) y_{min}, y_{max}, x_{min} and x_{max} were calculated, where $y_{min} \equiv$ vertical lower boundary, on the calorimeter surface, of the neutral jet particle flux impinging the calorimeter; $y_{max} \equiv$ vertical upper boundary; $x_{min} \equiv$ horizontal lower boundary; $x_{max} \equiv$ horizontal upper boundary. If y_{min}, y_{max}, x_{min}, x_{max} were inside the sensitive calorimeter surface, the jet neutral energy could be measured accurately. The neutral jet energy was defined as

$$\mathrm{E}_{non\ leading\ neutral} = \sum_{i=\mathrm{N}_{min}}^{\mathrm{N}_{max}} \mathrm{E}_{ie.m.} \tag{5.4}$$

where N_{min} and N_{max} were the numbers of the modules containing y_{min} and y_{max} respectively and $\mathrm{E}_{ie.m.}$ was the energy of the ith module in the electromagnetic section of the calorimeter. Out of the 20467 events passing the general selection cuts 71.5% were discarded because neither of the leading hadrons had the corresponding jet cone contained in the calorimeter sensitive area. Out of the $20467 \times 2 = 40934$ initial jets passing the general selection cuts, 5696 passed also the containment cuts.

5.4.5 Correction to the error introduced by the definition of the jet cone

The definition of the jet cone half-angle aperture generated an error in the calculation of $E_{non\ leading\ neutral}$. This is shown by figure 5.17, where $< \mathcal{Z} >$ calculated using all the experimental data, is plotted for different values of $\cos\Theta$.

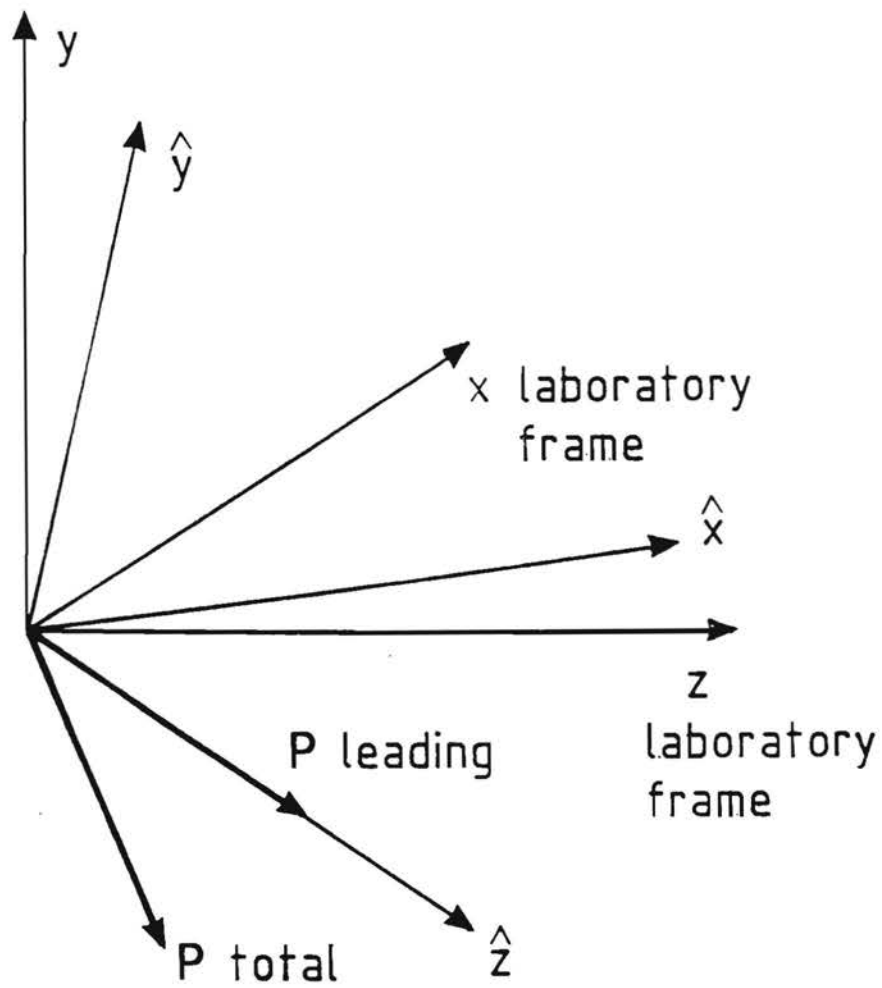

Auxiliary frame used in the calculation of $E_{non\ leading\ neutral}$

Figure 5.15

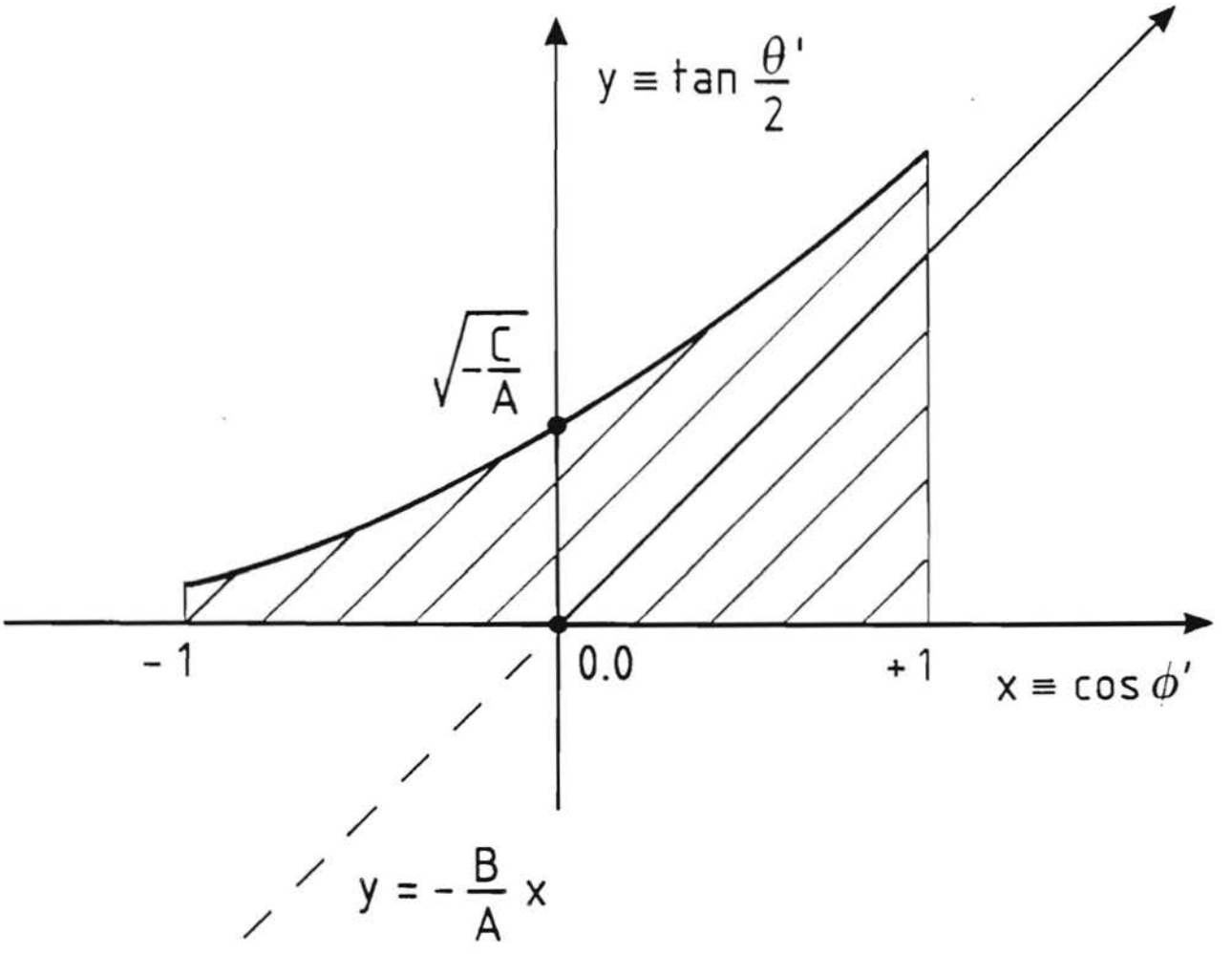

Diagram indicating the solid angle covered by the neutral jet particle flux expressed as a function of $\cos\phi'$ and $\tan\theta'$

Figure 5.16

The plateau of the curve is reached for $\cos\Theta$ lower than 0.93, the value used in this analysis. This means that some of the γ's of the jet were produced at wider angles than Θ and their energy was not measured completely by the calorimeter. To correct this loss the ratio $R \equiv < \frac{E_{neutral\ all}}{E_{in\ cone}} >$ was calculated for different ranges of $P_\perp$ and $\cos\theta^\star$ of the leading hadron running a PYTHIA[22] montecarlo which simulated the particles forming two high $P_\perp$ jets produced in the E711 experimental conditions (TABLE 5.3). $E_{neutral\ all}$ was the energy of all the γ's of the jet, $E_{in\ cone}$ was the energy of the γ's contained in the jet cone defined by $\cos\Theta \geq 0.93$. The experimental data was then corrected multiplying the measured $E_{non\ leading\ neutral}$ by R event by event.

5.5 Corrections and systematic errors of the calculation of the neutral energy of the jet

Two types of corrections were applied to $E_{non\ leading\ neutral}$. The first took into account the absorption in the target of a fraction of γs product of the decay of the neutral jet particles. The second estimated the release of energy by the leading hadron in EM calorimeter modules included in the sum of formula (5.4) which affected the correct calculation of $E_{non\ leading\ neutral}$. The correction for the latter effect introduced a systematic error on $< \mathcal{Z} >$ (called from now on $\Sigma_{\Delta E}$), estimated by a simulation program.

5.5.1 Correction for the absorption of γs in the target

Essentially all the neutral jet particles decay into γs which were detected in the EM calorimeter sections. A fraction of them interacted and started an

TABLE 5.3

$P_\perp$ leading	R	σ_R
2.5 - 3.5	1.106	0.003
3.5 - 4.5	1.170	0.002
4.5 - 5.5	1.120	0.003
5.5 - 6.5	1.210	0.015
6.5 - 7.5	1.000	0.013

$\cos\theta^\star$ leading	R	σ_R
-0.8 - -0.6	1.120	0.011
-0.6 - -0.4	1.120	0.011
-0.4 - -0.2	1.129	0.004
-0.2 - 0.0	1.159	0.003
0.0 - 0.2	1.158	0.003
0.2 - 0.4	1.153	0.003
0.4 - 0.6	1.109	0.008
0.6 - 0.8	1.197	0.008

electromagnetic shower in the target. As a consequence, a fraction of their energies could not be detected by the calorimeters. To calculate this fraction a montecarlo program (GEANT[23]) generated a number of γ's with the vertex uniformly distributed in the four different targets. GEANT is a CERN program which simulates the development of electromagnetic showers accurately using the electromagnetic interaction cross sections predicted by QED. The direction of the γ's was also uniform over the solid angle covered by the active region of

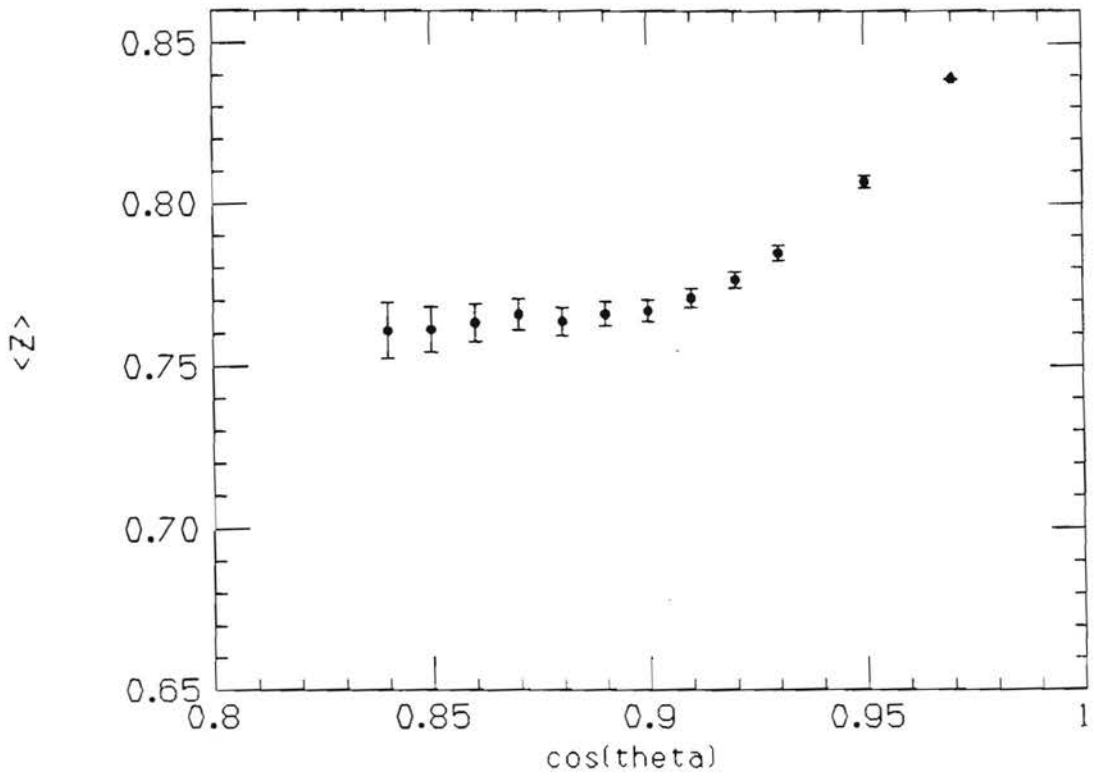

$< \mathcal{Z} >$ of all the selected events as a function of $\cos\Theta$, cosine of the cone aperture angle of the jet

Figure 5.17

the calorimeter. The fraction of energy deposited in the calorimeter was

$$c_{seen} = \frac{1}{\mathrm{N}} \times \sum_{i=1}^{\mathrm{N}} \frac{\mathrm{E}_{i\gamma seen}}{\mathrm{E}_{\gamma}}$$

where $\mathrm{E}_{i\gamma seen}$ was the energy of the i_{th} primary γ detected by the calorimeters, E_{γ} was the energy of the primary γ, N the number of primary γ's generated. The results of the montecarlo are listed in TABLE 5.4 The values of c_{seen} obtained for each target for energies of the primary γ ranging from 1 GeV to 500 GeV are listed. They are essentially the same over such a wide γ energy range, for a given target, because the cross sections of the e^+e^- pair production and bremsstrahlung, which are the dominant mechanisms in the electromagnetic shower at these energies, are essentially flat in this energy range. The c_{seen} used in this analysis for each target was the average of the c_{seen} calculated for the different E_{γ}. The correction for the γ absorption in each target consisted of dividing the energy experimentally measured (data) in the EM calorimeter by c_{seen}, as calculated for that target. The systematic error induced was estimated to be negligible due to the great statistical accuracy with which c_{seen} was calculated and the inherent accuracy of the simulation program[23].

5.5.2 Correction for the energy released by the leading particle in the EM section of the calorimeter

For each leading hadron $E_{non\ leading\ neutral}$ was calculated using equation (5.4) and corrected with c_{seen}. The sum in equation (5.4) included the modules containing the shower produced by the leading hadron in the EM section of the calorimeter. In this way a spurious contribution, which had to be limited and

TABLE 5.4

Beryllium target

E_γ in GeV	c_{seen}
1.	$0.971 \pm 0.2\%$
5.	$0.970 \pm 0.2\%$
10.	$0.970 \pm 0.2\%$
30.	$0.969 \pm 0.2\%$
100.	$0.969 \pm 0.2\%$

Average c_{seen} : $0.969 \pm 0.1\%$

Aluminium target

E_γ in GeV	c_{seen}
1.	$0.897 \pm 0.1\%$
5.	$0.896 \pm 0.1\%$
10.	$0.897 \pm 0.1\%$
30.	$0.898 \pm 0.1\%$

Average c_{seen} : $0.897 \pm 0.05\%$

Iron target

E_γ in GeV	c_{seen}
1.	$0.818 \pm 0.2\%$
5.	$0.819 \pm 0.2\%$
10.	$0.823 \pm 0.2\%$
30.	$0.823 \pm 0.2\%$
500.	$0.817 \pm 0.2\%$

Average c_{seen} : $0.820 \pm 0.1\%$

Tungsten target

E_γ in GeV	c_{seen}
1.	$0.594 \pm 0.3\%$
5.	$0.637 \pm 0.2\%$
10.	$0.650 \pm 0.2\%$
40.	$0.669 \pm 0.2\%$
50.	$0.670 \pm 0.2\%$

Average c_{seen} : $0.644 \pm 0.1\%$

corrected for, was present. It was limited by selecting only those leading hadrons that released less than 10% of their energy in the EM section of the calorimeter. About 33% of the leading particles passed this cut. In other words, the energy observed in the hadronic segments hit by the leading particle had to be greater than 90% of the magnetically determined track momenta.

It was corrected by simulating the shower produced by a hadron in the EM calorimeter section and calculating the average energy released. Hadrons of energy between 10 GeV and 200 GeV were generated, corresponding to the experimental leading particle energy spectrum range shown in figure 5.18. Only hadrons releasing 90% of their energy in the hadronic calorimeter section were generated according to the cut applied on the experimental data. The average energy released ($\equiv < \Delta E >$) by the primary hadron shower is listed in TABLE 5.5 as a function of the primary hadron energy. The correction to $E_{non\ leading\ neutral}$ was performed subtracting the $< \Delta E >$ corresponding to the energy of the leading hadron namely

$$< \mathcal{Z} > = \left\langle \frac{\mathrm{P}_{leading}}{\mathrm{P}_{leading} + \frac{fR}{c_{seen}} E_{non\ leading\ neutral}} \right\rangle$$
$$= \frac{1}{N} \sum_{i=1}^{N} \frac{\mathrm{P}_{leading,i}}{\mathrm{P}_{leading,i} + \frac{fR}{c_{seen}} E_{non\ leading\ neutral,i}}$$

where the index i refers to the ith leading particle and N is the total number of leading particles. Then

$$< \mathcal{Z} > = \frac{1}{N} \sum_{i=1}^{N} \frac{\mathrm{P}_{leading,i}}{\mathrm{P}_{leading,i} + \frac{fR}{c_{seen}} (E_{non\ leading\ neutral,i} - < \Delta E >_i)} \tag{5.6}$$

where $< \Delta E >_i$ is the estimate of the energy released in the EM calorimeter by the ith leading particle.

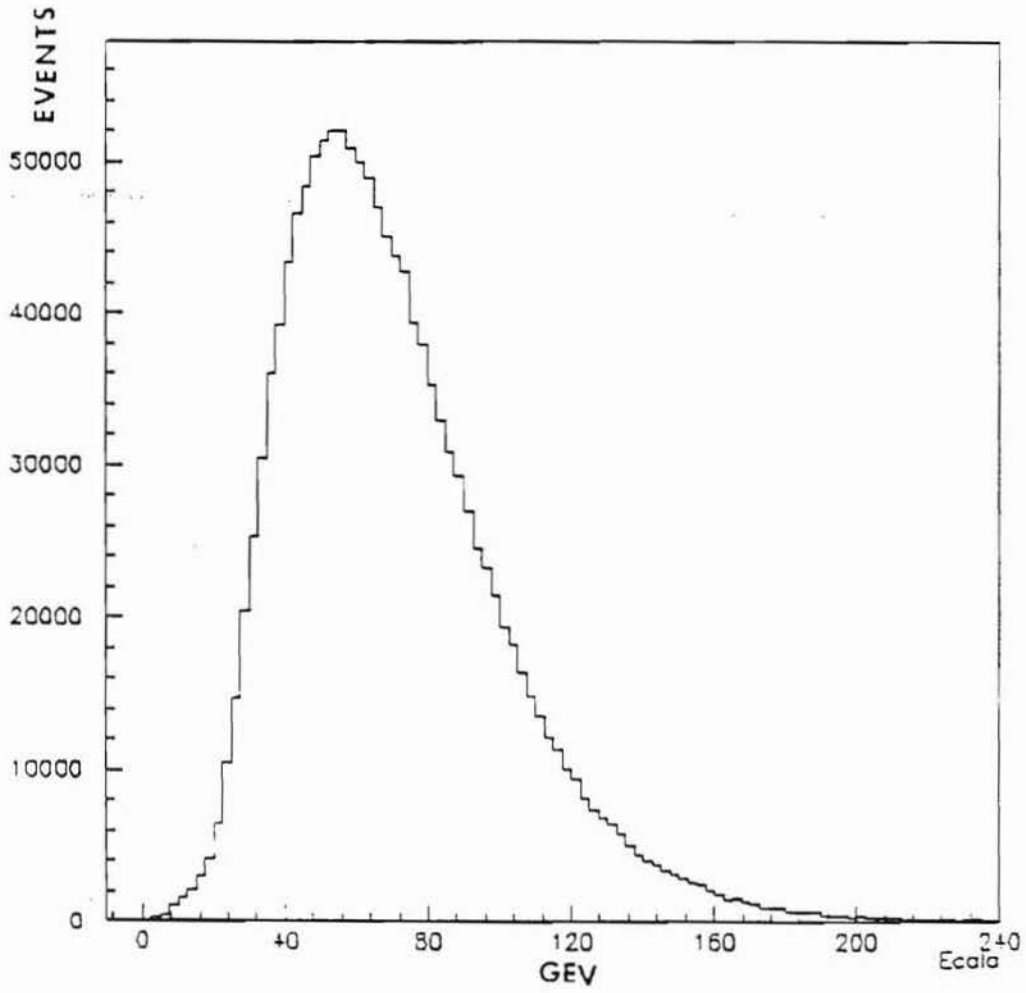

Energy of the leading particles measured by the calorimeter

Figure 5.18

5.5.3 *Calculation of the systematic error on $< \mathcal{Z} >$ induced correcting $E_{non\ leading\ neutral}$*

A systematic error was induced in the calculation of $< \mathcal{Z} >$ when the correction to $E_{non\ leading\ neutral}$ by $< \Delta E >$ was applied, due to the fact that $< \Delta E >$ was a mean energy released and not the actual energy released by a particular leading hadron. The error on $< \Delta E >$ was assumed to be of the order of the standard deviation σ of the distribution of ΔE. The values of σ as a function of the energy of the primary hadron are listed in TABLE 5.5. The systematic error induced in the calculation of $< \mathcal{Z} >$ was obtained considering that from (5.6)

$$< \mathcal{Z} > = \frac{1}{N}\sum_{i=1}^{N}\frac{1}{1 + f\frac{E_{non\ leading\ neutral,i}}{\mathrm{P}_{leading,i}} - f\frac{<\Delta E>_i}{\mathrm{P}_{leading,i}}}$$
$$\simeq \frac{1}{N}\sum_{i=1}^{N}\left(1 - f\frac{E_{non\ leading\ neutral,i}}{\mathrm{P}_{leading,i}} + f\frac{< \Delta E >_i}{\mathrm{P}_{leading,i}}\right)$$

since $f\frac{E_{non\ leading\ neutral,i}}{\mathrm{P}_{leading,i}}$ and $f\frac{<\Delta E>_i}{\mathrm{P}_{leading,i}}$ are small numbers. Hence

$$< \mathcal{Z} >= \left\langle\frac{\mathrm{P}_{leading}}{\mathrm{P}_{leading} + f \times E_{non\ leading\ neutral}}\right\rangle + \frac{f}{N}\sum_{1}^{N}\frac{< \Delta E >_i}{\mathrm{P}_{leading,i}} \qquad (5.7)$$

The systematic error on $< \mathcal{Z} >$ ($\equiv \Sigma_{\Delta E}$) was determined by the error in estimating the quantity $\frac{f}{N}\sum_1^N \frac{<\Delta E>_i}{\mathrm{P}_{leading,i}}$. Hence

$$\Sigma_{\Delta E} = \frac{f}{N}\sqrt{\sum_{i=1}^{N}\left(\frac{\sigma_i}{\mathrm{P}_{leading,i}}\right)^2} \qquad (5.8)$$

where the imprecision in estimating the release of energy equal to $< \Delta E >_i$ was σ_i. The latter depended on the primary hadron energy and was calculated interpolating linearly the values listed in TABLE 5.5.

TABLE 5.5

E_{inc} ≡ *energy of the impinging hadrons*

ΔE ≡ *average energy release in* EM

σ ≡ σ *of the energy release in* EM

N_E ≡ # *entries in the energy release plot*

E_{inc} (GeV)	ΔE (GeV)	σ (GeV)	N_E
10	0.01832	0.02441	74
20	0.01941	0.05221	62
30	0.0206	0.07100	38
40	0.02182	0.08029	75
50	0.02420	0.10124	79
60	0.02528	0.11857	85
80	0.02967	0.15323	45
100	0.03458	0.17496	217
125	0.03327	0.18300	467
150	0.04193	0.20214	44
175	0.04626	0.22773	74
200	0.05652	0.26518	102

CHAPTER 6

THEORETICAL INTERPRETATION

The existence of quarks is widely accepted in the current interpretations of the composition of hadronic matter. They interact via the strong forces which are described by Quantum Chromo Dynamics[1], a gauge theory with SU(3) color symmetry, in which the interaction between quarks is mediate by the gluon vector field. In the QCD-parton model high $P_\perp$ interactions are due to the scattering at high momentum transfer of a quasi free pointlike partons one in the beam with the other in the target. Such scattering is calculable perturbatively using the QCD interaction lagrangian. Experimental data and QCD-parton model predictions were found to be in excellent agreement[24][12][8][25][26]. Evidence for the existence of pointlike scattering centers in hadrons was experimentally found[27][28][29][30] in deep inelastic scattering of leptons with nucleons and in

high $P_\perp$ hadron production experiments[31][32][33]. These experimental results were explained by the parton model in which hadrons are composed of pointlike particles called partons[34][2][35][36][37][3]. It was a subsequent natural step to identify the constituent partons with the gluons and quarks of QCD.

Once the parton-parton cross sections are known, the parton model gives the description of the di-jet production cross section using the experimentally determined parton distribution functions. In a similar manner the di-hadron production cross section is calculated, the only difference being the introduction and use of fragmentation functions to describe the internal details of jet formation. The QCD theory is able to predict the parton-parton cross section when the scattered partons are produced at high $P_\perp$. In that case perturbative calculation techniques can be used and the cross sections accurately predicted. In that way also $< \mathcal{Z} >$, subject of this thesis, can be calculated and compared to the E711 data to check the degree of agreement between theory and experiment. The comparison also bears on whether the fragmentation process is influenced by global nuclear effects derived from the use of heavy nuclear targets in E711 instead of the 'pure' lepton-hadron or hadron-hadron collider beams used in the other experiments quoted so far.

6.1 QCD-parton model description of high $P_\perp$ jet production

According to the parton model collisions between two hadrons can result in collimated sprays of particles (jets) at high transverse momentum ($P_\perp$), as in

the reaction

$$A, B \rightarrow C, D + X$$

where A and B are the colliding hadrons, C and D are the two high $P_\perp$ jets, X means the rest of the particles. The colliding hadrons are assumed by the model to be composed of quarks and gluons (distributed with a density given by phenomenological 'distribution functions'), which behave as free particles in the high $P_\perp$ scattering process. The collision is assumed to happen between two partons, each belonging to one of the colliding hadrons and described by the cross section $\frac{d\sigma}{d\hat{t}}$. Two outgoing partons, generated from the scattering, subsequently 'fragment' into a spray of collimated particles, namely a jet. Therefore in such processes 4 jets are produced, two coming from the scattered partons, and the other two generated from the rest of the 'spectator' partons of beam and target hadrons. The last two jets are produced at low $P_\perp$ with respect to the direction of the colliding hadrons. The mechanism of the reaction is shown diagrammatically in figure 1.1, where a and b are the colliding partons, c and d are the outgoing partons that fragment into the jets C and D. Upon these assumptions, the high $P_\perp$ jet production cross section is calculable knowing the distribution functions, typically from deep inelastic lepton-hadron scattering experiments, and the parton-parton cross section which can be calculated up to different degrees of approximation in the QCD theoretical framework. Such approximations are meaningful only for processes in which the two jets C and D are produced at high $P_\perp$, in which case perturbative calculations can be applied.

6.1.1 Di-jet cross section

A theoretical expression of the production cross section of two jets at high and opposite $P_\perp$ based on the parton model and QCD calculation can be obtained as the convolution of probabilities. In the ensuing discussion it will be assumed that the masses of the colliding hadrons and partons and the transverse momenta (due to Fermi motion) of the partons inside their nucleons are negligible compared with their momenta. First, some kinematic definitions are necessary. In the C.o.M of the colliding hadrons (with the incident beam in the positive direction), one finds

$$p_a = \frac{x_a\sqrt{s}}{2}[1,0,0,1]$$

$$p_b = \frac{x_b\sqrt{s}}{2}[1,0,0,-1]$$

$$x_a x_b = \frac{M^2}{s} \tag{6.1}$$

$$x_a - x_b = X_F \tag{6.2}$$

x_a and x_b (the Bjorken scaling variables) are the longitudinal momentum fractions of parton a in the beam and parton b in the target, p_a and p_b are the measured jet momenta. M is the invariant mass formed by the two high $P_\perp$ jets. X_F is defined as :

$$X_F \equiv \frac{2P_l}{\sqrt{s}}$$

where P_l is the net longitudinal momentum of the two jet system and $\sqrt{s}$ is the C.o.M energy of the reaction. x_a and x_b determine the incident momenta of the colliding partons. The cross section for two-jet production at high $P_\perp$ in the

C.o.M of the colliding hadrons can be calculated starting from the infinitesimal inclusive scattering cross section for two hadrons into two partons c and d[12] :

$$d\sigma_{(A,B\to c,d+X)} = \sum_{a,b} \int dx_a dx_b G_{a/A}(x_a, Q^2) G_{b/B}(x_b, Q^2) \frac{d\sigma_{(a,b\to c,d)}}{d\hat{t}} \times \\ \times \frac{2\hat{s}}{\pi} \frac{d^3p_c}{E_c} \frac{d^3p_d}{E_d} \delta^4(p_a + p_b - p_c - p_d) \tag{6.3}$$

where p_c and p_d are the outgoing high $P_\perp$ jet momenta, $G_{a/A}(x_a, Q^2)$ and $G_{a/A}(x_a, Q^2)$ are the distribution functions for parton a in hadron A and b in hadron B respectively. $\hat{s}$ and $\hat{t}$ the usual Mandelstam variables for the parton parton system :

$$\hat{s} \equiv (p_a + p_b)^2$$

$$\hat{t} \equiv (p_a - p_c)^2$$

$$\hat{u} \equiv (p_b - p_c)^2,$$

E_c and E_d are the energies of the outgoing partons. $\frac{d\sigma_{(a,b\to c,d)}}{d\hat{t}}$ is the expression for the differential cross section of a parton-parton scattering process. The summation indices a and b run over all the possible parton combinations. Also in (6.3) an average over all the possible spin and color states of the colliding partons is implied. The δ function assures the conservation of the total momentum and therefore also the balance of the transverse momentum of the outgoing partons (the internal transverse motion of the incident partons is neglected in this calculation). The parameter Q, whose dimension is $[energy]^2$, introduces the scaling violation dependence of the distribution functions. It will be described in more detail later. Formula (6.3) is the di-jet infinitesimal cross section once one assumes that the jets are the product of the fragmentation of the partons c

and d. In that case an incoherent summation over all the possible c and d states (including all the possible spin and color states) is necessary to describe the final observed state. From (6.3) one obtains the following formula for the di-jet production cross section[12], in the limit of the collinear approximation ($\equiv$ parton Fermi motion neglected), expressed in terms of observables directly measurable :

$$\frac{d^3\sigma_{(A,B\to jet_1+jet_2+X)}}{dy_1\,dy_2\,dP_\perp^2} = \int \sum_{a,b,c,d} G_{a/A}(x_a,Q^2)G_{b/B}(x_b,Q^2)\frac{\hat{s}}{2}\frac{d\sigma_{(a,b\to c,d)}}{d\hat{t}}$$
$$\times\,\delta(x_a\frac{\sqrt{s}}{2}+x_b\frac{\sqrt{s}}{2}-P_\perp\cosh y_1-P_\perp\cosh y_2)\times$$
$$\times\,\delta(x_a\frac{\sqrt{s}}{2}-x_b\frac{\sqrt{s}}{2}-P_\perp\sinh y_1-P_\perp\sinh y_2)dx_a dx_b$$

where y_1 and y_2 are the jet_1 and jet_2 rapidities. Performing the integrations in dx_a and dx_b of the δ-functions one obtains[12] :

$$\frac{d^3\sigma_{(A,B\to jet_1+jet_2+X)}}{dy_1\,dy_2\,dP_\perp^2} = \sum_{a,b,c,d} x_a x_b G_{a/A}(x_a,Q^2)G_{b/B}(x_b,Q^2)\frac{d\sigma_{(ab\to c,d)}}{d\hat{t}} \quad (6.4)$$

with

$$x_a = \frac{P_\perp}{\sqrt{s}}(e^{y_1}+e^{y_2})$$

and

$$x_b = \frac{P_\perp}{\sqrt{s}}(e^{-y_1}+e^{-y_2})$$

It is interesting to note that if x_a and x_b are > 0.5, the distribution functions in (6.4) of the gluons and the sea quarks become negligible, and just the valence quarks contribute to the cross section. From (6.1) and (6.2) :

$$\frac{M^2}{s} = x_a(x_a - X_F)$$
$$\frac{M^2}{s} = x_b(x_b + X_F).$$

Another useful expression for the high $P_\perp$ di-jet production can be obtained by changing variables, going from $y_c, y_d, P_\perp^2$ to $M, Y, \cos\theta^\star$, where $Y = \frac{1}{2}\ln\frac{x_a}{x_b}$ is the di-jet rapidity and $\theta^\star$ is the angle in the C.o.M of the colliding partons. Using the proper Jacobian from (6.4) one finds

$$\frac{d^3\sigma}{dY d(M^2) d\cos\theta^\star} = \frac{M^2}{2s}\sum_{a,b,c,d} G_{a/A}(x_a, Q^2) G_{b/B}(x_b, Q^2)\frac{d\sigma_{(a,b\to c,d)}}{d\hat{t}} \qquad (6.5)$$

where now

$$x_a = \frac{M}{\sqrt{s}}e^Y, \qquad x_b = \frac{M}{\sqrt{s}}e^{-Y} \qquad (6.6)$$

Consequently the measurement of $d^3\sigma/dY(dM^2)d\cos\theta^\star$ at fixed Y and M^2 and energy (i.e. fixed x_a and x_b) gives direct information on the angular dependence of $d\sigma_{(a,b\to c,d)}/d\hat{t}$.

6.1.2 Di-hadron cross section

While it has been experimentally shown that jets are relatively easy to define at high C.o.M. of the reaction energies (UA1 and UA2 experiments[4][38][39][40][41] $\sqrt{s}$ from 540 to 630 GeV) at lower C.o.M. of the reaction energies that is much more difficult. The production of high $P_\perp$ di-hadron events are a suitable tool to test the QCD-parton model at lower energies ($\sqrt{s} \simeq$ from 30 to 60 GeV). It has been shown experimentally that high $P_\perp$ di-hadron events are substantially equivalent to the di-jet events[5][6]. The di-hadron scattering angle is a very good approximation of the di-jet one and the theoretical interpretation is facilitated, for the Fermi motion of the colliding partons is reduced in such events[10]. However, in order to make rigorous comparisons between high $P_\perp$ events and theory, the expression (6.5) for the cross section must be modified by

introducing the fragmentation functions $D_{c/H}(z, Q^2) \equiv$ probability of getting a hadron H from parton c with momentum fraction between z and $z+dz$ ($z = \frac{p_H}{p_c}$). The mechanism of production of two high $\mathrm{P}_\perp$ hadrons h_1 and h_2 is illustrated in figure 1.1, Q^2 is taken to be the same parameter introduced earlier in the distribution functions. Defining the measured quantities in the following way (still collinear kinematics approximations is assumed) :

$$\begin{aligned}
\Delta \equiv &\quad \mathrm{P}_\perp(hadron1) - \mathrm{P}_\perp(hadron2) = (z_1 - z_2)\mathrm{P}_\perp \\
Y_{di-hadron} \equiv &\quad \text{rapidity of the di-hadron system} \\
M_{di-hadron} \equiv &\quad \text{effective mass of the di-hadron system}
\end{aligned}$$

where z_1 and z_2 are the momentum fraction of the hadrons 1 and 2. Remembering that $\mathrm{P}_\perp = \frac{M}{2}\sin\theta^\star$ one obtains, neglecting the hadron mass compared its momentum :

$$M^2_{di-hadron} = z_1 z_2 M^2$$

$$Y = Y_h - \ln\frac{\sqrt{M_h^2 + \Delta^2}}{M_h} + \ln\left[\sqrt{\frac{z_1}{z_2}}\frac{1+\cos\theta^\star}{2} + \sqrt{\frac{z_2}{z_1}}\frac{1-\cos\theta^\star}{2}\right].$$

From (6.5) using the proper Jacobian for the change of variables it is possible to obtain[12] :

$$\begin{aligned}
&\frac{d^4\sigma}{d(M^2_{di-hadron})dY_{di-hadron}d\Delta d\cos\theta^\star} = \frac{M^2}{2s}\times \\
&\times\int\sum_{a,b,c,d} G_{a/A}(x_a, Q^2)G_{b/B}(x_b, Q^2)\frac{d\sigma_{(a,b\to c,d)}}{d\hat{t}}D_{c/H_1}(z_1, Q^2)D_{d/H_2}(z_2, Q^2)\times \\
&\times\delta\left[Y - Y_{di-hadron} + \ln\frac{\sqrt{M^2_{di-hadron} + \Delta^2}}{M_{di-hadron}} - \ln\left(\sqrt{\frac{z_1}{z_2}}\frac{1+\cos\theta^\star}{2} + \sqrt{\frac{z_2}{z_1}}\times\right.\right. \\
&\left.\left.\times\frac{1-\cos\theta^\star}{2}\right)\right]\delta(M^2 - z_1 z_2 M^2_{di-hadron})\times\delta[\Delta - (z_1 - z_2)\mathrm{P}_\perp]d(M^2)dY dz_1 dz_2
\end{aligned}$$

Performing three integrations and eliminating the δ functions one obtains[12] :

$$\frac{d^4\sigma}{d(M_h^2)dY_h d\Delta d\cos\theta^\star} = \int dz_1 D_{c/H_1}(z_1,Q^2)D_{d/H_2}(z_2,Q^2)\frac{2}{z_1 \mathrm{P}_\perp(z_1+z_2)}\times$$
$$\frac{M^2}{2s}\sum_{a,b,c,d} G_{a/A}(x_a,Q^2)G_{b/B}(x_b,Q^2)\frac{d\sigma_{(a,b\to c,d)}}{d\hat{t}} \tag{6.7}$$

where

$$Y = Y_h + \frac{1}{2}\ln(1+\frac{\Delta^2}{M_h^2}) - \ln(r\cos\theta^\star + \sqrt{1+r^2})$$
$$\sqrt{z_2} = \sqrt{z_1}(\sqrt{1+r^2} - r)$$
$$r = \frac{\Delta}{M_h \sin\theta^\star}$$
$$M = \frac{M_h}{\sqrt{z_1 z_2}}$$
$$\frac{M_h}{\sqrt{s}}e^{|Y|} \leq \sqrt{z_1} \leq min(1, r+\sqrt{1+r^2})$$

and where x_a and x_b are obtained through (6.6)

$$x_a = \sqrt{\frac{M_h^2+\Delta^2}{s z_1 z_2}}\frac{e^{Y_h}}{r\cos\theta^\star + \sqrt{1+r^2}}$$
$$x_b = \frac{r\cos\theta^\star + \sqrt{1+r^2}}{\sqrt{M_h^2+\Delta^2}}\frac{M_h^2}{\sqrt{s z_1 z_2}}e^{Y_h}.$$

6.1.3 Meaning of the Q^2 parameter

In first order approximation $\frac{d\sigma_{(a,b\to c,d)}}{d\hat{t}}$ is calculated in QCD using two body processes of the type depicted in the graphs of figure 6.1. In this approximation there is no Q^2 dependence of the distribution and fragmentation functions. However when the radiative corrections are taken into account, such as for instance

the one in figure 6.2 divergences appears in the calculation. That occurs when the radiated particle is collinear to the incoming parton leg and consequently the internal parton line connected to the previous two becomes 'on shell' (q^2 of the internal line becomes zero). Such configuration in QED would give corrections proportional to $\ln s/m^2_{fermion}$. Since in QCD all the partons are considered massless such correction become infinite (mass singularities). However it can be shown that mass singularities appears all in the same way in all order processes containing a given species of parton and can be factorized out[12]. Consequently they can be absorbed in the distribution and fragmentation functions (which are specified experimentally by measuring, for instance, lepton-nucleon deep inelastic scattering or the $e^+e^- \rightarrow$ *hadrons* process) which acquire a Q^2 dependence and lose their scale invariance.

Q^2 does not have unique definition, being in general a function of the kinematic variables which describe the subprocess. A definition which agrees weil with CCOR[5] and the E711 data[43] is $Q^2 \equiv \mathrm{P}^2_\perp$, where $\mathrm{P}_\perp$ is the transverse momenta of each of the two hadrons. Taking into account the mass singularities produced at all orders of perturbation theory and retaining only the leading logarithmic contributions (leading logarithmic approximation) a logarithmic Q^2 dependence is introduced in the fragmentation and distribution functions. The steps necessary to calculate distribution and fragmentation functions can be summarized as follows : first they are fitted from experimental data at some Q^2_0 reference value. Then the Q^2 logarithmic behaviour is introduced using the Altarelli-Parisi equations for the distribution functions[44] and the analogous ones for the fragmentation functions[45][46].

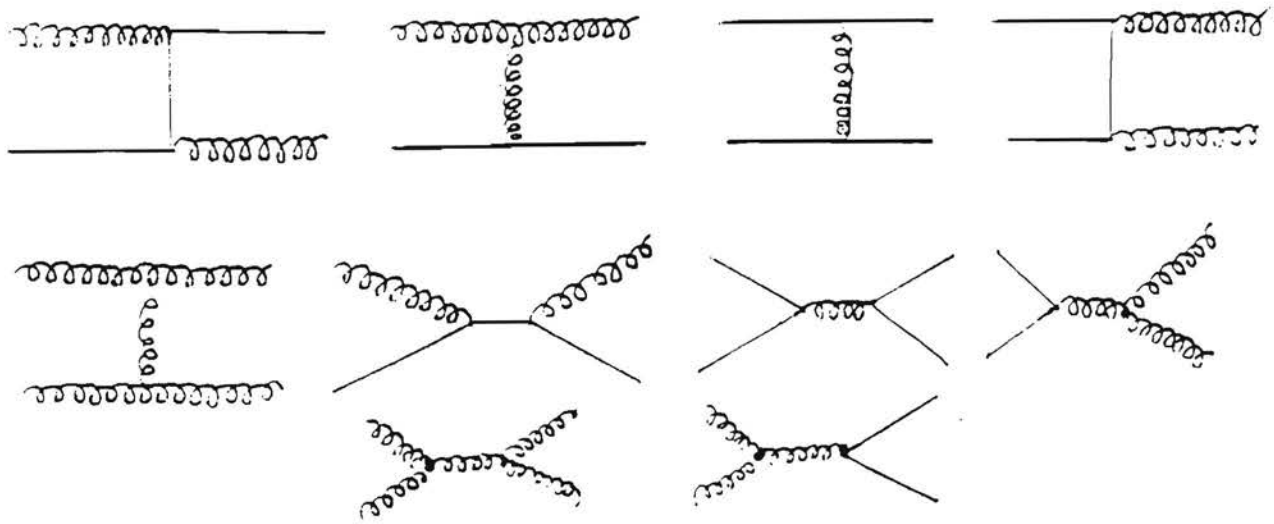

First order Feynman graphs of the parton-parton scattering subprocesses according to QCD

Figure 6.1

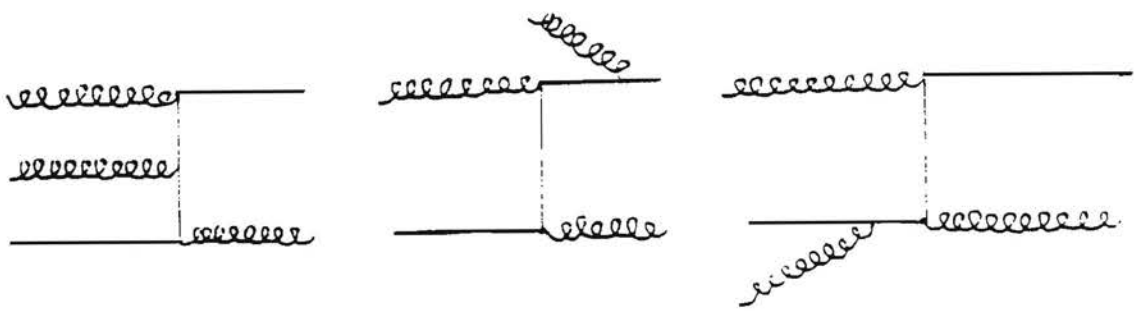

Radiative correction Feynman graphs of the parton-parton scattering subprocesses according to QCD

Figure 6.2

6.1.4 QCD calculation of $\frac{d\sigma}{d\hat{t}}$

The expression, $\frac{d\sigma}{d\hat{t}}$, appearing in (6.3), (6.4), (6.5), (6.7) can be written as

$$\frac{d\sigma_{(a,b\to c,d)}}{d\hat{t}} = \frac{1}{16\pi\hat{s}^2}|\mathcal{M}_{(a,b\to c,d)}|^2 \tag{6.8}$$

where $\mathcal{M}_{(a,b\to c,d)}$ is the scattering matrix element of the parton subprocesses. $\mathcal{M}_{(a,b\to c,d)}$ can be calculated in QCD to first order using the two body scattering processes listed in TABLE 6.1 When higher order terms are taken into account, other divergences, connected to loops graphs appear. They are treated using the dimensional regularization technique[12]. It is also possible to take into account certain vertex and gluon propagators correction replacing the strong coupling constant α with α_s, the strong running coupling constant, which depends on an $[energy]^2$ variable characteristic of the process In the leading logarithmic approximation such a variable can be identified with Q^2 of the fragmentation and distribution functions, namely $Q^2 \equiv \mathrm{P}_\perp$. The expression for α_s is given by[25] :

$$\alpha_s(Q^2) = \frac{12\pi}{(33-2n_f)\ln(Q^2/\Lambda^2)}$$

where n_f is the number of quark flavors, Λ is a scale factor whose order of magnitude is 100 MeV[12]. $\alpha_s(Q^2)$ becomes small when Q^2/Λ is large. Therefore QCD perturbative calculations are meaningful when $\mathrm{P}_\perp$ is much larger than Λ. They were applied successfully to the E711 data[43] in which the minimum $\mathrm{P}_\perp$ of the leading hadrons was $\simeq$ 1 GeV/c . The square of the matrix element $|\mathcal{M}_{(a,b\to c,d)}|^2$ in equations (6.3) and (6.4) can now be expressed as :

$$|\mathcal{M}_{(a,b\to c,d)}|^2 = 16\pi^2\alpha_s^2|\mathcal{A}_{(a,b\to c,d)}|^2 \tag{6.9}$$

where the values of $|\mathcal{A}_{(a,b\to c,d)}|^2$ are listed in TABLE 6.1[26] for the various subprocesses. Finally substituting (6.9) into (6.8) one obtains :

$$\frac{d\sigma_{(a,b\to c,d)}}{d\hat{t}} = \frac{\pi\alpha_s^2}{\hat{s}^2}|\mathcal{A}_{(a,b\to c,d)}|^2.$$

The cross sections measured by E711 agree[43] with the theoretical predictions given by (6.7) in the leading logarithmic approximation, using the distribution functions of ref. [13] set 1, the fragmentation functions given in ref. [47] and the values of $|\mathcal{A}_{(a,b\to c,d)}|^2$ of TABLE 6.1. It is therefore reasonable to continue using this framework to interpret other aspects of high $P_\perp$ particle production.

6.2 Calculation of $< \mathcal{Z} >$

The subject of this dissertation, $< \mathcal{Z} >$, can be calculated theoretically for instance by using (6.5) including the contribution of the fragmentation functions (neglecting the colliding partons Fermi motion) :

$$\frac{d^5\sigma}{dY d(M^2) d\cos\theta^\star dz_1 dz_2} = \frac{M^2}{2s}\sum_{a,b,c,d} G_{a/A}(x_a,Q^2)G_{b/B}(x_b,Q^2)\frac{d\sigma_{(a,b\to c,d)}}{d\hat{t}}\times$$
$$\times D_{c/H_1}(z_1,Q^2)D_{d/H_2}(z_2,Q^2)$$

$< \mathcal{Z} >$ can be expressed by :

$$< \mathcal{Z} > = \frac{1}{2}\left(\frac{\int dY \int d(M^2)\int d\cos\theta^\star \int dz_1 \int dz_2 \frac{d^5\sigma}{dY d(m^2) d\cos\theta^\star dz_1 dz_2} z_2}{\int dY \int d(M^2)\int d\cos\theta^\star \int dz_1 \int dz_2 \frac{d^5\sigma}{dY d(m^2) d\cos\theta^\star dz_1 dz_2}} + \right.$$
$$\left. + \frac{\int dY \int d(M^2)\int d\cos\theta^\star \int dz_2 \int dz_1 \frac{d^5\sigma}{dY d(m^2) d\cos\theta^\star dz_1 dz_2} z_1}{\int dY \int d(M^2)\int d\cos\theta^\star \int dz_1 \int dz_2 \frac{d^5\sigma}{dY d(m^2) d\cos\theta^\star dz_1 dz_2}}\right) \tag{6.10}$$

where the first fraction of the right hand side of (6.10) has the integrals extended over the range of phase space in which the leading hadron 2 was accepted geometrically by the apparatus and also passed all the analysis cuts. The same reasoning is valid for the range of integration of the integrals which appear in the second fraction of the right hand side of (6.10) where the leading hadron 1 contribution to $< \mathcal{Z} >$ is taken into account.

The integrals shown in (6.10) were actually obtain with a montecarlo program[48]. Two leading hadron events were initially generated with the variables x_1, x_2, z_1, z_2, ϕ and $\cos\theta^\star$ thrown randomly with a flat distribution over the kinematic range. x_1 is the Bjorken variable of the colliding parton 1, z_1 is the jet momentum fraction taken by the leading hadron 1, ϕ is the azimuthal angle around the beam axis and $\cos\theta^\star$ is the scattering angle in the parton-parton system. To save computer time, the kinematic range was chosen not to be as large as possible, but only slightly larger than the acceptance limitations of the experimental apparatus. Each event was assigned a weight w proportional to the value of the cross section expressed in the flatly thrown kinematic variables

$$w = \frac{d\sigma}{dx_1 dx_2 dz_1 dz_2 d\cos\theta^\star}$$

in order to reproduce the correct statistical frequency of the events. The generated events were then selected by a program which simulated the acceptance of the apparatus. Finally the accepted events, weighted by w, were used to fill the $< \mathcal{Z} >$ plots which are the theoretical counterpart of the experimental ones. With this procedure the integration described in over the appropriate phase space was performed automatically.

The 'ingredients' used to calculate the theoretical cross sections were

a) the parton-parton cross section calculated to the first order according to the Feynman diagrams calculated in TABLE 6.1

b) structure functions fit to data at a reference value of Q^2 ($Q^2 \equiv P_\perp$) and then evolved according to the Altarelli-Parisi equations. The structure function used were the Duke and Owens, set 1[13];

c) fragmentation functions fit to recently published EMC data [11] at a reference value of Q^2 and then evolved according to [45][46].

The montecarlo technique allowed to use non collinear kinematics for the colliding partons and for the fragmenting ones. A Fermi motion transverse momentum smearing of the colliding partons and a smearing of the leading hadron with respect to the fragmenting parton momentum were used completing the theoretical simulation.

TABLE 6.1

subprocess	cross section
$qq' \to qq'$	$\frac{4}{9}\frac{s^2+u^2}{t^2}$
$qq \to qq$	$\frac{4}{9}\left(\frac{s^2+u^2}{t^2}+\frac{s^2+t^2}{u^2}\right)-\frac{8}{27}\frac{s^2}{tu}$
$q\bar{q} \to q'\bar{q}'$	$\frac{4}{9}\frac{t^2+u^2}{s^2}$
$q\bar{q} \to q\bar{q}$	$\frac{4}{9}\left(\frac{s^2+u^2}{t^2}+\frac{u^2+t^2}{s^2}\right)-\frac{8}{27}\frac{u^2}{st}$
$gq \to gq$	$-\frac{4}{9}\left(\frac{s}{u}+\frac{u}{s}\right)+\frac{s^2+u^2}{t^2}$
$q\bar{q} \to gg$	$\frac{32}{27}\left(\frac{t}{u}+\frac{u}{t}\right)-\frac{8}{3}\frac{t^2+u^2}{s^2}$
$gg \to q\bar{q}$	$\frac{1}{6}\left(\frac{t}{u}+\frac{u}{t}\right)-\frac{3}{8}\frac{t^2+u^2}{s^2}$
$gg \to gg$	$\frac{9}{2}\left(3-\frac{tu}{s^2}-\frac{su}{t^2}-\frac{st}{u^2}\right)$

CHAPTER 7

PHYSICS RESULTS

7.1 Introduction

Having found a method to select a background free data sample of events and to calculate the jet physical quantities, the properties of the fragmentation process can now be studied. The subject of the present dissertation is the study of $< \mathcal{Z} >$ the average fraction of energy of the high $P_\perp$ jet carried by the 'leading hadrons'

$$< \mathcal{Z} > \equiv \left\langle \frac{E_{leading}}{E_{jet}} \right\rangle$$

where $E_{leading}$ is the energy of the 'leading hadron', E_{jet} is the energy of the jet to which it is associated. The energy of the leading hadron was calculated using

the wire chamber information, E_{jet} was calculated measuring the neutral energy of the jet absorbed by the EM section of the calorimeter.

The fragmentation mechanism that determines $< \mathcal{Z} >$, studied so far in collider experiments using lepton-lepton, lepton-hadron and hadron-hadron beams and described according to those experimental results, could be affected by the presence of nuclear forces when heavy targets are used instead of $\overline{p}$, p or leptons. The assumption of the independence of the fragmentation process, which leads to the factorization of the fragmentation functions, could not be valid any more. That hypothesis is checked by comparing the $< \mathcal{Z} >$ versus $\cos\theta^{\star}$ distributions for the different targets (Be, Al, Fe and W). $\cos\theta^{\star}$ is the cosine of the angle between the leading hadron and the beam direction in the C.o.M. frame of the two leading hadrons. The quantity $< \mathcal{Z} >$ is calculated when at least one of the leading particles had its jet cone lying inside the calorimeter sensitive area (the 'single jet' plots) and when both tracks satisfied this cut ('two jets' plots). Then a comparison between the E711 data (all the targets together) and previous data and a comparison between theoretical predictions, according to the QCD-parton model, and the E711 data are made.

7.2 Comparison between different types of targets

In E711 four different targets were used, Be, Al, Fe and W. By comparing results from targets in a wide range of atomic number (A from 9 to 184) the presence of nuclear effects on the fragmentation mechanism can be studied. Those effects would also be reflected in the $< \mathcal{Z} >$ distributions as function of

$\cos\theta^\star$. If these distributions do not show any statistically significant differences the independent fragmentation schemes and factorized parton-parton scattering calculations could be expected to describe the data.

7.2.1 Comparison

In TABLE 7.1 through TABLE 7.4, $< \mathcal{Z} >$ is listed for various $\cos\theta^\star$ ranges and for the different targets. Figures 7.1 and 7.2 show the results for the 'single jet' and 'two jets' events respectively. Within errors, the curves are alike for different targets.

7.2.2 Conclusions

The conclusion which can be drawn from the above results is that experimentally the fragmentation process of a parton into a jet in high $P_\perp$ reactions is independent of nuclear effects. This conclusion is in harmony with the A dependence exponent α, being consistent with 1, found in a previous analysis of the E711 data[43]. Consequently, from now on the $< \mathcal{Z} >$ data will be shown and discussed all together, with no distinction among the different targets.

7.3 Comparison between previous data

The E711 data can be compared with data collected in previous experiments. The CCOR collaboration[5] performed an experiment at CERN, at the ISR where

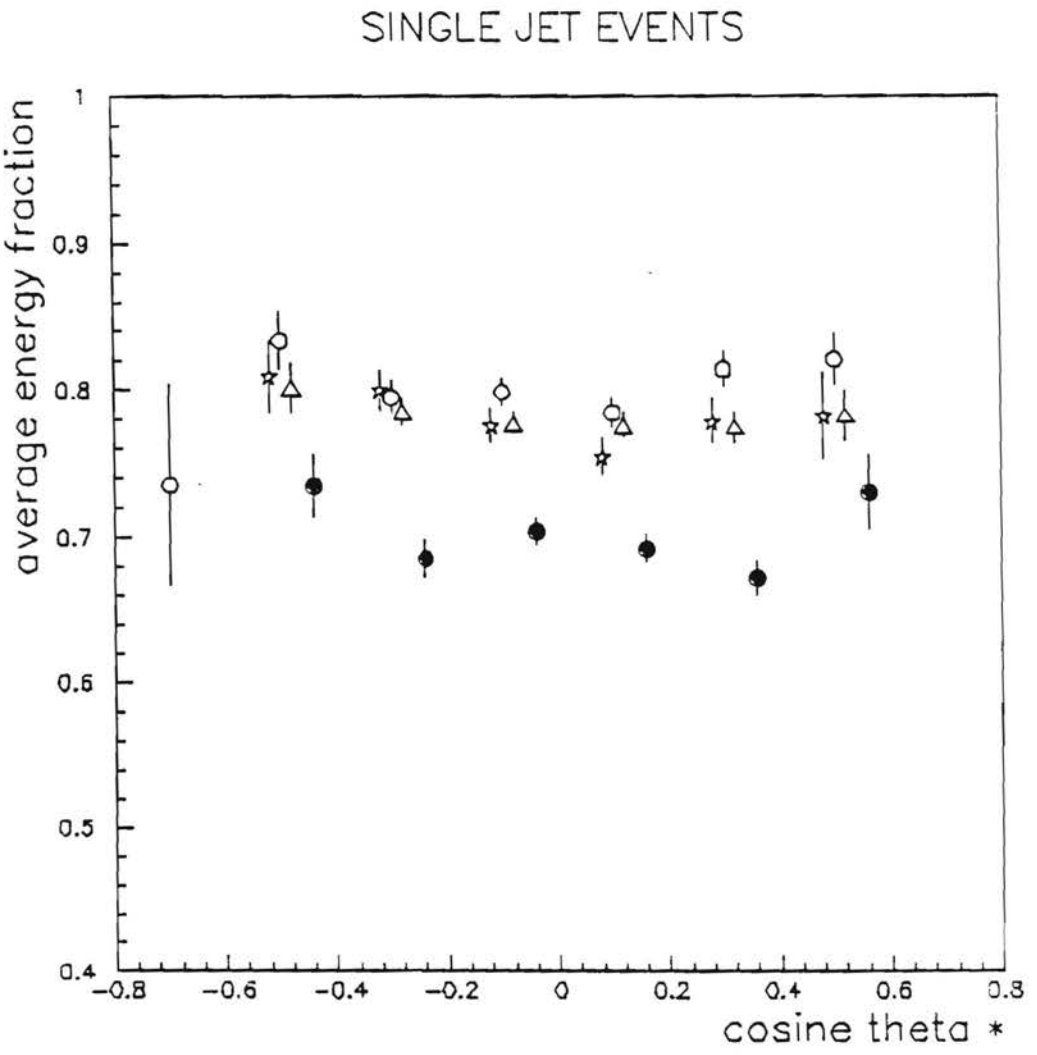

$< \mathcal{Z} >$, function of $\cos\theta^\star$ for different targets and single jet events

- ○ Be target
- ⋆ Al target
- △ Fe target
- ● W target

Figure 7.1

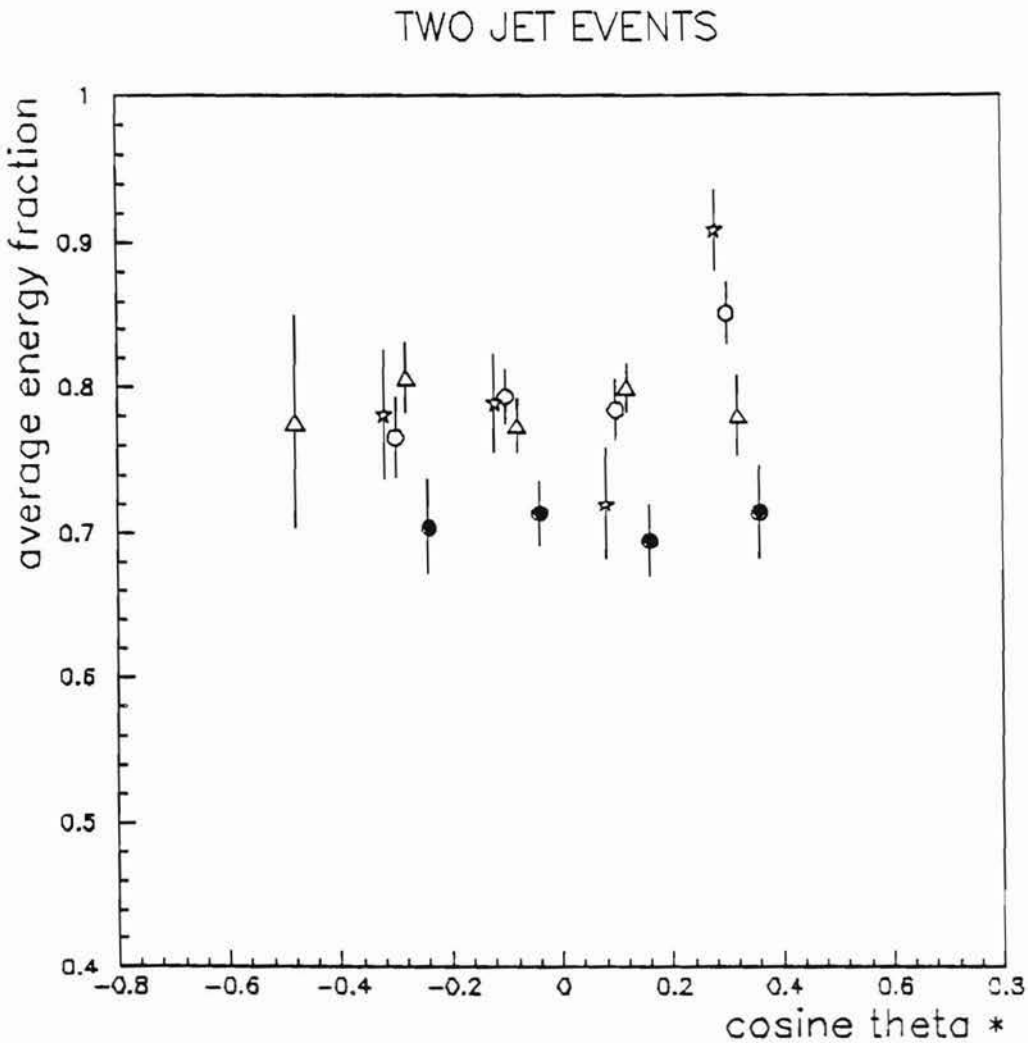

$< \mathcal{Z} >$ as a function of $\cos\theta^\star$ for different targets and two jet events

o Be target

⋆ Al target

△ Fe target

• W target

Figure 7.2

TABLE 7.1

List of $< \mathcal{Z} >$ as a function of $\cos\theta^{\star}$of the leading hadron for Be target

$\cos\theta^{\star}$ leading range	$< \mathcal{Z} > \pm sys. \pm stat.$ single jet	entries in plot	$\sigma_{\mathcal{Z}}$
-0.8 - -0.6	$0.7357 \pm 0.0237 \pm 0.0645$	7	0.1706
-0.6 - -0.4	$0.8340 \pm 0.0063 \pm 0.0189$	86	0.1752
-0.4 - -0.2	$0.7953 \pm 0.0026 \pm 0.0111$	233	0.1693
-0.2 - 0.0	$0.7991 \pm 0.0021 \pm 0.0087$	366	0.1664
0.0 - 0.2	$0.7852 \pm 0.0021 \pm 0.0094$	357	0.1776
0.2 - 0.4	$0.8147 \pm 0.0015 \pm 0.0120$	187	0.1641
0.4 - 0.6	$0.8217 \pm 0.0042 \pm 0.0170$	63	0.1350
0.6 - 0.8	$0.0000 \pm 0.0000 \pm 0.0000$	0	0.0000

$\cos\theta^{\star}$ leading range	$< \mathcal{Z} > \pm sys. \pm stat.$ two jets	entries in plot	$\sigma_{\mathcal{Z}}$
-0.8 - -0.6	$0.0000 \pm 0.0000 \pm 0.0000$	0	0.0000
-0.6 - -0.4	$0.0000 \pm 0.0000 \pm 0.0000$	0	0.0000
-0.4 - -0.2	$0.7661 \pm 0.0065 \pm 0.0267$	41	0.1712
-0.2 - 0.0	$0.7939 \pm 0.0036 \pm 0.0184$	83	0.1674
0.0 - 0.2	$0.7848 \pm 0.0040 \pm 0.0204$	73	0.1747
0.2 - 0.4	$0.8514 \pm 0.0090 \pm 0.0198$	29	0.1066
0.4 - 0.6	$0.0000 \pm 0.0000 \pm 0.0000$	0	0.0000
0.6 - 0.8	$0.0000 \pm 0.0000 \pm 0.0000$	0	0.0000

TABLE 7.2

List of $< \mathcal{Z} >$ as a function of $\cos\theta^{\star}$of the leading hadron for Al target

$\cos\theta^{\star}$ leading range	$< \mathcal{Z} > \pm sys. \pm stat.$ single jet	entries in plot	$\sigma_{\mathcal{Z}}$
-0.8 - -0.6	$0.0000 \pm 0.0000 \pm 0.0000$	0	0.0000
-0.6 - -0.4	$0.8095 \pm 0.0080 \pm 0.0238$	37	0.1447
-0.4 - -0.2	$0.8001 \pm 0.0029 \pm 0.0138$	156	0.1721
-0.2 - 0.0	$0.7766 \pm 0.0023 \pm 0.0121$	210	0.1750
0.0 - 0.2	$0.7555 \pm 0.0023 \pm 0.0128$	221	0.1899
0.2 - 0.4	$0.7796 \pm 0.0020 \pm 0.0155$	131	0.1777
0.4 - 0.6	$0.7826 \pm 0.0068 \pm 0.0288$	38	0.1773
0.6 - 0.8	$0.0000 \pm 0.0000 \pm 0.0000$	0	0.0000

$\cos\theta^{\star}$ leading range	$< \mathcal{Z} > \pm sys. \pm stat.$ two jets	entries in plot	$\sigma_{\mathcal{Z}}$
-0.8 - -0.6	$0.0000 \pm 0.0000 \pm 0.0000$	0	0.0000
-0.6 - -0.4	$0.0000 \pm 0.0000 \pm 0.0000$	0	0.0000
-0.4 - -0.2	$0.7822 \pm 0.0111 \pm 0.0428$	23	0.2055
-0.2 - 0.0	$0.7900 \pm 0.0079 \pm 0.0321$	32	0.1817
0.0 - 0.2	$0.7209 \pm 0.0079 \pm 0.0368$	33	0.2116
0.2 - 0.4	$0.9086 \pm 0.0188 \pm 0.0198$	14	0.0742
0.4 - 0.6	$0.0000 \pm 0.0000 \pm 0.0000$	0	0.0000
0.6 - 0.8	$0.0000 \pm 0.0000 \pm 0.0000$	0	0.0000

TABLE 7.3

List of $< \mathcal{Z} >$ as a function of $\cos\theta^{\star}$of the leading hadron for Fe target

$\cos\theta^{\star}$ leading range	$< \mathcal{Z} > \pm sys. \pm stat.$ single jet	entries in plot	$\sigma_{\mathcal{Z}}$
-0.8 - -0.6	$0.0000 \pm 0.0000 \pm 0.0000$	0	0.0000
-0.6 - -0.4	$0.8019 \pm 0.0061 \pm 0.0163$	101	0.1641
-0.4 - -0.2	$0.7858 \pm 0.0025 \pm 0.0096$	329	0.1747
-0.2 - 0.0	$0.7783 \pm 0.0020 \pm 0.0076$	518	0.1718
0.0 - 0.2	$0.7766 \pm 0.0021 \pm 0.0083$	466	0.1794
0.2 - 0.4	$0.7758 \pm 0.0011 \pm 0.0107$	271	0.1756
0.4 - 0.6	$0.7837 \pm 0.0033 \pm 0.0171$	86	0.1588
0.6 - 0.8	$0.0000 \pm 0.0000 \pm 0.0000$	0	0.0000

$\cos\theta^{\star}$ leading range	$< \mathcal{Z} > \pm sys. \pm stat.$ two jets	entries in plot	$\sigma_{\mathcal{Z}}$
-0.8 - -0.6	$0.0000 \pm 0.0000 \pm 0.0000$	0	0.0000
-0.6 - -0.4	$0.7767 \pm 0.0379 \pm 0.0623$	6	0.1526
-0.4 - -0.2	$0.8071 \pm 0.0055 \pm 0.0233$	49	0.1630
-0.2 - 0.0	$0.7744 \pm 0.0031 \pm 0.0175$	101	0.1755
0.0 - 0.2	$0.8004 \pm 0.0033 \pm 0.0164$	100	0.1644
0.2 - 0.4	$0.7812 \pm 0.0074 \pm 0.0260$	34	0.1518
0.4 - 0.6	$0.0000 \pm 0.0000 \pm 0.0000$	0	0.0000
0.6 - 0.8	$0.0000 \pm 0.0000 \pm 0.0000$	0	0.0000

TABLE 7.4

List of $< \mathcal{Z} >$ as a function of $\cos\theta^{\star}$of the leading hadron for W target

$\cos\theta^{\star}$ leading range	$< \mathcal{Z} > \pm sys. \pm stat.$ single jet	entries in plot	$\sigma_{\mathcal{Z}}$
-0.8 - -0.6	$0.0000 \pm 0.0000 \pm 0.0000$	0	0.0000
-0.6 - -0.4	$0.7350 \pm 0.0062 \pm 0.0203$	88	0.1901
-0.4 - -0.2	$0.6858 \pm 0.0025 \pm 0.0129$	293	0.2210
-0.2 - 0.0	$0.7045 \pm 0.0020 \pm 0.0092$	434	0.1913
0.0 - 0.2	$0.6927 \pm 0.0021 \pm 0.0100$	367	0.1921
0.2 - 0.4	$0.6723 \pm 0.0012 \pm 0.0122$	251	0.1939
0.4 - 0.6	$0.7308 \pm 0.0052 \pm 0.0250$	49	0.1749
0.6 - 0.8	$0.0000 \pm 0.0000 \pm 0.0000$	0	0.0000

$\cos\theta^{\star}$ leading range	$< \mathcal{Z} > \pm sys. \pm stat.$ two jets	entries in plot	$\sigma_{\mathcal{Z}}$
-0.8 - -0.6	$0.0000 \pm 0.0000 \pm 0.0000$	0	0.0000
-0.6 - -0.4	$0.0000 \pm 0.0000 \pm 0.0000$	0	0.0000
-0.4 - -0.2	$0.7045 \pm 0.0061 \pm 0.0320$	44	0.2119
-0.2 - 0.0	$0.7143 \pm 0.0034 \pm 0.0216$	88	0.2024
0.0 - 0.2	$0.6955 \pm 0.0046 \pm 0.0248$	62	0.1952
0.2 - 0.4	$0.7150 \pm 0.0080 \pm 0.0315$	32	0.1783
0.4 - 0.6	$0.0000 \pm 0.0000 \pm 0.0000$	0	0.0000
0.6 - 0.8	$0.0000 \pm 0.0000 \pm 0.0000$	0	0.0000

they studied events in which at least one π° with high $P_\perp$ was produced in a colliding beam experiment and collected data for different reaction C.o.M. energies : 31.0 GeV , 44.8 GeV and 62.4 GeV . They presented the $< \mathcal{Z} >$ inclusive plot at different ranges of $P_\perp$ of the leading π°s for single particle inclusive triggers (figure 7.3) and the same when $M_{di-hadron} > 8.$ GeV/c^2 (figure 7.4) requiring that two π°s at high and opposite $P_\perp$ were detected. They also presented the inclusive plot of $< \mathcal{Z} >$ for different $x_\perp (\equiv \frac{2P_\perp}{\sqrt{s}})$ ranges from the single particle inclusive sample (figure 7.5) and for symmetric pair data when $M_{di-hadron} > 8.$ GeV/c^2 (figure 7.6). The E711 data (38.7 GeV C.o.M. of the reaction energy) is shown by black circles superimposed upon the same plots. They are the 'single jet' events, all the targets, in figures 7.3 and 7.5 and the 'two jets' events (all the targets) in the other figures. There is a general agreement in the $< \mathcal{Z} >$ versus $P_\perp$ plots and a good agreement in figures 7.5 and 7.6. This agreement strengthens the nuclear independence hypothesis and the validity of the independent fragmentation (i.e. factorization) as the CCOR data was taken with proton-proton interactions.

7.4 Comparison between the E711 data and theory

7.4.1 Theoretical predictions

The theoretical predictions were obtain with the montecarlo program described in 6.2. The generated events were then selected by a program which simulated the acceptance of the apparatus. The accepted events were used to fill the $< \mathcal{Z} >$ plots which are the theoretical counterpart of the experimental ones.

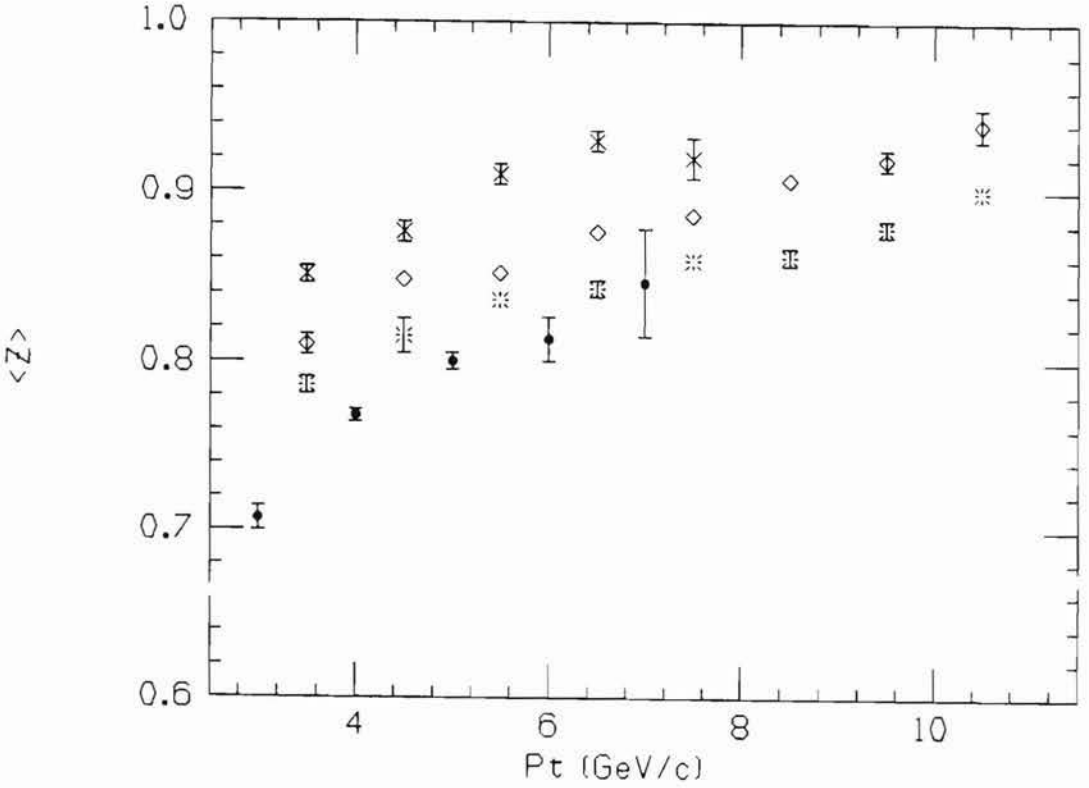

Comparison between the inclusive CCOR[24] data with single π° detected and the E711 data. Plot of $< \mathcal{Z} >$ versus $P_\perp$ of the leading hadron

× CCOR data at $\sqrt{s} = 31$ GeV

◇ CCOR data at $\sqrt{s} = 44.8$ GeV

* CCOR data at $\sqrt{s} = 62.4$ GeV

• E711 data at $\sqrt{s} = 38.7$ GeV

Figure 7.3

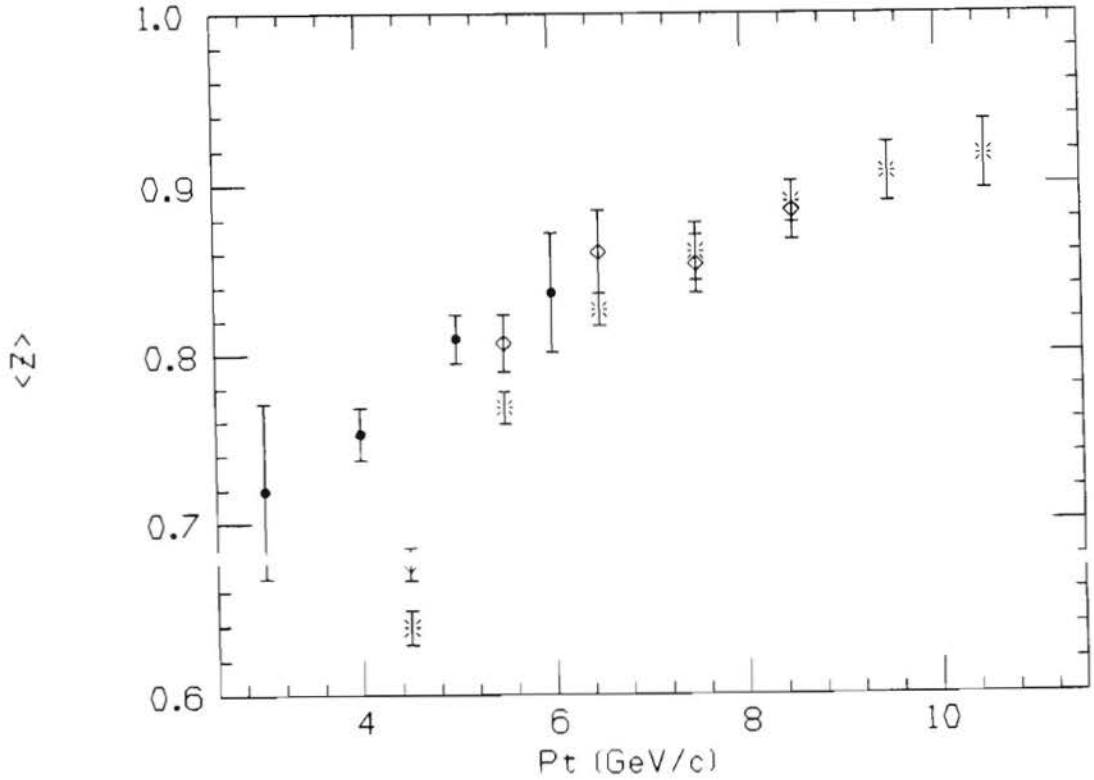

Comparison between the CCOR[24] data with two π° detected and $M_{\pi^\circ\pi^\circ} > 8$ GeV/c^2 and the E711 data. Plot of $< \mathcal{Z} >$ versus $P_\perp$ of the leading hadron

◇ CCOR data at $\sqrt{s} = 44.8$ GeV

* CCOR data at $\sqrt{s} = 62.4$ GeV

• E711 data at $\sqrt{s} = 38.7$ GeV

Figure 7.4

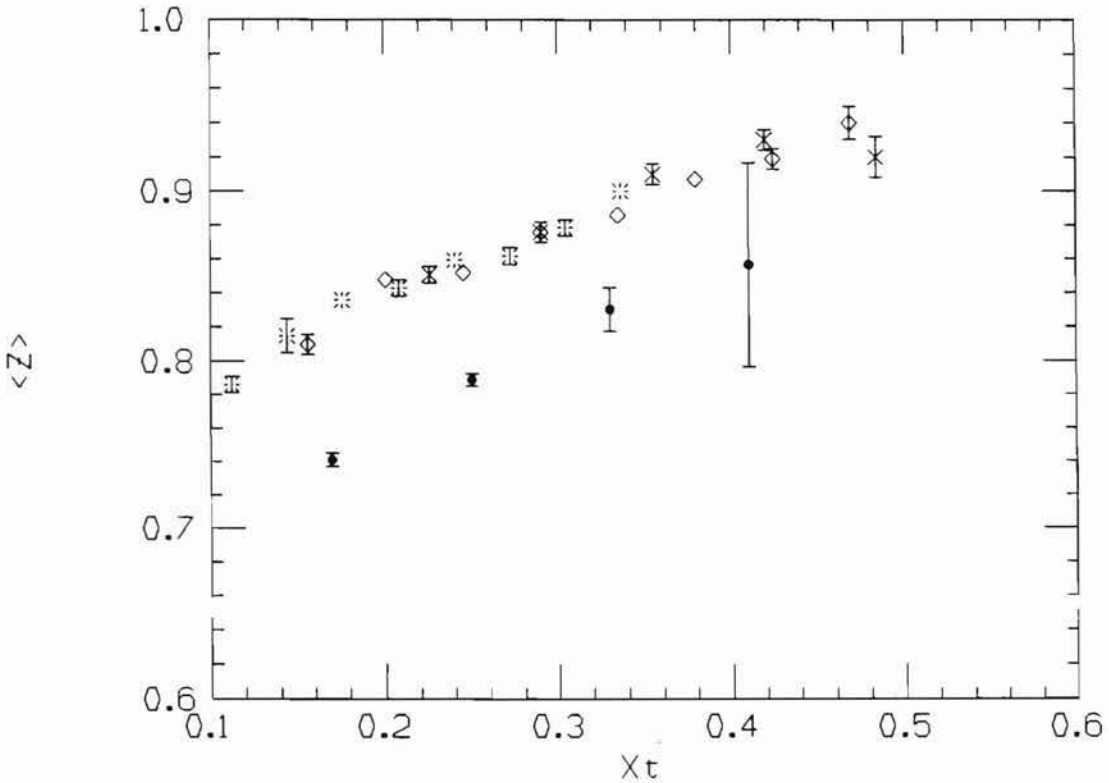

Comparison between the inclusive CCOR[24] data with single π° detected and the E711 data. Plot of $< \mathcal{Z} >$ versus $x_\perp$ of the leading hadron

× CCOR data at $\sqrt{s} = 31$ GeV

◇ CCOR data at $\sqrt{s} = 44.8$ GeV

∗ CCOR data at $\sqrt{s} = 62.4$ GeV

• E711 data at $\sqrt{s} = 38.7$ GeV

Figure 7.5

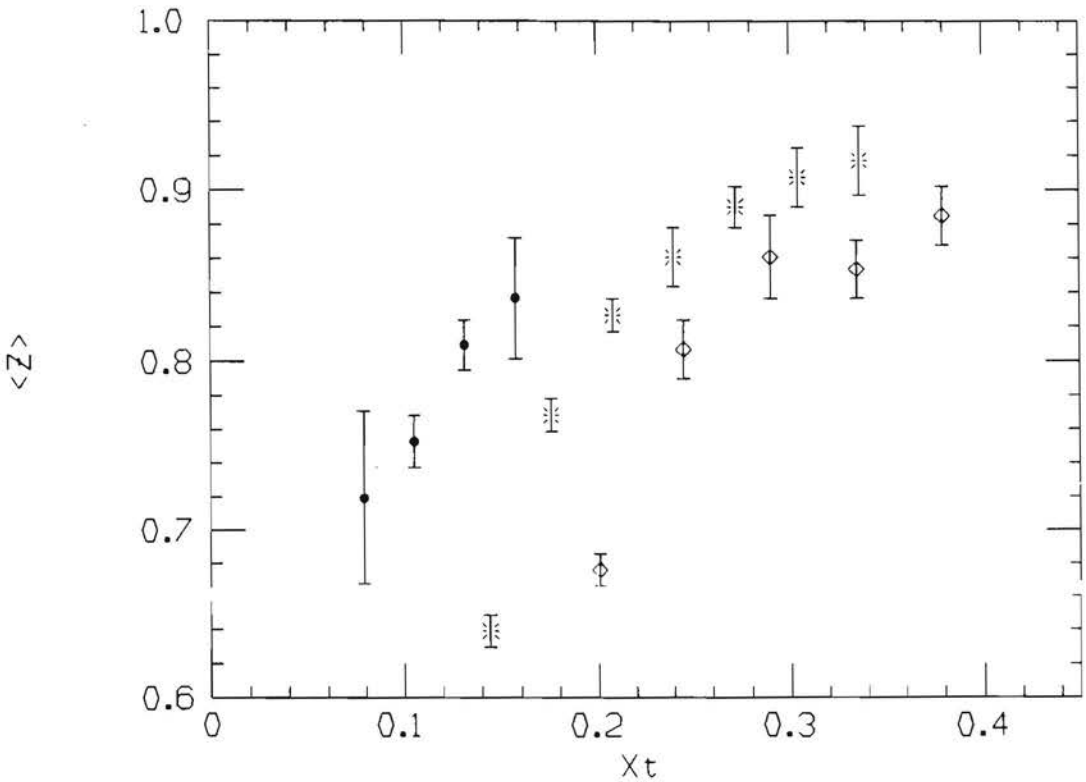

Comparison between the CCOR[24] data with two π° detected and $M_{\pi^\circ\pi^\circ} > 8$ GeV/c^2 and the E711 data. Plot of $< \mathcal{Z} >$ versus $x_\perp$ of the leading hadron

◇ CCOR data at $\sqrt{s} = 44.8$ GeV

∗ CCOR data at $\sqrt{s} = 62.4$ GeV

• E711 data at $\sqrt{s} = 38.7$ GeV

Figure 7.6

7.4.2 Data plots and theoretical comparison

The data are shown for all the targets together. The quantity $< \mathcal{Z} >$ is plotted as a function of $P_\perp$ (figures 7.7 through 7.12), $\cos\theta^\star$ (figures 7.13 through 7.18) and versus $\cos\theta^\star$ in selected bins of $M_{di-hadron}$ (figures 7.19 through 7.42). The data shown are 'single jet' and 'two jets' events when the hadron has positive charge, negative charge and either one. In all the figures black circles represent the data, while open triangles show the theoretical predictions. Errors bars on the experimental data are the square root of the statistical and systematic errors added in quadrature.

7.4.3 Conclusions

In general the theoretical distribution agree with the data. Moreover the following conclusions can be drawn from the inspection of the experimental plots :

a) the fragmentation process is independent of the amount of nuclear matter crossed. This can be seen by the essential flatness of the $< \mathcal{Z} >$ plot as a function of $\cos\theta^\star$ and is also demonstrated by the lack of a nuclear dependence effect on the fragmentation process;

b) the point stressed in a) is confirmed by the flatness of the plot $< \mathcal{Z} >$ versus $\cos\theta^\star$ for various $M_{di-hadron}$ slices (figures 7.19 through 7.42);

c) $< \mathcal{Z} >$ does depend on $P_\perp$ in agreement with the predictions of the QCD parton model described in chapter 6;

d) the agreement between the present data and the previous experimental results from *pp* interactions confirms the independence of the fragmentation process from nuclear effects in high $P_{\perp}$ interactions.

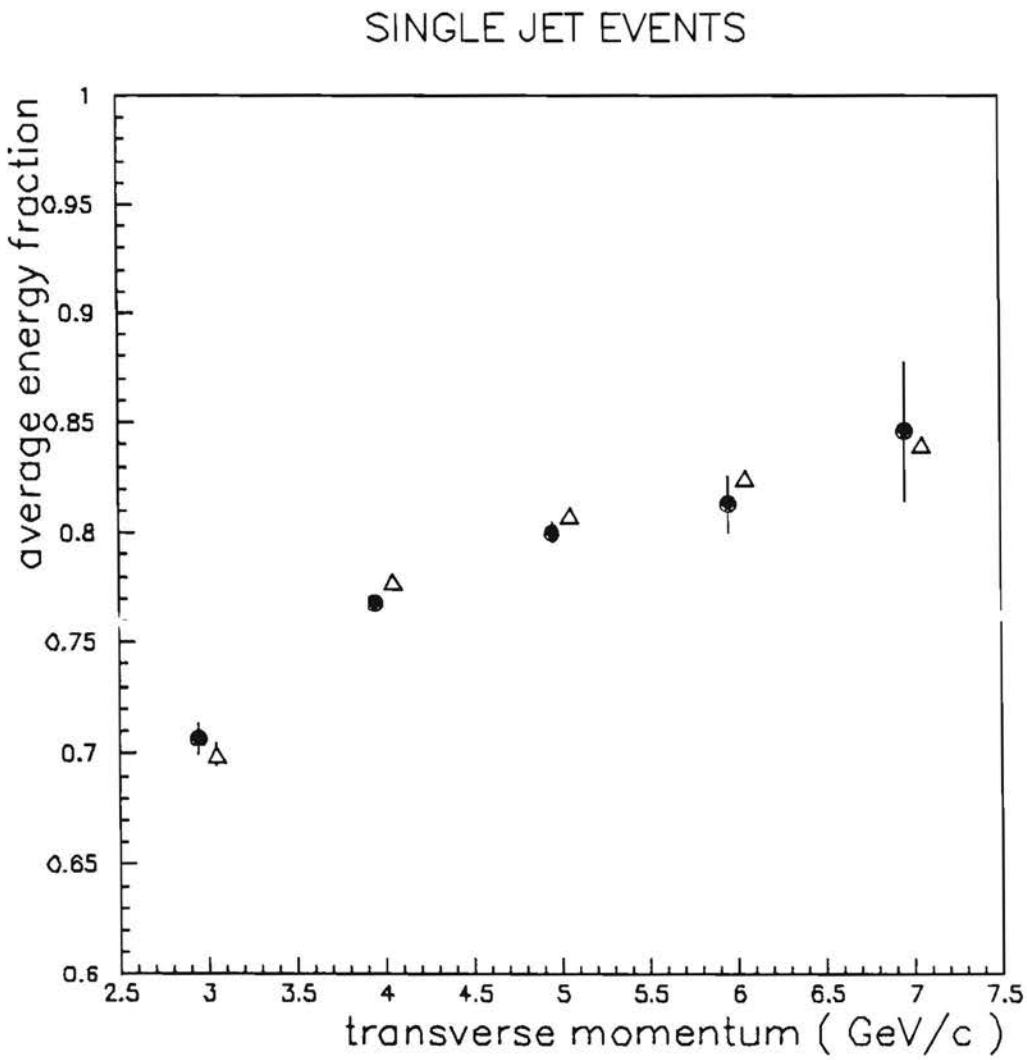

$< z >$, function of $P_\perp$ of the leading hadron for single jet events

• experimental data

△ theoretical predictions

Figure 7.7

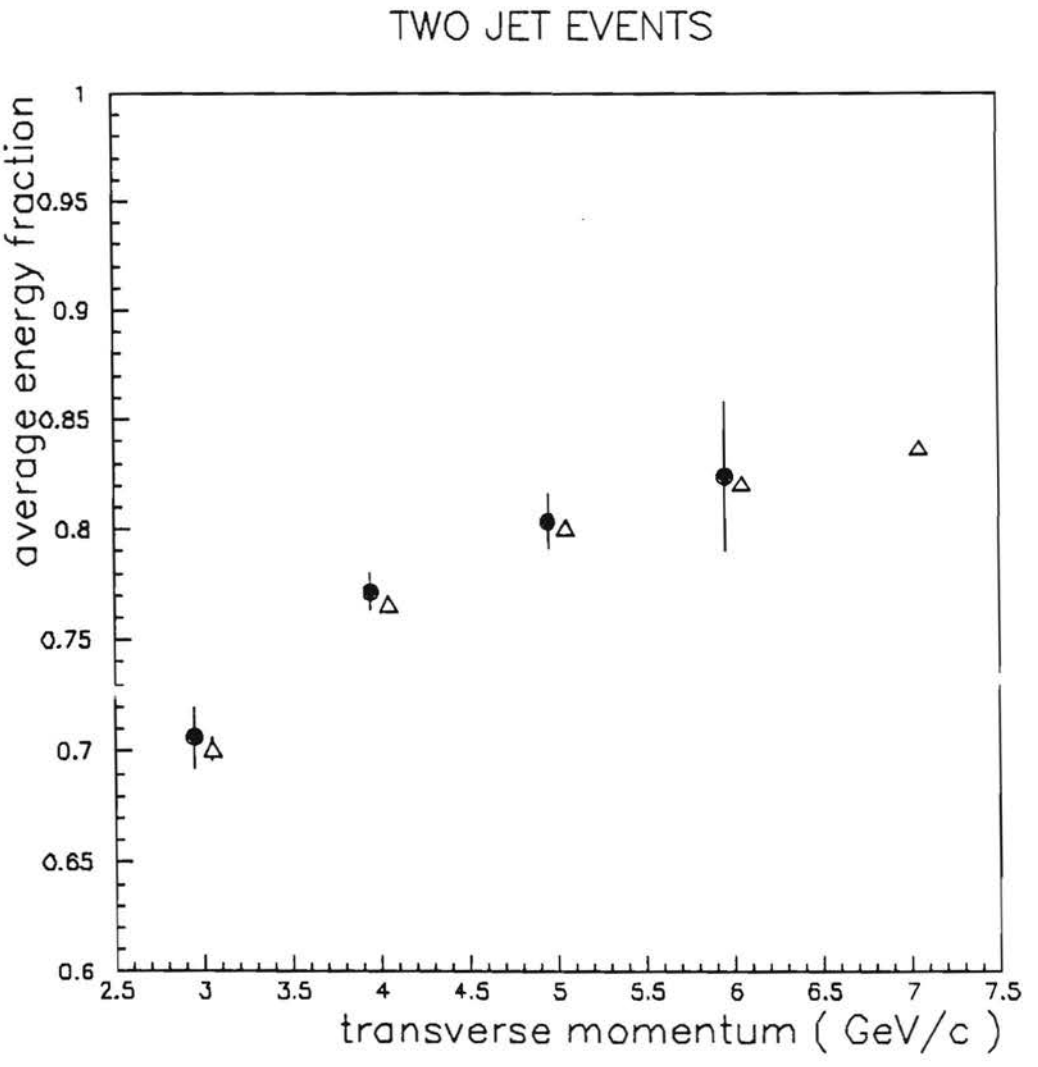

$< \mathcal{Z} >$, function of $P_\perp$ of the leading hadron for two jet events

● experimental data

△ theoretical predictions

Figure 7.8

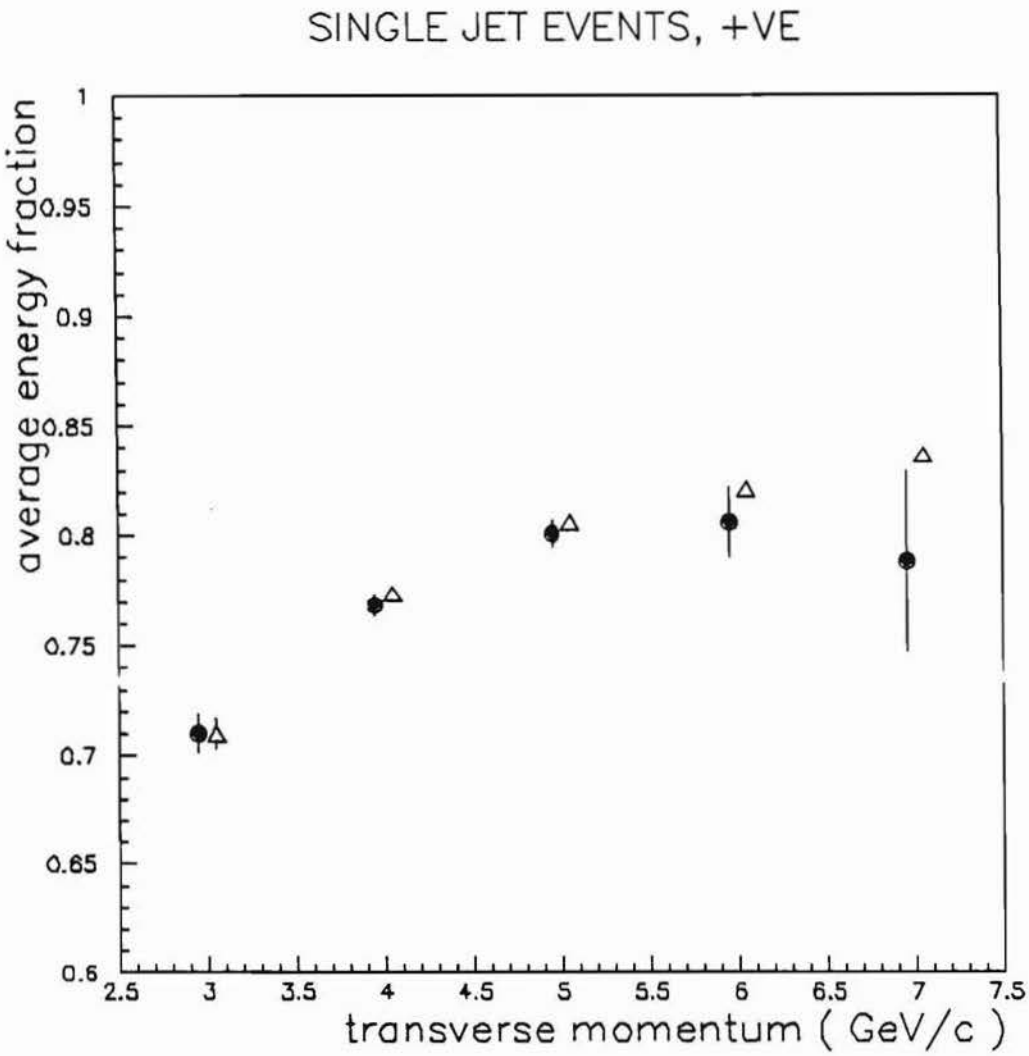

$< z >$, function of $P_\perp$ of the leading hadron for single jet events and positive leading hadron charge

- • experimental data
- △ theoretical predictions

Figure 7.9

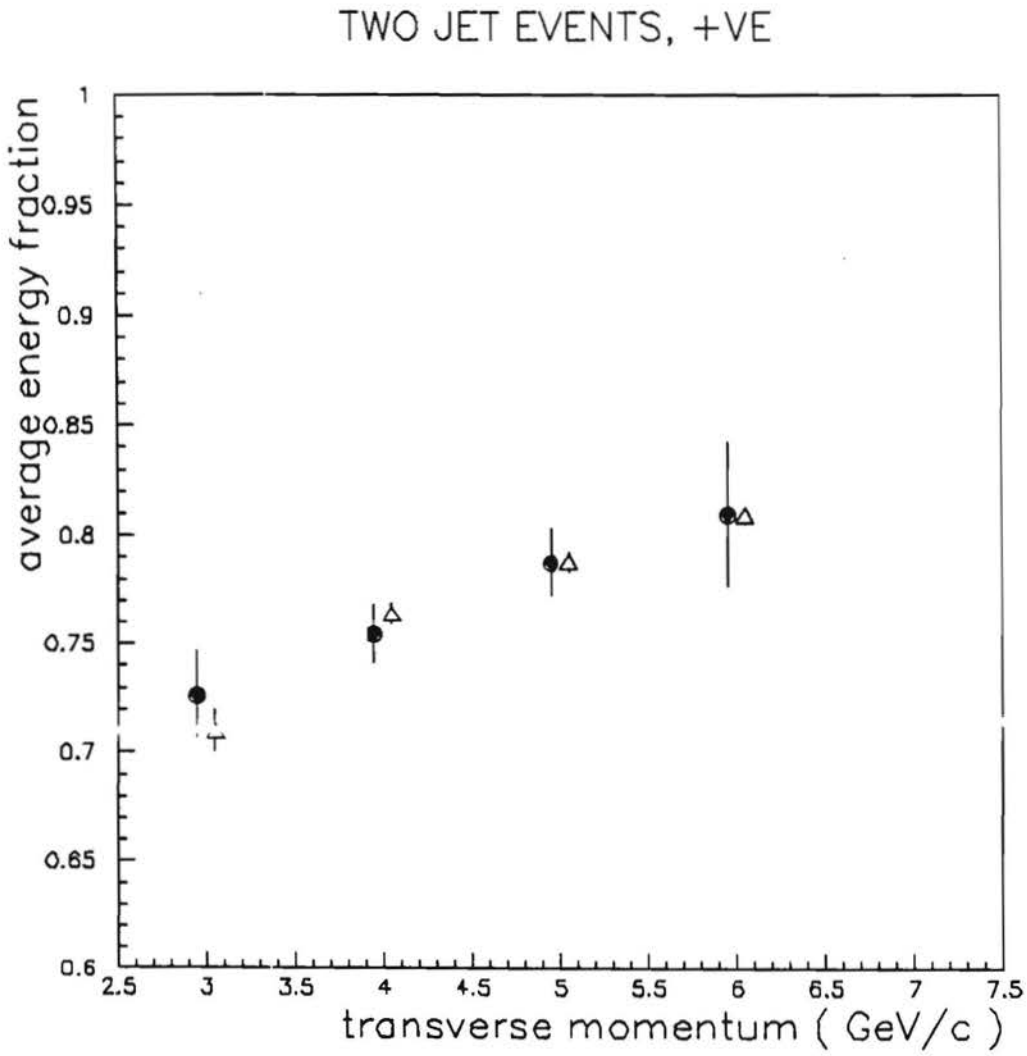

$< \mathcal{Z} >$, function of $P_\perp$ of the leading hadron for two jet events and positive leading hadron charge

- • experimental data
- △ theoretical predictions

Figure 7.10

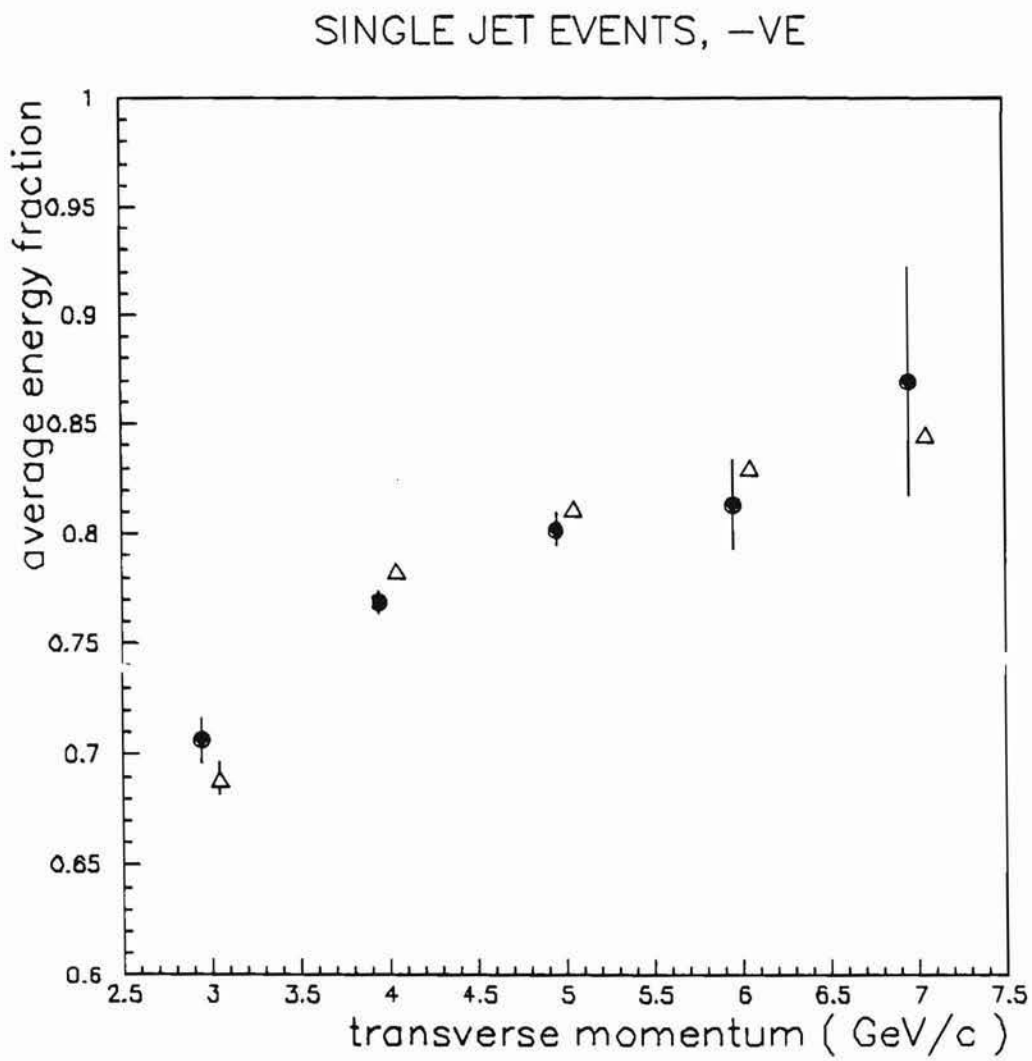

$< z >$, function of $P_\perp$ of the leading hadron for single jet events and negative leading hadron charge

- • experimental data
- △ theoretical predictions

Figure 7.11

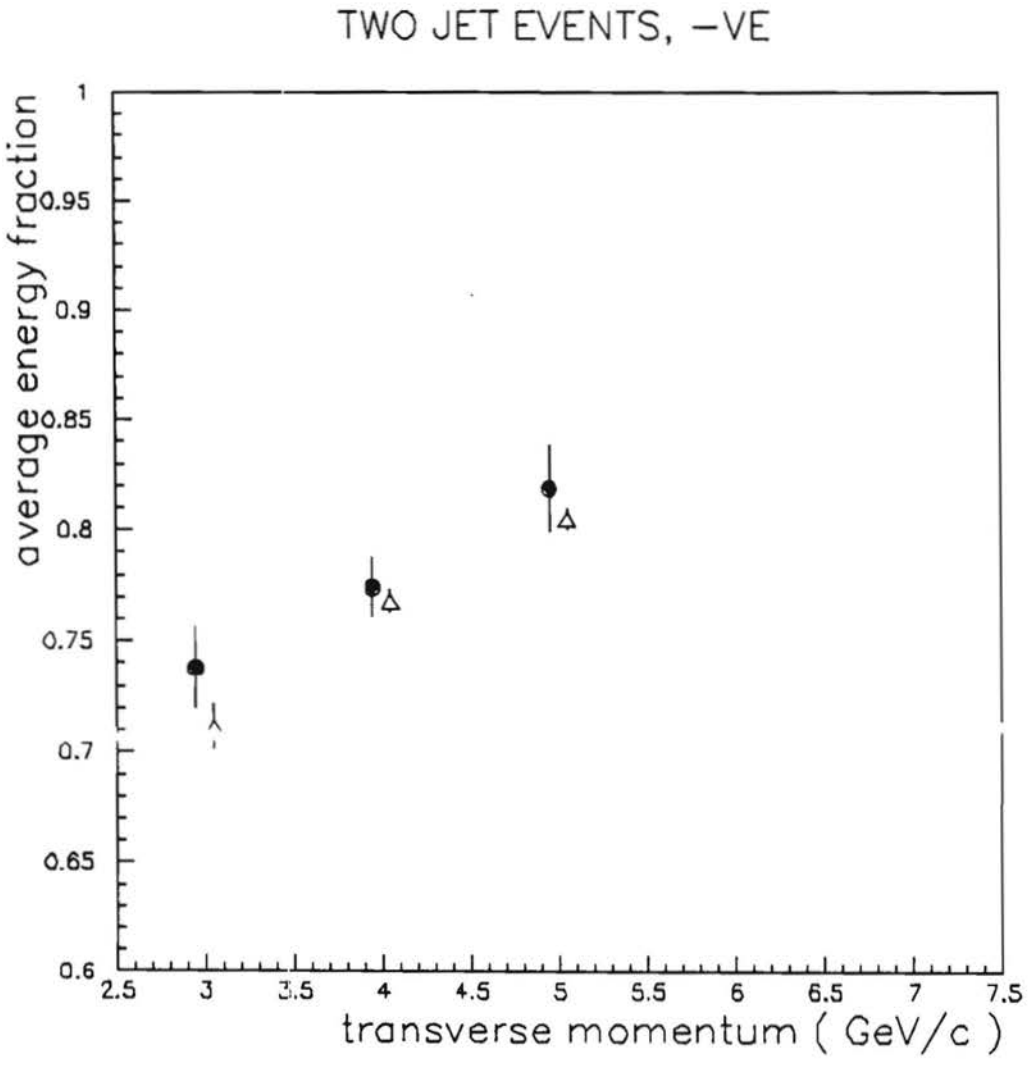

$< \mathcal{Z} >$, function of $P_\perp$ of the leading hadron for two jet events and negative leading hadron charge

- ● experimental data
- △ theoretical predictions

Figure 7.12

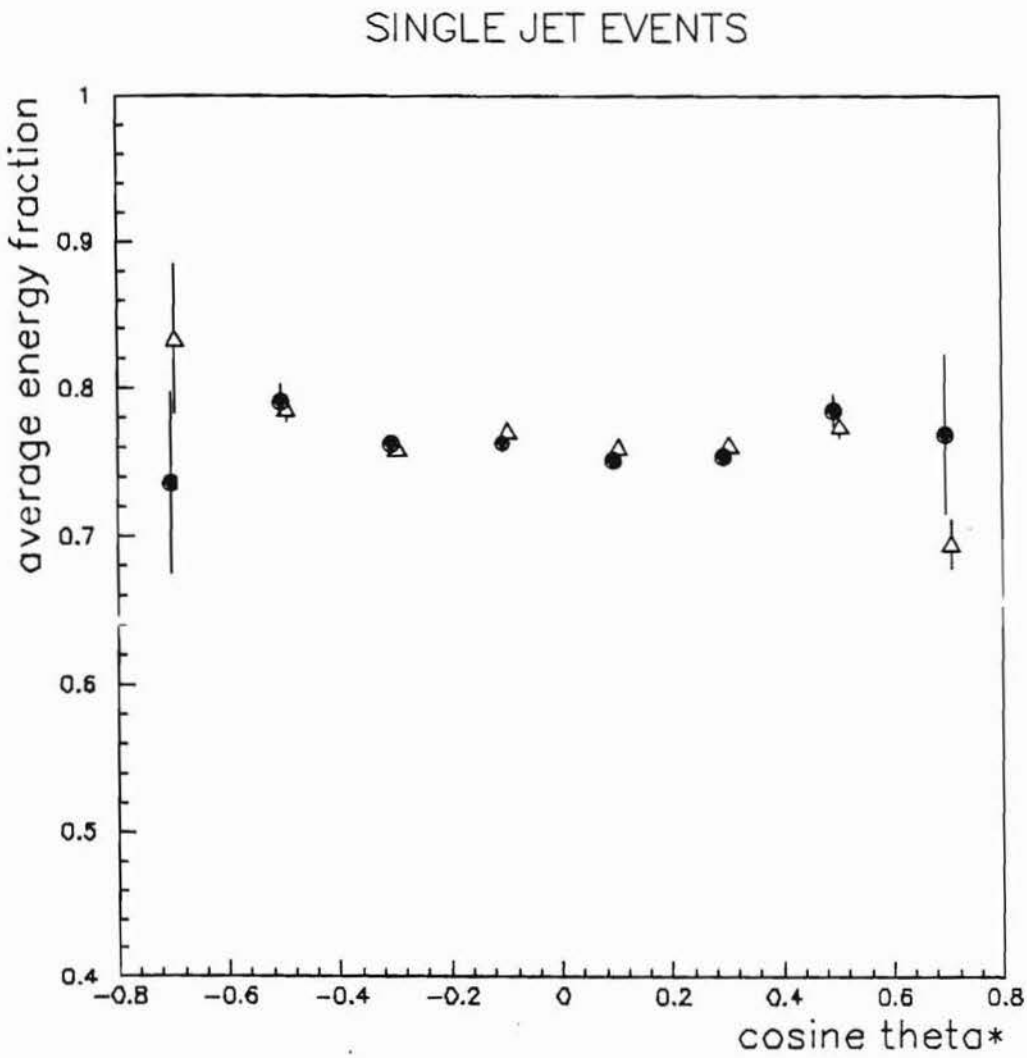

$< z >$, function of $\cos\theta^*$ of the leading hadron for single jet events

• experimental data

△ theoretical predictions

Figure 7.13

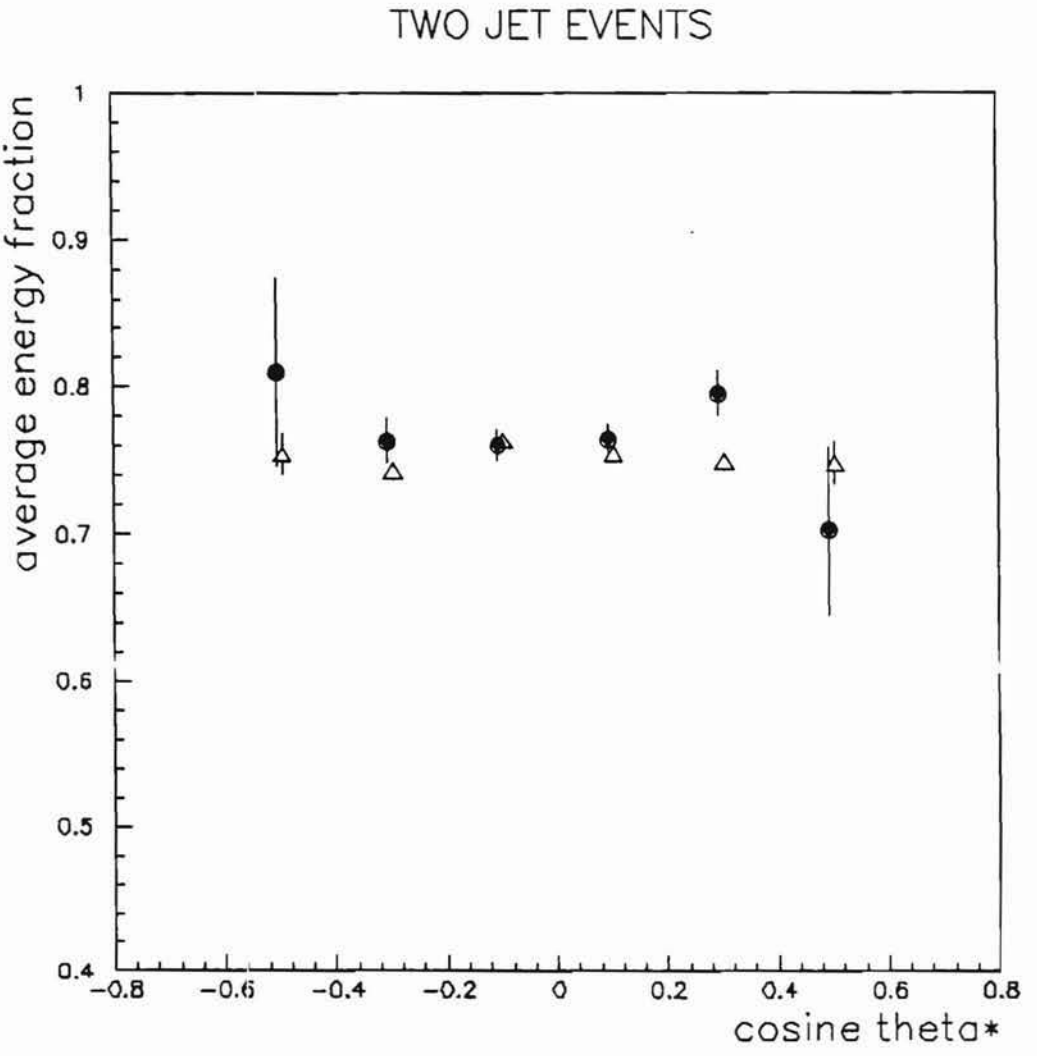

$< \mathcal{Z} >$, function of $\cos\theta^\star$ of the leading hadron for two jet events

• experimental data

△ theoretical predictions

Figure 7.14

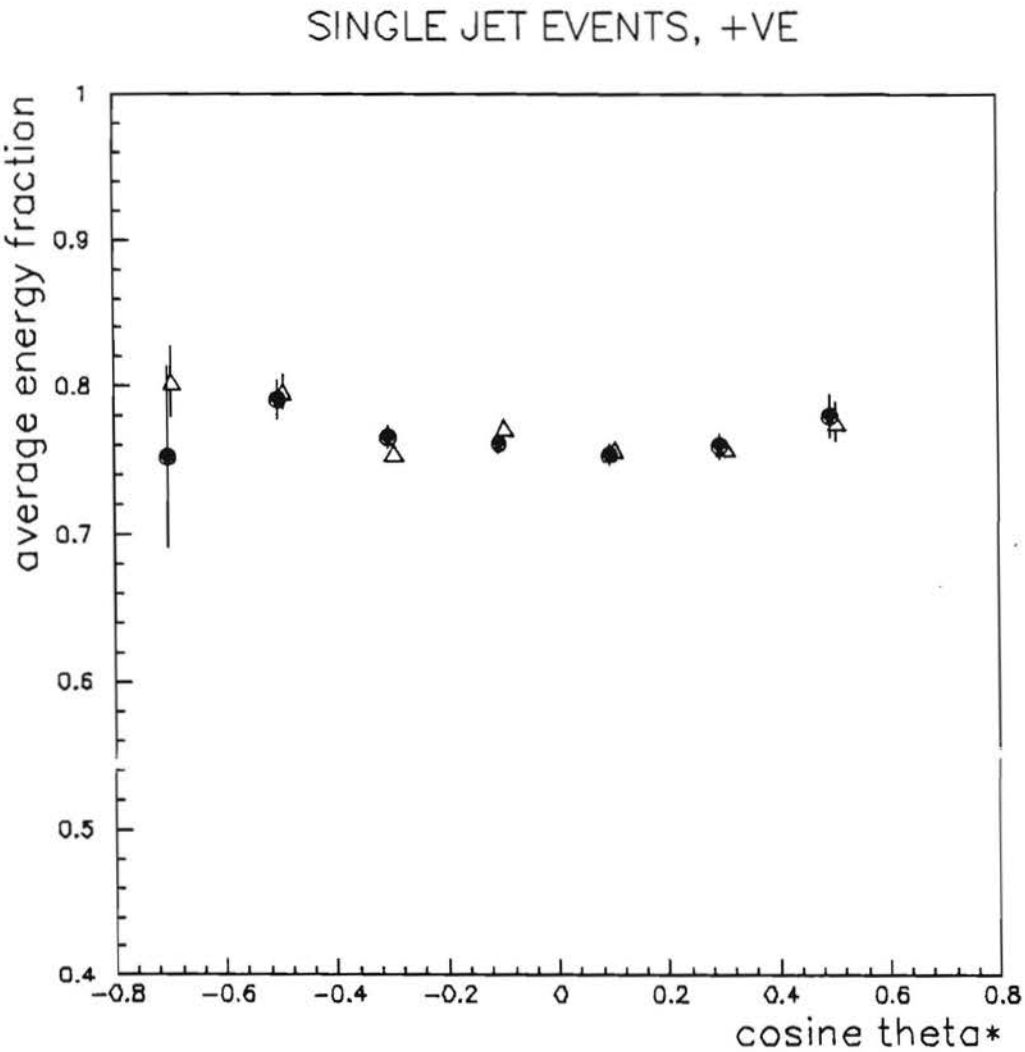

$< \mathcal{Z} >$, function of $\cos\theta^\star$ of the leading hadron for single jet events and positive leading hadron charge

- • experimental data
- △ theoretical predictions

Figure 7.15

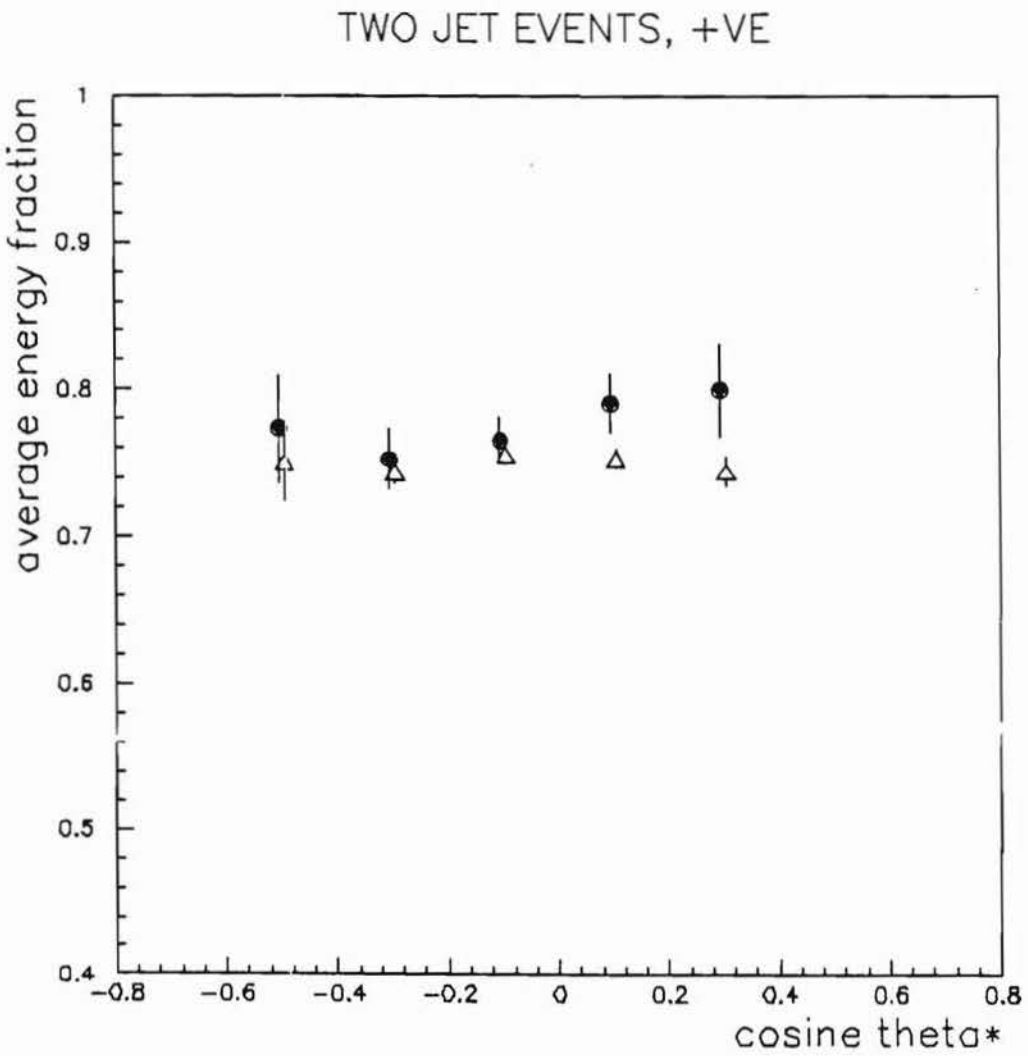

$< \mathcal{Z} >$, function of $\cos\theta^*$ of the leading hadron for two jet events and positive leading hadron charge

- • experimental data
- △ theoretical predictions

Figure 7.16

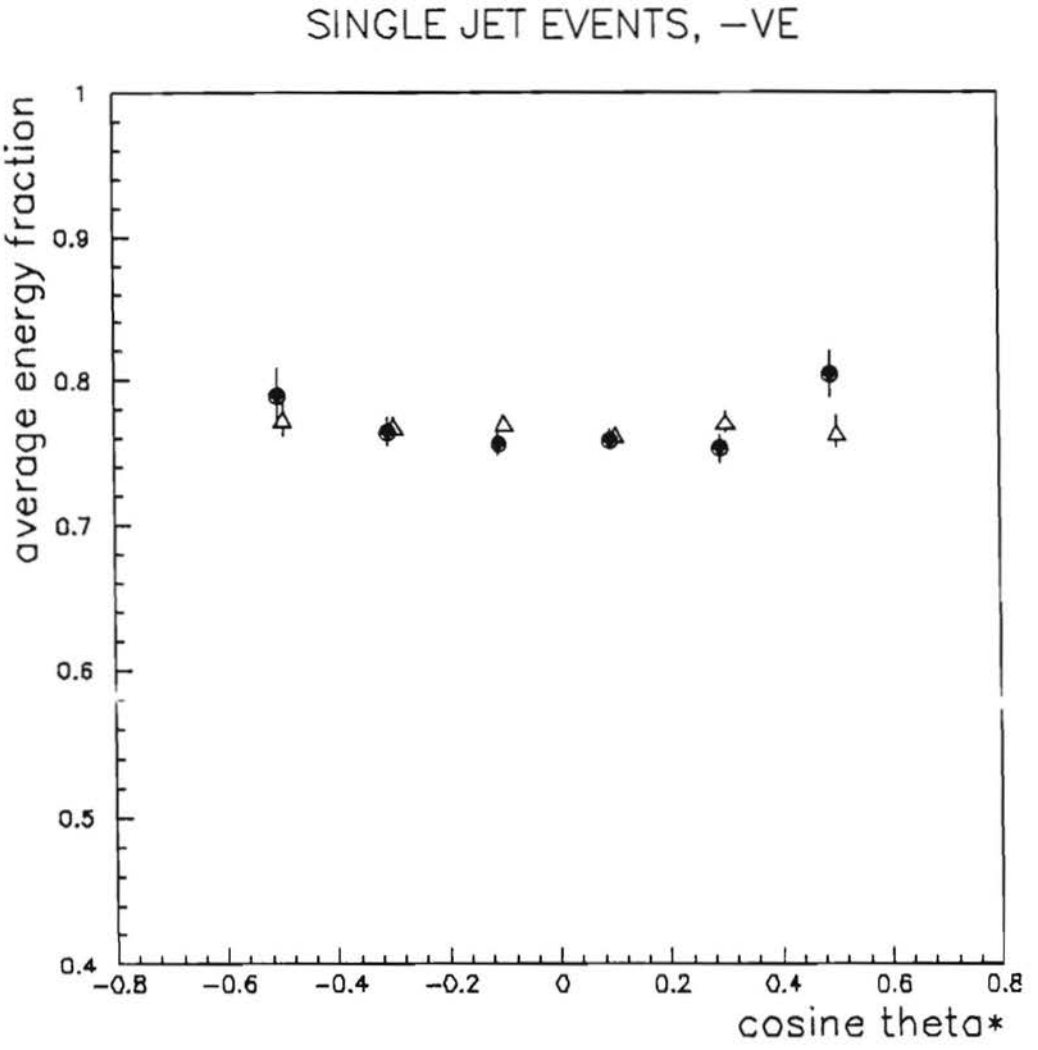

$< \mathcal{Z} >$, function of $\cos\theta^*$ of the leading hadron for single jet events and negative leading hadron charge

- • experimental data
- △ theoretical predictions

Figure 7.17

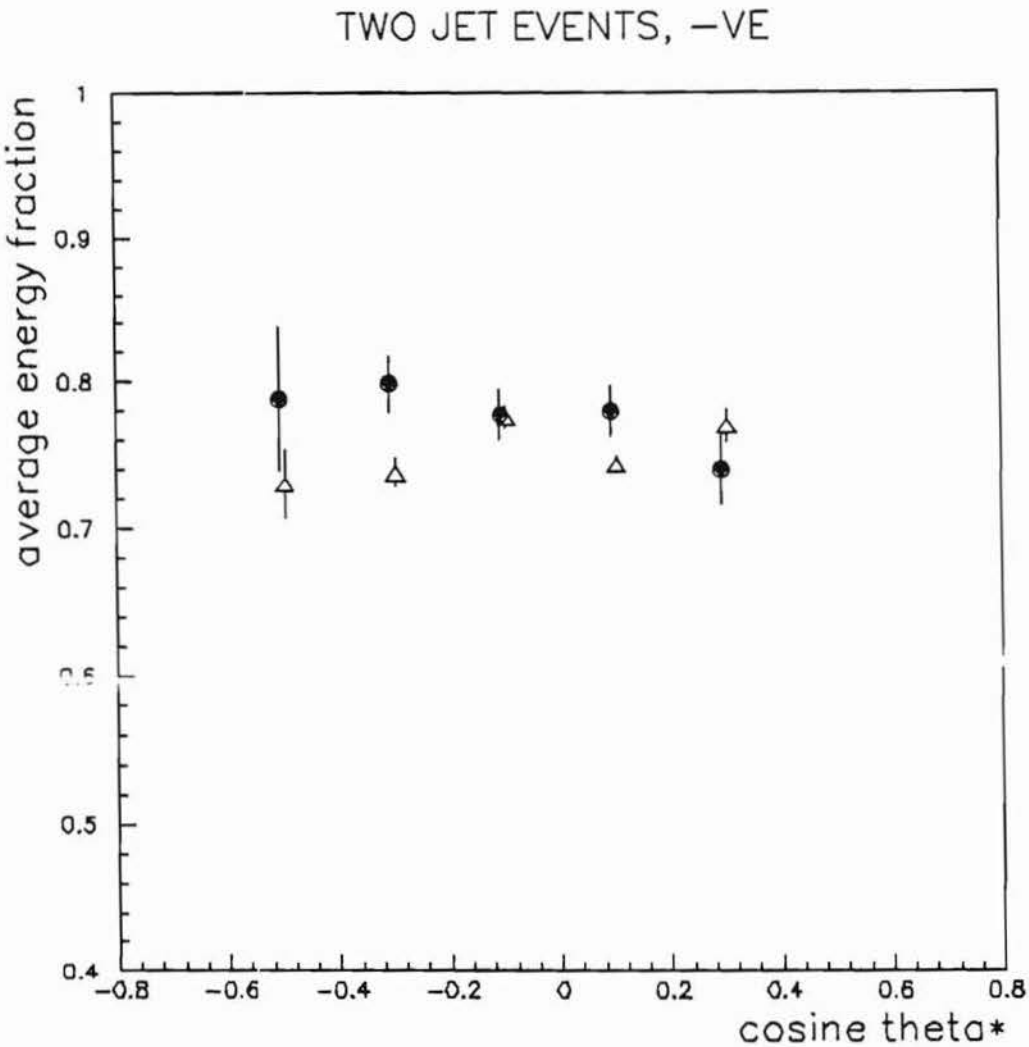

$< \mathcal{Z} >$, function of $\cos\theta^*$ of the leading hadron for two jet events and negative leading hadron charge

- • experimental data
- △ theoretical predictions

Figure 7.18

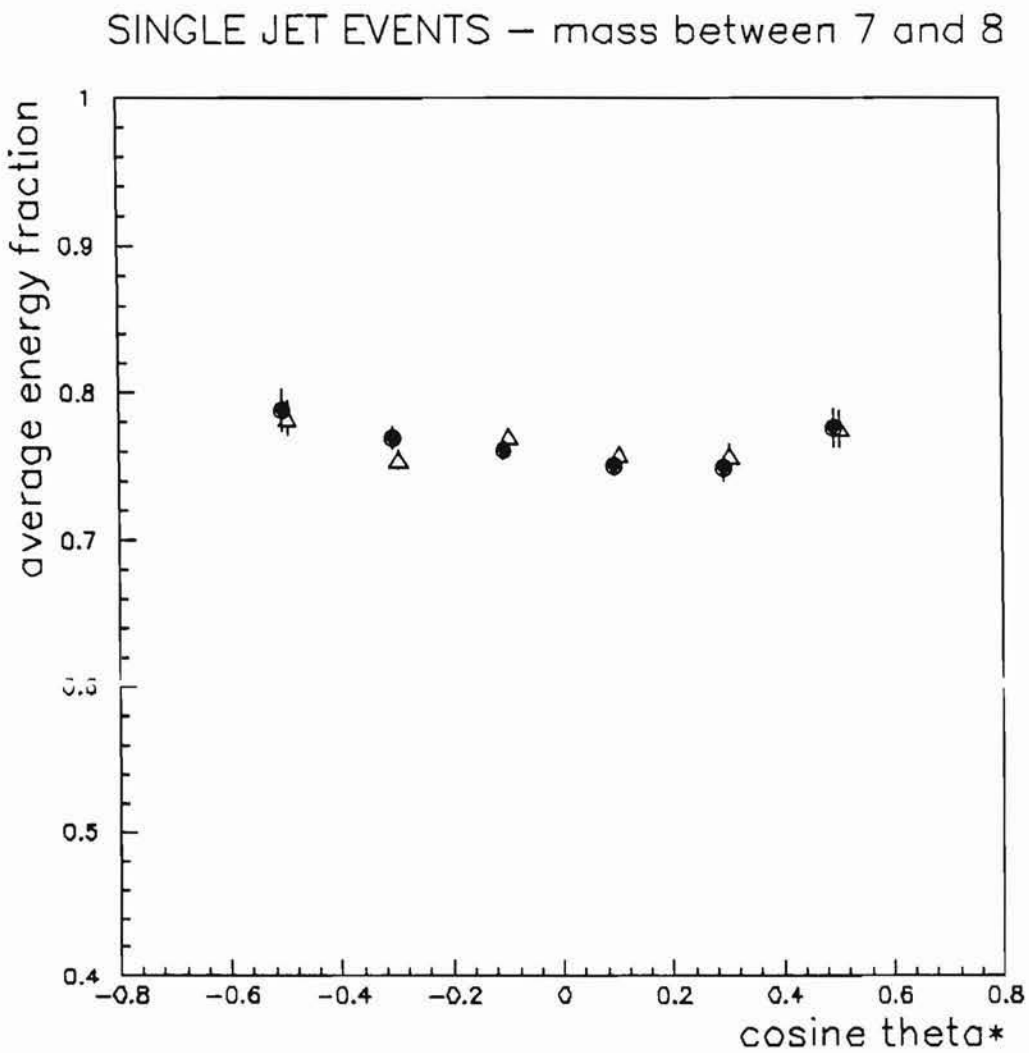

$< \mathcal{Z} >$, function of $\cos\theta^\star$ of the leading hadron for single jet events and $7 < M_{di-hadron} < 8$ GeV/c^2

- ● experimental data
- △ theoretical predictions

Figure 7.19

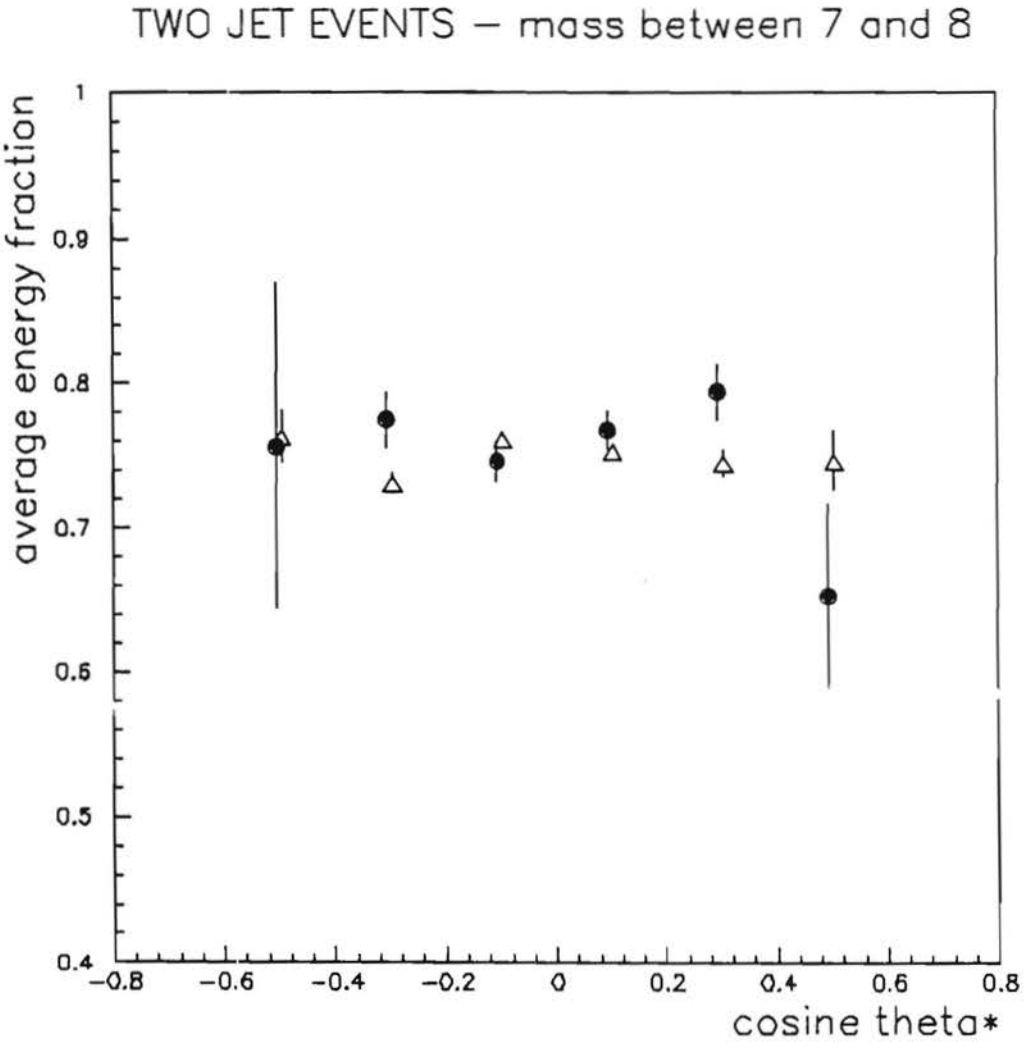

$< \mathcal{Z} >$, function of $\cos\theta^\star$ of the leading hadron for two jet events and $7 < M_{di-hadron} < 8$ GeV/c^2

- • experimental data
- △ theoretical predictions

Figure 7.20

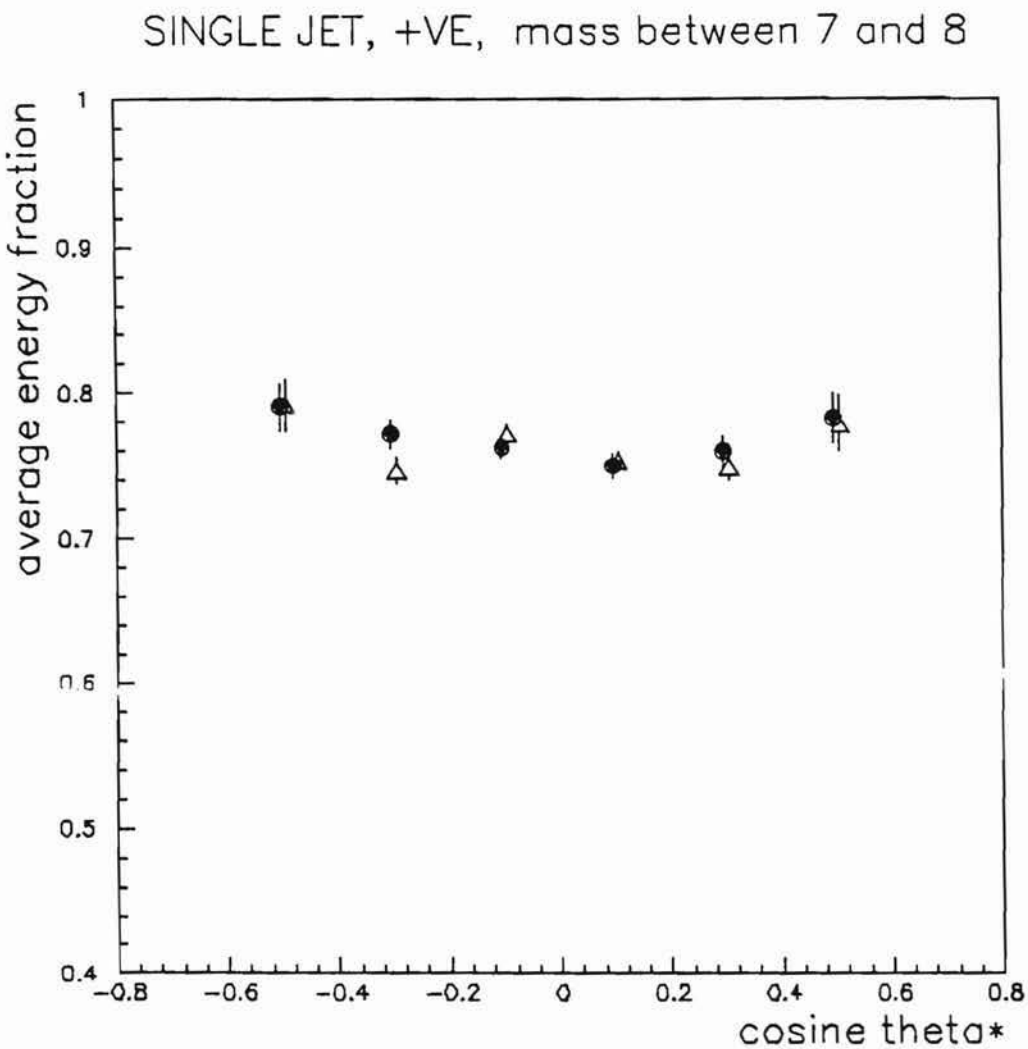

$< \mathcal{Z} >$, function of $\cos\theta^*$ of the leading hadron for single jet events and $7 < M_{di-hadron} < 8$ GeV/c^2 and positive leading hadron charge

- • experimental data
- △ theoretical predictions

Figure 7.21

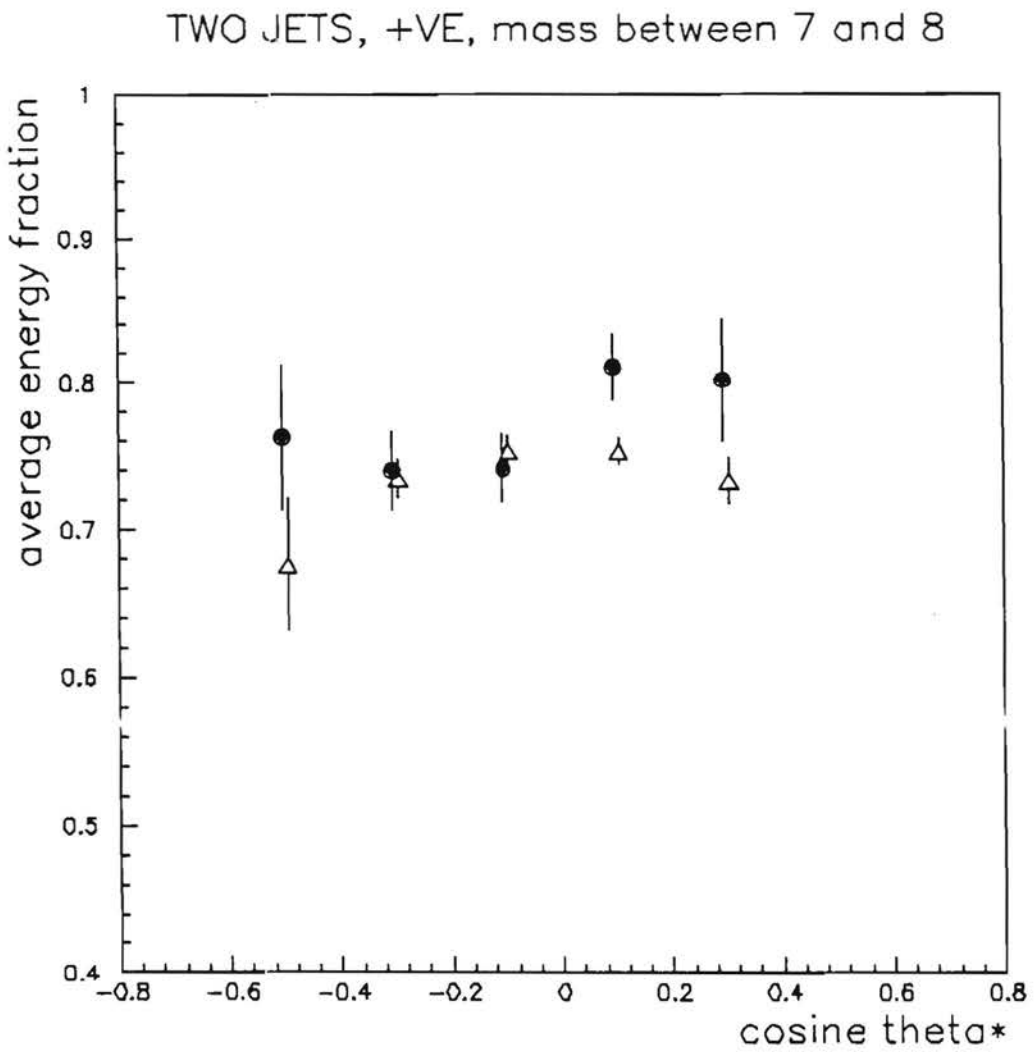

$< \mathcal{Z} >$, function of $\cos\theta^*$ of the leading hadron for two jet events and $7 < M_{di-hadron} < 8$ GeV/c^2 and positive leading hadron charge

- ● experimental data
- △ theoretical predictions

Figure 7.22

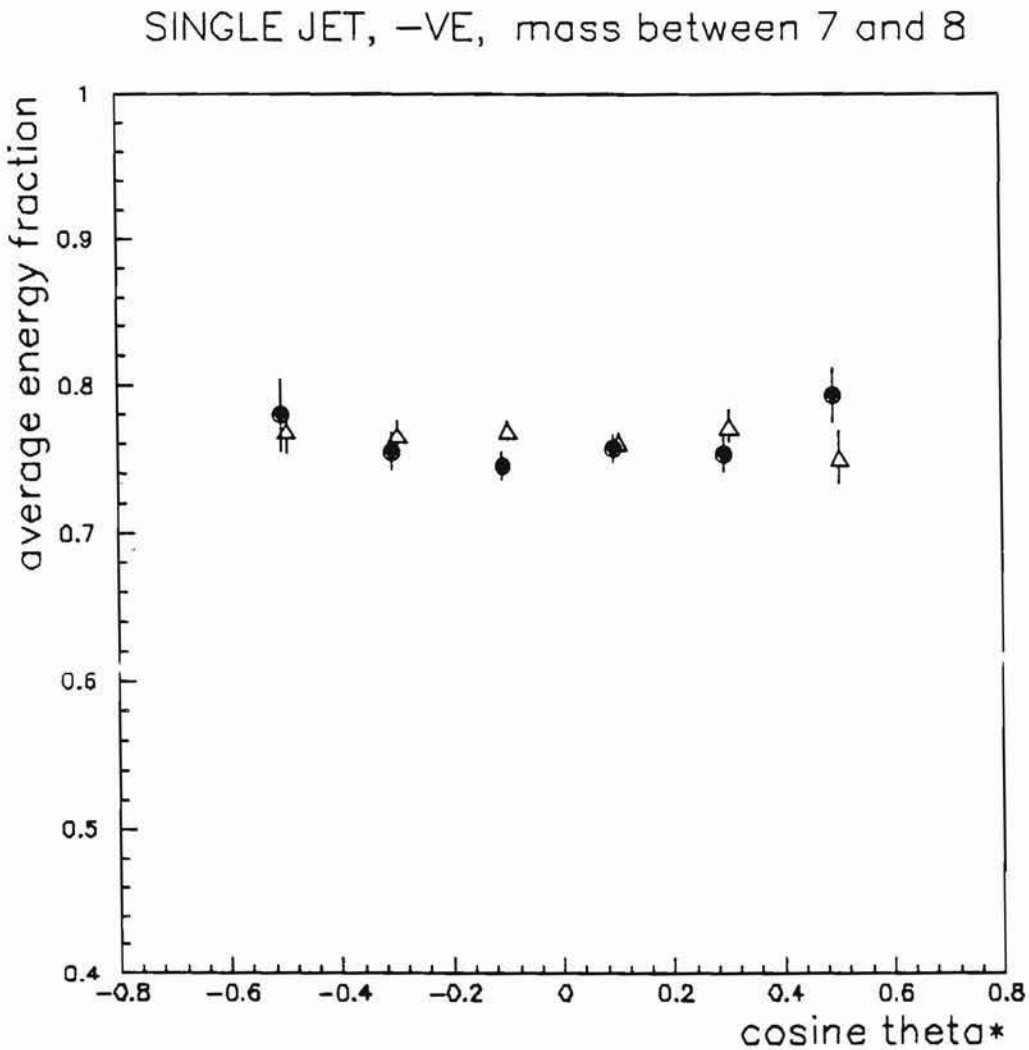

$< \mathcal{Z} >$, function of $\cos\theta^*$ of the leading hadron for single jet events and $7 < M_{di-hadron} < 8$ GeV/c^2 and negative leading hadron charge

- • experimental data
- △ theoretical predictions

Figure 7.23

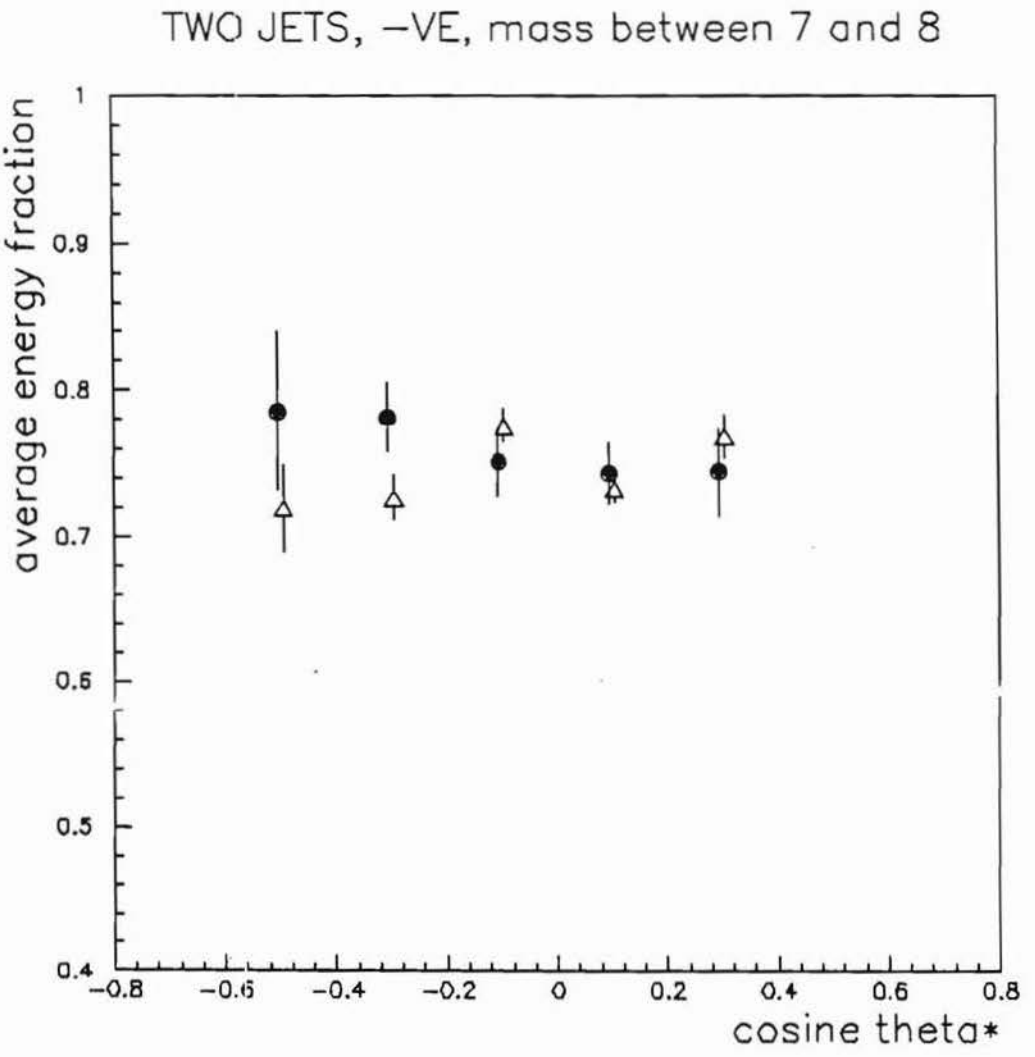

$< \mathcal{Z} >$, function of $\cos\theta^*$ of the leading hadron for two jet events and $7 < M_{di-hadron} < 8$ GeV/c^2 and negative leading hadron charge

- • experimental data
- △ theoretical predictions

Figure 7.24

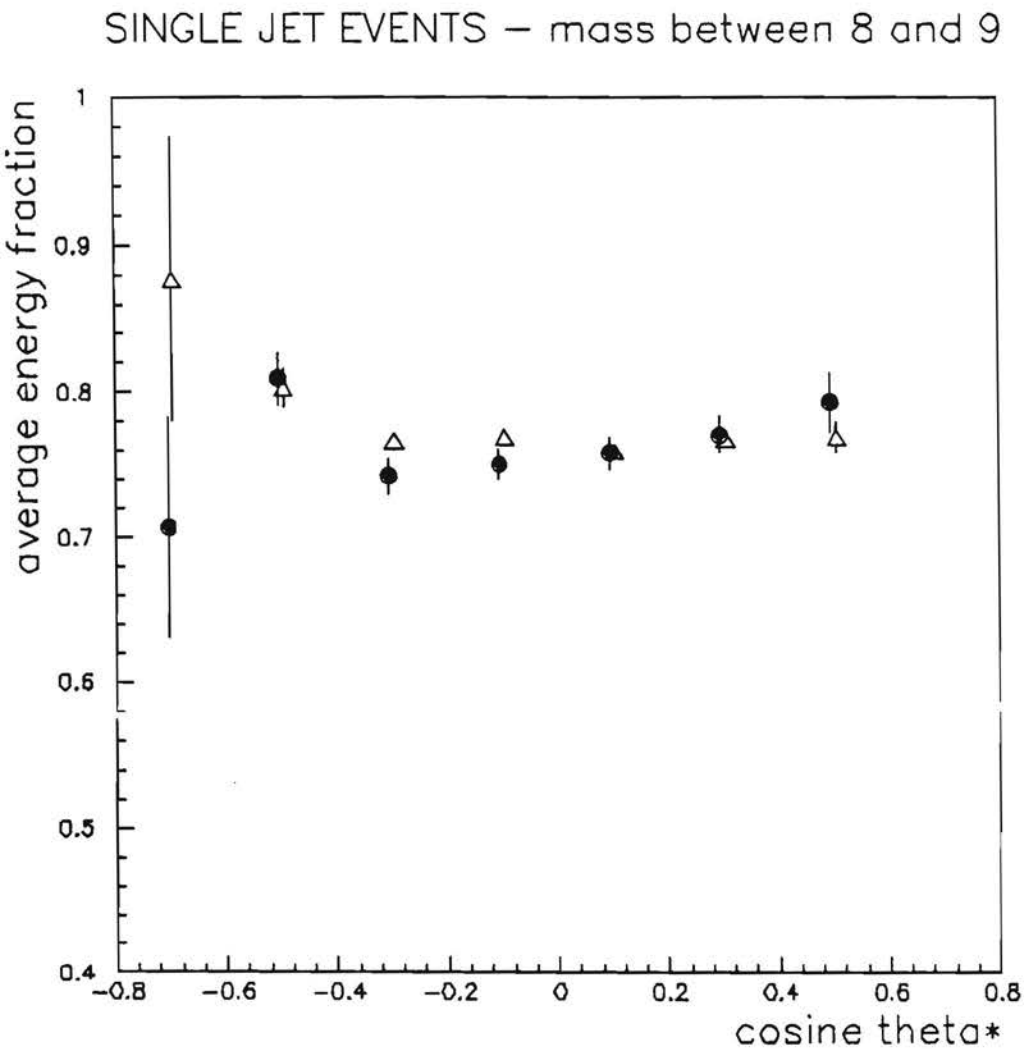

$< \mathcal{Z} >$, function of $\cos\theta^*$ of the leading hadron for single jet events and $8 < M_{di-hadron} < 9$ GeV/c^2

- ● experimental data
- △ theoretical predictions

Figure 7.25

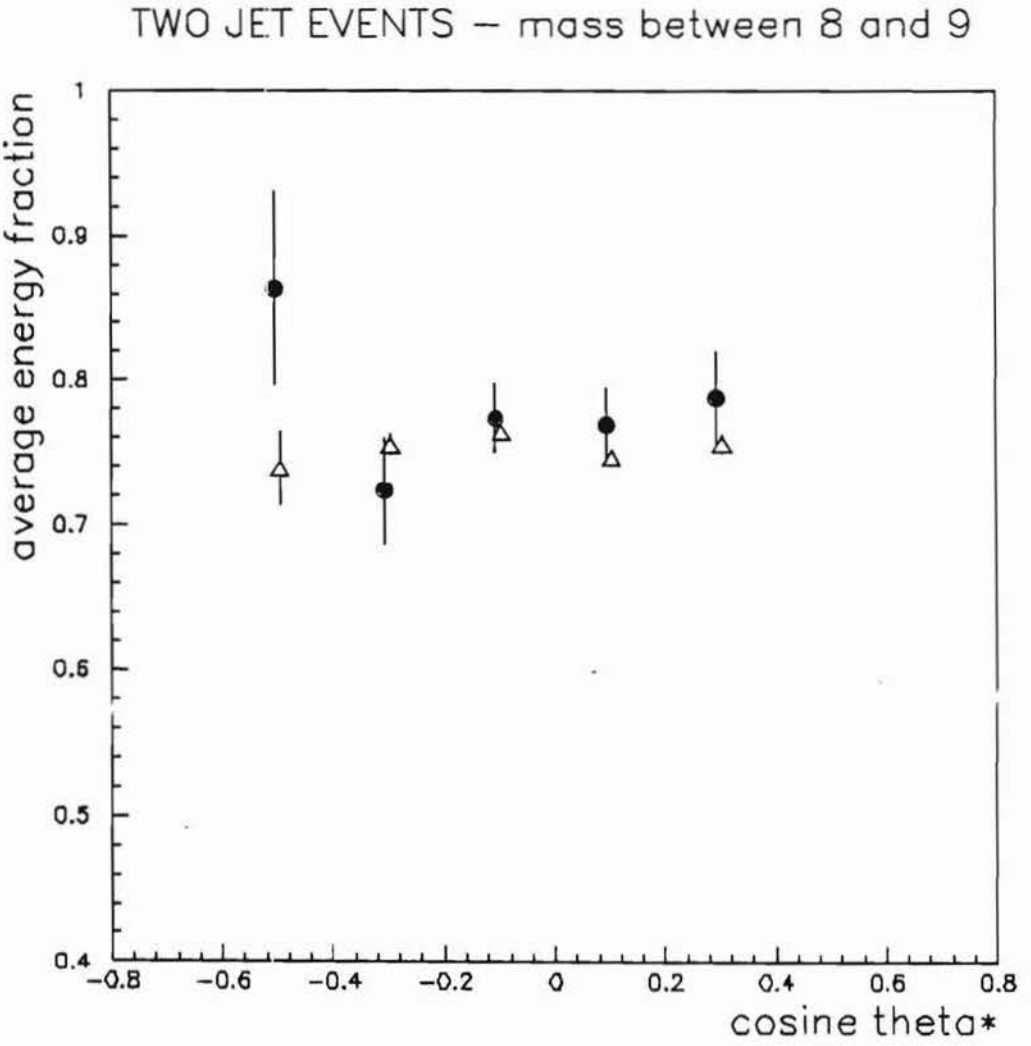

$< \mathcal{Z} >$, function of $\cos\theta^*$ of the leading hadron for two jet events and $8 < M_{di-hadron} < 9$ GeV/c^2

- • experimental data
- △ theoretical predictions

Figure 7.26

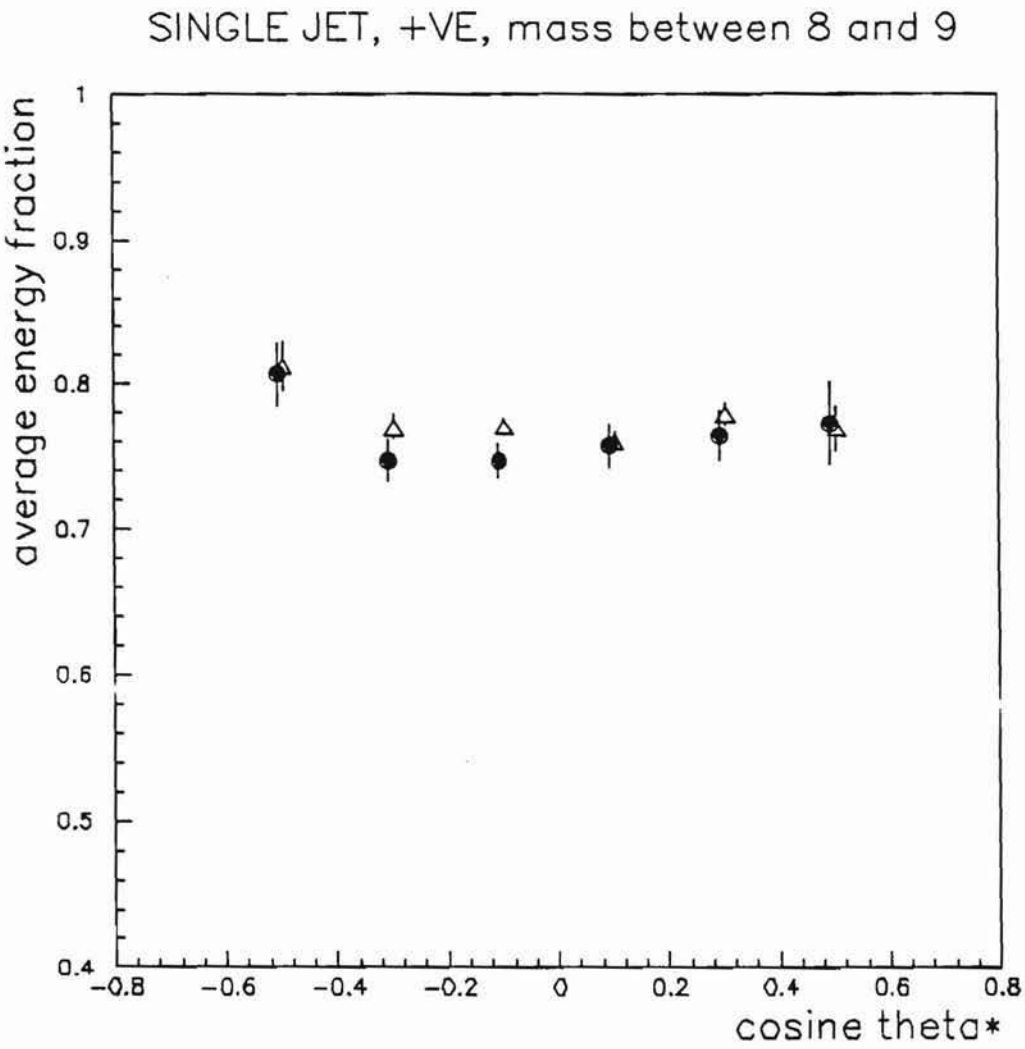

$< \mathcal{Z} >$, function of $\cos\theta^*$ of the leading hadron for single jet events and $8 < M_{di-hadron} < 9$ GeV/c^2 and positive leading hadron charge

• experimental data

△ theoretical predictions

Figure 7.27

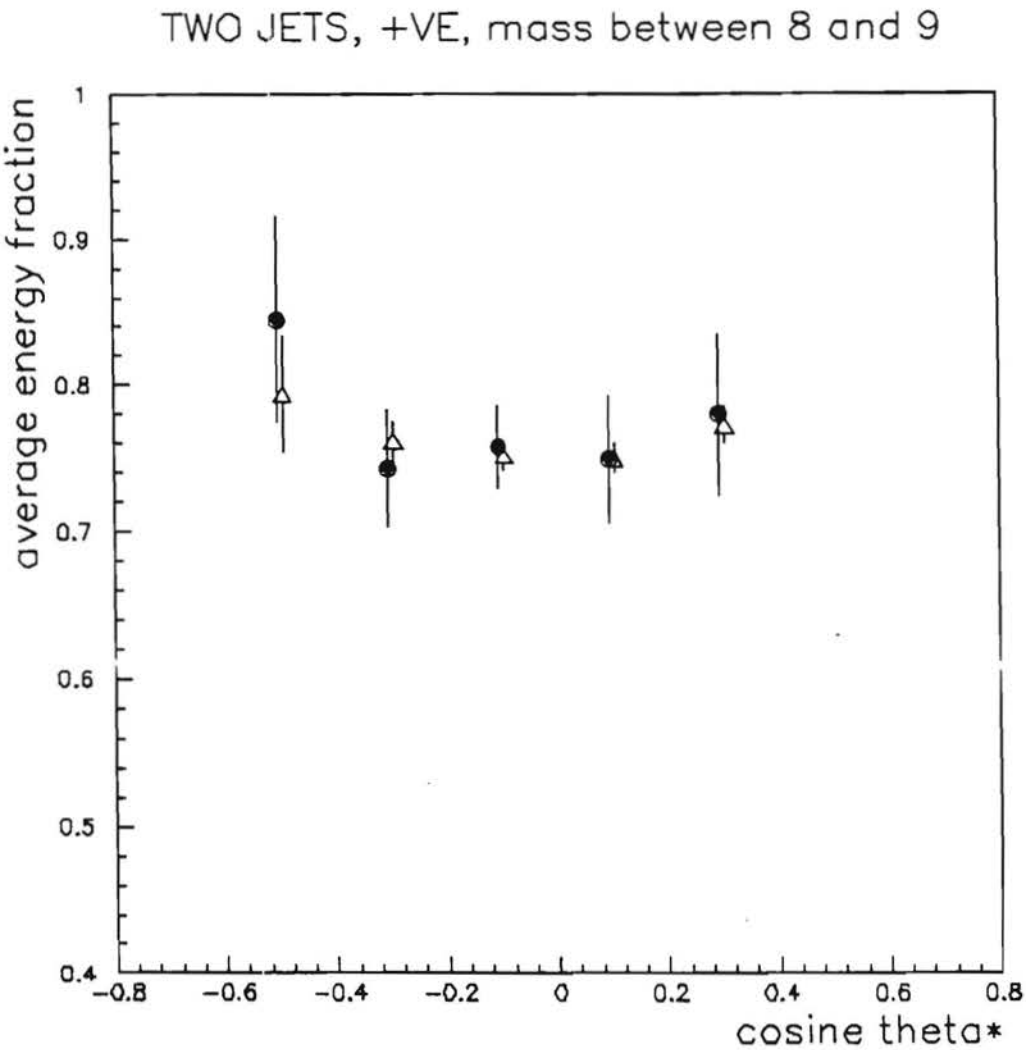

$< \mathcal{Z} >$, function of $\cos\theta^*$ of the leading hadron for two jet events and $8 < M_{di-hadron} < 9$ GeV/c^2 and positive leading hadron charge

- • experimental data
- △ theoretical predictions

Figure 7.28

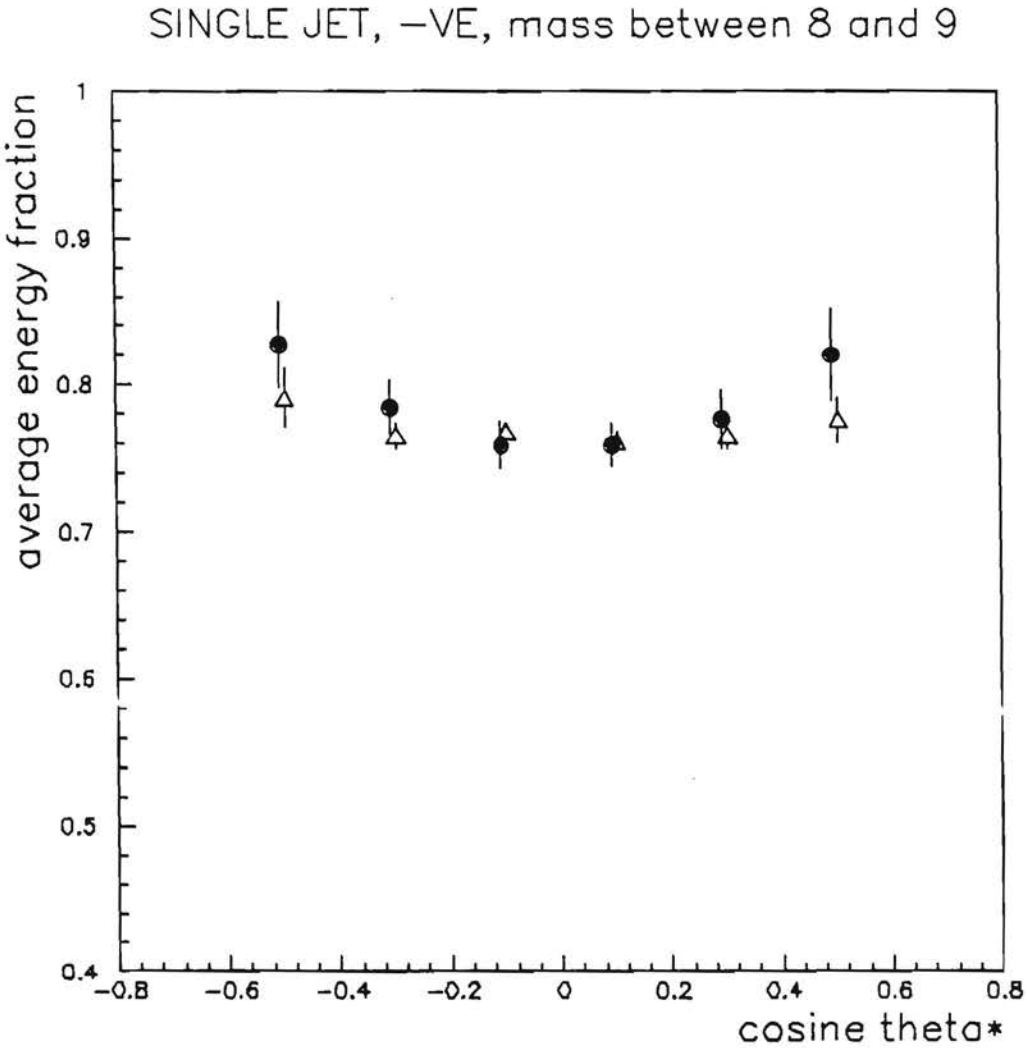

$< \mathcal{Z} >$, function of $\cos\theta^\star$ of the leading hadron for single jet events and $8 < M_{di-hadron} < 9$ GeV/c^2 and negative leading hadron charge

- • experimental data
- △ theoretical predictions

Figure 7.29

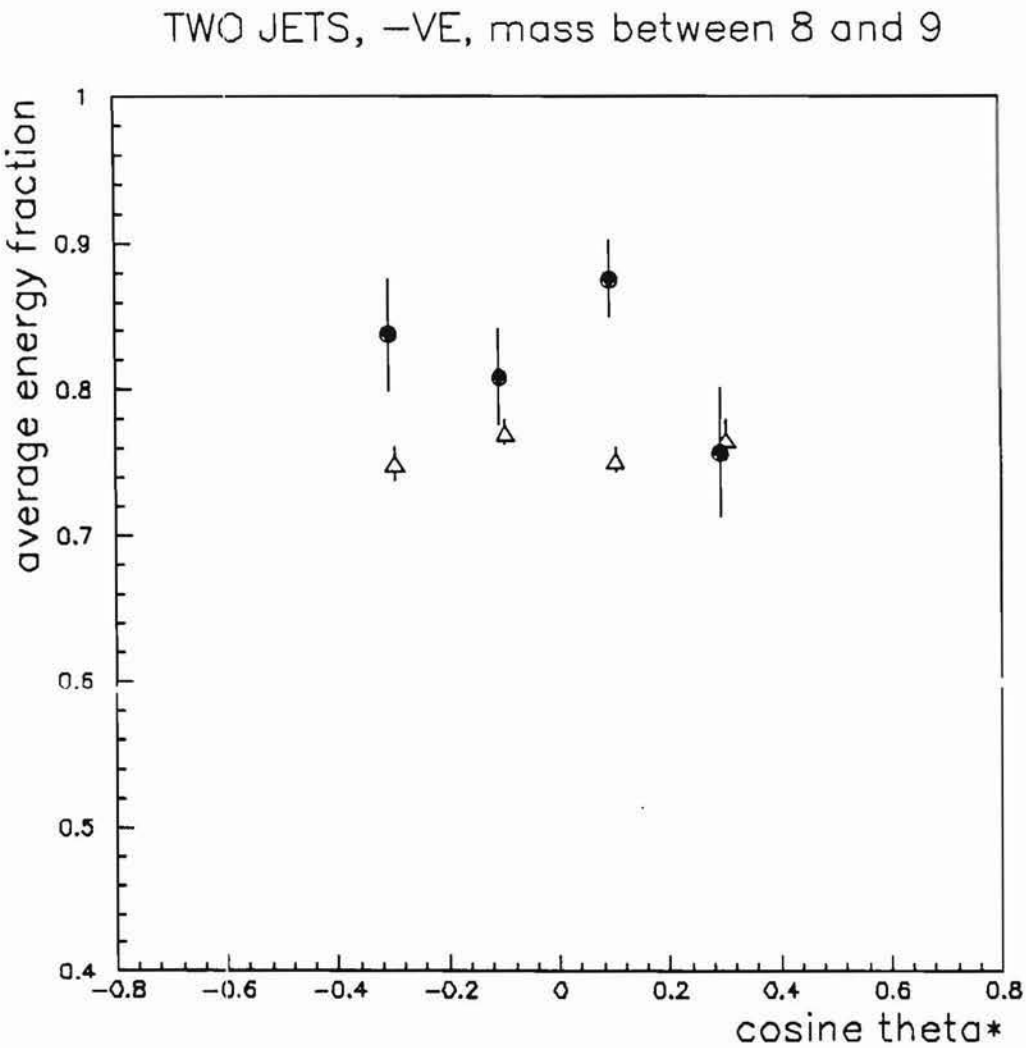

$< \mathcal{Z} >$, function of $\cos\theta^{\star}$ of the leading hadron for two jet events and $8 < M_{di-hadron} < 9$ GeV/c^2 and negative leading hadron charge

- • experimental data
- △ theoretical predictions

Figure 7.30

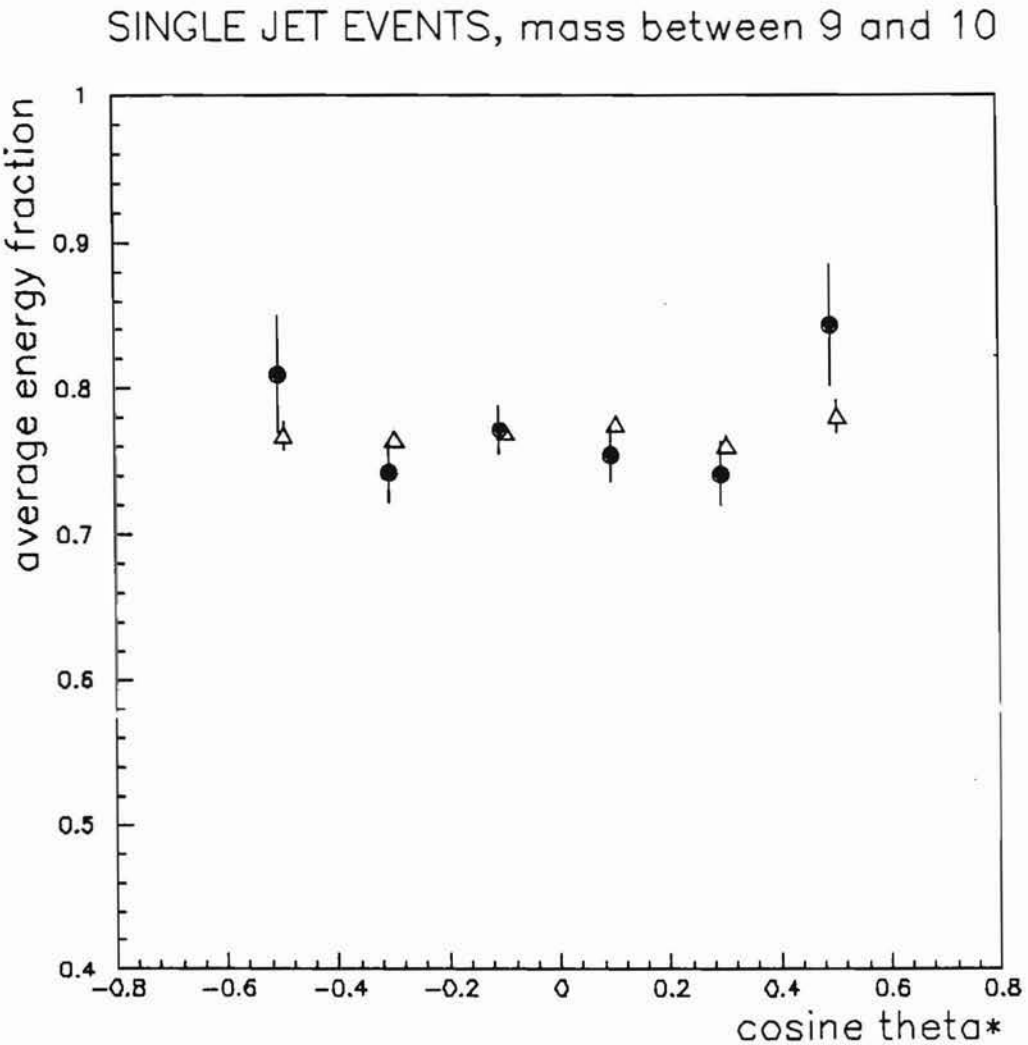

$< \mathcal{Z} >$, function of $\cos\theta^\star$ of the leading hadron for single jet events and $9 < M_{di-hadron} < 10$ GeV/c^2

- • experimental data
- △ theoretical predictions

Figure 7.31

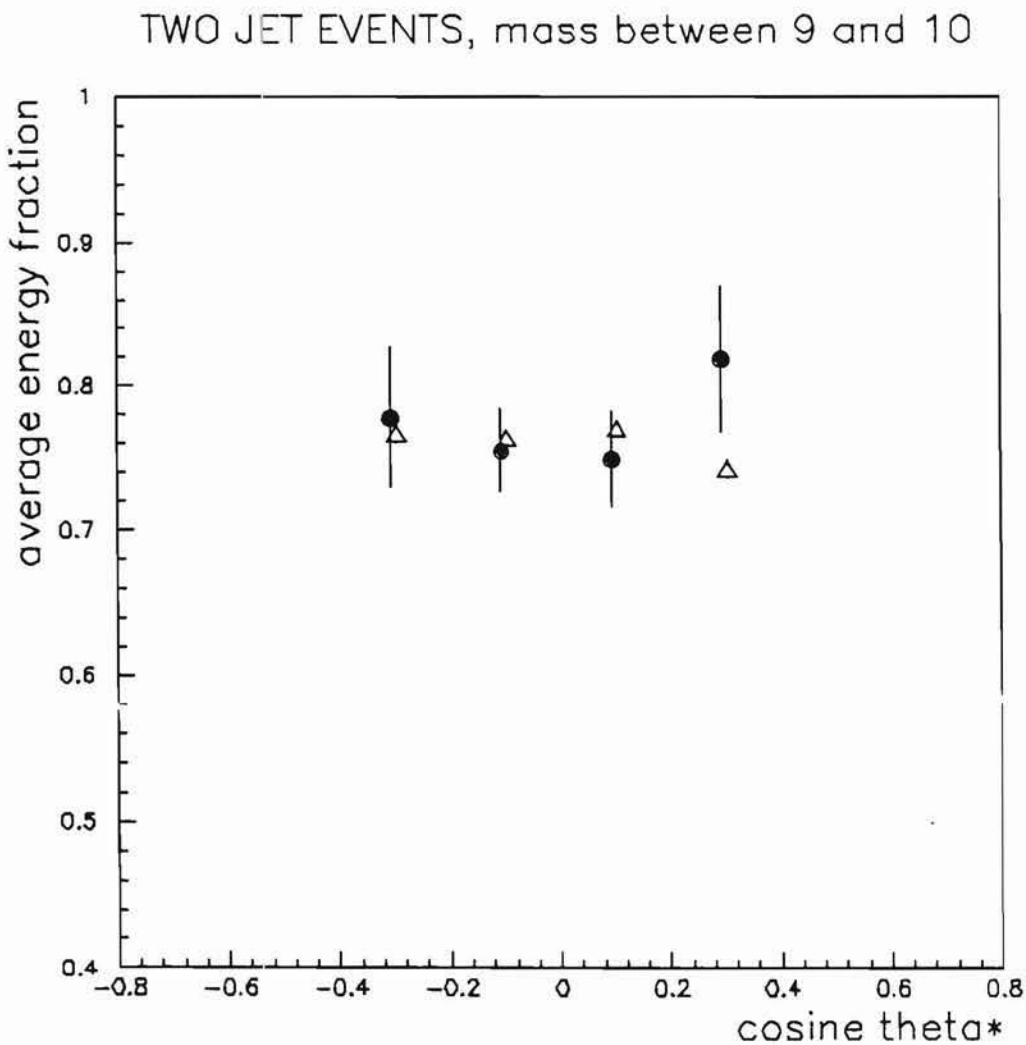

$< \mathcal{Z} >$, function of $\cos\theta^{\star}$ of the leading hadron for two jet events and $9 < M_{di-hadron} < 10$ GeV/c^2

• experimental data

△ theoretical predictions

Figure 7.32

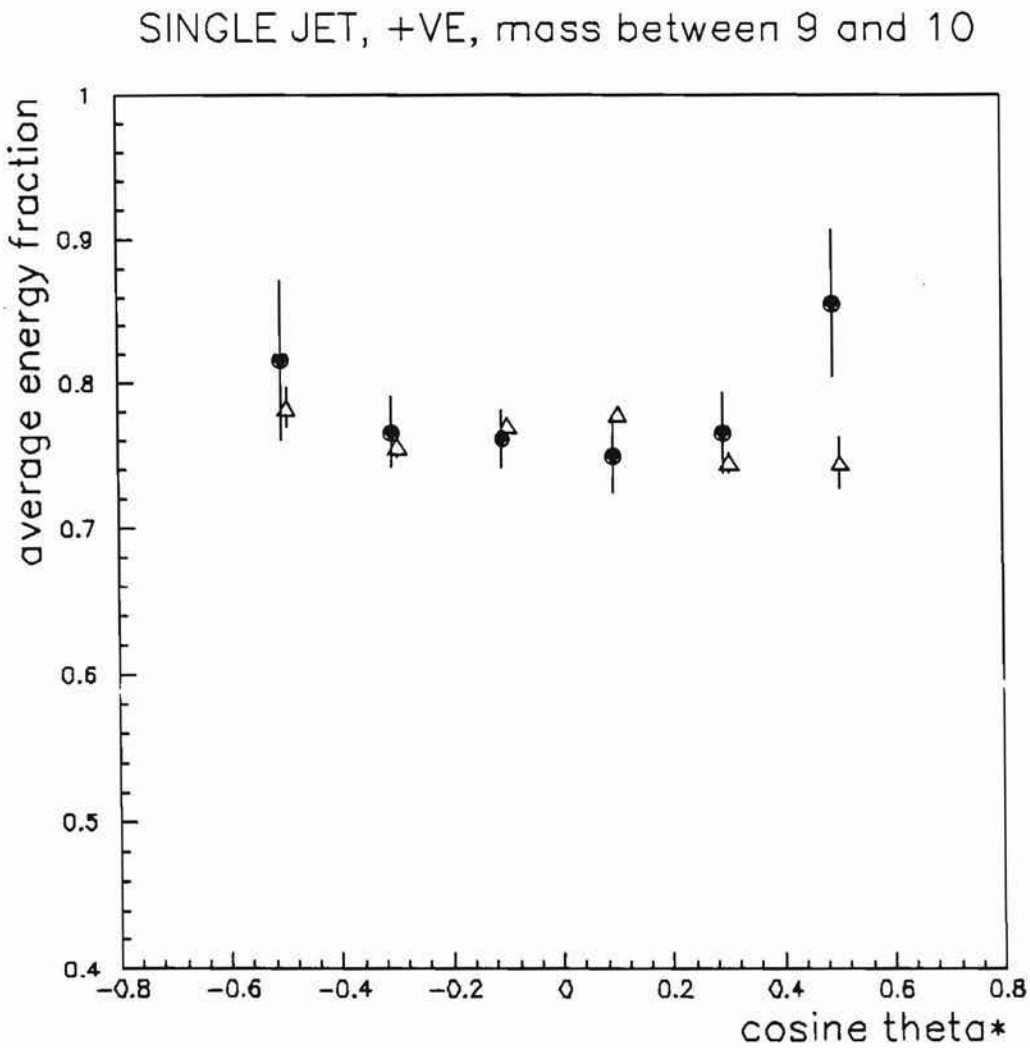

$< \mathcal{Z} >$, function of $\cos\theta^{\star}$ of the leading hadron for single jet events and $9 < M_{di-hadron} < 10$ GeV/c^2 and positive leading hadron charge

- • experimental data
- △ theoretical predictions

Figure 7.33

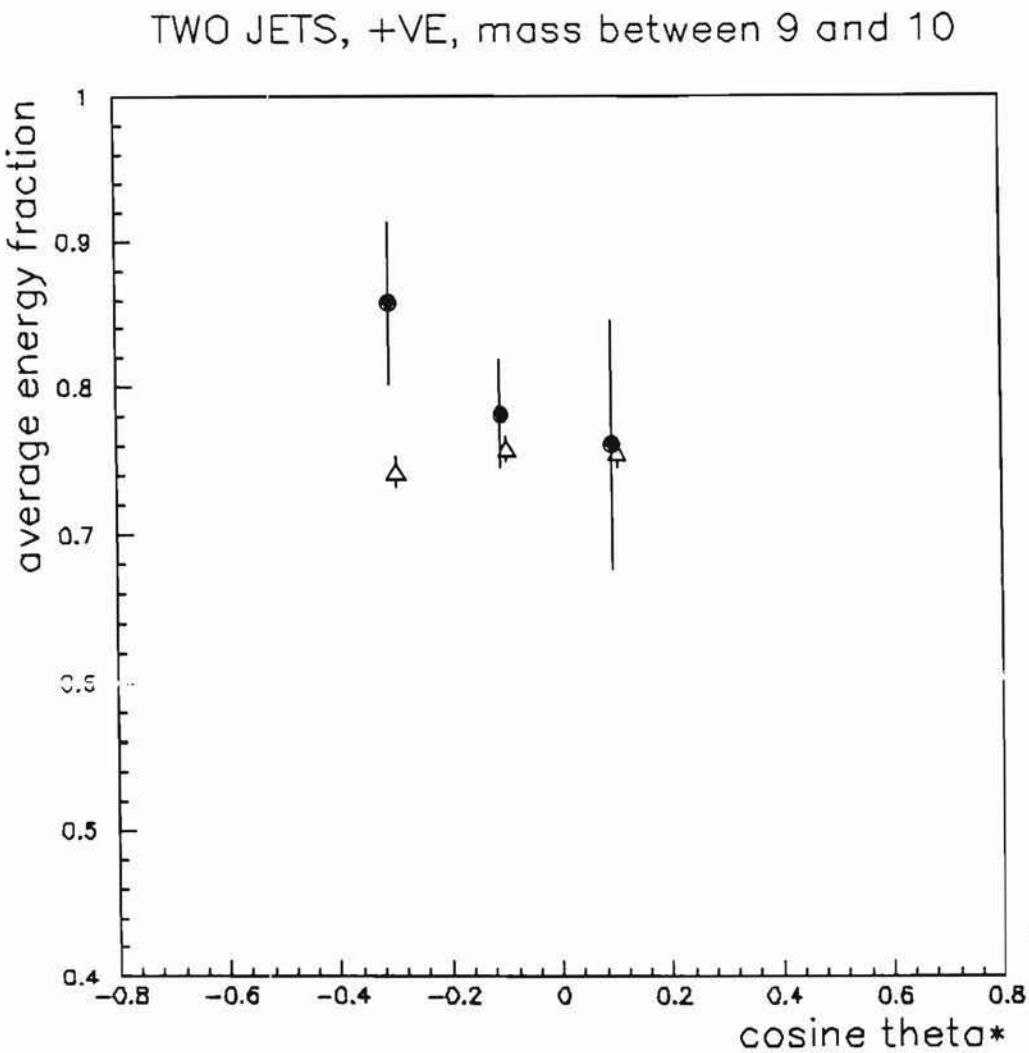

$< \mathcal{Z} >$, function of $\cos\theta^{\star}$ of the leading hadron for two jet events and $9 < M_{di-hadron} < 10$ GeV/c^2 and positive leading hadron charge

- ● experimental data
- △ theoretical predictions

Figure 7.34

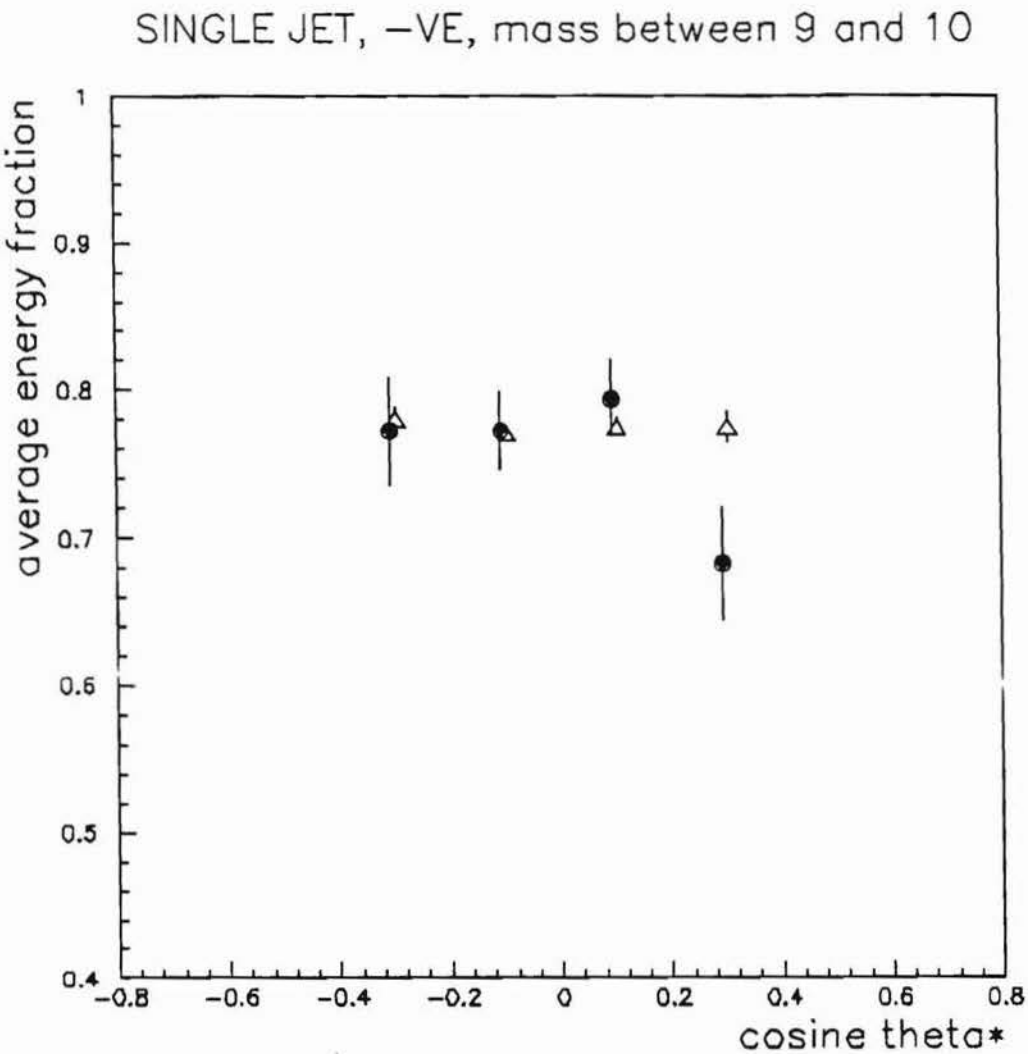

$< \mathcal{Z} >$, function of $\cos\theta^*$ of the leading hadron for single jet events and $9 < M_{di-hadron} < 10$ GeV/c^2 and negative leading hadron charge

• experimental data

△ theoretical predictions

Figure 7.35

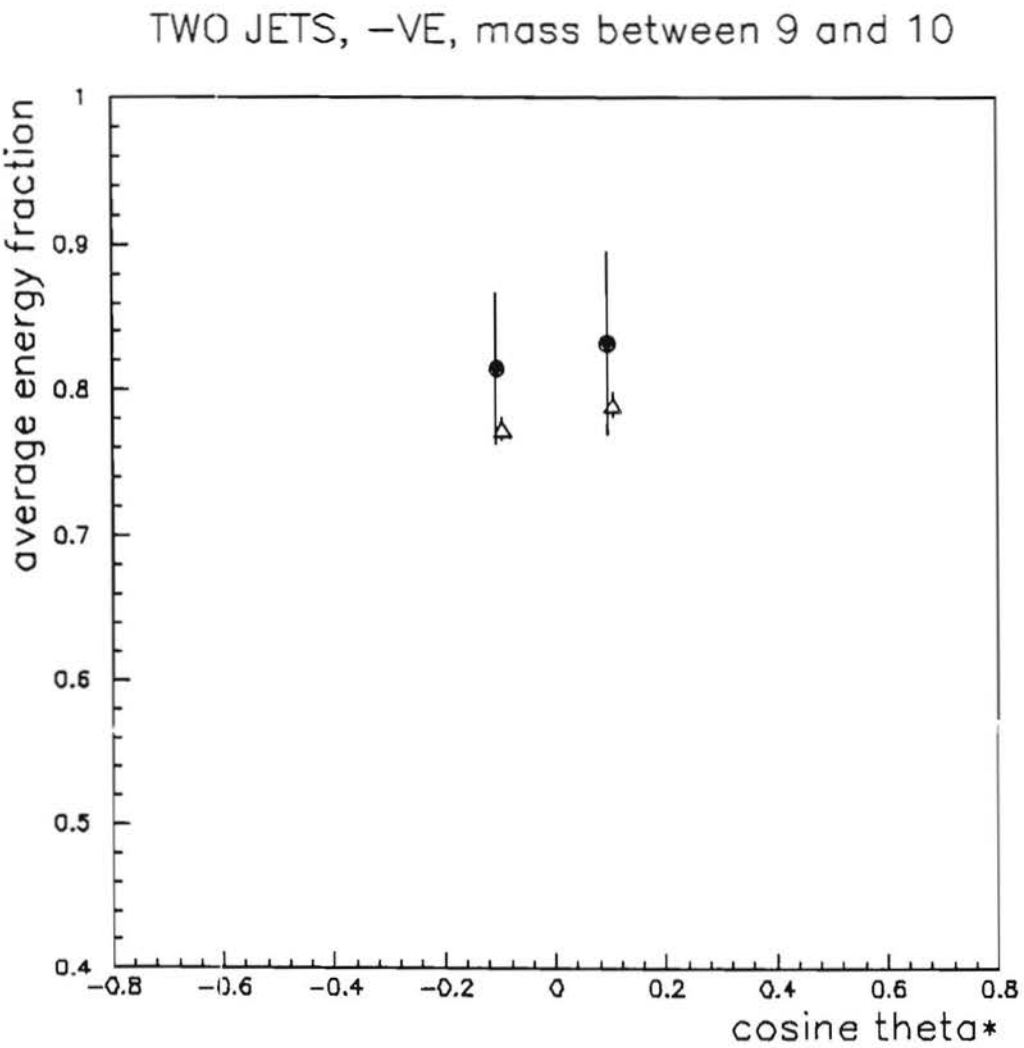

$< \mathcal{Z} >$, function of $\cos\theta^\star$ of the leading hadron for two jet events and $9 < M_{di-hadron} < 10$ GeV/c^2 and negative leading hadron charge

- • experimental data
- △ theoretical predictions

Figure 7.36

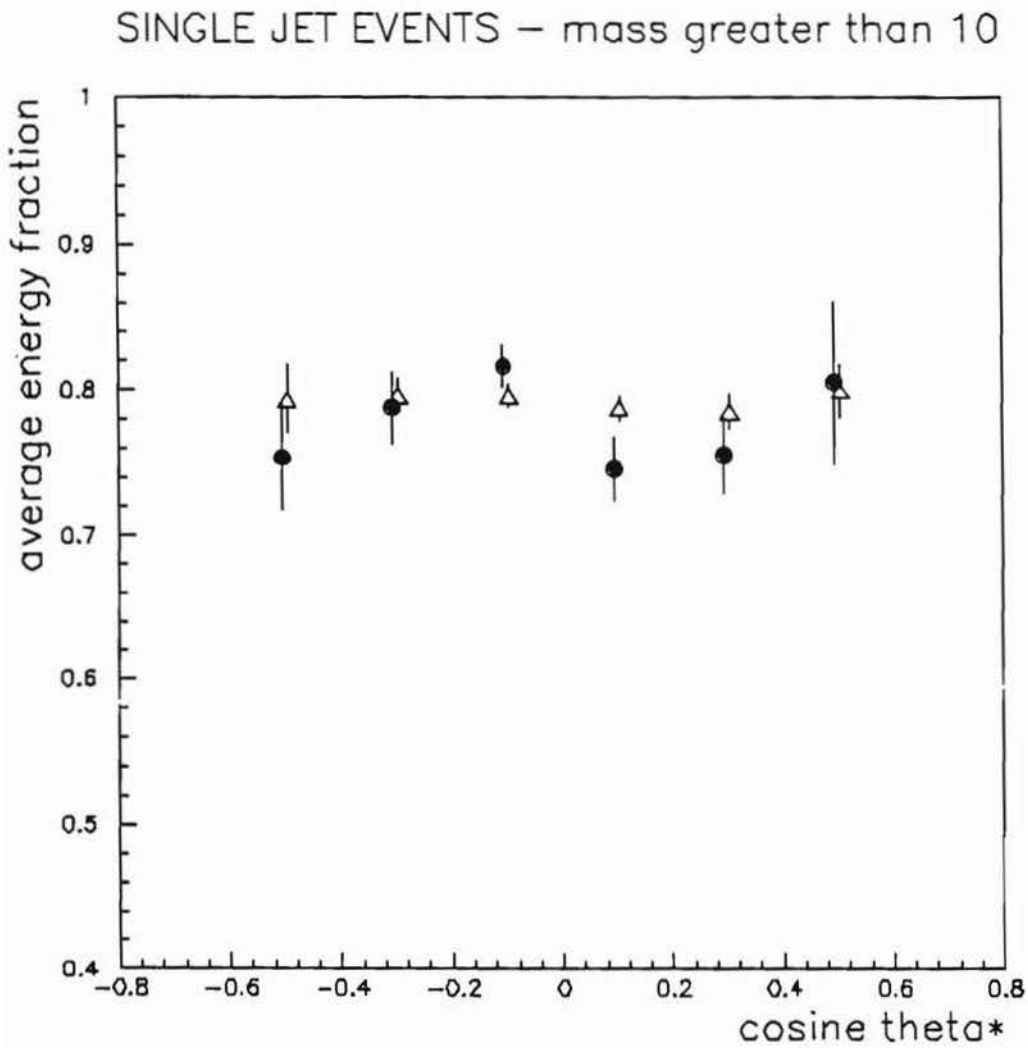

$< Z >$, function of $\cos\theta^{\star}$ of the leading hadron for single jet events and $M_{di-hadron} > 10$ GeV/c^2

- • experimental data
- △ theoretical predictions

Figure 7.37

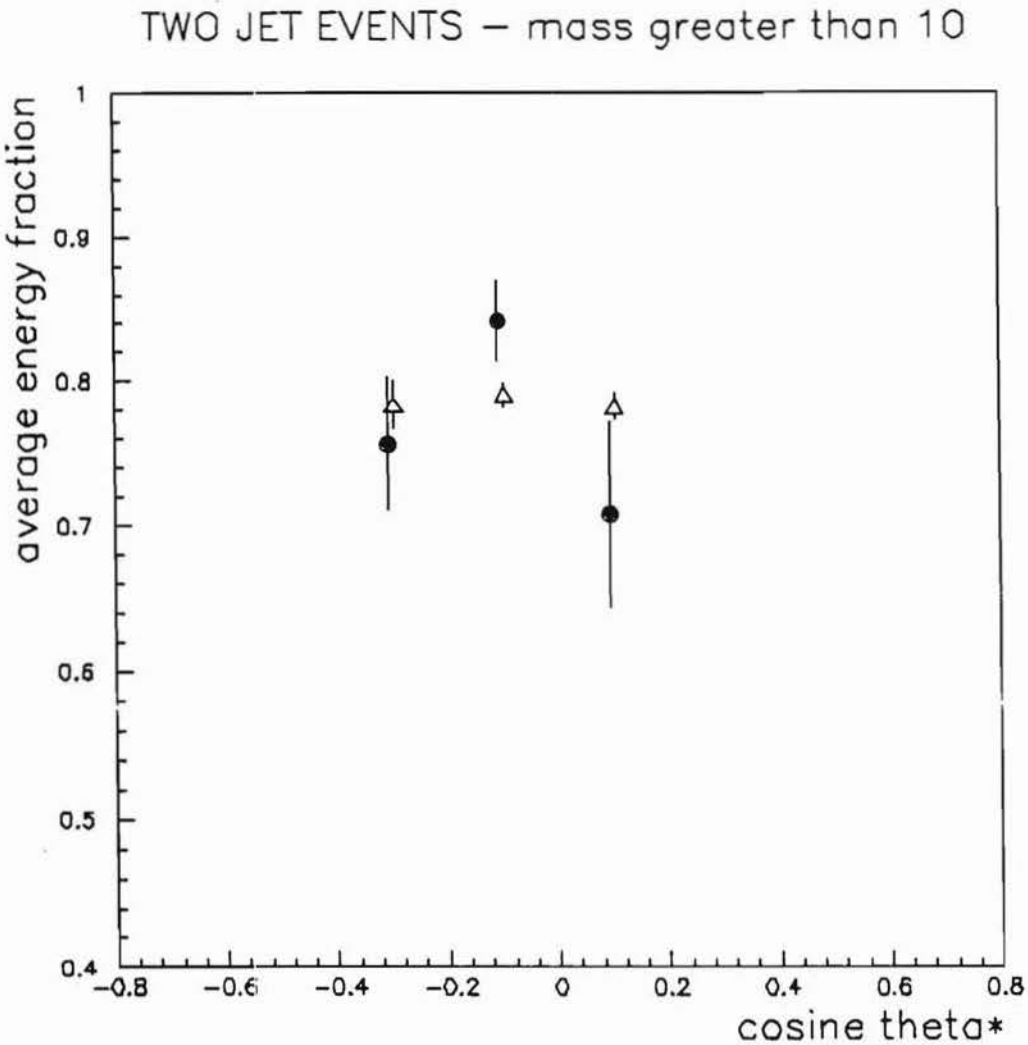

$< \mathcal{Z} >$, function of $\cos\theta^\star$ of the leading hadron for two jet events and $M_{di-hadron} > 10$ GeV/c^2

- • experimental data
- △ theoretical predictions

Figure 7.38

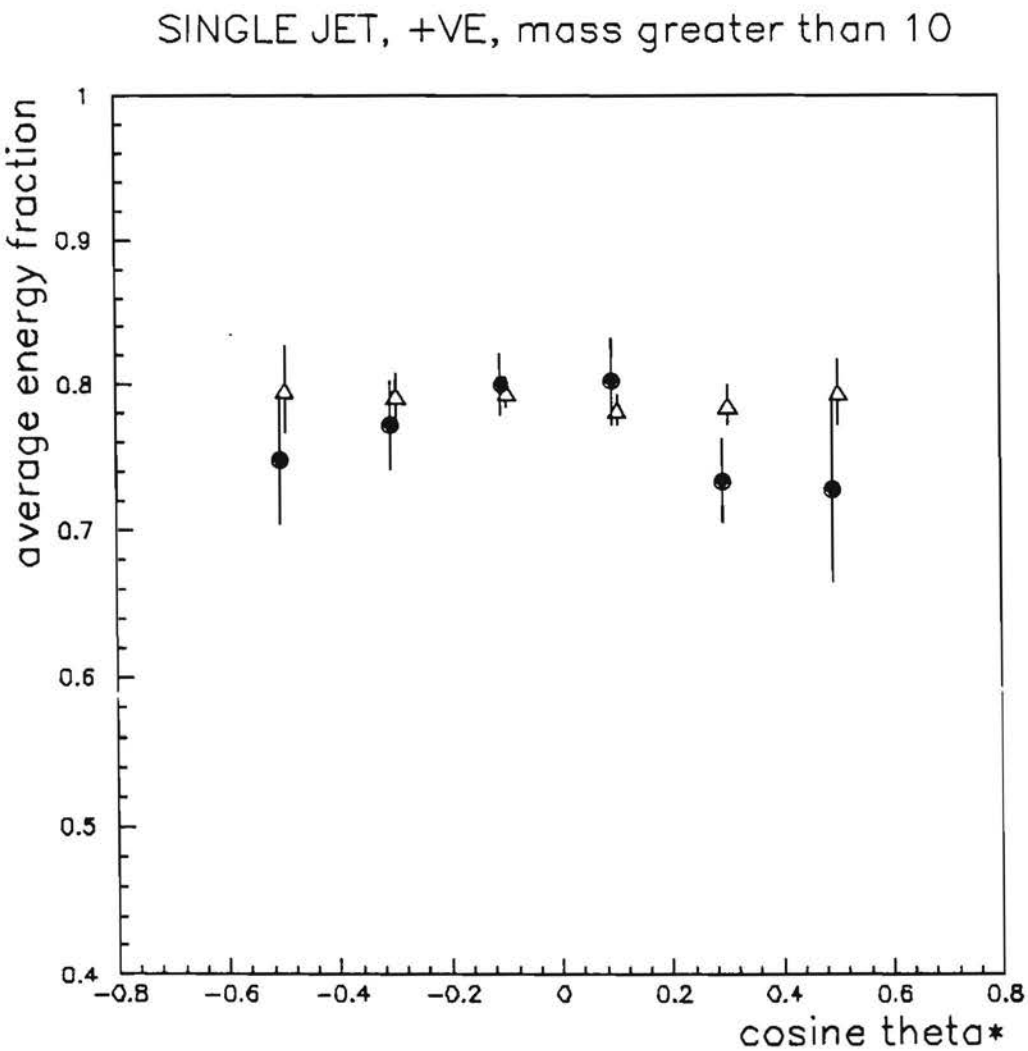

$< \mathcal{Z} >$, function of $\cos\theta^{\star}$ of the leading hadron for single jet events and $M_{di-hadron} > 10$ GeV/c^2 and positive leading hadron charge

- • experimental data
- △ theoretical predictions

Figure 7.39

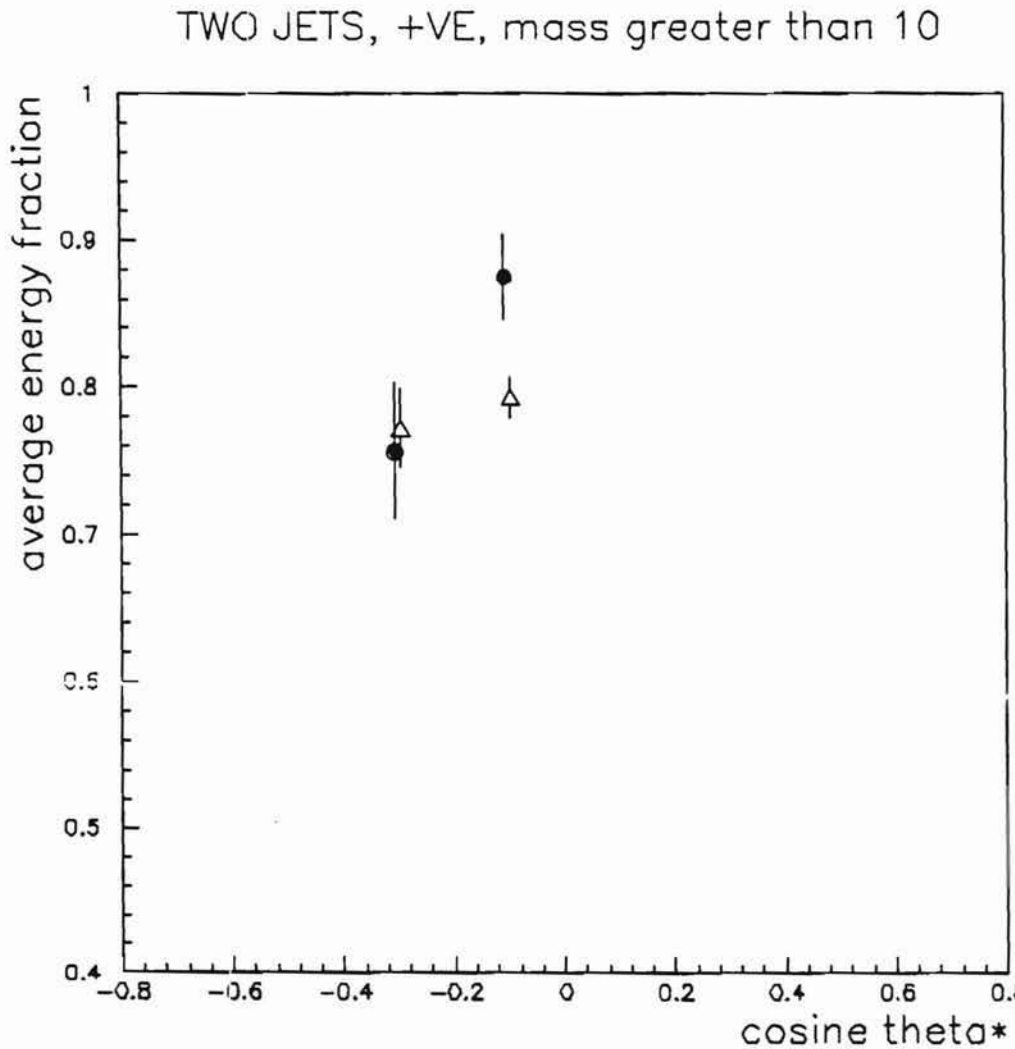

$< \cdot \mathcal{Z} >$, function of $\cos\theta^*$ of the leading hadron for two jet events and $M_{di-hadron} > 10$ GeV/c^2 and positive leading hadron charge

- • experimental data
- △ theoretical predictions

Figure 7.40

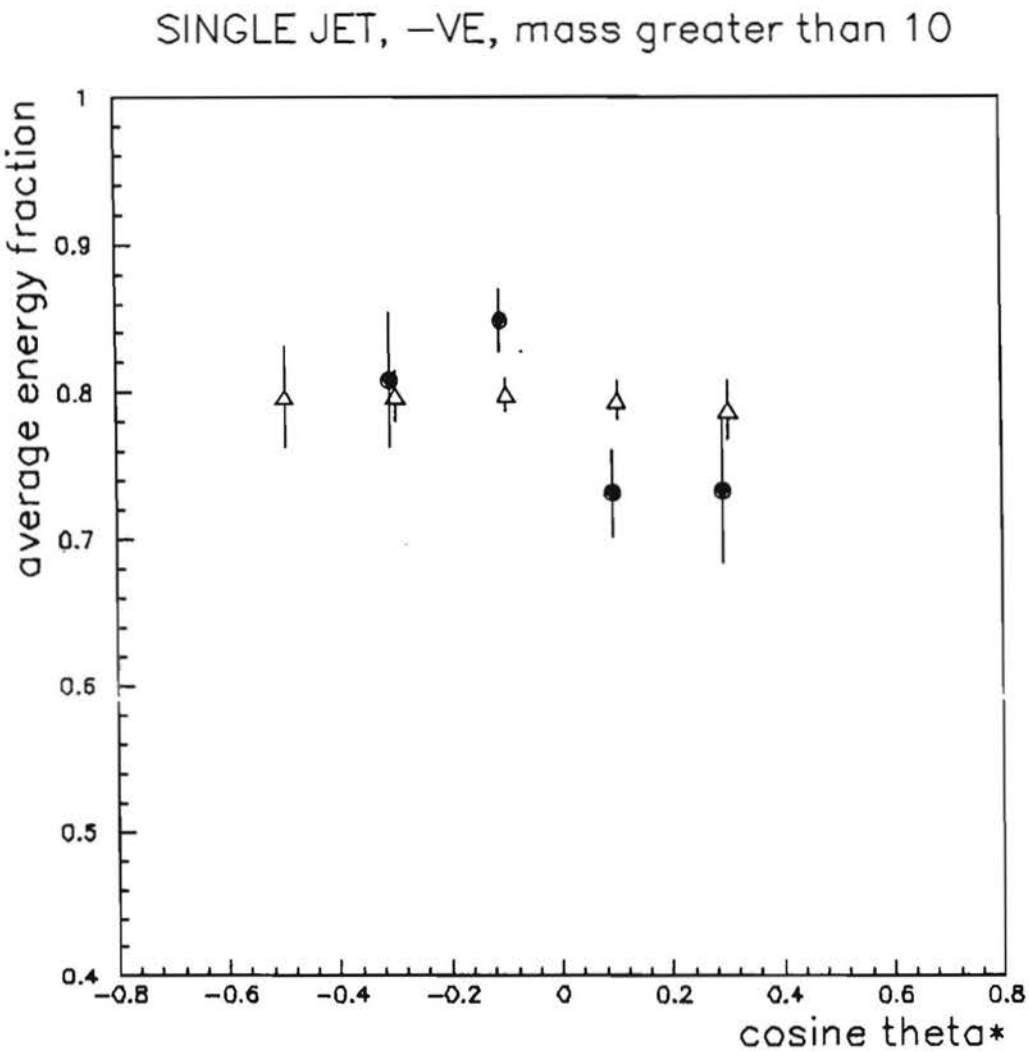

$< \mathcal{Z} >$, function of $\cos\theta^*$ of the leading hadron for single jet events and $M_{di-hadron} > 10$ GeV/c^2 and negative leading hadron charge

- • experimental data
- △ theoretical predictions

Figure 7.41

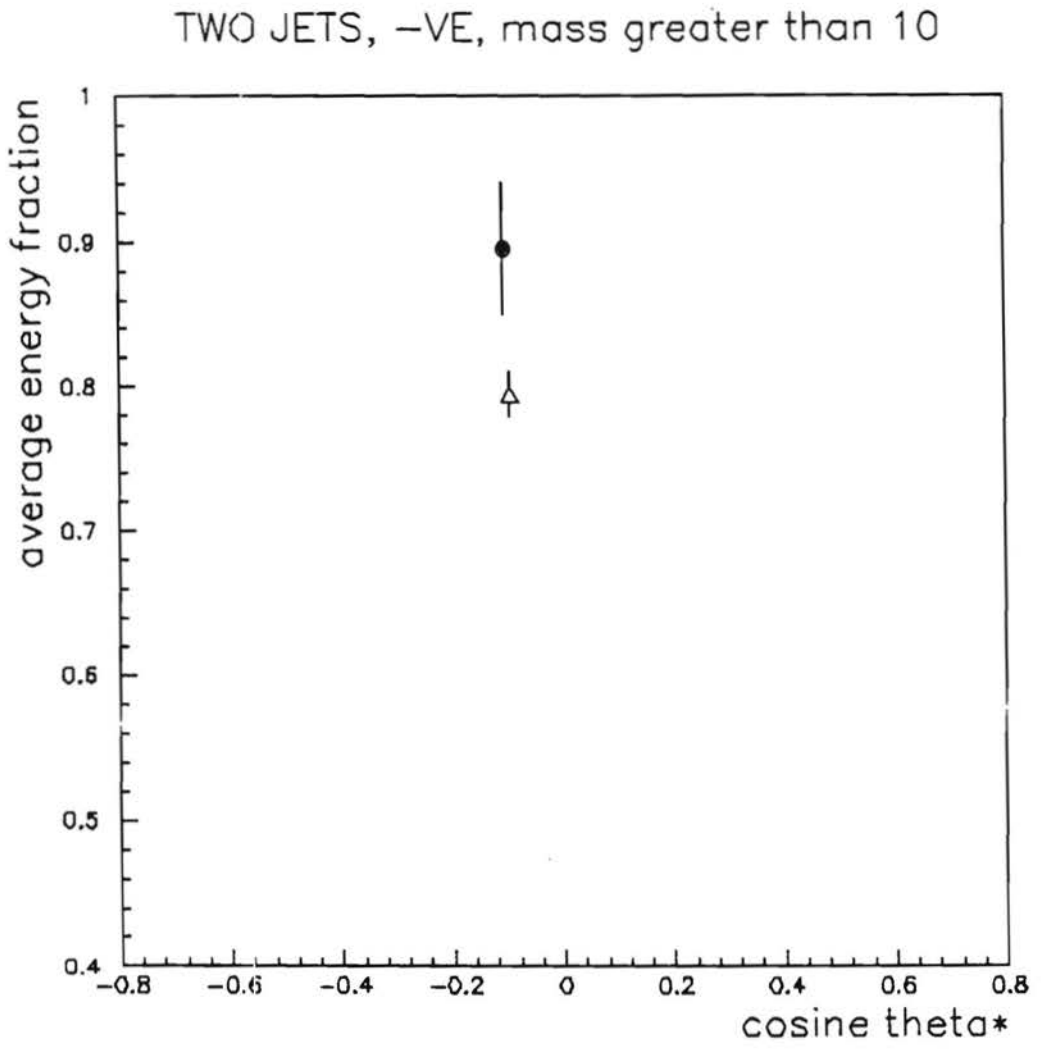

$< Z >$, function of $\cos\theta^*$ of the leading hadron for two jet events and $M_{di-hadron} > 10$ GeV/c^2 and negative leading hadron charge

- • experimental data
- △ theoretical predictions

Figure 7.42

CHAPTER 8

CONCLUSIONS

The average energy fraction of the high $P_\perp$ jet carried by leading hadrons has been measured in a $\sqrt{s} = 38.76$ GeV proton-nucleon scattering. The fragmentation process has been shown to be independent on the nuclear target used (Be, Al, Fe, W), when $< \mathcal{Z} >$ is expressed as a function of $P_\perp$ of the leading hadron, $\cos\theta^\star$ or the mass of the di-hadron pair.

The $< \mathcal{Z} >$ distributions are in agreement with the CCOR data, particularly when $< \mathcal{Z} >$ is expressed in terms of the scaling variable $x_\perp$ (see figures 7.5 and 7.6).

Finally, the present data agrees with the theoretical predictions made by a QCD model, in the leading logarithmic approximation.

REFERENCES

[1] H. Fritzsch, M. Gell-Mann and H. Leutwyler, Phys. Lett. 437B, 365 (1973)

[2] J.D. Bjorken and E.A. Paschos, Phys. Rev. 185, 1975 (1969)

[3] S.M. Berman, J.D. Bjorken, J.B. Kogut, Phys. Rev. D 4 : 3388 (1971)

[4] M. Banner et al., Phys.Lett. B 118 : 203 (1982)

[5] A.L.S Angelis et al., Nuclear Physics B209, 284 (1982)

[6] A.L.S. Angelis et al., Physica Scripta 19, 116 (1979)

[7] M. Jacob, P. Landshoff, Physics Reports 48 C, 286 (1978)

[8] J.F. Owens, Phys. Rev. D 20 : 221 (1979)

[9] J.Gunion and B.Pettersson, Phys.Rev. D22,629 (1980)

[10] R.Baier et al., Zeitschrift fur Physik C 2, 265 (1979)

[11] EMC collaboration, CERN-EP/89-25, January 31st, 1989

[12] J.F.Owens, Review Modern Physics 59, 465 (1987)

[13] D.W. Duke and J.F. Owens, Phys. Rev. D 30, 49 (1984)

[14] S. Pordes, Fermilab, private communication.

[15] A. Ito, W. Bosworth, J. Rutherford, A. Lynch, L. Tung, and W. Yang, Fermilab publication, TM 1200 - 2311.00 (1983)

[16] F. Sauli, *Principles of operation of multiwire proportional and drift chambers*, CERN 77-09, (1977).

[17] M.Crisler, Calorimeter Experimental Design Report, E711 internal memo (1984)

[18] J.F.Bartlett et al., Fermilab Multi User's Guide, PN-97.5(1979)

[19] CAMAC system, Atomic Energy Commission report TID-25875, Washington D.C.

[20] Fermilab-EP- Interactive Control System User's manual, version 1.00

[21] V.White et al.,IEEE Transaction on Nuclear Science NS-34,763 (1987)

[21] C.H.Georgiopoulos, J.H.Goldman, D.Levinthal and M.F.Hodous, Nuclear Inst. and Methods, A249, 451 (1986)

[22] The LUND montecarlo programs, CERN long writeup, 3 April 1987

[23] GEANT3 manual, CERN DATA HANDLING DIVISION, DD/EE/84-1 (1987)

[24] J.F. Owens, E.Reya and M. Gluck, Phys. Rev. D 18, 1501 (1978)

[25] R.P.Feynman, R.D. Field, G.C.Fox, Phys.Rev. D 18,3320 (1978)

[26] B.L.Combridge, J.Kripfganz and J.Ranft, Phys.Lett. 70B, 234 (1977)

[27] E.D. Bloom et al., Phys. Rev. Lett. 23, 930 (1969)

[28] M. Breidenbach et al., Phys. Rev. Lett. 23, 935 (1969)

[29] A. Bodek et al., Phys. Rev. Lett. 30, 1087 (1973)

[30] J.S. Poucher et al., Phys. Rev. Lett. 32, 9118 (1974)

[31] J.W. Cronin et al., Phys. Rev. D 11, 3105 (1975)

[32] B. Alper et al., Phys. Lett. 44B, 521 (1973)

[33] F.W. Busser et al., Phys. Lett. 46B, 471 (1973)

[34] J.D. Bjorken, Phys. Rev. 179, 1547 (1969)

[35] J.B. Kogut and L. Susskind, Phys. Rep. 8C, 75 (1973)

[36] S.D. Ellis and M.B. Kislinger, Phys. Rev. D9, 2027 (1974)

[37] R.P. Feynman, Phys. Rev. Lett. 23 : 1415 (1969)

[38] G. Arnison et al., Phys. Lett. B 123 : 115 (1983)

[39] G. Arnison et al., Phys. Lett. B 132 : 214(1983)

[40] T. Akesson et al., Phys. Lett. B 118 : 185 (1982)

[41] T. Akesson et al., Phys. Lett. B 123 : 133 (1983)

[42] D.A. Levinthal, Ph.D. thesis, Columbia University, 1980

[43] K.R.Turner, Ph.D. thesis, Florida State University, 1989

[44] G.Altarelli and G.Parisi, 1977, Nucl.Phys. B126, 298

[45] T.Umematsu, Phys.Lett. 79B,97(1978)

[46] J.F.Owens, Phys.Lett. 76B, 85(1978)

[47] J.F.Owens, Phys.Rev. D 19,3279 (1979)

[48] D.H. Levinthal, private communication

[49] U. Fano, Ann. Rev. Nucl. Sci. **13**, 1 (1963)

[50] D.Krause and G.Koizumi, Fermilab Report # TM-607(1975)

APPENDIX A

A.1 Introduction

This appendix is devoted to the description of the procedure used to calculate the energy of a particle hitting the calorimeters. There are three different categories of particles to consider :

a) minimum ionizing particles

b) γ, electrons and positrons

c) hadrons.

• Minimum ionizing particles.

A minimum ionizing particle (typically a μ with energy ≥ 370 MeV and less than few hundreds GeV) interacts with matter losing energy only by ionization of the medium crossed. The rate of energy loss is described by the Bethe-Bloch equation[49] :

$$\left\langle \frac{dE}{dx} \right\rangle_{inc} = \frac{D Z_{med} \rho_{med}}{A_{med}} \left(\frac{Z_{inc}}{\beta_{inc}} \right)^2 \left[\ln \frac{2 m_e \gamma_{inc}^2 \beta_{inc}^2 c^2}{I} - \beta_{inc}^2 - \frac{\delta}{2} - \frac{C}{Z_{med}} \right] (1 + \nu) \tag{A.1}$$

where $D = 0.3071$ MeV cm^2/g, Z_{med} and A_{med} are the charge and mass numbers of the medium, ρ_{med} is the density of the medium, I, δ, C, ν are phenomenological functions. $I \cong 16(Z_{med})^{0.9}$ eV when $Z_{med} > 1$. δ, C, ν are negligibly small in scintillator and for relativistic particles. (A.1) has a minimum when $\gamma_{inc} \simeq 3.57$ ($\gamma_{inc} \equiv \frac{1}{\sqrt{1-\beta_{inc}^2}}$ and β_{inc} is referred to the incident particle) and very slowly rises for larger γ_{inc}. The energy loss of a 5 GeV μ in the electromagnetic part of the calorimeter is shown in figure A.1, result of a simulation of 1000 events, and also in figure A.2[43] for experimental data (energy deposited in the calorimeter module H2UW-2 expressed in ADC counts). The Landau behaviour is typical of an interaction in which the particle is not fully contained in the calorimeter and the energy release is small.

• γ, e^+ and e^-

γ, e^+ and e^- interact with matter only electromagnetically. γ's above few MeV mainly convert into e^+e^- pair. Electrons and positrons of energy above 10 MeV mainly produce bremsstralhung γ's and ionize the medium. e^+ can also annihilate and produce a γ. When one of these particles, with energy in the GeV range, hit the calorimeter an electromagnetic shower developed. Since the first section of the calorimeter was about 30 radiation lengths long, all the electromagnetic showers were fully contained in it.

• Hadrons.

When a high energy hadron penetrates matter, interacts, produces a shower.

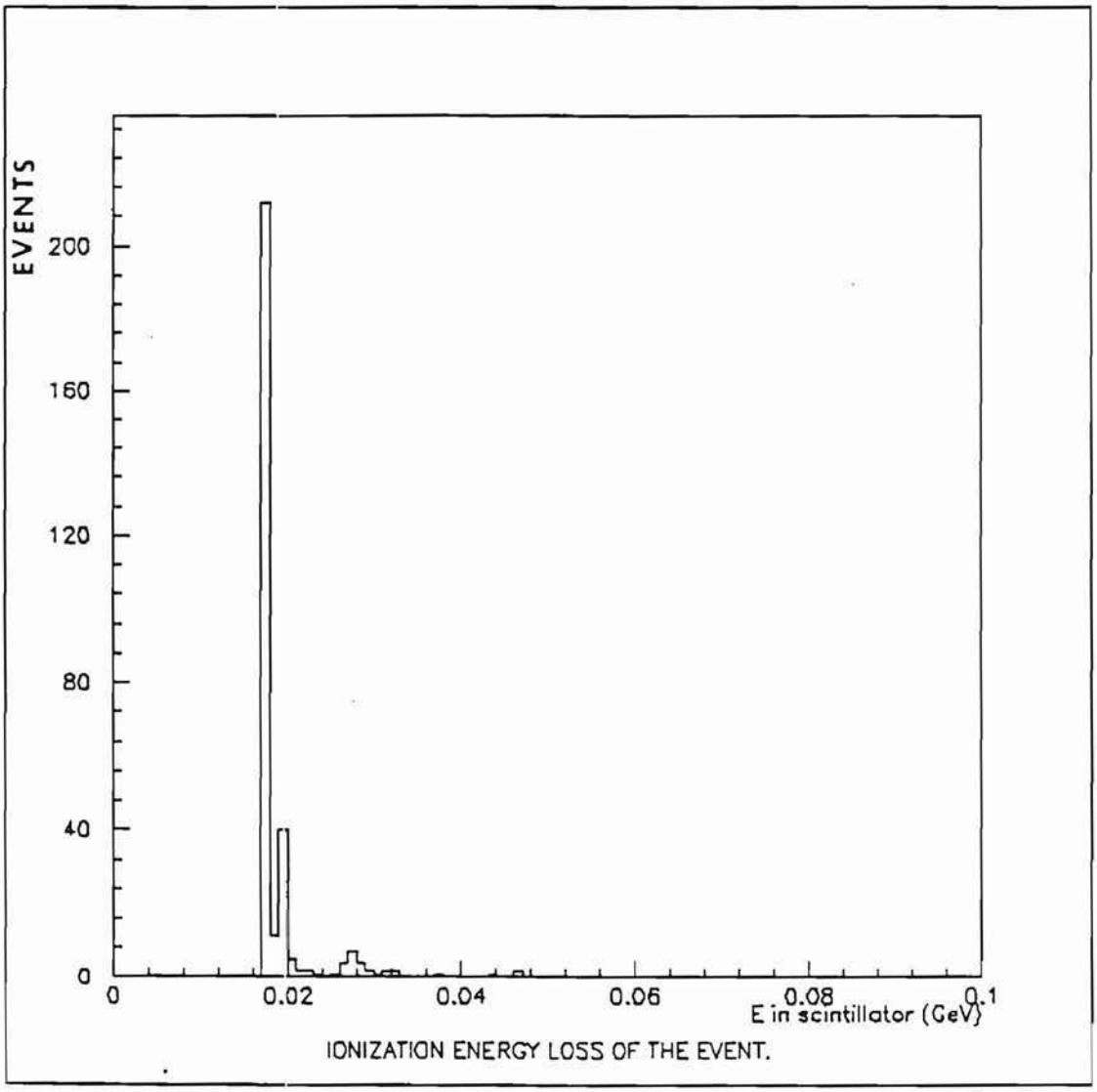

Simulation of the ionization loss of muons in the EM calorimeter

Figure A.1

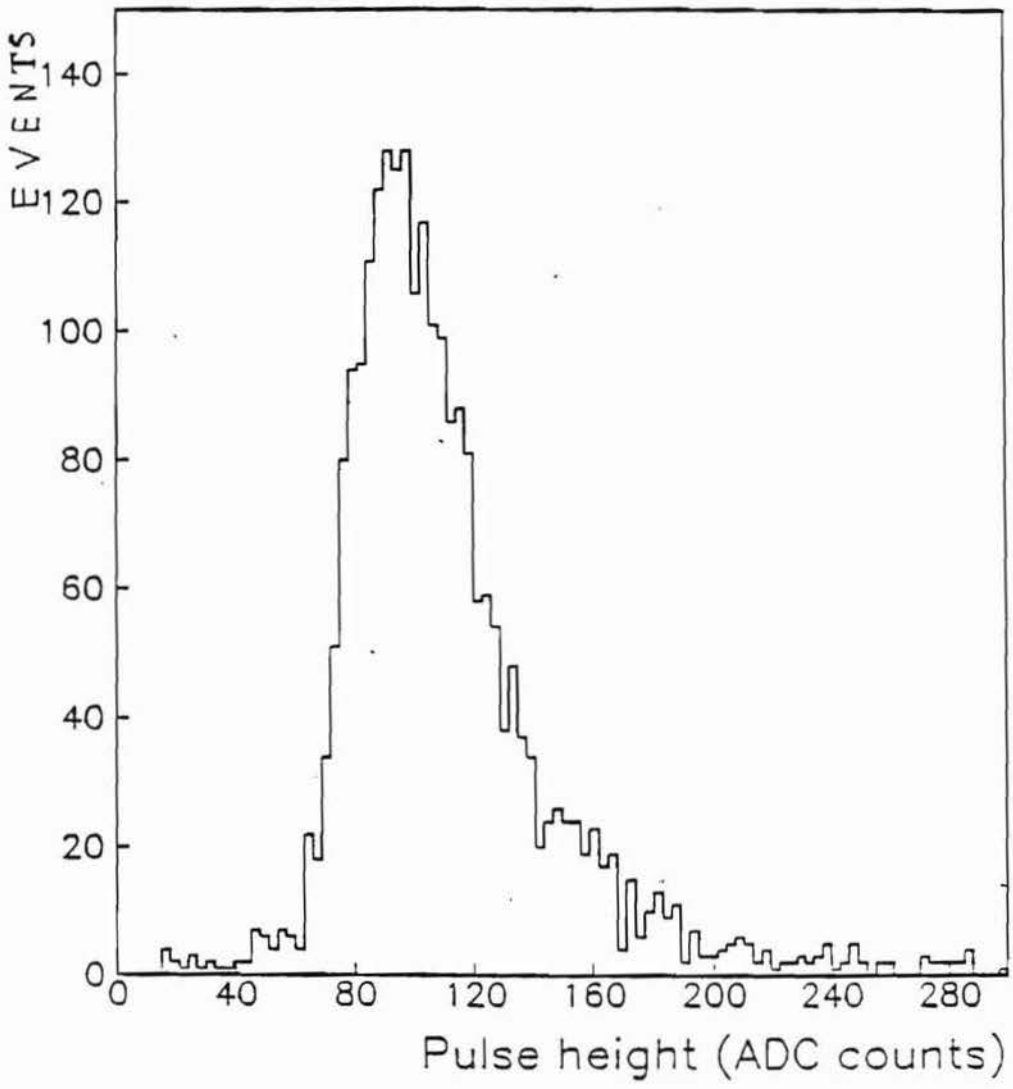

ADC count distribution when a muon passed through calorimeter module H2UW (calibration data)[43]

Figure A.2

Hadrons, γ's, e^+ and e^- are produced in the process. All the charged particles produced lose energy by ionization of the medium crossed.

The first step of the calibration of the calorimeter was the determination of the energy deposited by ionizing particles in the calorimeter modules knowing the ADC counts of the corresponding PMTs. In order to achieve that, muons coming to the experimental hall parallel to the beam direction were used. Muons are minimum ionizing particles and the average energy deposited in the scintillator depends only on the thickness crossed. Since the direction of the muons was selected along $\hat{\mathbf{z}}$ by means of some scintillator counters in coincidence used as trigger, the average amount of energy they deposited was known. To this energy it corresponded the average ADC counts ($\equiv \langle \mathrm{ADC}_\mu \rangle$) of histograms of the type of the one of figure A.2. For the data collected during the data taking runs the energy ($\equiv$ E) deposited in the calorimeter modules by the particles corresponding to N_{ADC} ADC counts of the phototube was given by :

$$\mathrm{E} = \frac{\mathrm{N_{ADC}}}{\langle \mathrm{ADC}_\mu \rangle} \times \frac{High}{Low} \times \left\langle \frac{d\mathrm{E}}{dx} \right\rangle \delta x$$

where δx is the thickness of the scintillator. $\frac{High}{Low}$ is the ratio between the gain of the phototube when its voltage was set to the level for muon detection (higher gain) and the gain for the detection of particles during the data taking. The energy deposited in a calorimeter module by the particles was calculated taking the average of the corresponding west and east PMTs :

$$\begin{aligned} \mathrm{E}_{module} &= \frac{1}{2}(\mathrm{E}_{west} + \mathrm{E}_{east}) \\ &= \frac{1}{2}\left[\frac{N_{ADC\ west}}{\langle \mathrm{ADC}_\mu \rangle_{west}}\left(\frac{High}{Low}\right)_{west} + \frac{N_{ADC\ east}}{\langle \mathrm{ADC}_\mu \rangle_{east}}\left(\frac{High}{Low}\right)_{east}\right]\left\langle \frac{d\mathrm{E}}{dx} \right\rangle \delta x. \end{aligned}$$

The second step of the calibration was the calculation of the energy of the primary particles that showered in the calorimeters. Two methods were used for the electromagnetic and hadronic showers. For the first case a montecarlo simulation has been used, a direct test beam measure was used for the second case.

A.2 Calibration of the electromagnetic shower

Only the electromagnetic section of the calorimeters needed to be considered since the shower was completely contained in it. The simulation program[23] was organized as follows : γ's of various energies ($E_\gamma = 10, 25, 50, 100$ GeV) were generated with momentum along the $\hat{\mathbf{z}}$ direction. They showered in the 14 slabs of 1/4" scintillator and 13 slabs of 1/2" lead forming the EM section of the calorimeter. The γs were allowed to interact with the following mechanisms :

(a) e^+e^- pair production

(b) photoelectric effect

(c) Compton effect

(d) photofission of nuclei.

The electron and positrons produced were allowed to interact with the following mechanisms :

(e) bremsstralhung γ production

(f) Coulomb multiple scattering

(g) δ ray production

(h) energy loss by ionization of the medium

(i) annihilation of the e^+ with an e^- of the medium and production of a γ.

In an electromagnetic shower the energy the phototubes can detect is only produced by the mechanism (h) in the scintillator pieces. Figure A.3 shows $E_{\gamma seen}$ ($\equiv$ the average detected ionization loss energy in the scintillator of the EM calorimeter) for the values of E_γ previously mentioned. The gaussian shape of the distribution is expected since the shower was completely absorbed in the EM section of the calorimeters. In TABLE A.1 $E_{\gamma seen}$, σ_E ($\equiv$ the r.m.s. of the detected ionization loss energy in the scintillator), the error on $E_{\gamma seen}$ and $\frac{E_{\gamma seen}}{E_\gamma}$ are tabulated. $\frac{E_{\gamma seen}}{E_\gamma}$ is essentially constant independent of E_γ as expected from the linearity of the calorimeter. The value of $\frac{E_{\gamma seen}}{E_\gamma}$ assumed in this analysis is the mean of the four values of TABLE A.1

$$d \equiv \left\langle \frac{E_{\gamma seen}}{E_\gamma} \right\rangle = 0.0258 \pm 0.0001$$

For each energy, the resolution σ of the electromagnetic calorimeter was given by

$$\sigma = \frac{\sigma_E}{\left(E_{\gamma seen}/E_\gamma\right)} = \frac{E_\gamma}{E_{\gamma seen}}\sigma_E.$$

Therefore

$$\frac{\sigma}{E_\gamma} = \frac{\sigma_E}{E_{\gamma seen}}.$$

In TABLE A.1

$$\frac{\sigma}{E_\gamma}\sqrt{E_\gamma} = \frac{\sigma}{\sqrt{E_\gamma}}$$

is tabulated at 10, 25, 50 and 100 GeV . Its value is essentially constant around 45%.

In figure A.4 the radius of the shower is plotted, for the same E_γ 's. It is $\sim$ 0.6 cm, independent of E_γ and in 1. cm of radius 83% of the shower energy is

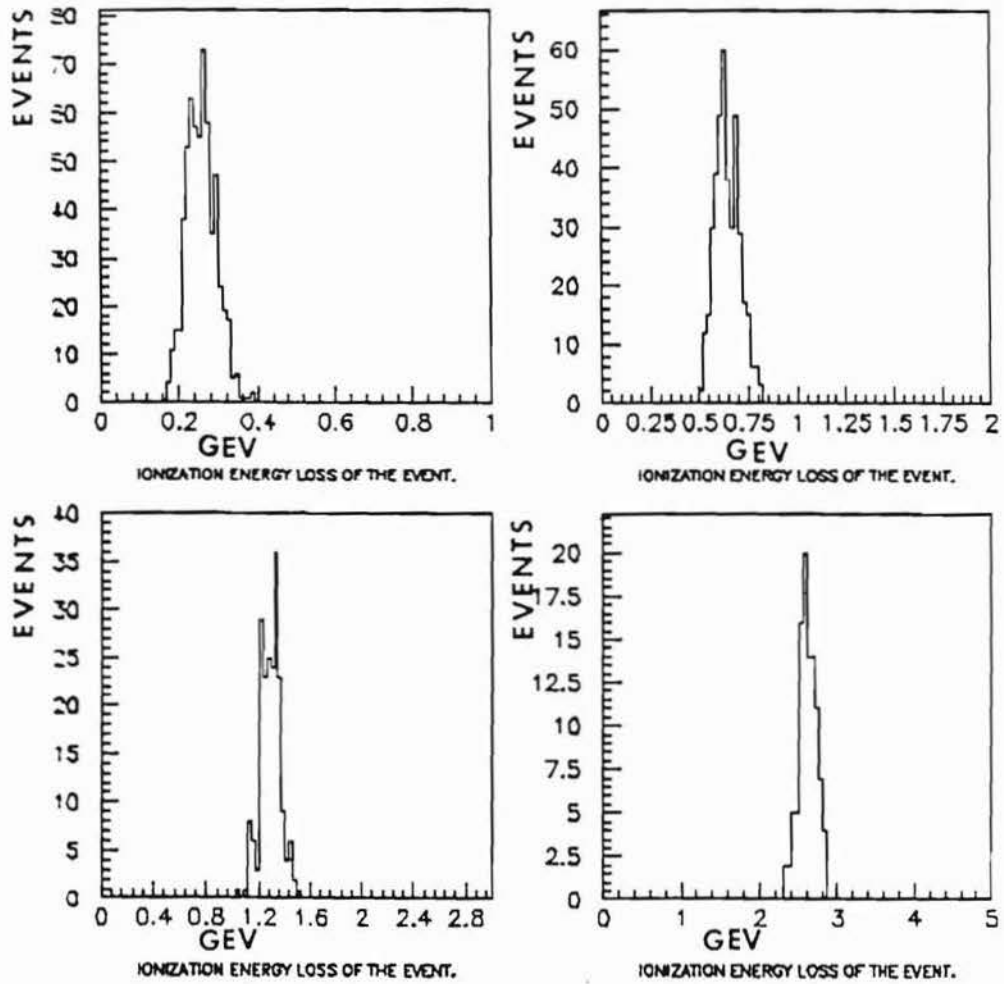

a) energy of primary γ = 10 GeV

b) energy of primary γ = 25 GeV

c) energy of primary γ = 50 GeV

d) energy of primary γ = 100 GeV

Simulation of the energy loss of γ of 10, 25, 50 and 100 GeV in the EM calorimeter section

Figure A.3

contained on average. The values of $< r >$ are shown in TABLE A.2 for various E_γ.

The initial energy E_γ of a γ which deposited an amount $\mathcal{E}$ of energy in the electromagnetic calorimeter is given by

$$E_\gamma = \frac{\mathcal{E}}{d} = \frac{\mathcal{E}}{0.0258} \qquad (A.2)$$

A.3 Calibration for hadronic showers[43]

A test beam calibration was used for the hadronic showers. The gain of the calorimeter PMTs was set at *High Gain* all throughout the calibration. A proton beam of energy 48.8 GeV$\pm$2.7% was used. A small dipole magnet[50] was used to bend the beam in the vertical direction and illuminate the two calorimeters. The ADC value of each PMT was scaled by its corresponding $\langle ADC_\mu \rangle$, so that the energy in minimum ionizing particle units was calculated for each phototube. A way to express the energy of the incident particle is to use a set of four constants, C_i, $i = 1, \ldots, 4$ one for each calorimeter section, and write the equation :

$$E_{beam} = \sum_{i=1}^{4} C_i P_i \qquad (A.3)$$

where

$$P_i = \sum_{j=1}^{2} \sum_{k=1}^{16} \frac{N_{ADC\ ij}}{\langle ADC_\mu \rangle_{ij}}$$

namely P_i is the sum of the ADC counts of all the PMTs scaled by their muon average. j is the west/east side index, k is the module index and i is the index of the calorimeter sections. $N_{ADC\ ij}$ are the ADC counts of the PMT signals, and

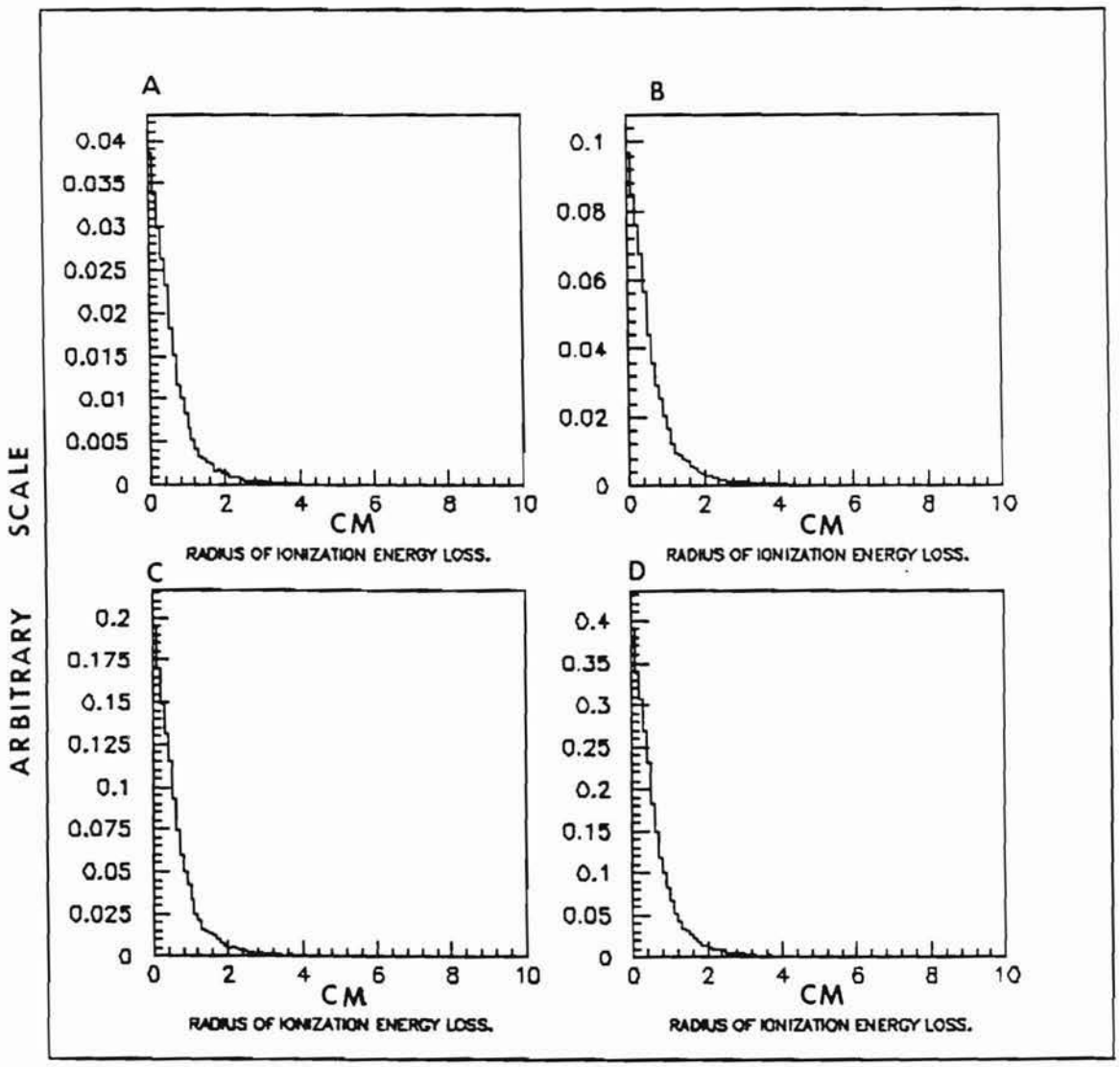

a) energy of primary γ = 10 GeV

b) energy of primary γ = 25 GeV

c) energy of primary γ = 50 GeV

d) energy of primary γ = 100 GeV

Radius of the simulated shower produced by γ of 10, 25, 50 and 100 GeV in the EM calorimeter section

Figure A.4

TABLE A.1

$E_\gamma \equiv$ energy of incident γ (GeV)	$E_{\gamma seen} \equiv < E >$ deposited in scintillator (GeV)	$\sigma_E \equiv$ r.m.s. of E deposited (GeV)	Error on $< E >$ deposited in scintillator (GeV)	$\frac{E_{\gamma seen}}{E_\gamma}$	$\frac{\sigma}{\sqrt{E_\gamma}}$
10	0.258	0.03656	0.00149	0.0258	0.45
25	0.645	0.06168	0.003084	0.0258	0.48
50	1.290	0.08055	0.005696	0.0258	0.44
100	2.607	0.1121	0.01121	0.02607	0.43

$$\text{Value of } d \equiv \left\langle \frac{E_{\gamma seen}}{E_\gamma} \right\rangle = 0.0258 \pm 0.0001$$

TABLE A.2

E_γ (GeV)	$< r >$ of the shower (cm)	Energy of the shower in scintillator contained in 1 cm radius/total energy of the shower in scintillator
10	0.598	83%
25	0.597	83%
50	0.590	84%
100	0.598	83%

$< ADC_\mu >_{ij}$ are the corresponding average muon ADC counts. The C_i can be considered constants relating on average the number of m.i.p.'s deposited in the ith calorimeter section to the energy lost by the *hadronic* shower in the section. Since E_{beam} is known, the C_i can be obtained minimizing

$$\chi^2 = \sum_{l=1}^{N_{events}} \left(\frac{E_{beam} - \sum_{i=1}^{4} C_i P_i}{\sigma} \right)_l^2$$

where l runs over the number of events selected for the calibration. σ is the error on $E_{beam} - \sum_{i=1}^{4} C_i P_i$, namely

$$\sigma = \sqrt{\sigma_{beam}^2 + \sigma_{calorimeter}^2} \tag{A.4}$$

where σ_{beam} is the r.m.s. of the energy of the test beam, $\sigma_{calorimeter}$ is the resolution of the calorimeter energy.

The minimization of the χ^2 with respect to the C_i gave the result listed in TABLE A.3[43]. The errors on the C_i's are purely statistical. The systematic errors were estimated from the difference between calibration constants for two different test beam runs. They were 5%, 2%, 9% and 19% for the four constants respectively. In figure A.5[43] the total energy of the calorimeter calculated using (A.3) is shown.

TABLE A.3[43]

Test beam run number	114
number initial events	9924
# events after hodoscope m.i.p.'s cut	7641
# events after calorimeter m.i.p.'s cut	7371
# events after EM section m.i.p.'s cut	6649
# events after y position cut	5726
# events after y position difference cut	5184
C_1 (EM section of the calorimeter)	0.446 ± 0.002
C_2 (H1 section of the calorimeter)	0.930 ± 0.004
C_3 (H2 section of the calorimeter)	0.855 ± 0.009
C_4 (H3 section of the calorimeter)	0.92 ± 0.03

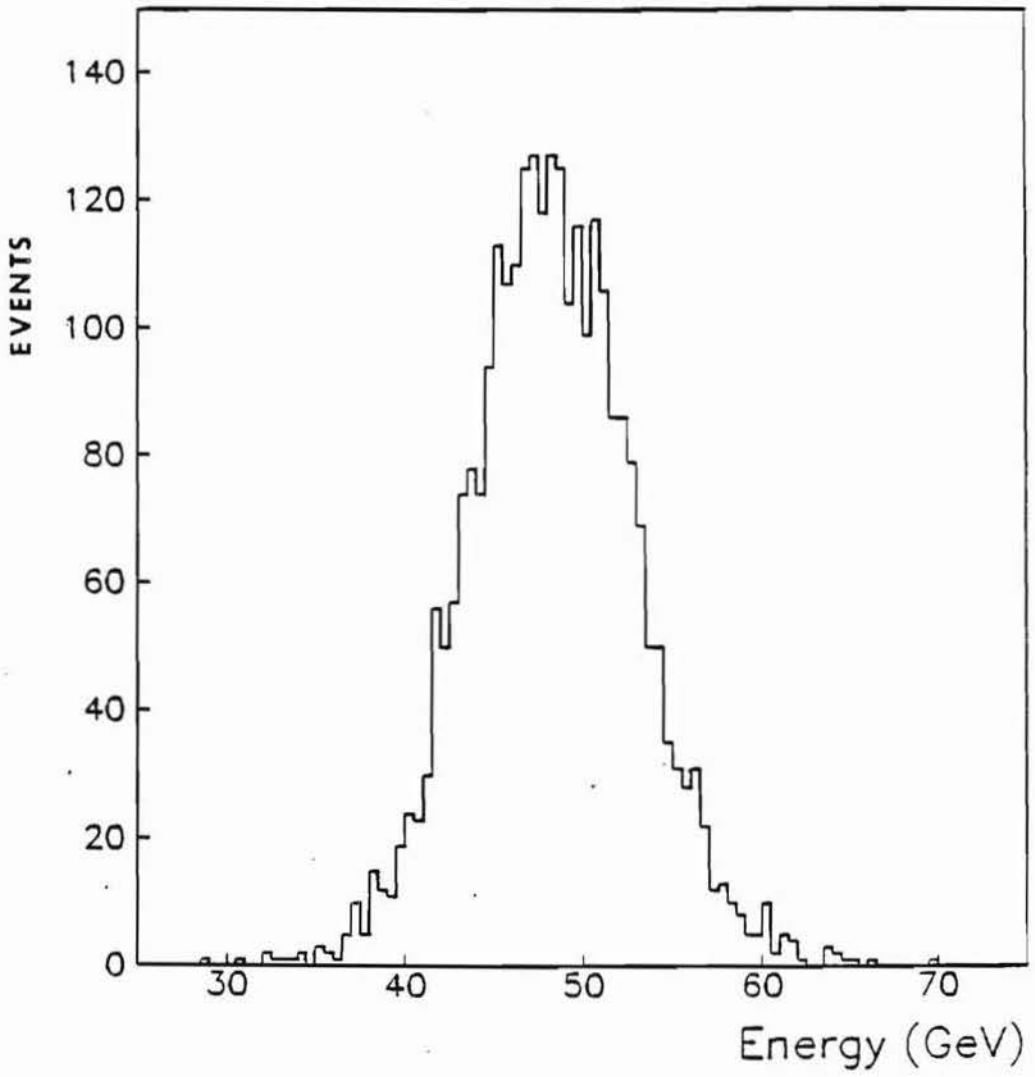

Total energy measured by the calorimeter using software calibration[43]

Figure A.5

APPENDIX B

This appendix is devoted to the proof of formula (5.2). Let us recall the definition of the auxiliary frame, still in the laboratory frame, used in (5.2) :

1) $\hat{\mathbf{z}}$ lies along the direction of the leading hadron.

2) $\hat{\mathbf{x}}$ lies in the plane formed by the leading hadron direction and $\mathbf{P}_{total}$ of the di-hadron system, in the direction opposite to $\mathbf{P}_{total}$ with respect to $\hat{\mathbf{z}}$.

3) The $\hat{\mathbf{y}}$ direction is according to the right hand rule (see figure 5.15).

Let ϕ', θ' be the azimuthal and polar angles of a soft particle in the auxiliary frame. Let $\mathbf{P}_{soft}$, $\mathbf{P}_{le}$ be the momenta of the soft and leading particles in the laboratory frame. Let us consider a frame still with respect to the laboratory, having $\hat{\mathbf{z}}$ along $\mathbf{P}_{total}$ and let us call it 'P_{total} frame'. Let $\mathbf{P}_{\perp soft}$, $\mathbf{P}_{\perp le}$, $\mathrm{P}_{||soft}$, $\mathrm{P}_{||le}$ be the transverse and longitudinal (along $\hat{\mathbf{z}}$) components of the soft and leading particles in that frame. A suitable Lorentz boost along $\hat{\mathbf{z}}$ of the P_{total} frame enables to calculate the particle momenta in the C.o.M. of the di-hadron system. Let $\mathbf{P}'_{soft}$ and $\mathbf{P}'_{le}$ the momenta respectively of the soft and leading particles in the di-hadron C.o.M. frame just mentioned. Let us finally assume that the mass of the soft and leading particles are negligible with respect to their

momenta so that $|\mathrm{E}| = |\mathbf{P}|$. One can now write :

$$\cos\Theta_{soft} \equiv \frac{\mathbf{P}'_{soft}\cdot\mathbf{P}'_{le}}{\mathrm{P}'_{soft}\cdot\mathrm{P}'_{le}}$$

Now

$$\mathbf{P}'_{soft}\cdot\mathbf{P}'_{le} = \mathrm{P}'_{\|soft}\cdot\mathrm{P}'_{\|le} + \mathbf{P}'_{\perp soft}\cdot\mathbf{P}'_{\perp le} =$$
$$= \mathrm{P}'_{\|soft}\cdot\mathrm{P}'_{\|le} + \mathbf{P}_{\perp soft}\cdot\mathbf{P}_{\perp le}$$

the last passage being possible thanks to the invariance of the transverse component of $\mathbf{P}$ with respect to the Lorentz boost. Therefore

$$\cos\Theta_{soft} = \frac{\gamma(\mathrm{P}_{\|soft} - \beta\mathrm{P}_{soft})\gamma(\mathrm{P}_{\|le} - \beta\mathrm{P}_{le}) + \mathbf{P}_{\perp soft}\cdot\mathbf{P}_{\perp le}}{\gamma(\mathrm{P}_{soft} - \beta\mathrm{P}_{\|soft})\gamma(\mathrm{P}_{le} - \beta\mathrm{P}_{\|le})}$$

where βc is the speed of the di-hadron system in the P_{total} frame (and obviously also in the laboratory frame) and $\gamma \equiv \frac{1}{\sqrt{1-\beta^2}}$. Hence

$$\cos\Theta_{soft} = \frac{(\mathrm{P}_{\|soft} - \beta\mathrm{P}_{soft})(\mathrm{P}_{\|le} - \beta\mathrm{P}_{le}) + (1-\beta^2)\mathbf{P}_{\perp soft}\cdot\mathbf{P}_{\perp le}}{(\mathrm{P}_{soft} - \beta\mathrm{P}_{\|soft})(\mathrm{P}_{le} - \beta\mathrm{P}_{\|le})}$$

Now, since $\mathbf{P}_{\perp soft}\cdot\mathbf{P}_{\perp le} = \mathbf{P}_{soft}\cdot\mathbf{P}_{le} - \mathrm{P}_{\|soft}\mathrm{P}_{\|le}$ one obtains

$$\cos\Theta_{soft} =$$
$$= \frac{(1-\beta^2)\mathbf{P}_{soft}\cdot\mathrm{P}_{le} + \beta^2\mathrm{P}_{\|soft}\mathrm{P}_{\|le} - \beta(\mathrm{P}_{\|soft}\mathrm{P}_{le} + \mathrm{P}_{\|le}\mathrm{P}_{soft}) + \beta^2\mathrm{P}_{le}\mathrm{P}_{soft}}{(\mathrm{P}_{soft} - \beta\mathrm{P}_{\|soft})(\mathrm{P}_{le} - \beta\mathrm{P}_{\|le})} \tag{B.1}$$

We now want to write $\cos\Theta_{soft}$ in terms of ϕ' and θ' angles of $\mathbf{P}_{soft}$ in the auxiliary frame. Let α be the angle between $\mathbf{P}_{le}$ and $\mathbf{P}_{total}$ $(0 \le \alpha \le \pi)$.
Then $\mathrm{P}_{\|le} = \mathrm{P}_{le}\cos\alpha$. Also, recalling the definition of the auxiliary frame, in that frame $\mathbf{P}_{total}$ has the following form :

$$\mathbf{P}_{total} = [-\sin\alpha, 0, \cos\alpha]\mathrm{P}_{total}$$

Since

$$\mathbf{P}_{soft} = [\sin\theta'\cos\phi', \sin\theta'\sin\phi', \cos\theta']\mathrm{P}_{soft}$$

by definition, one finally obtains :

$$\mathrm{P}_{||soft} = \frac{\mathbf{P}_{soft} \cdot \mathbf{P}_{total}}{\mathrm{P}_{total}} = (\sin\alpha \sin\theta' \cos\phi' + \cos\theta' \cos\alpha) \cdot \mathrm{P}_{soft}$$

Inserting $\mathrm{P}_{||le}$ and $\mathrm{P}_{||soft}$ into (B.1)

$$\cos\Theta_{soft} = \frac{(1-\beta^2)\cos\theta' + \beta^2\cos\alpha(-\sin\alpha\sin\theta'\cos\phi' + \cos\theta'\cos\alpha)}{[1-\beta(-\sin\alpha\sin\theta'\cos\phi' + \cos\theta'\cos\alpha)](1-\beta\cos\alpha)} +$$
$$+ \frac{-\beta(-\sin\alpha\sin\theta'\cos\phi' + \cos\theta'\cos\alpha + \cos\alpha) + \beta^2}{[1-\beta(-\sin\alpha\sin\theta'\cos\phi' + \cos\theta'\cos\alpha)](1-\beta\cos\alpha)}$$

Now the goal is to determine the relation between θ' and ϕ' when one requires $a < \cos\theta_{soft} \leq 1$ (a=0.95 in the analysis of chapter 3). It follows

$$a < \frac{(1-\beta^2)\cos\theta' + \beta^2\cos\alpha(-\sin\alpha\sin\theta'\cos\phi' + \cos\theta'\cos\alpha)}{[1-\beta(-\sin\alpha\sin\theta'\cos\phi' + \cos\theta'\cos\alpha)](1-\beta\cos\alpha)} +$$
$$+ \frac{\beta(\sin\alpha\sin\theta'\cos\phi' - \cos\theta'\cos\alpha - \cos\alpha) + \beta^2}{[1-\beta(-\sin\alpha\sin\theta'\cos\phi' + \cos\theta'\cos\alpha)](1-\beta\cos\alpha)}$$

The denominator of the fraction is certainly bigger than 0. Consequently

$$a[1-\beta(-\sin\alpha\sin\theta'\cos\phi' + \cos\theta'\cos\alpha)](1-\beta\cos\alpha) < (1-\beta^2)\cos\theta' +$$
$$+ \beta^2\cos\alpha(-\sin\alpha\sin\theta'\cos\phi' + \cos\theta'\cos\alpha) +$$
$$+ \beta(\sin\alpha\sin\theta'\cos\phi' - \cos\theta'\cos\alpha - \cos\alpha) + \beta^2$$

Hence

$$\sin\theta'\cos\phi'[a\beta\sin\alpha(1-\beta\cos\alpha) + \beta^2\cos\alpha\sin\alpha - \beta\sin\alpha] +$$
$$+ \cos\theta'[-\beta\cos\alpha(1-\beta\cos\alpha) + \beta^2 - 1 - \beta^2\cos^2\alpha + \beta\cos\alpha] +$$
$$+ a(1-\beta\cos\alpha) + \beta\cos\alpha - \beta^2 < 0$$

Making the substitution :

$$\cos\theta' = \frac{1-\tan^2\frac{\theta'}{2}}{1+\tan^2\frac{\theta'}{2}}$$

and

$$\sin\theta' = \frac{2\tan\frac{\theta'}{2}}{1+\tan^2\frac{\theta'}{2}}$$

calorimeter section 197

A.2 ADC count distribution when a muon passed through calorimeter module H2UW (calibration data)[43] 198

A.3 Simulation of the energy loss of γ of 10, 25, 50 and 100 GeV in the EM calorimeter section 202

A.4 Radius of the simulated shower produced by γ of 10, 25, 50 and 100 GeV in the EM calorimeter section 204

A.5 Total energy measured by the calorimeter using software calibration[43] 208

one obtains

$$\tan^2\frac{\theta'}{2}[a+1-\beta^2(a\cos^2\alpha-\cos^2\alpha+2)]+ \\ +2\cos\phi'\tan\frac{\theta'}{2}(1-a)\beta(\beta\cos\alpha-1)\cos\alpha+(a-1)(1-\beta\cos\alpha)^2<0. \tag{B.2}$$

Let

$$A\equiv a+1-\beta^2(a\cos^2\alpha-\cos^2\alpha+2)$$

$$B\equiv 2(1-a)\beta(\beta\cos\alpha-1)\cos\alpha$$

$$C\equiv(a-1)(1-\beta\cos\alpha)^2$$

Then (B.2) becomes

$$A\tan^2\frac{\theta'}{2}+B\cos\phi'\tan\frac{\theta'}{2}+C<0 \tag{B.3}$$

It easy to check that $A>0$, $B\leq 0$, $C\leq 0$. The equation (B.3) is a second degree inequality in $\tan\frac{\theta'}{2}$. To solve it one has first to solve the equation

$$A\tan^2\frac{\theta'}{2}+B\cos\phi'\tan\frac{\theta'}{2}+C=0\Rightarrow\tan\frac{\theta'}{2}=\frac{B\cos\phi'\pm\sqrt{B^2\cos^2\phi'-4AC}}{2A} \tag{B.4}$$

The condition imposed earlier, $\cos\Theta_{soft}\leq 1$, implies $\tan\frac{\theta'}{2}\geq 0$ as well. Therefore, from (B.4) one derives

$$0\leq\tan\frac{\theta'}{2}<\frac{B\cos\phi'\pm\sqrt{B^2\cos^2\phi'-4AC}}{2A}$$

namely the formula (5.2).